REDUCTION OF NO_X EMISSION FOR LEAN PREVAPORIZED-PREMIXED COMBUSTORS

by

John C.Y. Lee

A dissertation submitted in partial fulfillment of
the requirements for the degree of

Doctor of Philosophy

University of Washington

2000

Program Authorized to Offer Degree: Mechanical Engineering

University of Washington
Graduate School

This is to certify that I have examined this copy of a doctoral dissertation by

John C.Y. Lee

and have found that it is complete and satisfactory in all respects,
and that any and all revisions required by the final
examining committee have been made.

Chair of Supervisory Committee:

____
Philip C. Malte

Reading Committee:

____
John C. Kramlich

____
Ann M. Mescher

Date: ____________________________

University of Washington

Abstract

REDUCTION OF NO_X EMISSSION FOR LEAN PREVAPORIZED-PREMIXED COMBUSTORS

by John C.Y. Lee

Chairperson of the Supervisory Committee: Professor Philip C. Malte
Department of Mechanical Engineering

The purpose of this research is to examine the formation and to determine the means of prevention of NO_X emission in lean prevaporized-premixed (LPP) combustion for application to gas turbine engines. The focus of this study is twofold: 1) examination of the effects of prevaporizer-premixer design and operation on NO_X formation and 2) examination of the effects of fuel type on NO_X formation.

Three generations of prevaporizing-premixing injector technology are used, beginning with very simple single stage prevaporizing-premixing injectors and continuing through to a staged prevaporizer-premixer (this is termed the SPP) of advanced design for which a patent has been applied. Parametric analysis conducted includes the effects of inlet temperature, injection pattern, degree of premixing and, of particular interest, fuel type.

The developmental history of the prevaporizing-premixing injectors used is discussed. A detailed review of the experimental results obtained for the SPP injector is presented. The research focuses on the full characterization of the SPP and the jet-stirred reactor (JSR) fed by the SPP. Effects including stage inlet temperature split, stage airflow split, stage residence time split and fuel variation are investigated to characterize the SPP and the NO_X formation in the JSR. A laser absorption technique is employed to quantify the degree of premixing at the SPP outlet.

Additionally, a separate multi-sampling port jet-stirred reactor is tested to provide detailed information on the temperature distribution within the JSR. Several chemical kinetic mechanisms are tested in conjunction with simple chemical reactor models (CRMs) of the JSR to enhance the understanding of the various NO_X formation mechanisms. A large hydrocarbon oxidation mechanism with pollutant formation chemistry is studied to enhance the understanding of the liquid fuel oxidation and NO_X formation processes.

The results show that complete vaporization of both pure and multi-component, commercial fuels is obtained with the SPP and that the premixing is nearly perfect. With the JSR fed by the SPP, the formation of NO_X from commercial liquid fuels, such as No. 2 diesel fuel, is within a factor two of the NO_X emission from natural gas. That is, the NO_X emission from liquid fuel firing is not significantly increased as is typically found with other injectors used in LPP combustion systems.

TABLE OF CONTENTS

LIST OF FIGURES

LIST OF TABLES

ACKNOWLEDGMENTS

The author wishes to express utmost gratitude to his advisor and mentor, Professor Philip C. Malte, for his constant support, guidance, demand for excellence and understanding. This work would not have been possible without his personal involvement and enthusiasm. In addition, Professor John C. Kramlich is also acknowledged for his often insightful suggestions and comments throughout this undertaking. Appreciation also goes to Professors Ann M. Mescher and Dilip R. Ballal for taking interest in this research and for agreeing to be on the thesis committee.

Sincere appreciation also goes to my AGTSR industrial mentors, Dr. Michael A. Benjamin of the Gas Turbine Fuel Systems Division at the Parker Hannifin Corporation and Dr. Robert C. Steele of the SoLoNO$_X$ Combustion Engineering Department at Solar Turbines, Incorporated. This research would not have been possible without their continued encouragement and financial support. Dr. Benjamin has been instrumental in making the development and fabrication of the staged prevaporizing-premixing injector a reality. In addition, the author is most thankful for Dr. Benjamin's continued interest and faith in the SPP technology.

Professor Robert W. Dibble of the Mechanical Engineering Department at the University of California at Berkeley is thanked for his generosity for providing assistance, technical advice and the hardware for the laser absorption experiments.

The author would also like to express sincere appreciation to the following companies for their generous equipment donation to the University of Washington's (UW) combustion program:

- John Fluke Corporation for donating the data acquisition and test instruments.

- Watlow Controls Company for donating the temperature controllers and power relays.

- Acer Computer Company for donating the laptop computers.

- Motorola, Honeywell and SenSym for donating the semiconductor pressure sensors.

In particular, the John Fluke Corporation has donated over $100,000 in test instruments over the past three years without any reservation.

The author also wishes to thank his fellow graduate students who have made this endeavor a most interesting and enjoyable one: Dr. Teodora Rutar for willingness to share her office with me and for putting up with my bad temper at times, Dr. David G. Nicol for his guidance and discussion on chemical reactor modeling and for his companionship on those lonely Saturdays, Dr. Jon H. Tonouchi for his help on converting the large hydrocarbon mechanisms and for his "stories" and Mr. Jacob Jun Liu for his reminder that everything is "pretty easy." Sincere thanks also goes to Mr. Tom Collins of the Mechanical Engineering machine shop for his invaluable suggestions and assistance in the design and fabrication of various injector and reactor components, Mr. George Andexler of the Mechanical Engineering electronics shop for his expertise and help in designing and fabricating various electronic circuitries, Mr. David Rice of the Material Science Engineering Department for his assistance in the fabrication and curing of the ceramic reactors, Mr. Bob Morely of the Physics & Astronomy Department for his assistance in fabricating and repairing the quartz sampling probes and for reminding me that I need to treat my wife better and Mr. Jim Duncan of the Gas Turbine Fuel Systems Division at the Parker Hannifin Corporation for his assistance in drawing and fabricating all of the components for the SPP injector. All these colleagues have helped to make life at the University of Washington more enjoyable and rewarding.

Acknowledgement also goes to close friends, Dr. Greg Jackson, Dr. Mark North and Mr. Steve Leung who at times provided the necessary words of wisdom and support. Lastly, the author is forever indebt to his wife, Emily, for her unwavering support, understanding and patience. Without her, this undertaking would not have been possible.

DEDICATION

To Emily, Jason, Mom & Dad and, especially, Justin.

CHAPTER 1: INTRODUCTION

The abatement of NO_X as driven by increasing environmental regulations has been the central focus of the gas turbine industry for the past two decades. Emission standards for NO_X in certain regions of the world are as low as 3 ppmv (corrected to 15% O_2) when operating on natural gas. With the advancement in technology, such as catalytic combustion, active control, and hybrid fuels, further reduction in regulated emission standards is expected. In fact, world financial bodies, such as the World Bank and the International Monetary Fund, require compliance of emission standards for all financed gas turbine sales.

In the past, water or steam injection has been used as the norm for NO_X reduction in both diffusion burning and “so-called” lean premixed (LP) systems. This method presents significant increases in capital, operational, and maintenance costs due to its need for water treatment and higher fuel consumption. The current interest is in the development of dry, ultra-lean premixed combustion systems. Many of these ultra-lean premixed systems approach the lean blowout or lean stability limit of the flame leading to severe consequences involving combustor oscillation, flashback, and blowout.

The emphasis of this research work is to study the formation and to determine the means of reduction of NO_X emission for dry, LP and dry, LPP high intensity combustion systems with focus on the effects of fuel variation. Furthermore, effects of inlet temperature, injection pattern, premixer residence time and degree of premixing are also considered. Both experimental and modeling results are presented for the atmospheric pressure jet-stirred reactor. The focus of the experimental work is realized through the use of a novel, staged prevaporizing-premixing injector that can operate on both gaseous and liquid fuels.

1.1 BACKGROUND AND JUSTIFICATION

Since the late 1980s and early 1990s every land based gas turbine (GT) manufacturer has placed high priority on the development of dry, LP combustion systems to meet ever more demanding NO_X emissions requirements. From Asea and Brown Boveri's (ABB) Environmental (EV) burners (Aigner and Muller, 1992 and Sattelmayer et al., 1992) and General Electric's (GE) Double Annual Counter-Rotating Swirler (DACRS) and Dry Low NO_X (DLN) burners (Leonard and Stegmaier, 1993 and Davis, 1996), to Solar Turbines' $SoLoNO_X$ designs (Rawlins, 1995 and Cowell et al., 1996), the research and development efforts have been focused on the reduction of NO_X emission through the use of dry, LP and dry, LPP technology.

Sub 15 ppmv (15% O_2) NO_X emissions have been reported by several GT manufacturers for production engines running on natural gas. Further reduction in NO_X to single digit levels (Joshi et al., 1994, Davis, 1996, Snyder et al., 1996, Steinbach et al., 1998, Dutta et al., 1997, Schlatter et al., 1997, Lipinski et al., 1998, Ozawa et al., 1998) has also been achieved by further "leaning-out" the flame, but this has led to several difficulties associated with lean flames. In particular, issues regarding combustion instability or oscillation leading to flashback and blowout of the flame, increased emissions and structural damage are of primary concern (Advanced Gas Turbine Systems Research, 1999).

For liquid fuels, the NO_X emission remains quite high. Currently, only ABB with its AEV (Advanced EV) burner has achieved NO_X emission levels below 25 ppmv on a dry basis for mid size engines running on No. 2 diesel fuel as published in their sales literature (1998) and discussed by Steinbach et al., 1998. Other GT manufacturers, particularly those with high compression ratio aeroderivative engines, are experiencing difficulties with insufficient fuel vaporization and mixing and with coking, flashback and autoignition. In fact, certain manufacturers have returned to using steam or water injection to control the NO_X emission to levels less than 40 ppmv. Thus, the challenge remains in determining the optimum method for the prevaporization and premixing of the liquid fuel and air prior to combustion.

As for fuel flexibility, an alternative to natural gas is synthetic gas or “snygas,” which consists mainly of CO and H_2 (and inerts). Syngas can be produced from many sources. One approach is the gasification of solid fuels, like coal. The quality of the natural gas is another important issue. Although U.S. natural gas is typically at least 88% methane by mole and frequently as high in CH_4 as 95 to 96%, natural gas in other parts of the world can be high in non-methane hydrocarbons. As for liquid fuel alternatives, the range is very broad. In developing nations, it is not unusual to see gas turbine engine power plants operating on residual fuel or Bunker C (see Shih, 1997). In some countries where the petrochemical and pharmaceutical industries are underdeveloped, such as India (see Andhrapradesh Industries, 1998), an important choice is naphtha – a light cut similar to gasoline (see Narula, 1998, Brushwood and McElwee, 1998, Molière et al., 1998, and Lee and Malte, 1999a). It is important to note that fuel choices are quite broad and unlimited (see Odgers and Kretschmer, 1986), and these choices are, in many cases, intimately tied to geo-political and economic factors.

In many cases, the use of alternative fuels does not cause much of a concern when applied to conventional diffusion burning gas turbine engines. In these diffusion combustion systems, water or steam is injected to control the levels of NO_X output. On the other hand, for a “well-tuned,” dry, low-NO_X, LP or LPP gas turbine engine designed for natural gas or No. 2 diesel fuel, any variation in the fuel properties may cause difficulties with regard to flashback, autoignition, excessive oscillations and high emissions (see Janus et al., 1997). Consequently, there is an increasing interest in the gas turbine industry to address the issue of fuel variability and fuel flexibility and the associated problems with flashback and autoignition (see Advanced Gas Turbine Systems Research, 1998 and 1999).

In order to understand the pollutant characteristics of commercial (or blended) fuels, one must first understand the pollutant characteristics of the constituents of the blended fuels. The current research builds on previous work conducted at the University of Washington. Additionally, the current research complements studies performed by Zelina and Ballal (1996), Zelina et al. (1996) and Blust et al. (1997) involving the use of an atmospheric pressure toroidal JSR.

One of the primary focuses of the present research is on fuel variability. Both academic and industrial research communities have expressed strong interest in understanding the lean premixed combustion behavior of various fuels ranging from syngas to natural gas and from the light distillates (e.g., naphtha) to the heavy distillates (e.g., Bunker C). Again fuel variability presents concerns in regards to NO_X emission (the focus of this research), coking, autoignition and flashback.

Another concern of this research is in the processes involved in optimizing the prevaporizing and premixing of the liquid fuel and air prior to combustion. Because of the complex nature of the commercial fuels, prevaporizing and premixing procedures must address the specific characteristics of the various components in the parent liquid fuel. Fuel properties such as boiling points, evaporation rates and autoignition conditions must be considered. The present research is performed with the use of a patent pending, dual fuel, staged prevaporizing-premixing injector that was developed at the University of Washington (Lee and Malte, 1999b).

Furthermore, detailed large hydrocarbon (C_3^+) oxidation mechanisms with pollutant formation chemistry are tested with chemical reactor models to provide enhanced understanding of the JSR-SPP liquid fuel combustion process.

1.2 OBJECTIVES AND APPROACH

The objective of this research is to study NO_X emission reduction for liquid fuels through the use of various injector designs under dry, LPP conditions. An atmospheric pressure jet-stirred reactor is used to simulate the NO_X formation in the primary zone of modern low NO_X LP gas turbine combustors. The effects of fuel type, inlet temperature, injection pattern and injector flow pattern on the formation of NO_X are studied.

Chemical reactor models are employed to further the understanding of the various NO_X formation pathways. The chemical reactor models include a single perfectly stirred reactor (PSR) model, a two PSR model in series [with and without the addition of a plug flow reactor (PFR)] and a three PSR in series model. The current CRM computer code, known as MARK III, was initially developed by Pratt and later modified by Nicol (1995). Chemical kinetic mechanisms used in the CRM code are from Miller and Bowman (1989), the Gas Research Institute (1996 and 1999) and Maurice et al., 1999.

The approach used to accomplish this research includes both experimental and numerical aspects listed as follows:

- Atmospheric pressure testing of a multi-sampling port JSR. This multi-sampling port JSR has 20 sampling (or viewing) ports located at various heights and radial positions. Data collected provide enhanced understanding of the reactor temperature and the reactor wall thermal distributions. The reactor thermal profile data allows better understanding of the effects of jet entrainment as provided through the use of different nozzle configurations.

- Atmospheric pressure testing of the dual fuel SPP attached to a standard JSR. The following parametric effects are studied in detail:

    - ➢ Fuel Type: Tests include fuel types such as methanol, straight alkanes, aromatics and commercial fuels. The fuel carbon to hydrogen molar ratio is from 0.25 to 1.0.

  - Inlet Temperature Split in the SPP: The effect of inlet temperature on NO_X emission is studied in detail. An optimum split condition is determined.

  - Airflow Split in the SPP: The airflow split has significant effect on the mixing intensity of each stage that influences the overall mixing in the injector. An optimum split condition is determined with the aid of the laser absorption technique that provides quantitative measurements of the degree of mixing.

  - Residence Time Split in the SPP: Both long and short residence time configurations are tested and an optimum SPP configuration is determined for the reduction of NO_X emission.

- Use of simple perfectly stirred reactor and plug flow reactor models to interpret the chemistry trends in the JSR-SPP setup. Development of empirical correlation of NO_X with fuel type for application to high-intensity, dry, lean premixed combustion.

- Interaction with Dr. Lourdes Maurice of Wright Laboratory for the validation of the higher order (C_3^+) hydrocarbon mechanism.

1.3 ORGANIZATION

The basic organization of this dissertation is structured in accordance with the chronological progression of injector development effort. Each chapter is intended to build upon the work of the previous chapters. The dissertation is structured in the following order:

- Chapter 2: Experimental apparatus associated with the setup, diagnosis and operation of the jet-stirred reactor are described in detail. Computer aided design (CAD) drawings of the JSRs are provided in the Appendix. A unique laser diagnostic technique is also presented. Modernization efforts with the use of feedback loop control, state-of-the-art sensors and data acquisition instruments are discussed. Operating procedures are also described in detail.

- Chapter 3: Full description of the first generation injector. Conceptual framework and results are presented.
- Chapter 4: Full description of the second generation injector. CAD drawings are presented in the Appendix. Design theory and results from two different parametric studies are presented.
- Chapter 5: Full description of the SPP injector. CAD drawings are presented in the Appendix. Techniques embodied in the SPP prototype are discussed. Optimal operating conditions for the prototype SPP and JSR are determined. Detailed discussion on the effects of fuel type is presented.
- Chapter 6: NO_X formation chemistry, chemical kinetic mechanisms and chemical reactor models for LP combustion are presented. Modeling results of the high temperature oxidation of several fuels are presented and compared to experimental results.
- Chapter 7: The major conclusions of the research and recommendations for continued work are discussed and proposed.

1.4 MAJOR FINDINGS

The formation of NO_X for various injectors tested under dry, lean premixed conditions has been examined as a function of various parameters. Experimental results have been obtained for atmospheric pressure testing of a 15.8 cc jet-stirred reactor and the results have been compared to chemical reactor models using various kinetic mechanisms. The major findings are:

- Successful development of a liquid fuel atomizer of the Nukiyama-Tanasawa type with high turndown ratio suitable for generating fine spray droplets (diameters of 15 μm or less) for a wide range of liquid fuels.

- Preflame fuel oxidation and pyrolysis have been observed in the form of coke and gum formation for injectors operating with high inlet temperatures and long residence times, but without the occurrence of autoignition.

- Successful development of a staged prevaporizing-premixing injector that can provide a high degree of premixing for both LP and LPP processes. The staged prevaporizing and premixing injector provides quick and intense vaporization and mixing of the fuel and air leading to optimized reduction of NO_X formation. The SPP technique shows great promise for applications to industrial LPP combustion processes.

- Jet mixing is very effective for obtaining a high degree of premixing in both the SPP injector and the JSR. Measurements of the degree of fuel and air mixedness as a function of airflow split in the SPP have been obtained quantitatively with a simple laser absorption technique.

- An NO_X emission trend that is independent of injection nozzle (or nozzle block) configuration for fuels with C:H ratio ranging from 0.25 to 0.5.

- An NO_X emission that is independent of injector length indicating that the mixing intensity in the SPP is high.

- The effect of injector inlet temperature is minimal if the degree of premixing is high.

- NO_X emission is most sensitive to fuel type for light hydrocarbons, aromatic hydrocarbons and methanol.

- NO_X emission data for fuels containing small amounts of fuel bound nitrogen indicate that the fuel bound nitrogen is completely converted to fuel NO_X under LPP combustion processes.

- The NO_X emission with the commercial liquid fuels (i.e., No. 2 diesel fuel and light naphtha) is no more than a factor two greater than that found for natural gas. This indicates the potential for low-emission, liquid-fired, practical combustors.

- CO formation increases linearly with increasing fuel C:H ratio for most hydrocarbon fuels with the exception of methanol and light gaseous hydrocarbons fuels (i.e., methane and ethane).

- A near linear relationship exists between NO_X and CO (and C:H ratio) for most hydrocarbon fuels tested with the exception of methanol and aromatic hydrocarbons.

- In general, chemical reactor modeling confirms the experimental NO_X and CO trends.

- Single PSR modeling with CO/H_2 fuels with variable CO to H_2 ratio appears to explain the measured NO_X formation trends based on the Zeldovich and N_2O mechanisms.

- The dual PSR model indicates the importance of prompt NO formation under the LP and LPP combustion processes.

- The three PSR model in conjunction with the GRI 3.0 mechanism provides the best prediction of the experimental values.

CHAPTER 2: JET-STIRRED REACTOR SETUP, DIAGNOSTICS AND OPERATION

The development and use of the laboratory jet-stirred reactors have come a long way. Since its introduction by Longwell and Weiss (1955), several research groups (e.g., Malte and Pratt, 1974, Singh et al., 1979, Steele, 1995, Blust et al., 1997, and Bengtsson et al., 1998) have employed various types of JSRs for studying combustion and pollutant formation kinetics. Thornton (1989) performed a considerable amount of reactor development work that has led to the current inverted, truncated cone shape JSRs that are utilized at the UW to study the NO_X formation chemistry for various fuels under LP and LPP combustion conditions.

The current atmospheric pressure jet-stirred reactor has been tested with three different prevaporizing-premixing injectors, including the 1st generation, 2nd generation, and 3rd generation or SPP injectors, that will be described in detail in Chapters 3, 4 and 5, respectively. Figure 2.1 is a simple representation of the atmospheric pressure JSR system that consists of a ceramic JSR, an injector (the one shown is the SPP), an ignition system, several flow control and monitoring hardware for both the air and fuel streams, inlet temperature control circuitry, pressure monitoring components and a data acquisition system. Additionally, diagnostic tools are required for flame temperature measurements, emission gas sampling and fuel and air unmixedness characterization. The setup and operation of the JSR experiments and diagnostic techniques are discussed in the following sections.

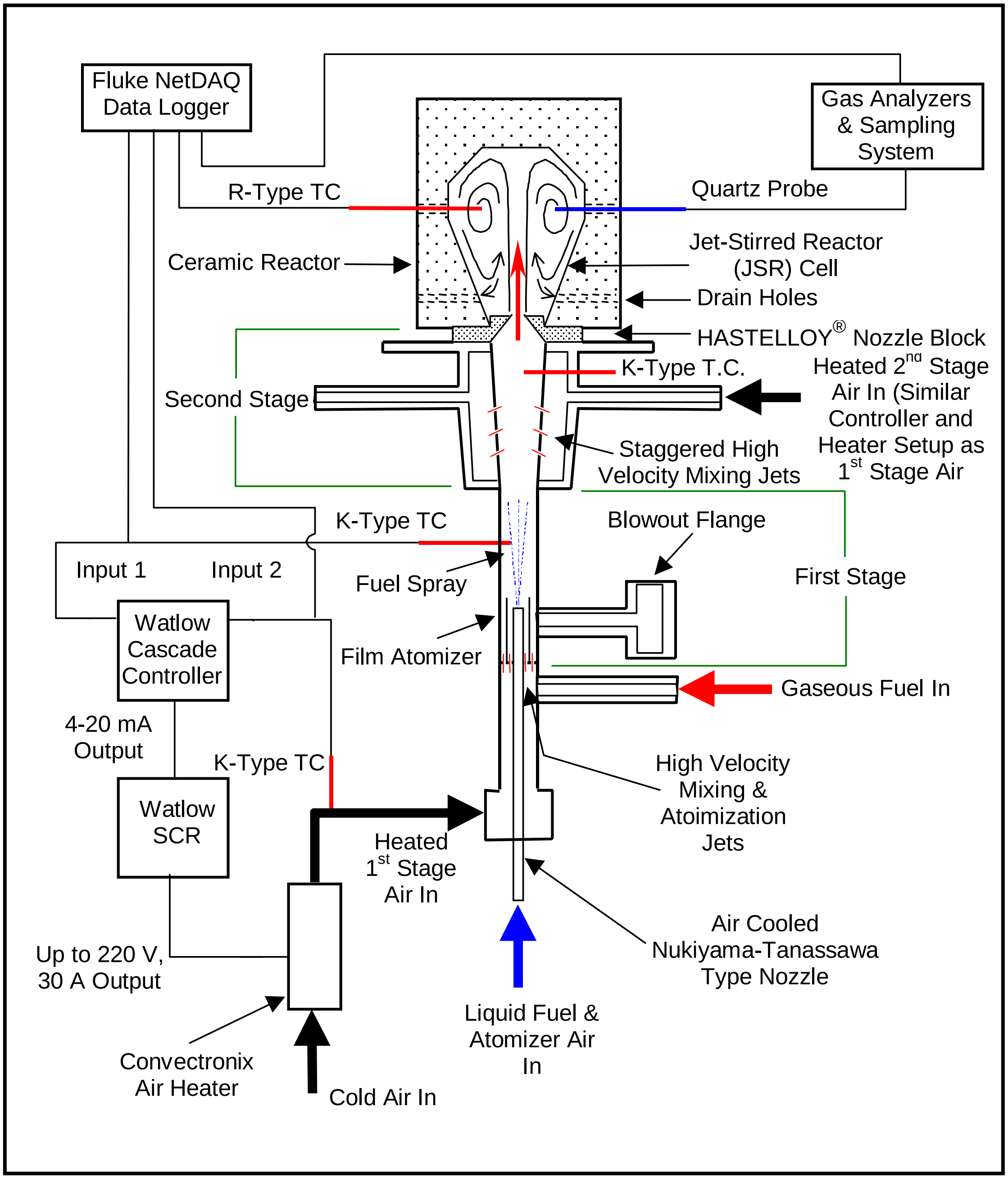

Figure 2.1. Schematic Drawing of the Atmospheric Pressure JSR, of 15.8 cc Volume, with the Staged Prevaporizing-Premixing Injector and Accessories.

2.1 JET-STIRRED REACTOR

The main attraction of the jet-stirred reactor technique for studying pollutant formation chemistry is the approximation of the JSR to that of a well-stirred reactor (WSR) where the temperature and species concentrations are spatially uniform in the time-mean (or measured) domain. The approach of the JSR to that of a WSR is an indication that the rate of mixing is rapid and intense (i.e., relatively short mixing times) as compared to the rates of pollutant formation (i.e., relatively long chemical times). In other words, the JSR is characterized by small (<<1) Damköhler (Da) values. This high intensity mixing in the JSR is provided by the high velocity jet(s) formed as the fuel and air mixture accelerates through the nozzle block. In order to generate the high velocity jet(s), significant pressure drop (> 10%) across the nozzle block is required and this is seldom seen in practical combustion systems which usually operate with less than 5% pressure drop across the injector-combustor sections. Nevertheless, the approach to the WSR condition simplifies application of diagnostic measurements and chemical reactor models.

2.1.1 JET-STIRRED REACTOR CONSTRUCTION

Two atmospheric pressure jet-stirred reactors are used in this research. The standard JSR, similar to the one used by Steele (1995) and Capehart (1995), has four sampling/viewing ports located 90° apart at the 65% height and four exhaust holes also located 90° apart near the bottom (20% height) of the reactor as shown in Figures 2.2 and 2.3. As depicted in Figure 2.1, one of the ports is used for the gas sampling probe and another is used for the R-type thermocouple. During measurements, the remaining two ports (i.e., the viewing ports) are plugged to prevent excessive amount of heat loss and flow distortion. The standard JSR is used for most of the studies.

Due to the lack of understanding of the reactor flow and thermal fields, another JSR is fabricated with sampling ports located at the 20%, 45%, 65%, 80% and 93% heights (see Figure 2.4). The multi-sampling port JSR also has over fifteen thermocouples imbedded in its wall at various locations as shown in Figure 2.5. The new reactor allows detailed thermal and flow profiling of the reactor and at the same time provides significant insight to the amount of wall heat loss. Both JSR profile and wall heat loss data provide critical input data for modeling of the reactor.

Both the standard and multi-sampling port JSRs have an identical internal cavity volume of 15.8 cc. The reactors have internal dimensions identical to those of the atmospheric pressure JSR used in previous research as described in the Ph.D. thesis of Steele (1995). The height of the reactor is 45 mm, the diameter (at the widest point) is 25 mm, and the nominal wall thickness is 50 mm. The present reactor is constructed from high purity (94^+%) castable alumina (AP Green Model Greencast 94 Plus). The present standard JSR, unlike past reactors, has been in use for four years and have shown little thermal cycling and high temperature deterioration due to the high alumina content. Detailed computer aided design (CAD) drawings and construction procedures for the two JSRs are found in Appendix A.

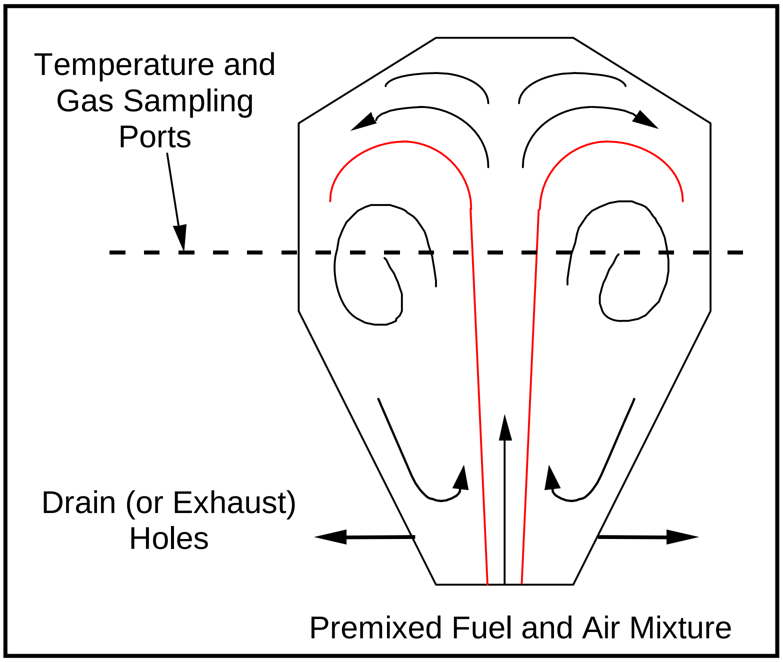

Figure 2.2. Jet-Stirred Reactor and Flow Pattern for Single Centered Jet.

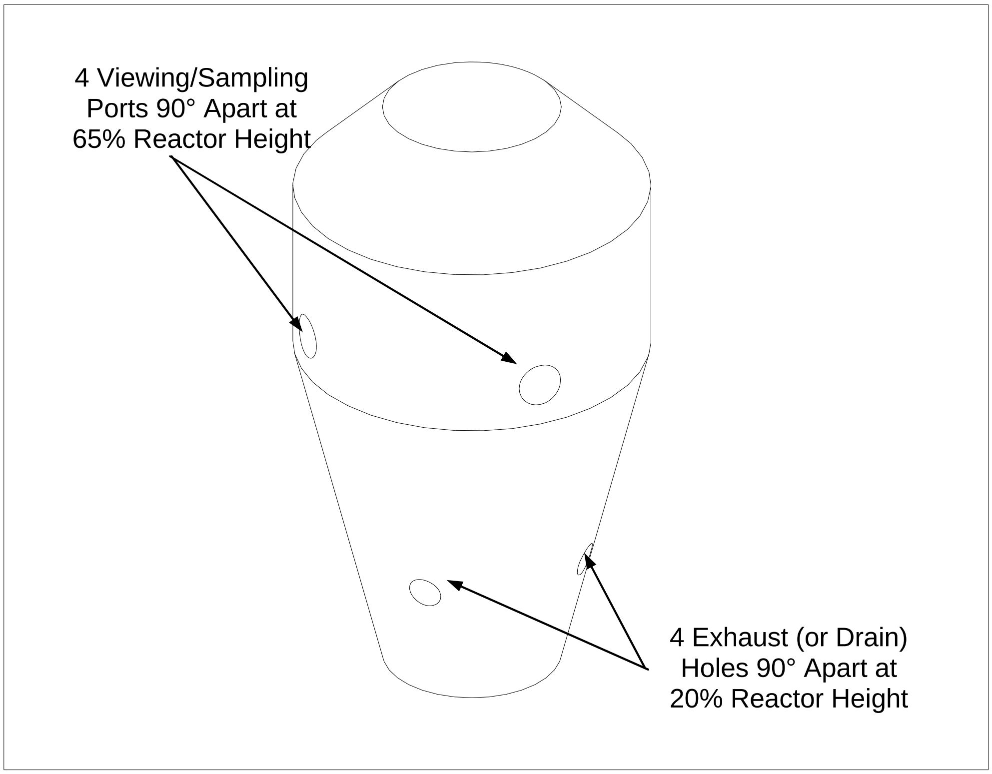

Figure 2.3. 3D View of the Standard Jet-Stirred Reactor Cavity.

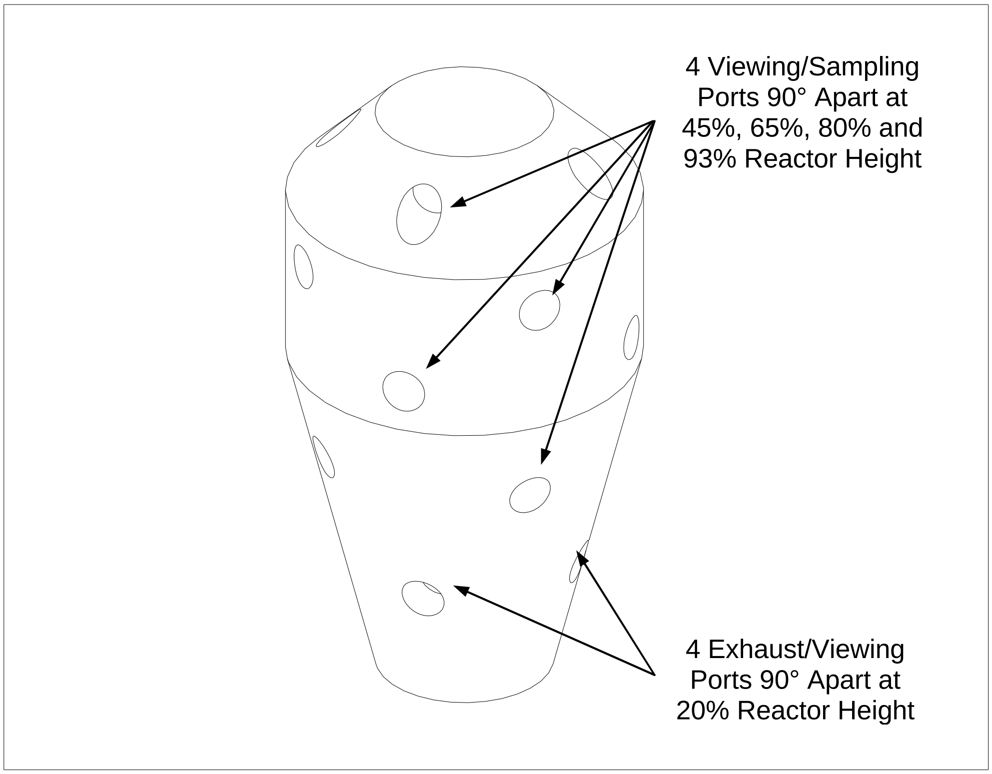

Figure 2.4. 3D View of the Multi-Sampling Port Jet-Stirred Reactor Cavity.

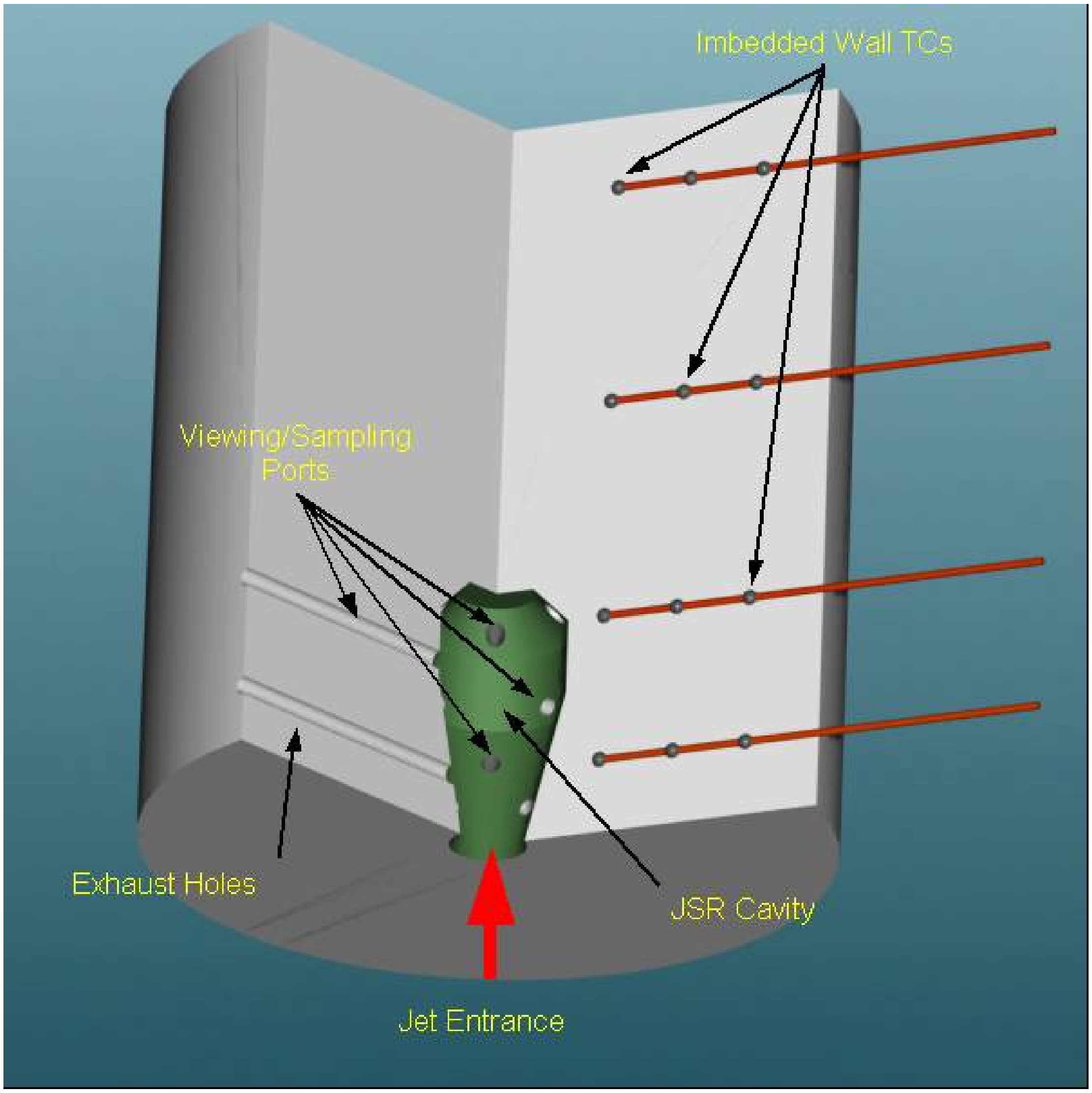

Figure 2.5. Cutaway View of the Multi-Sampling Port JSR.

2.1.2 NOZZLE BLOCKS, JET STIRRING AND JSR THERMAL MAPPING

Stirring of the reactor cavity is accomplished either by using a single jet (as shown in Figure 2.2) or by using multiple jets. The jets are formed in the nozzle block, which is constructed of either INCONEL® or HASTELLOY®. The nozzle block also serves as the interface between the prevaporizing-premixing injector and the JSR cavity.

For the present research, three different jet inlet nozzle blocks are used, including nozzles with a single, centered jet of either 2 or 4 mm diameter (d_{jet}) and a nozzle with eight diverging jets each having a 0.965 mm diameter. Representative drawings are shown in Appendix B and by Steele et al. (1997). Table 2.1 (at the end of this sub-section) is a listing of the various nozzle blocks used in combination with the three generations of LPP injectors.

The purpose of this sub-section is to show and discuss how the temperature and concentration fields in the JSR behave and are affected by the nozzle block used.

The injector and jet conditions obtained with the three nozzle blocks used with the 2nd generation prevaporizing-premixing injector (i.e., the jet-inlet total temperature) are listed in Table 2.2. The exit temperature of the prevaporizing-premixing injector is 523 K. For the 2 mm nozzle, the pressure of 2.1 atm in the prevaporizing-premixing chamber indicates choked nozzle flow. For the other cases, the nozzle flow is subsonic. For example, for the 4 mm nozzle, the pressure loss between the prevaporizing-premixing injector and the JSR is only about 0.1 atm (i.e., a 10% pressure loss). The jet velocities listed in Table 2.2 are based on expansion of a jet to 1 atm (the nominal pressure within the JSR cavity), a specific heat ratio of 1.35 and a mixture molecular weight of 30 kg/kmol. The mass entrained by the jet at full reactor height (45 mm) relative to the original mass of the jet is evaluated using the Ricou-Spalding formula (Equation 2.9, Beér and Chigier, 1983).

For a given jet inlet nozzle, the different fuels are burned in essentially equivalent macroscopic thermal fields. This is illustrated in Figure 2.6. Additionally, since the airflow rate is held constant, the flow fields are essentially equivalent. For the 2 and 4 mm nozzles, the reactor clearly exhibits two distinct zones. This is shown in Figures 2.6 through 2.10, which respectively show profiles of temperature, NO_X, CO, CO_2 and O_2 across the JSR. The jet zone is located in the center of the reactor, which comprises about 10 to 20% of the total JSR volume. The recirculation zone surrounding the jet zone comprises 80 to 90% of the total JSR volume. The recirculation zone has characteristic dimensions of about 4 cm height by 1 cm thickness. For operation of the reactor at the conditions used with the 2nd generation injector (3.2 ms residence time, 1790 K combustion temperature and 523 K inlet jet temperature), the characteristic time scales of the JSR flow are 1 ms for one cycle of the recirculation zone by a fluid particle, and 0.05 ms for one turn-over of an inlet-jet eddy (i.e., $\tau \approx d_{jet}/U_{jet}$). The nominal number of cycles made by a fluid particle in the JSR is estimated to be about 4 (based on the reactor flow analysis of Thornton et al., 1987). Examination of the length and time scales of gas turbine LP combustors indicate that compared to the JSR:

- The recirculation zone size is somewhat greater in LP combustors (several centimeters characteristic length).

- The number of cycles of a fluid particle in the recirculation zone of LP combustors is less.

- The integral scale of the eddies entering the LP combustor from the premixer outlet stream (jet) is larger and the inlet jet velocity is lower, leading to a larger jet inlet eddy turnover time (as large as 1 ms).

Since the reactor is operated at constant airflow rate, the fuel flow rate is adjusted to give the desired combustion temperature. This is 1790 K (corrected) at the standard temperature measuring location (65% reactor height and $r/R_0 = 0.63$). The fuel-air equivalence ratio, as determined by mass flow rates and exhaust gas analysis, is 0.62 ± 0.04 for combustion with the single, centered jet. With the diverging-jet nozzle, it is necessary to increase the fuel-air equivalence ratio to 0.73 ± 0.04 in order to attain 1790 K at the standard temperature measuring location. Temperature probing of the reactor (through the drain holes) shows a hot region of 1900 K peak temperature in the lower central part of the JSR. This explains the higher fuel-air equivalence ratio of the diverging-jets reactor and, as well as, the greater amount of NO_X measured for the diverging-jets reactor (see Figure 2.7). The nominal combustion temperatures for this work are:

- JSR with a single, centered jet: 1790 K.
- JSR with the diverging jets: 1850 K.

With a single, centered jet, the macroscopic recirculation pattern in the JSR is from centerline to the outer part of the reactor as shown in

Figure 2.2. Temperature profiling across the reactor at 65% height shows a depression of temperature on centerline compared to a nearly uniform temperature along the remainder of the reactor radius. This is plotted in Figure 2.6. As shown in Figures 2.6 and 2.7, 80 to 90% of the cross-sectional area of the JSR is nearly uniform in temperature and NO_X concentration. Mainly, this is the recirculation zone of the reactor. Peak CO concentrations of about 1 to 2% by mole are measured slightly off centerline as shown in Figure 2.8 for methane (natural gas) combustion. In the recirculation zone, the CO concentration falls to about 0.2 to 0.3% by mole. The other species measured [CO_2 (see Figure 2.9) and O_2 (see Figure 2.10)] show uniformity in the recirculation zone similar to that noted in Figure 2.7 for the NO_X. The standard gas sample measuring location is within the recirculation zone at 65% reactor height and $r/R_0 = 0.71$.

It is desired for the jet-stirred reactor to exhibit spatial uniformity in the measured (time-mean) temperature and gas composition. When this condition is attained, the reactor is assumed to be *well stirred* and the time-mean rates of reaction are assumed the same everywhere within the reactor. However, at combustion temperatures the oxidation reactions are very rapid, with a characteristic chemical time of order 0.01 to 0.1 ms. Thus, the hydrocarbon fuel converts very rapidly to CO, H_2 and H_2O. For a reactor operating with a residence time of a few milliseconds (the case here), it is essentially impossible to fully disperse the fuel throughout the reactor prior to the onset of oxidation. Consequently, the JSR exhibits the two zones stated above, the non-uniform jet (in which the fast oxidation reactions are concentrated) and the surrounding recirculation zone. The recirculation zone is the region of CO oxidation, super-equilibrium concentrations of free radical (O, H, and OH) and non-thermal NO_X formation by free radical attack on N_2. It has been argued by Steele et al. (1998) that JSRs operated lean premixed at atmospheric pressure are essentially well-stirred with respect to NO_X formation from N_2. This follows if the NO_X is formed mainly by influence of O and H through the Zeldovich and nitrous oxide mechanisms.

With the diverging jets nozzle, the macroscopic flow undergoes recirculation from the outer part of the reactor to the centerline. Because of the use of multiple small jets, the temperature and concentration profiles at 65% reactor height are nearly “flat.” This is seen for temperature in Figure 2.6. The CO concentration varies from about 0.1 to 0.2% by mole from the outer wall of the reactor to the centerline. NO_X profiles are plotted in Figure 2.7.

To fully understand the JSR thermal field and its correlation to the formation of NO_X, detailed thermal mapping of the multi-sampling port JSR is performed with the 2nd generation injector in conjunction with the three nozzle blocks as listed in Table 2.2. Test and operating conditions are identical for all cases. The nominal fuel-air equivalence ratio (ϕ) is held constant at 0.69, the inlet temperature is fixed at 523 K and the total airflow is set at 30, 40 and 50 slpm corresponding to approximate residence times of 5.7, 4.0 and 3.2 ms, respectively. Figures 2.11 through 2.13 represent the thermal profiles for the three different nozzle blocks. The red line located on the right hand side of each profile is the location of the reactor wall. The standard exhaust port is located at the 0.376 in height. The standard height for gas sampling and reactor gas temperature measurements is at 1.125 in or 65% of the reactor height. The standard location of the gas sampling probe is at r = 0.9 cm or $r/R_0 = 0.71$. The standard placement point for the R-type thermocouple used for reactor gas temperature measurements is r = 0.8 cm or $r/R_0 = 0.63$.

As can be seen in Figure 2.10 (i.e., the 2 mm case), the degree of thermal uniformity increases with increasing mixing intensity as provided by the increase in the throughput. The single centered jet shows a high degree of penetration. For the 50 slpm case, the reactor is essentially uniformly filled by one large recirculation zone as indicated by the light blue zone. Temperature and gas samples extracted from this zone would be representative of the overall reactor performance.

Thermal profiling of the 4 mm case is shown in Figure 2.12. As can be seen, the reactor is fairly uniform for the high throughput case, except for a small hotspot region (as indicated by the pink zone) located above the standard 65% sampling height. This region of higher temperature is most likely caused by reduced reactor uniformity and slower mixing rates since the jet zone is larger and mixing is not as intense as the 2 mm case. Thus, the hot spot is not “smoothed-out”. This small hotspot confirms the slightly higher NO_X yield from the 4 mm nozzle as shown in Figure 2.7.

Thermal profiling of the diverging jets nozzle case is shown in Figure 2.13. As can be seen the thermal field of the diverging jets case is quite different from the single centered jet cases. The recirculation zone is situated in the center of the reactor. The jets have much less penetration, but much faster ignition due to the increase in entrainment rates (see Table 2.2). All three cases shown in Figure 2.13 indicate that for the diverging jets nozzle:

- There exists a high temperature zone in the lower portion of the reactor since ignition is quicker due to the increase in entrainment rates and penetration is less due to the reduced jet momentum.

- There is a tendency for the flow to prematurely exit the reactor via the drain holes leading to increased heat loss and, thus, a lower overall reactor temperature.

Consequently, in order to match the flame temperature of 1790 K as measured at the standard sampling location in the 2 and 4 mm cases, higher fuel flow rates or ϕs are required leading to a higher temperature region in the lower portion of the reactor and an overall slight increase in NO_X formation.

Figures 2.11 through 2.13 also indicate that the rate of heat loss per unit time increases with decreasing throughput. This is further illustrated in Figure 2.14 where the reactor wall heat loss per unit mass flow is plotted as a function of throughput and nozzle block configuration for various wall locations. For all cases, the reactor is operated on methane at a nominal fuel-air equivalence ratio of 0.69 and an inlet temperature of 523 K. The reactor wall heat loss per unit mass flow (or wall heat transfer parameter) is defined as:

$$q'' = \frac{T_{TC,in} - T_{TC,out}}{ln(r_{TC,out} / r_{TC,in}) \cdot \dot{Q}_{air}} \quad \text{.......................................Eq. 2.1}$$

where q" is the wall heat transfer parameter in K/slpm, T_{TC} is wall TC temperature in Kelvins, r_{TC} is the radial distance or location of the wall TC from the reactor centerline and $\dot{Q}_{air}$ is the volumetric flow rate of air in slpm. As can be seen in

Figure 2.14, the rate of heat loss per unit mass flow increases with decreasing throughput. Additionally, the wall heat transfer parameter measured in the lower portion of the reactor is considerably less for the diverging jets cases further confirming the tendency for the flow to prematurely exit the JSR via the drain holes. In general, the amount of wall heat loss is approximately 5% of the total heat input.

Thus, to approach adiabatic and the WSR conditions, a high throughput (or short reactor residence time) condition should be used in conjunction with the single, centered jet nozzle blocks. For the SPP parametric investigations, a single, 4 mm, centered jet nozzle block with a nominal reactor residence time of 2.3 ms is used for all test conditions. The associated injector pressure drop can be up to approximately 30%.

Table 2.1. Nozzle Blocks used for the Various LPP Injectors

1st Generation Injector	***2nd Generation Injector***	***SPP Injector***
Single, 2 mm Diameter, Straight Channel, Centered Jet	Single, 2 mm Diameter, Straight Channel, Centered Jet	Single, 4 mm Diameter, Converging Channel, Centered Jet
	Single, 4 mm Diameter, Straight Channel, Centered Jet	
	8-Hole, 0.965 mm Diameter, Straight Channel, Diverging Jets	

Table 2.2. Jet Nozzle Configuration and 2nd Generation Prevaporizing-Premixing Injector Conditions.

Nozzle Configuration	***Injector Pressure (atm)***	***Jet Velocity, U_{jet} (m/s)***	***Entrained Mass / Original Jet Mass***	***Injector Residence Time (ms)***
Single, Centered Jet d_{jet} = 2 mm	2.1	445	2.89	140
Single, Centered Jet d_{jet} = 4 mm	1.1	165	0.95	80
Eight Diverging Jets d_{jet} = 0.965 mm	1.4	305	7.07	95

(Prevaporizer-Premixer Temperature = 523 K)

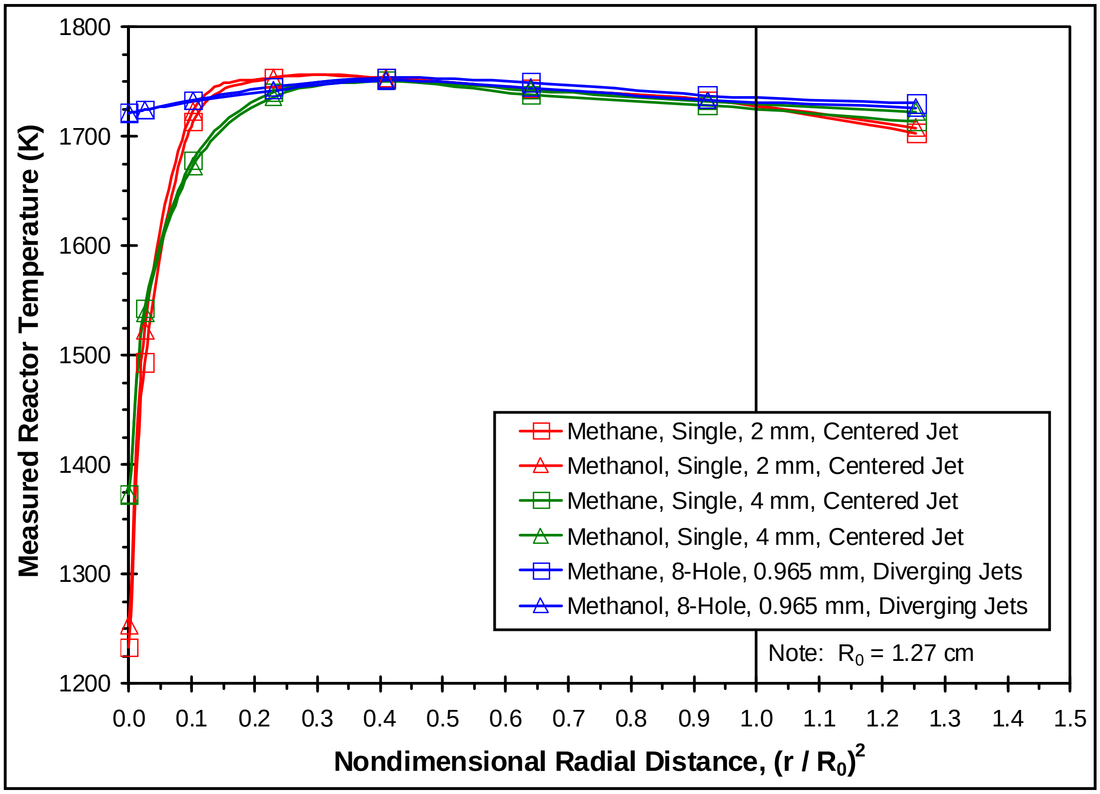

Figure 2.6. As-Measured (Uncorrected) Temperature Profiles for the Three Nozzles - Combustion of Methane and Methanol. Centerline = 0.0 and Cavity Wall = 1.0.

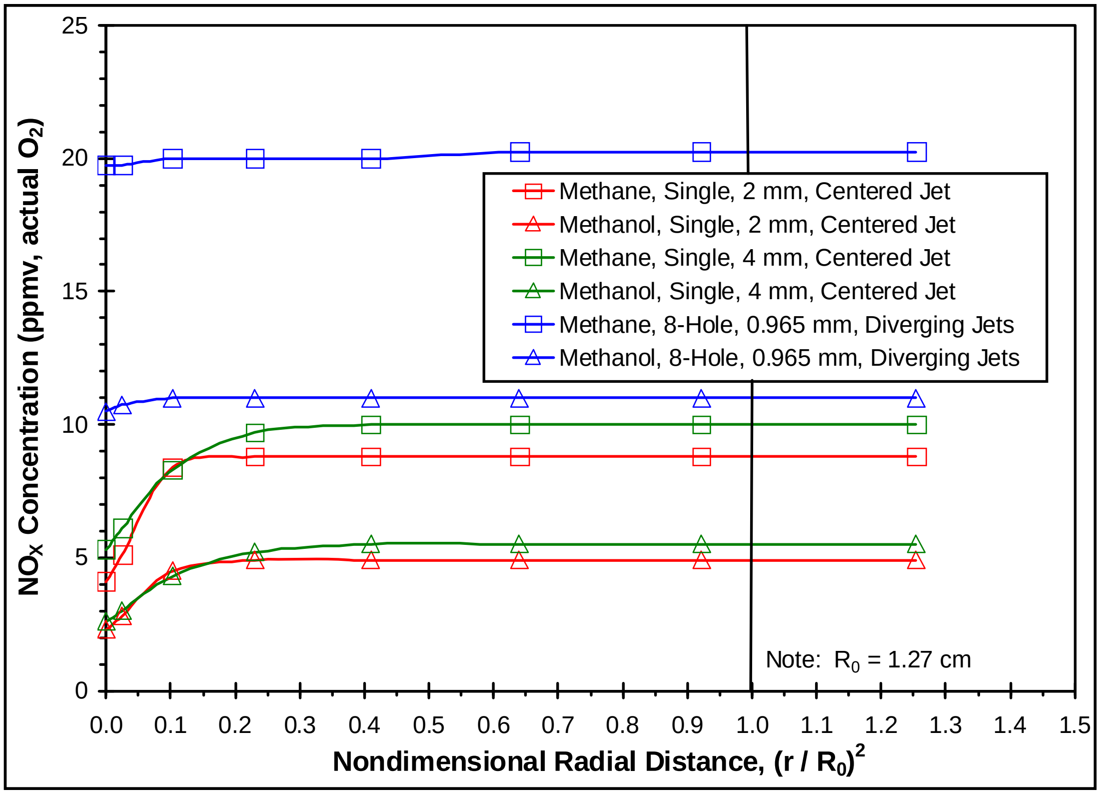

Figure 2.7. As-Measured (Dry, Actual O_2) NO_X Profiles for the Three Nozzles – Combustion of Methane and Methanol. Centerline = 0.0 and Cavity Wall = 1.0.

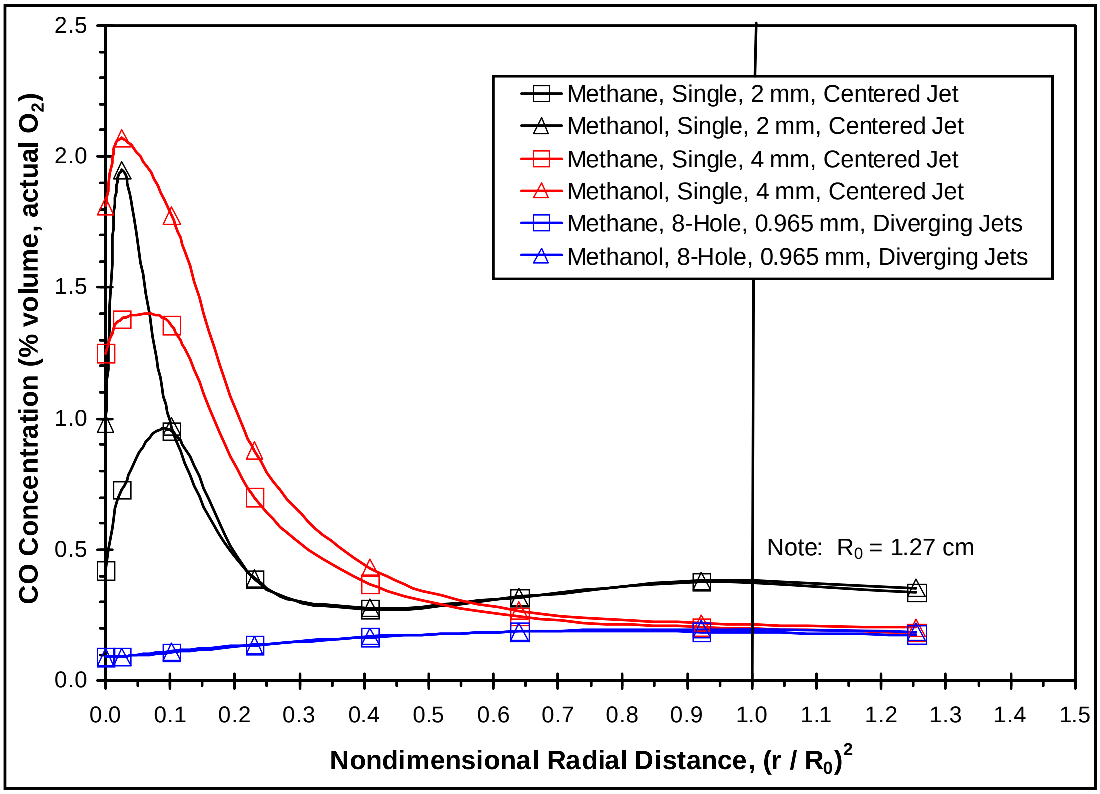

Figure 2.8. As-Measured (Dry, Actual O_2) CO Profiles for the Three Nozzles – Combustion of Methane and Methanol. Centerline = 0.0 and Cavity Wall = 1.0.

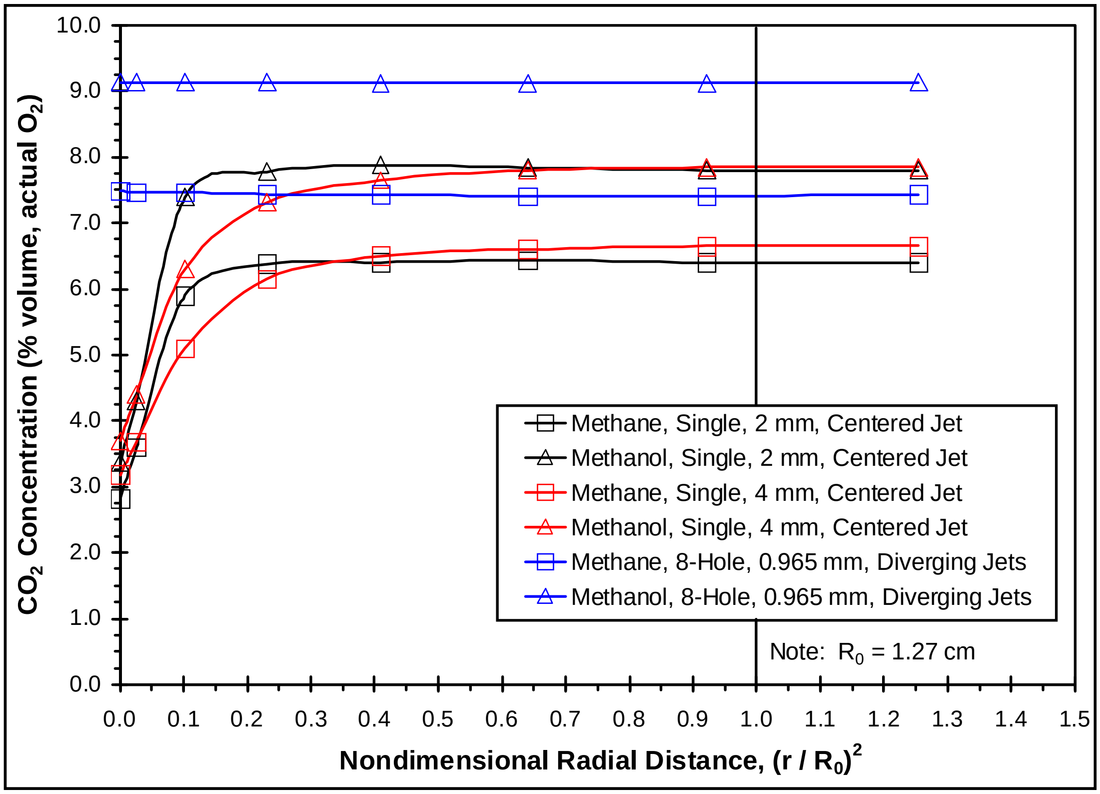

Figure 2.9. As-Measured (Dry, Actual O_2) CO_2 Profiles for the Three Nozzles – Combustion of Methane and Methanol. Centerline = 0.0 and Cavity Wall = 1.0.

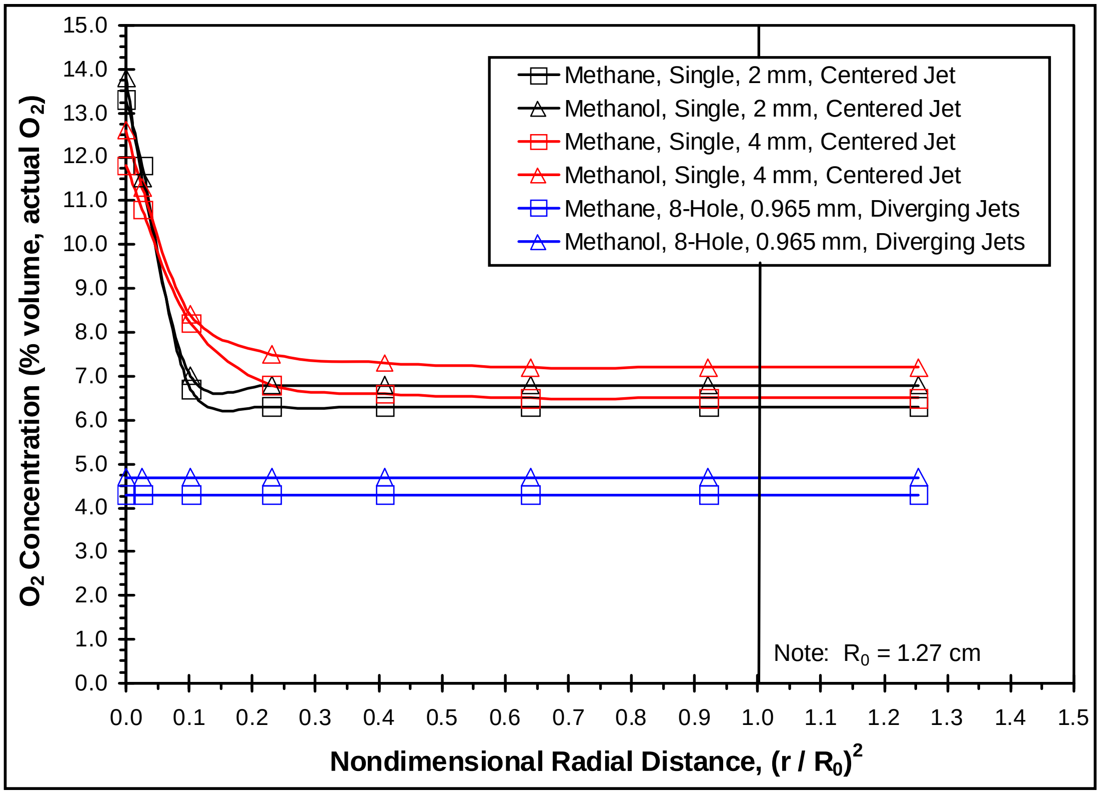

Figure 2.10. As-Measured (Dry, Actual O_2) O_2 Profiles for the Three Nozzles – Combustion of Methane and Methanol. Centerline = 0.0 and Cavity Wall = 1.0.

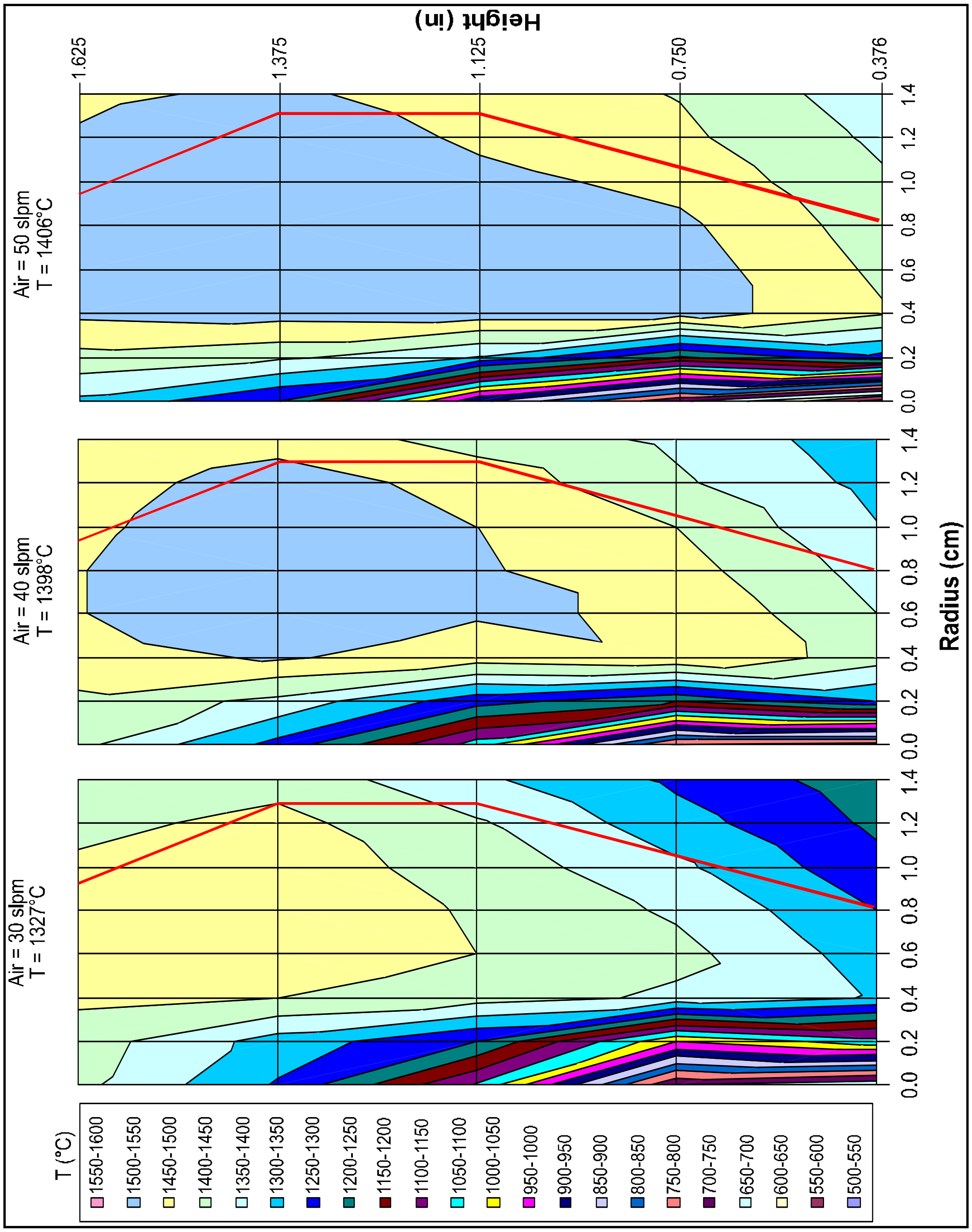

Figure 2.11. Thermal Profile Mapping of the JSR with the Single, 2 mm, Centered Jet Nozzle ($\phi = 0.69$, $T_{inlet} = 523$ K, Fuel = Natural Gas).

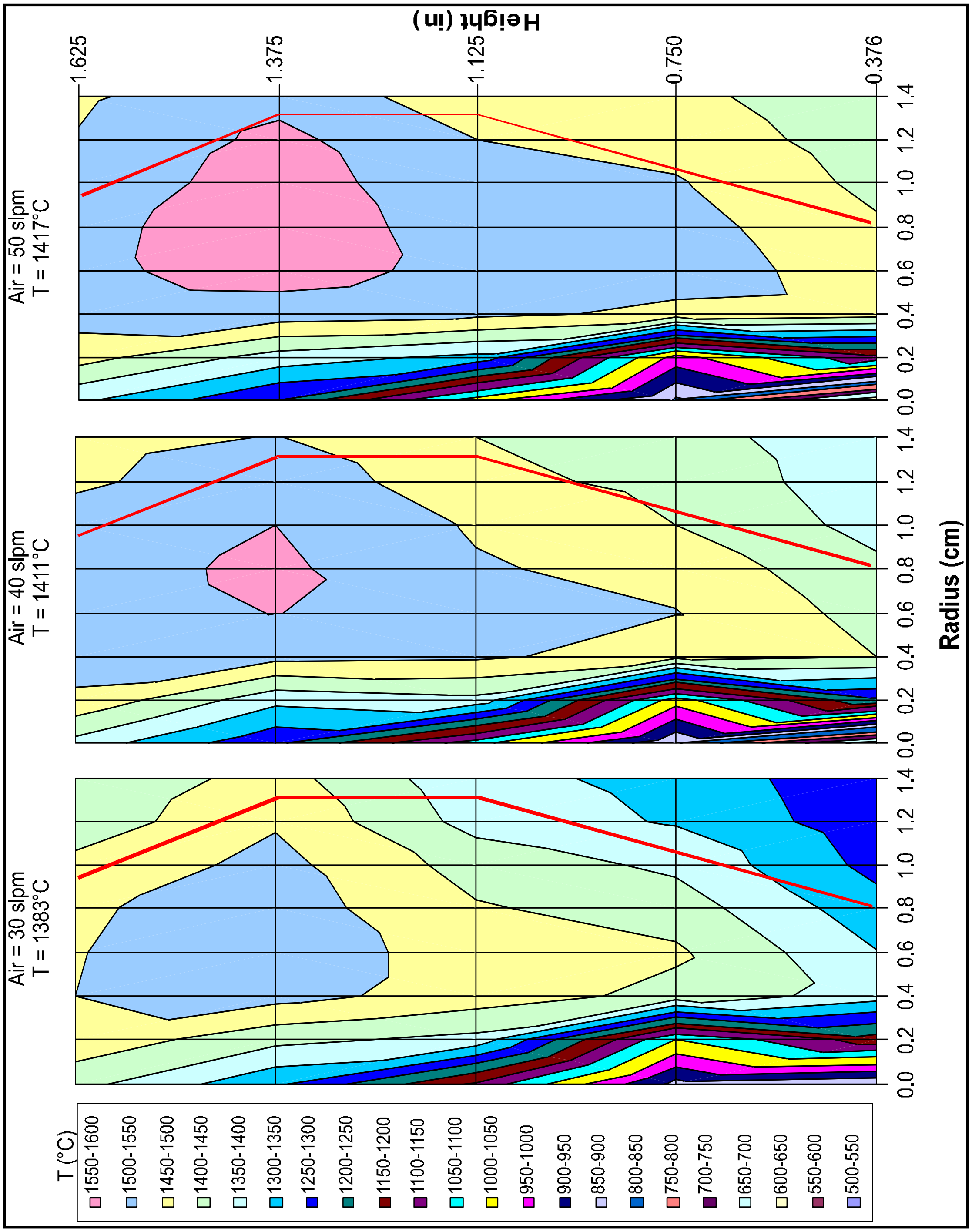

Figure 2.12. Thermal Profile Mapping of the JSR with the Single, 4 mm, Centered Jet Nozzle ($\phi = 0.69$, $T_{inlet} = 523$ K, Fuel = Natural Gas).

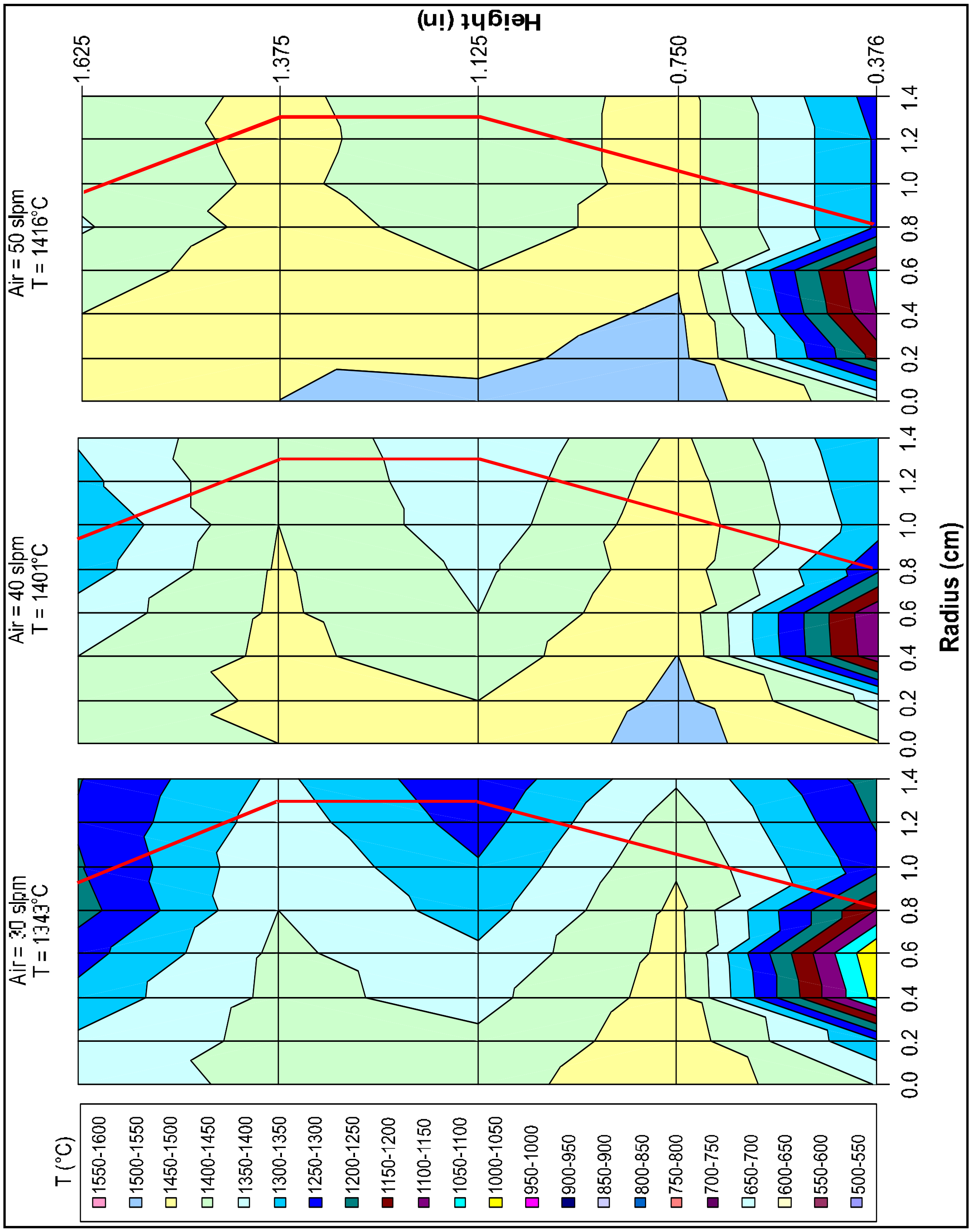

Figure 2.13. Thermal Profile Mapping of the JSR with the 8-Hole, 0.965 mm, Diverging Jets Nozzle ($\phi = 0.69$, $T_{inlet} = 523$ K, Fuel = Natural Gas).

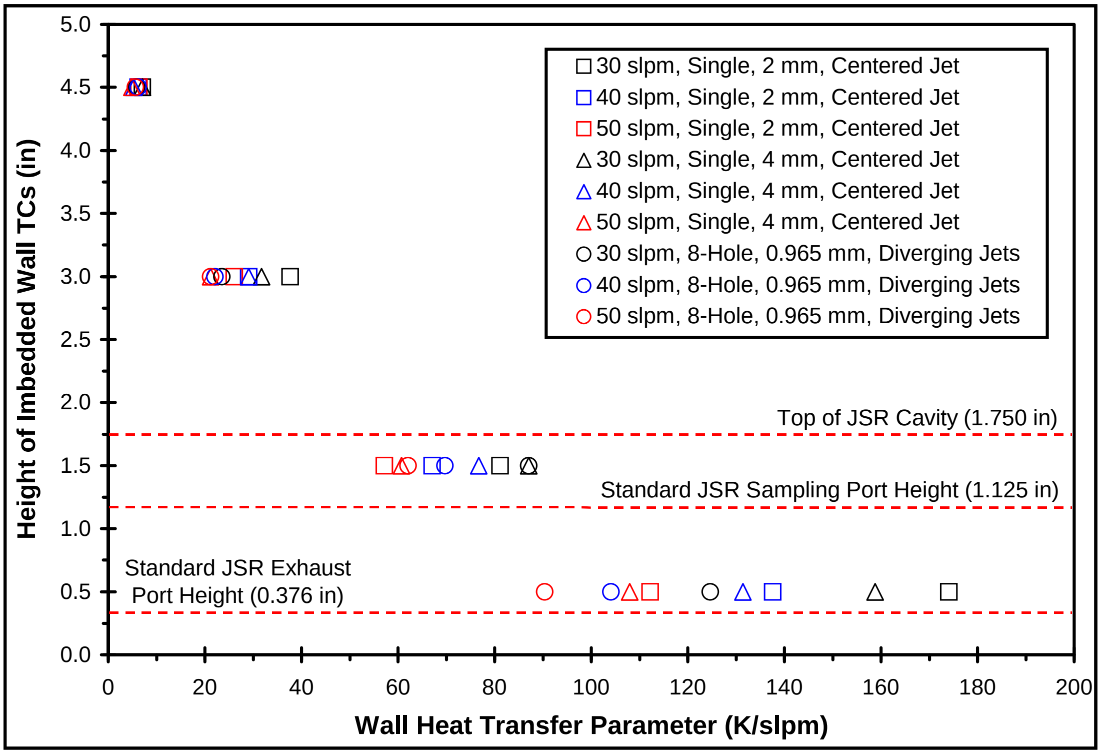

Figure 2.14. JSR Ceramic Reactor Body Wall Heat Loss Profile for Various Throughput and Nozzle Block Configurations ($\phi = 0.69$, $T_{inlet} = 523$ K, Fuel = Natural Gas). See Figures 2.5 and A.9 for Location of Imbedded Wall TCs.

2.2 IGNITION SYSTEM

The ignition system used is similar to the high voltage (HV) spark discharge type used by Steele (1995) and Capehart (1995). The system consists of a regulated alternating current (AC) power supply (Superior Electric Model 116 Powerstat), an induction type high voltage discharge coil (Webster Electric Model 812-6A010 Ignition Transformer), and a spark probe made from a 3.175 mm (1/8 in) diameter double bore ceramic insulating sheath (Omega Engineering Model TRX 04018) with two 0.762 mm (0.030 in) diameter stainless steel wires used as probe leads. The maximum discharge voltage is 8.5 kV with a maximum discharge current of 0.02 A. The nominal discharge energy is 80 J. This energy is sufficient to ignite a premixed hydrogen and air mixture that is used for reactor startup. The high voltage spark ignition system is presented in Figure 2.15.

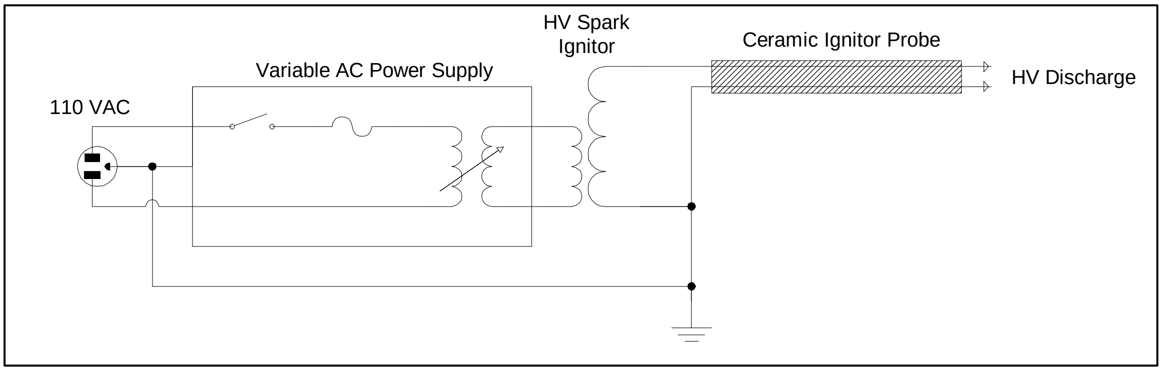

Figure 2.15. Schematic Diagram of the High Voltage Spark Discharge Ignition System.

2.3 FLOW SUPPLY AND CONTROL

For steady operation of the JSR, stable and accurate flow control of both the air and fuel is required. Additionally, temporal variation in flow can lead to unmixedness of the fuel and air mixture that will result in higher NO_X yields. Furthermore, unsteadiness in the flow could possibly lead to combustion oscillation (see Keller, 1995). Consequently, all flows to the JSR are monitored and controlled independently. Gaseous medium flow control and monitoring can be achieved through either the conventional needle valve-rotameter arrangement or via the state-of-the-art thermal mass flow control (MFC) technique as shown in Figures 2.16 and 2.17. Calibration and accuracy of the rotameters are described in Steele (1995). The MFCs are calibrated at the factory and the calibration is usually good for a period of one year. Liquid fuel flow control is accomplished with the use of the traditional needle valve-rotameter setup as shown in Figure 2.18. For example, flows entering the SPP include first stage air, second stage air, atomizer air, and gaseous and/or liquid fuel(s). All streams entering the injector are monitored and controlled independently.

Detailed description of the conventional needle valve-rotameter setup is provided in Steele (1995) and Capehart (1995). For this research a different liquid rotameter (Fisher Porter Model FP-1/16-19.5-G-6 ¾ /61) with various float material (including sapphire, stainless steel and tantalum) is employed in conjunction with a high performance metering valve (Parker Model 2A-H4L-V-SS-TC) having a non-rotating stem design to provide accurate and precise control of the liquid fuel flow. The float type and the associated calibration curve for the various liquid fuels are presented Appendix C. For calibration, the liquid flow rates are determined via the bucket-and-stopwatch technique. All liquid flow rates are linearly proportional to the rotameter scale and are independent of the backpressure, which is provided by N_2 at a nominal operating pressure of 50 psig, since the medium is considered as incompressible as expected.

The thermal mass flow controls are incorporated because of the increased complexity of the SPP and the need for accurate and simple flow control. The MFC system includes a four-channel electronic control module (Brooks Instrument Model 0154E Microprocessor Control and Readout Unit) used to independently control and monitor the thermal mass flow controllers (shown in Figure 2.19). The control module also communicates with a data logger and provides flow rate data on each of the MFCs. Specifications of the four MFCs are listed in Table 2.3. As can be seen, the MFCs provide a very high degree of accuracy and repeatability. In addition, the MFCs have fast response time and the electronic circuitry automatically adjusts for fluctuations in pressure and temperature. The gaseous fuel MFC is used for various gaseous fuels. Three gaseous fuels are used in this research and their respective correction factors based on a standard calibration gas of nitrogen are listed in Table 2.4. The actual flow rate can be determined by the following equation:

$$\dot{Q}_{actual}\,(slpm) = \dot{Q}_{display}\,(slpm)\,\frac{k_{actual\ gas}}{k_{calibration\ gas}} \quad \text{.................. Eq. 2.2}$$

It must be pointed out that the accuracy of any MFC is strongly dependent on the purity of the medium used. The correction factors listed in Table 2.4 are strongly dependent on the viscosity and density of the medium in use. In addition, the accuracy of and leakage in the flow supply system is checked for every test condition by performing a carbon balance. The carbon balance is based on cross checking the ϕ obtained from the measured flow rates and the ϕ obtained by the measured CO/CO_2 and O_2 concentrations. Typical difference between the measured MFC ϕ and the CO/CO_2 and O_2 ϕ is less than 3%.

Table 2.3. Specifications for the Thermal Mass Flow Controllers.

Medium Type	***MFC Model***	***Maximum Flow Rate (SLPM)***	***Accuracy (% Full Scale)***	***Repeatability (% Full Scale)***	***Response Time (ms)***	***Cal. Gas***
Air (SPP 1st Stage)	Unit UFC 1100A-60	60	±1	±0.2	400-800	Air
Air (SPP 2nd Stage)	Unit UFC 1100A-60	60	±1	±0.2	400-800	Air
Air (SPP Atomizer)	Unit UFC 1100A-10	10	±1	±0.2	400-800	Air
Gaseous Fuel	Unit UFC 1100A-10	10	±1	±0.2	400-800	N_2

Table 2.4. Correction Factors for the Gaseous Fuel MFC

Medium Type	***Correction Factor, k***
Air	1.001
Nitrogen	1.000
Methane	0.752
Ethane	0.482
Propane	0.331

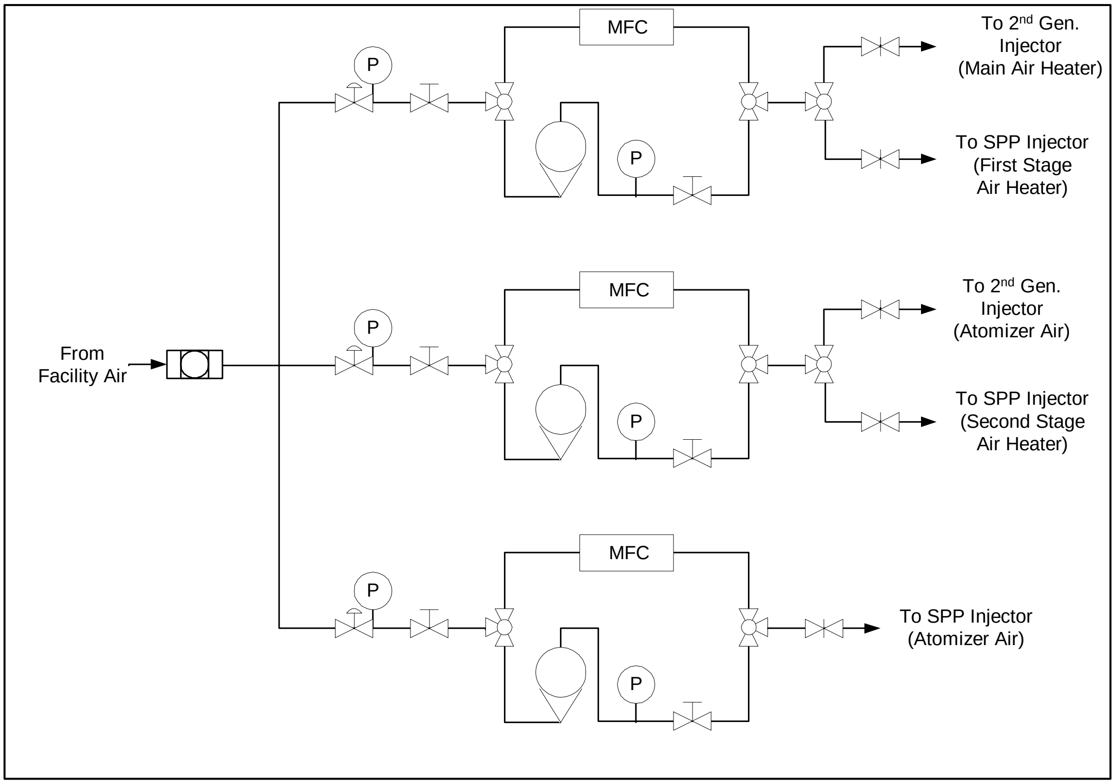

Figure 2.16. Schematic Diagram of the Flow Control System for Air Supply.

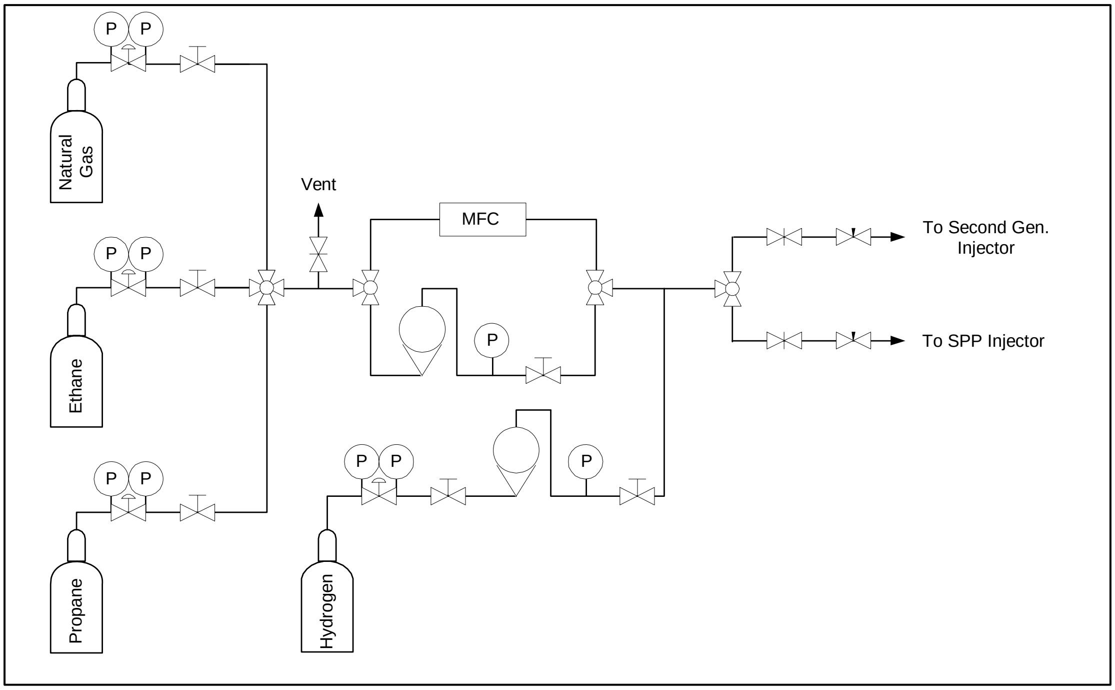

Figure 2.17. Schematic Diagram of the Flow Control System for Gaseous Fuel Supply.

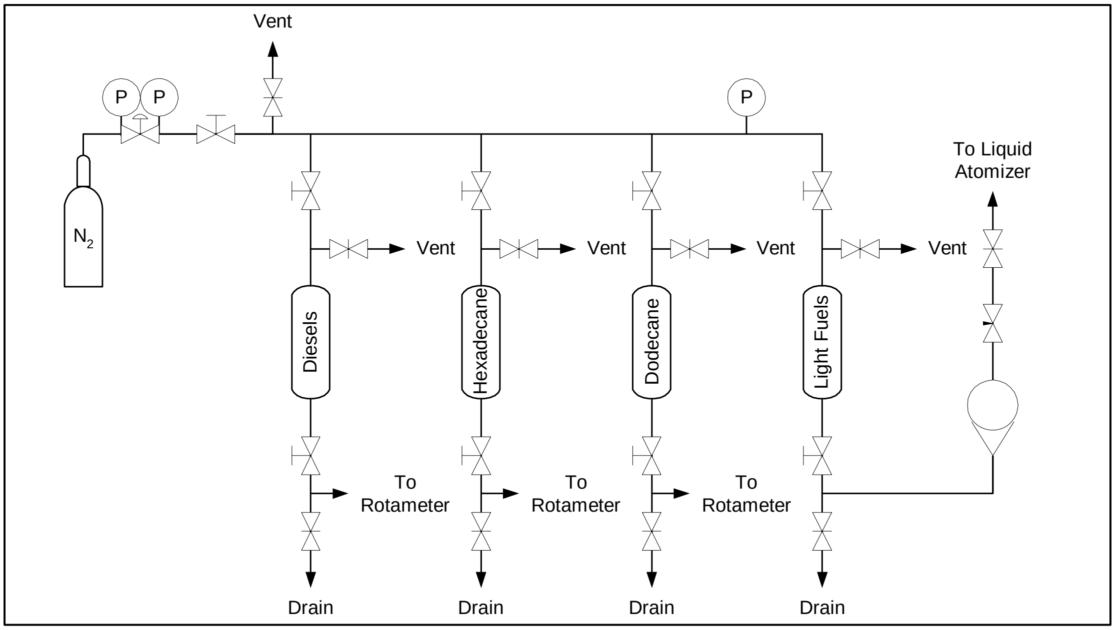

Figure 2.18. Schematic Diagram of the Flow Control System for Liquid Fuel Supply.

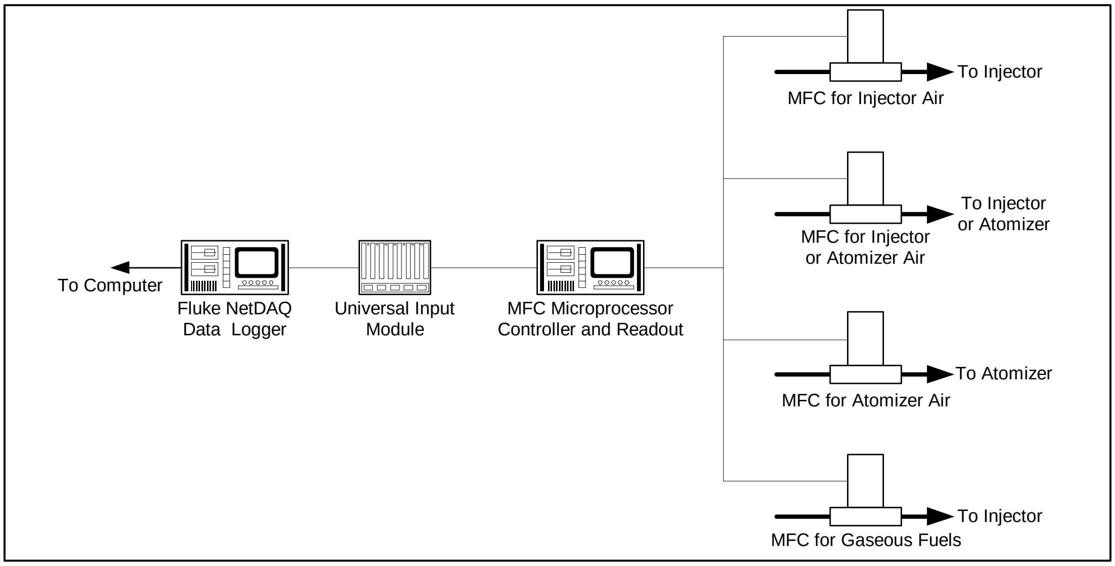

Figure 2.19. Schematic Diagram of the Thermal Mass Flow Control System.

2.4 INLET TEMPERATURE CONTROL

For studying the effects of inlet temperature and preheat on NO_X formation, accurate, precise and responsive control of the JSR inlet (or injector) temperature is required. Inlet temperature control is also important from a safety standpoint since an excessive amount of preheat will lead to autoignition or spontaneous reaction of the fuel and air mixture in the injector of an LP system. Spadaccini and TeVelde (1982) provide correlations of autoignition delay time as a function of injector temperature and pressure for several commercial fuels. It is important to note that for non-adiabatic conditions and lean mixtures, the autoignition delay time is also dependent on the wall heat loss and free radical concentration. In addition, excess preheat can also lead to preflame reactions, such as coking and gumming, that can have detrimental effects on the injector flow pattern. Preflame reactions can also lead to flow oscillation, impairing inlet temperature control and yielding higher levels of NO_X. Inlet temperature control is especially critical for the SPP since it is used to study NO_X formation under high preheat (up to 900 K) conditions. For the SPP, two temperature controllers are used to independently control the temperature in each stage of the injector.

The following are criteria used to determine the level of preheat:

- Preflame chemical reactions: Because of the long prevaporizer-premixer residence time (> 80 ms) used in the 1st and 2nd generation injectors, a significant amount of preflame oxidation occurs for all liquid fuels when the inlet temperature is set at approximately 100°C above the normal boiling point of the fuel. This condition is relaxed for the SPP design since the residence time in the high temperature second stage is short (between 5 to 12 ms). For a given inlet temperature, the possibility of preflame reactions increases with increasing fuel size. This is observed through fluctuations of the inlet temperature and injector pressure. These fluctuations are most probably driven by preflame reactions. Further indication of fuel oxidation is determined through the use of a gas chromatograph [Perkin Elmer Model Autosystem Gas Chromatograph (GC)] equipped with a packed column (Haye Model Sep P) and a flame ionization detector (FID). Once oxidation occurs, C_1 and C_2 hydrocarbon traces are observed in the premixer. Coking and gumming in the premixer has been observed for the 1st generation injector and will be discussed in Section 3.1. However, preflame reactions have not been observed for the other two injectors.

- Energy required for vaporization: A minimum amount of energy is required for the vaporization of a liquid fuel. This energy includes the latent heat of vaporization, which is a function of the fuel type and the droplet heat-up energy (see Kanury, 1975 and Lefebvre, 1989). In this study, the “heaviest” laboratory fuel investigated is hexadecane, $C_{16}H_{34}$, with a normal boiling point of 558 K and a latent heat of about 360 kJ/kg. A minimum inlet temperature of 523 K is adequate for fully vaporizing the hexadecane and all of the laboratory fuels used in this study.

Although an inlet temperature of 523 to 623 K is on the low end for most gas turbines, which normally run between 600 and 800 K, the modest 523 to 623 K inlet temperature should not significantly affect the NO_X trends as a function of fuel type obtained in this study.

Inlet temperature control is achieved through the use of cascade type temperature controllers (Watlow Controls Model 989 Microprocessor-Based Temperature/Process Controller). The cascade controller is an auto-tuning, proportional-integral-derivative (PID), open loop feedback controller that employs the heater sheath temperature and the injector inlet temperature as dual inputs (see Watlow Controls, 1997). The heater sheath temperature is essentially the temperature of the air measured immediately downstream of the heater exit and is a close approximation of the heater element surface temperature. Cascade controllers are generally used in systems with long thermal lag times typical of the injectors used in this research (due to the material of construction and non-adiabaticity of the system). With cascade control, overshoot is minimized while enabling quick attainment of set point values. In addition, the heater sheath temperature is used as the outer loop controller input and its operating range can be adjusted to prevent overheating and meltdown of the heater element. These characteristics are particularly beneficial since they reduce thermal cycling of the heater element and thus extend system component life.

The cascade controllers are used to control the heat output from convective type air heaters (Convectronics Model 007-10135). Solid-state power relays or SCRs (Watlow Controls DIN-a-mite Style B) are used to regulate heater current draw that is monitored by an ammeter (Simpson Model 370) and supplied by a 220 VAC power regulator (Superior Electric Model 1256C Powerstat). Presented in Figure 2.20 is the wiring diagram of the inlet temperature control system.

Due to the autoignition criteria and preflame reactions within the injector, the degree of preheat is dependent on the injector design, overall flow rate and fuel type. Testing has shown that for the 2nd generation injector, a maximum preheat temperature of 523 K is possible when operating on liquid fuels at a nominal JSR residence time of 3.2 ms. For the SPP, a maximum inlet temperature of 723 K is possible when operating on liquid fuels at a nominal JSR residence time of 2.3 ms. As for the gaseous fuels, much higher preheat conditions are allowable. For natural gas, an inlet temperature of 908 K has been achieved with the SPP.

As a cautionary note, the air heaters are particularly prone to failure due to the following reasons:

- The heating elements are exposed to an oxidizing environment under high temperature conditions.

- The heaters are operated near the lowest recommended flow rate and are prone to overheat and meltdown.

Other heaters and air preheating techniques have been investigated. It has been concluded that the current heater arrangement provides the most cost effective solution.

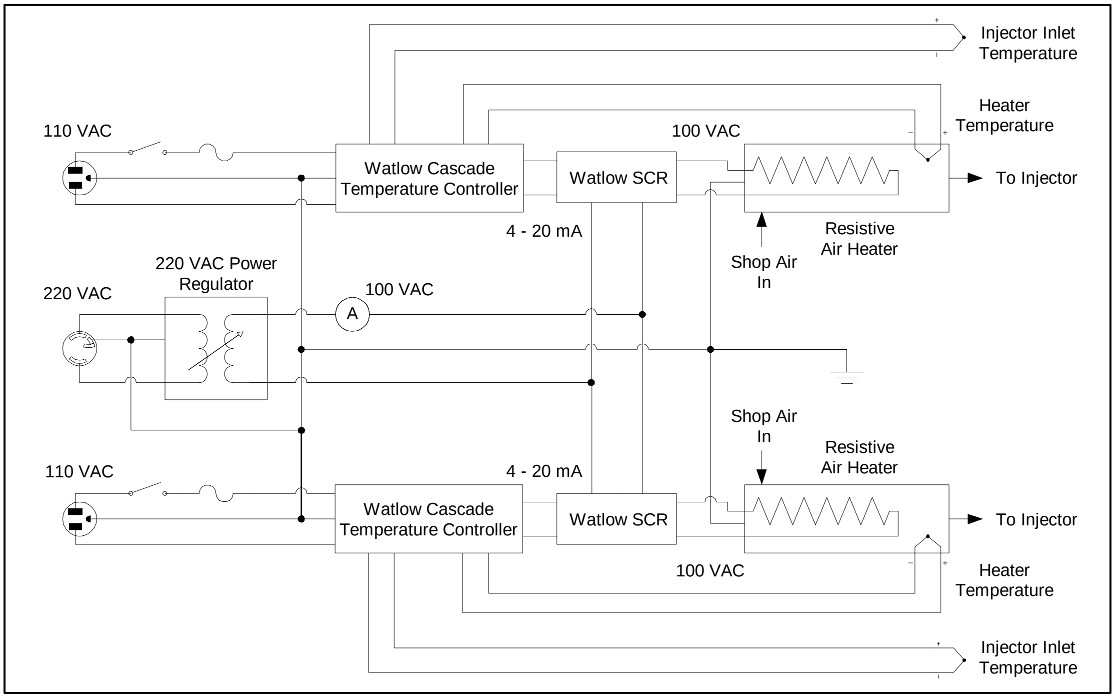

Figure 2.20. Schematic Diagram of the Inlet Temperature Control System

2.5 COMBUSTION TEMPERATURE MEASUREMENT

Combustion temperature is measured with a 0.127 mm (0.005 in) diameter R-type (platinum/platinum-13% rhodium) thermocouple (TC) coated with a ceramic compound (Aremco Model Ceramabond 569) as described by Burton et al. (1992) to prevent catalytic oxidation of CO, H_2, and hydrocarbons at the thermocouple surface. Shown in Figure 2.21 are the JSR temperature profiles for several coated and uncoated TCs of either 0.127 mm or 0.254 mm diameter wires. As can be seen, due to catalytic effects the measured temperatures for the uncoated TCs are considerably higher than the coated ones and approach the complete combustion temperature. In addition, spherical hot junction beads formed by the 0.254 mm wires have nominal diameters of 0.60 mm. This is approximately four times the surface area of the beads formed by the 0.127 mm wires and leads to greater heat loss as indicated by the lower temperature seen in Figure 2.21.

Construction procedures of the R-type thermocouple are described in Appendix D. The standard temperature measuring location is at $r/R_0 = 0.63$ – the location of the highest measured TC temperature at the 65% reactor height.

The measured thermocouple temperature is corrected for radiation and conduction losses (typically, about a 30 to 50 K correction). Rutar et al. (1998) provide a detailed description of the gas temperature correction analysis. The radiation correction is based on a three-body exchange between the thermocouple tip, reactor wall and cold spots (e.g., the jet entrance and exhaust holes) and is detailed in Appendix D. Inner reactor wall temperatures are obtained by focusing on the inner reactor wall through one of the viewing ports with a disappearing filament type optical pyrometer (Pyrometer Instruments Model Pyro Micro-Optical Pyrometer) with an uncertainty of ±10 K. The measured reactor wall temperature is generally about 158 K lower than the measured TC temperature further indicating the significance of reactor wall heat loss. The difference between the measured TC temperature and the reactor wall temperature is essentially independent of changes in flame temperature for a fixed reactor residence time. As for the effects of reactor residence time, the difference in the measured TC temperature and the reactor wall temperature increases by a few degrees as the reactor residence time is increased. This slight increase is within the uncertainty of measured wall temperature and a nominal value of 158 K is used for all cases for the difference in the measured TC temperature and the reactor wall temperature.

Uncertainty in the combustion temperature measurements is judged to be ±20 K. The uncertainties are caused by slight differences in the construction of the thermocouples, slight misplacements of the thermocouple in the reactor and uncertainties in the thermocouple heat loss correction. It is important to note that due to the Arrhenius dependence of NO_X formation on the combustion temperature (see Steele, 1995) slight variations in the corrected combustion temperature will have significant ramifications on the predicted NO_X output when chemical reactor modeling work is conducted.

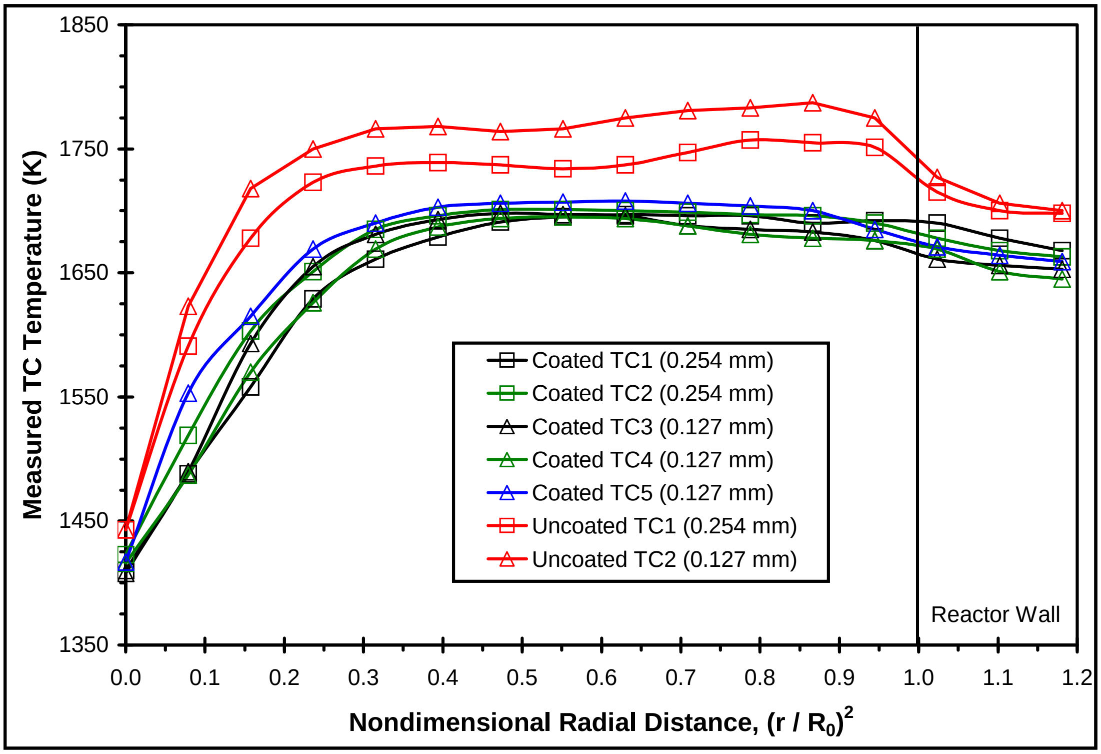

Figure 2.21. Effects of Coating on Measured Thermocouple Temperature (Combustion of Methane and Air, $\phi = 0.63$, $T_{inlet} = 423$ K, $\tau = 3.3$ ms)

2.6 GAS SAMPLING

The gas sampling system is similar to the systems used by Steele (1995) and Capehart (1995). Gas composition is measured by drawing combustion gas through a small, water-cooled, quartz sampling probe and routing the gas through water removal impingers and into a bank of gas analyzers, including process analyzers for NO-NO_X, CO, CO_2 and O_2 as shown in Figure 2.22. The chemiluminescent method is used for the NO-NO_X analyzer (Thermo Electron Model 10). The CO (Horiba Model VIA-510) and CO_2 (Horiba Model PIR-2000) analyzers use the non-dispersive infrared analysis method. The O_2 sensor (Servomex Model 572) is of the paramagnetic type. Suction is provided by a metal bellows pump (Senior Flexonics Model MB-158) capable of drawing approximately 74.5 kPa (22 inHg) of vacuum.

In order to minimize the disturbance of the JSR flow field as well as to minimize internal probe reactions, the uncooled tip of the probe is made as small as practical (i.e., 3 mm outer diameter by 4 cm length). The probe design (shown in Figure 2.23) is slightly different from that used by Steele (1995) and Capehart (1995) which incorporates a flow constriction at the probe tip for aerodynamic quenching (or cooling) to suppress further gas phase reaction of the sampled gases in the probe (see Kramlich and Malte, 1978 and Malte and Kramlich, 1980). This tip constriction design was not used in this study for the following reasons:

- Tip constriction exacerbates the collapse and devitrification (see Ainslie et at., 1962) of the quartz tip walls leading to a significant reduction in flow. This behavior is found to be associated with a significant reduction in measured NO_X yield.

- Aerodynamic quenching is countered by reheat of the sampled gases under the current probe setup where sampled gases are not water cooled in the 4 cm long tip section.

Since the probe tip is not constricted and the sampling line pressure is approximately 30 kPa, choking of the flow either at the tip entrance where a vena contracta can possibly form or at the junction where the uncooled tip is fused to the water jacket is possible. Simple one-dimensional gas dynamic analysis of the 4 cm long tip section indicates that the flow is most likely choked at the tip-water jacket fuse joint. This leads to a nominal residence time of approximately 0.075 to 0.1 ms in the uncooled tip section of the quartz sampling probe leading to minimal amounts of chemical reaction in this section.

The remainder of the probe, which sits outside of the JSR cavity, is jacketed and cooled with water flow and maintained at a low pressure (30 kPa typically) to suppress further chemical reaction in the probe. The residence time in this section is approximately 0.4 ms. The water is maintained sufficiently warm to prevent condensation in the probe. Loss of NO_X because of the solubility of NO_2 in water has not been observed in the present work so long as all sample lines are maintained dry and the only point of condensation is at the impingers. Placement of an NO_2-to-NO converter (Thermo Electron Model 300) in the sample line just after the probe (and upstream of the impingers) has not caused a change in measured NO_X, further confirming no loss of NO_X (see Rutar, 2000). From time-to-time, the GC-FID is employed to check for light hydrocarbon gases (in the C_1 to C_3 range) in the JSR. Typically, total measured hydrocarbon for the JSR recirculation zone is small (i.e., less than 100 ppmv). The standard gas sampling location is at $r/R_0 = 0.71$.

Leak testing of the vacuum sampling system is performed prior to data collection by passing pure nitrogen through the tip of the sample probe and checking the O_2 level in the gas sample. An O_2 level under 0.1% is considered acceptable.

Uncertainty in the measurement of NO_X is influenced by the response and calibration of the chemiluminescent NO-NO_X analyzer, by reactions and absorption within the sample probe and conditioning system and by the degree of day-to-day repeatability of the experiments. Lowest uncertainty is associated with the NO-NO_X analyzer. For example, inaccuracy in the concentration of span gas used to calibrate the analyzer would affect all NO_X measurements by the same proportion and consequently should not affect the NO_X trends with respect to fuel type. Greater uncertainty is associated with the probe and conditioning system. However, in light of the precautions and checks explained above, the uncertainty is judged to be small, less than ±0.5 ppmv (dry, 15% O_2) NO_X. Greatest uncertainty is associated with the repeatability of the experiments. Particularly, small changes in the thermal field of the JSR from day-to-day can affect the NO_X. This aspect of uncertainty appears to be at least ±0.5 ppmv (dry, 15% O_2) NO_X.

As for the inaccuracy in the concentration of span gas used to calibrate the analyzer, the manufacturers recommend that span gas more than three years old or under 500 psig should be replaced. Failure to do so will lead to desorption of the span gas from the gas cylinder wall leading to higher span gas concentrations. This issue has been encountered in the NO_X data obtained for the 2nd generation injector, but not for the 1st generation and SPP injectors. Despite the uncertainty in NO span gas concentration that affects the absolute value of the measurements, the overall trend remains valid since the data was collected over a period of one week. As for the data reported in this work, the values are as measured and no adjustment are made to account for the drift in span gas quality.

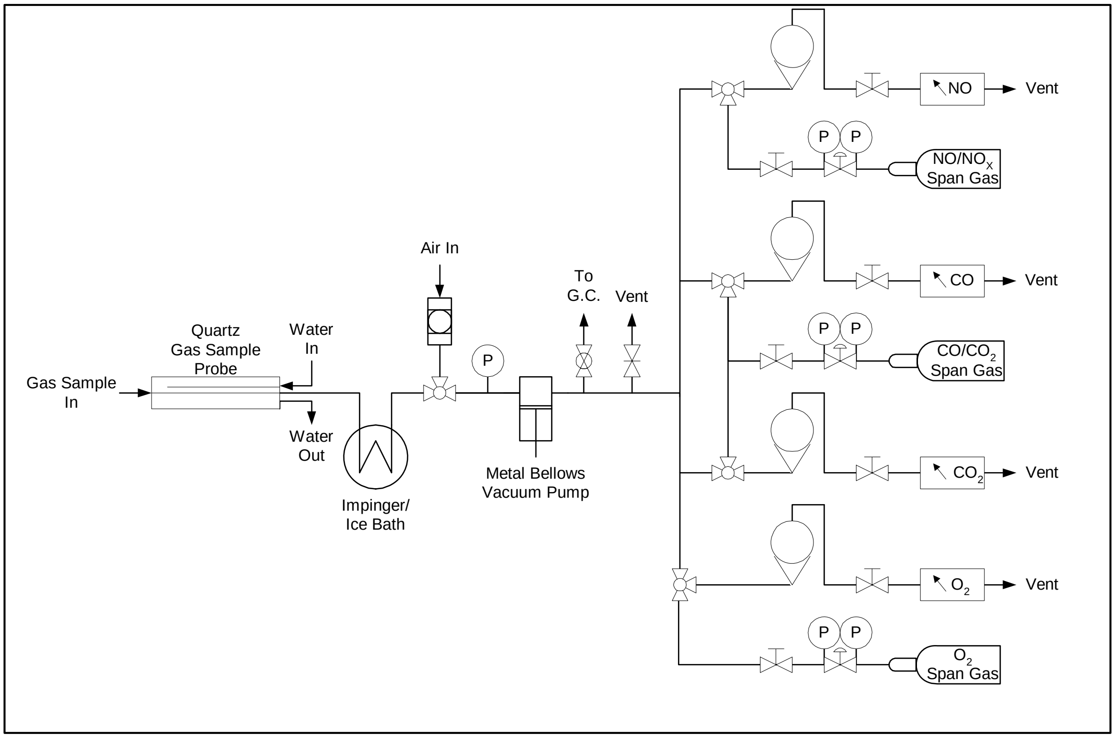

Figure 2.22. Schematic Diagram of the Gas Sampling System.

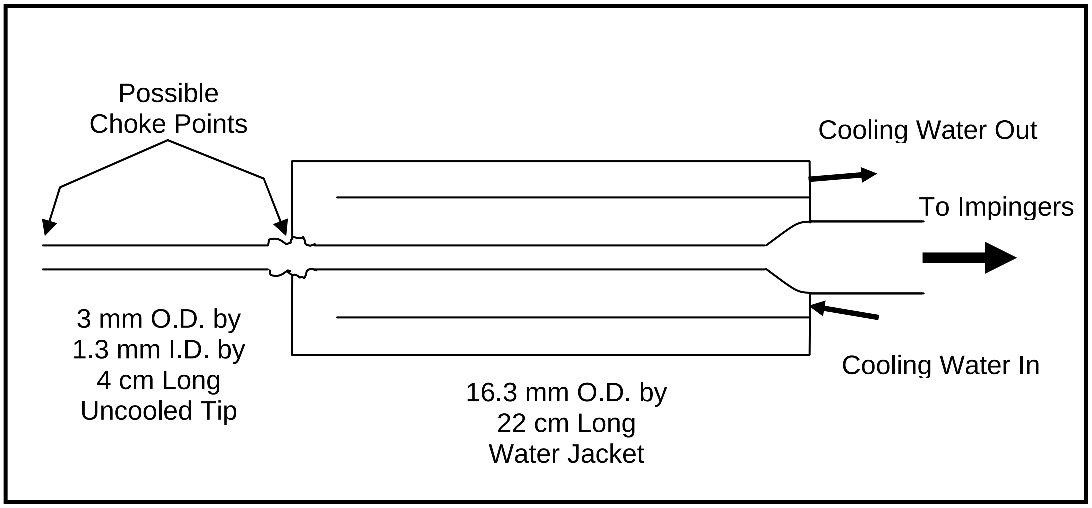

Figure 2.23. Schematic Drawing of the Quartz Sampling Probe (Not to Scale).

2.7 PRESSURE MONITORING

Information on the inlet to the outlet pressure drop, pressure oscillation and overpressure of the injector can be obtained from careful monitoring of the static pressure along the length of the injector. Pressure sensors with fast response times (on the order of 1 ms) are required for detailing pressure oscillation. Current state-of-the-art semiconductor-based pressure sensors can provide such quick response characteristics and are utilized in this study.

The static pressure in the SPP injector at various axial locations (see Figures 5.2 and G.1) is monitored through both traditional pressure gages of the spring suspended type (Ashcroft Model 595-04 and 595-06) and semiconductor-based pressure sensors. The addition of the electronic pressure transducers allows rapid and accurate acquisition of pressure data. Various pressure transducers are used and their specifications are listed in Table 2.5. Additionally, all pressure sensors are fully temperature-compensated and preamplified. The analog output signals are all linearly proportional to the input pressure. The pressure transducers are calibrated with a Fluke Model 718-100US Pressure Calibrator. Representative wiring/flow diagram for the pressure measuring hardware is shown in Figure 2.24.

Table 2.5. Solid State Pressure Transducer Specifications.

Model	***Full Range (kPa)***	***V_{in} / V_{out} (VDC)***	***Accuracy (% Full Scale)***	***Sensitivity (mV/kPa)***	***Response Time (ms)***
Honeywell 142PC30G	200	12 / 5	±0.75	24.2	1
Honeywell 242PC30M	200	12 / 5	±1.5	24.2	1
Honeywell 40PC100G1A	700	5 / 4.5	±1.0	5.8	1
Honeywell 40PC250G1A	1700	5 / 4.5	±1.0	2.3	1
Motorola MPX5500DP	500	5 / 4.7	±2.5	9.0	1
Motorola MPX5700DP	700	5 / 4.7	±2.5	6.4	1
Motorola MPX5700GP	700	5 / 4.7	±2.5	6.4	1

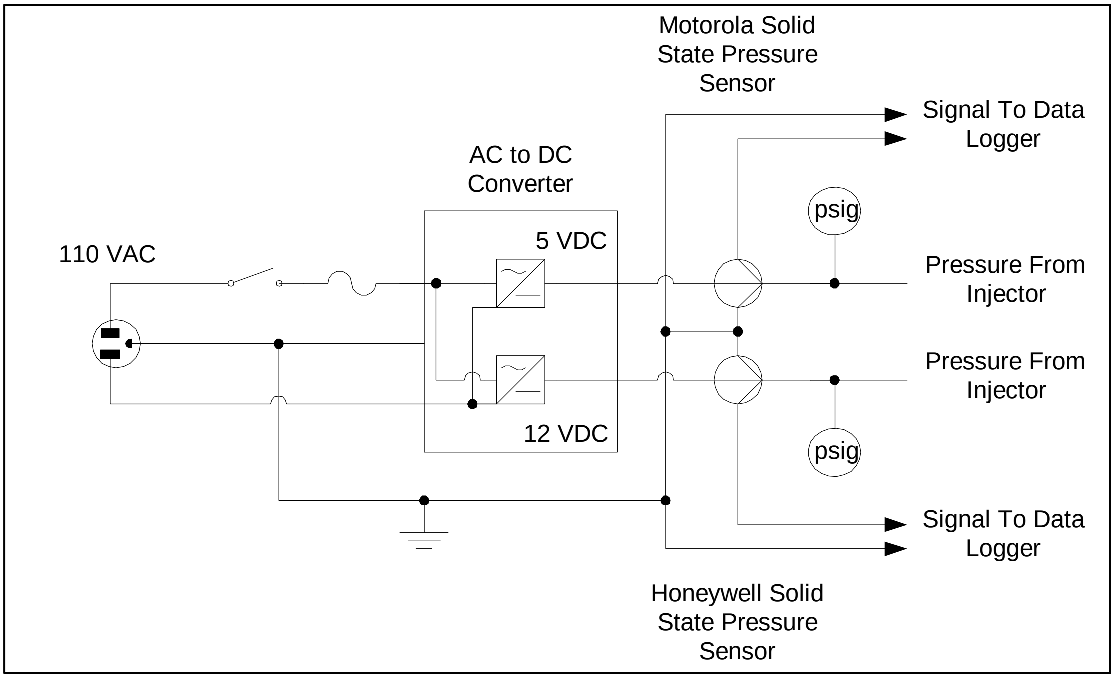

Figure 2.24. Schematic Diagram of the Pressure Monitoring System.

2.8 LASER ABSORPTION (DEGREE OF MIXING) MEASUREMENTS

Limited cost effective diagnostic tools are available for measurements of unmixedness of fuel and air mixtures. One technique involves probe sampling of the fuel and air mixture as mentioned in Section 2.6. This technique can be fairly inexpensive but the information obtained is generally averaged over a long time constant of several seconds and may misrepresent the actual flow behavior. It is primarily useful for detecting spatial variations in fuel-air ratio exiting an injector. Other techniques usually involve the use of a high power laser system, such as Rayleigh scattering (see Yee et al., 1983 and Halthore and Gouldin, 1986) or laser induced fluorescence (Foglesong et al., 1999, Krämer et al., 1999 and Stufflebeam et al., 1999). These systems are generally optically complex and are quite cost prohibitive. A fairly simple and inexpensive alternative is the laser absorption technique (LAT). LAT systems have been in use since the early 1970s. Extensive LAT developments have been performed by several research groups (Mongia, 1998, Yoshiyama et al., 1996, Perrin and Hartmann, 1989, Tsuboi et al., 1985 and McMahon et al., 1972). Most of the components for the LAT system used in this research were provided by the Laser Diagnostic Group at the University of California at Berkeley (UCB) and are available for under $10,000.

LAT is utilized in this research to investigate the degree of mixing of the fuel and air mixture as it departs from the SPP injector. This rather simple diagnostic tool is based on the strong absorption characteristics of electro-magnetic radiation of 3.39 μm wavelength by various hydrocarbons (see Tsuboi et al., 1985). Temporal fluctuations averaged over a line-of-sight pathlength are measured with the current LAT system. In the present application, the line-of-sight measurements are made along a 12.7 mm (0.5 in) diametric path that is 2 mm above the injector opening with the nozzle block and JSR removed. Measurements made without the nozzle block provide the most conservative (or worst) estimate of the degree of mixing since the converging nozzle has the effect of directing the flow and increasing the flow uniformity. Temporal information is obtained with the present setup. No spatial information can be deduced with the current line-of-sight LAT system, though efforts are underway at UCB to develop a LAT system that can provide spatial resolution (Dibble, 1999).

The LAT consists of a 5.0 mW, 3.392 μm wavelength helium-neon laser [Trius Engineering Model TE-10(P)-339] powered by a 1800-2600 VDC, 6.5 mA power supply (Voltex S-22-00), a neutral density filter (Spectrogon Model 713.703.590), two ultra-violet (UV) grade plano-convex lenses (Edmond Scientific Model J08006), a narrow bandwidth, infrared (IR) band pass filter centered at a wavelength of 3.399 μm (Corion Model No. 3399-4X), a highly sensitive IR detector (Boston Electric Model PDI-2TE-4) that is thermal electrically cooled and maintained at 5°C (Vigo System Model CTTC-02/110) and a digitizing oscilloscope (Fluke Model PM3384A CombiScope) as shown in Figure 2.25. The ancillary optical components are necessary for the following reasons:

- The neutral density filter is required since the laser power is overrated for the highly sensitive detector.
- The plano-convex focusing lens are required to minimize the effects of beam steering due to the differences in index of refraction as the laser beam passes through the high temperature jet.
- The narrow bandwidth, infrared band pass filter is required to filter out any non-laser radiation that is emitted from the hot injector metal surfaces.

Absorption of light at a certain wavelength (e.g., 3.39 μm) as it passes through a medium is given by the Lambert-Beer Law:

$$\frac{I}{I_0} = exp(-\alpha \cdot X \cdot P_{total} \cdot L) \quad \text{Eq. 2.3}$$

where I is the mean laser transmission, I_0 is the reference or base intensity of the laser, α ($cm^{-1}atm^{-1}$) is the absorption coefficient at the given wavelength and is a function of both temperature and pressure, X is the mole fraction of the hydrocarbon, P_{total} (atm) is the total pressure and L (cm) is the pathlength of the absorbing medium.

To confirm the goodness of the LAT system, both methane and propane measurements for laser transmission as a function of temperature are compared to the data of Yoshiyama et al. (1996) and Perrin and Hartmann (1989).

The data of Yoshiyama et al. (1996) are based on the use of the molar extinction coefficient, ε (cm^2/mol), that was found to be relatively temperature independent between 285 and 420 K. The molar extinction coefficient is related to the transmission intensity as:

$$log_{10} \frac{I}{I_0} = -\varepsilon \cdot C \cdot L \quad \text{Eq. 2.4}$$

where C (gmol/cm^3) is the concentration of hydrocarbon. The following are molar extinction coefficients for methane and propane determined at 298 K (see Yoshiyama et al., 1996):

$$\varepsilon_{methane} = 1.10 \cdot 10^5 \left(\frac{P}{P_0} \right)^{-0.302} \quad \text{Eq. 2.5}$$

$$\varepsilon_{propane} = 1.04 \cdot 10^{5} \left(\frac{P}{P_0} \right)^{-0.046} \quad \text{.............................. Eq. 2.6}$$

where P (kPa) is the total pressure and P_0 is the reference pressure equal to 101.3 kPa.

Perrin and Hartmann (1989) determined the absorption coefficient for the 3.39 μm laser for methane diluted in N_2 for a gas temperature of 293 to 787 K and a pressure of 1 atm. The data can be expressed as an exponential function of temperature as follows:

$$\alpha_{methane} = 22.89 \cdot exp(-0.003033 \cdot T) \quad \text{............. Eq. 2.7}$$

The transmission data is collected with the digitizing oscilloscope over a period of 50 ms at a rate of 10 samples per millisecond with a total of 500 samples. The standard deviation in the transmission (σ) and the mean transmission (<X>) are determined for the 500 samples and the ratio of σ/<X> is defined as the unmixedness (see Mongia, 1998). The noise base at various inlet temperature conditions is determined in the absence of fuel flow with only the flow of the preheated air. The results indicate that the baseline noise inherent in the laser/electronic system is independent of the inlet temperature and is constant with a value of σ/<X> of 2.3%. The unmixedness results for various SPP conditions are presented and discussed in detail in Chapter 5.

One inherent difficulty with the fairly inexpensive 3.39 μm wavelength IR helium-neon laser is its lack of stability in output intensity. The variation or "drift" in the intensity emitted by the laser has been reported by others (Perrin and Hartmann, 1989 and Sample, 1999). The drift is of low frequency with a period of approximately 20 minutes and its magnitude can be as high as ±30% of the norm. In order to account for the effects of laser drift, additional optics are required. This approach is not undertaken in the present study. In order to determine the base intensity of the laser,

I_0, the fuel flow is immediately shutoff after the collection of the transmission data, I. This approach is reasonable since the laser drift frequency is low. Additionally, the issue with laser drift should have minimal effect on the unmixedness measurements since the data are collected over a period of 50 ms.

Shown in Figure 2.26 is the variation in the time-mean transmission of both methane-air and propane-air streams measured for the SPP as the inlet temperature is varied from 293 to 600 K. Also plotted are the results of Yoshiyama et al., 1996 (molar extinction method) and Perrin and Hartmann, 1989 (absorption coefficient method) applied to the experimental temperature and concentration conditions. As can be seen, the measured methane data correlates well with the data of Perrin and Hartmann (1989). In all cases, the trend of reduced absorption with increasing temperature is strongly observed.

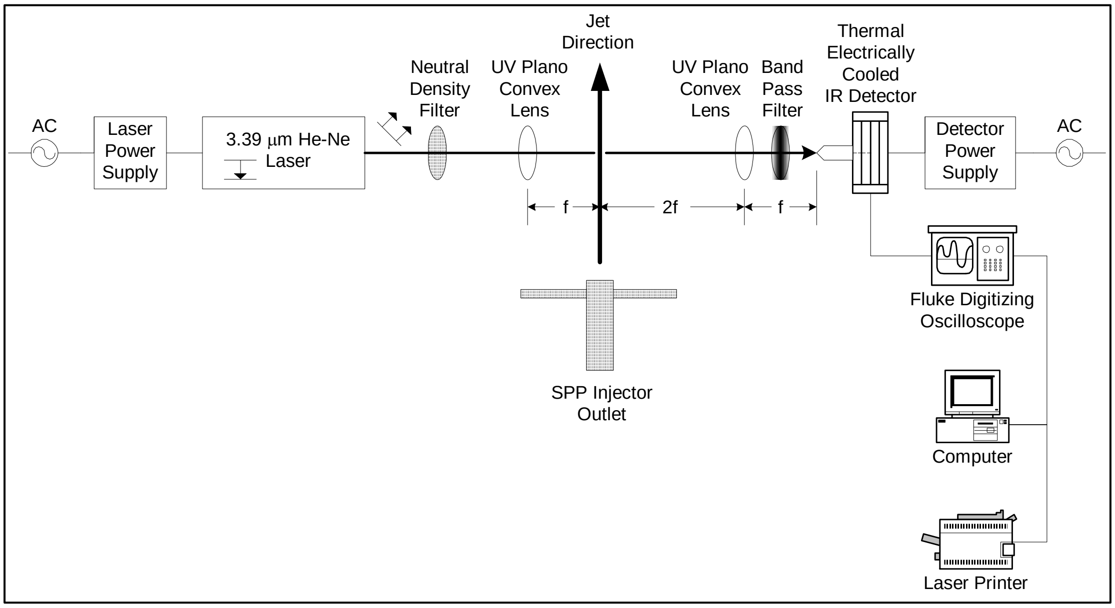

Figure 2.25. Schematic Diagram of the Laser Absorption System.

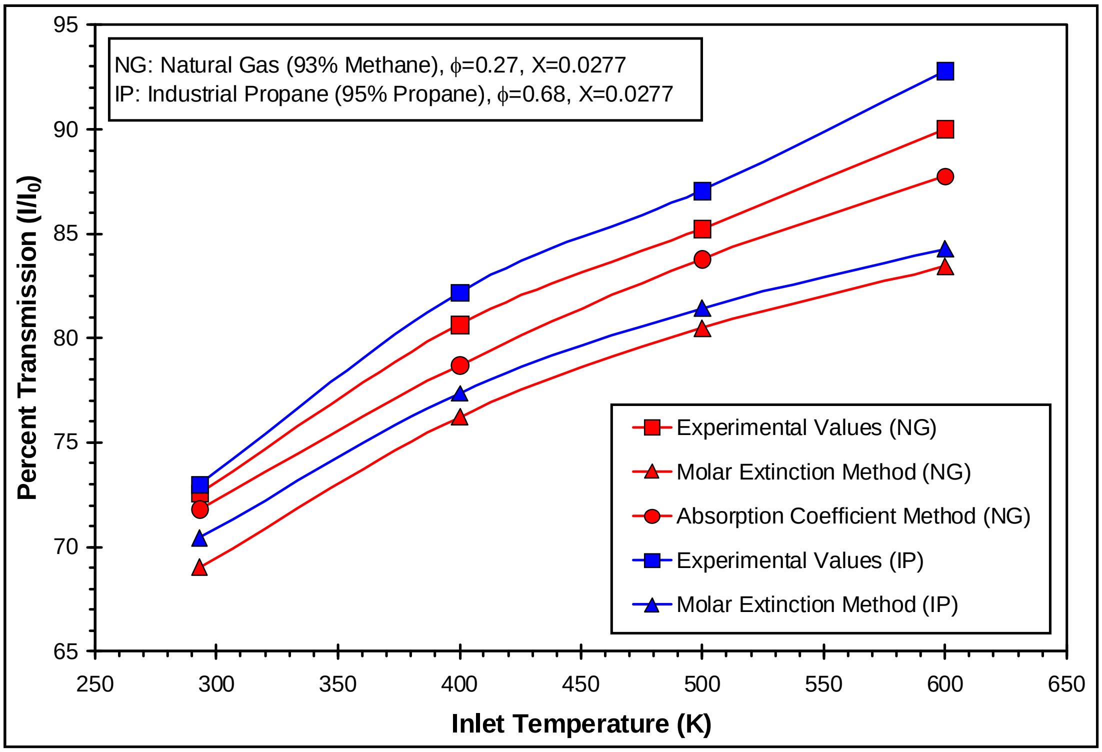

Figure 2.26. Effects of Mixture Inlet Temperature on the Transmission of the 3.39 μm He-Ne Laser for Methane/Air and Propane/Air Mixtures at 1 Atm.

2.9 DATA ACQUISITION

The data acquisition (DAQ) system as shown in Figure 2.27 consists of a Pentium II class computer communicating with four data loggers via a local-area, 10-base-2 (serial) network protocol. The computer is used to control the data loggers and to record all data downloaded from the data loggers through application of an easy-to-use software package (Fluke Model 2640A-912 NetDAQ Logger with Trending). The setup files for the four data loggers are shown in Appendix E. Each data logger is capable of measuring AC or DC voltages, resistance, DC current flow, frequency and temperature from various thermocouple types on twenty independent channels. Incoming signals are preprocessed and preconditioned in an input module (Fluke Model 2620A-100 Universal Input Module). The signal is then adjusted and post-processed (which includes analog to digital conversion) within the data logger to the proper engineering units and displayed on the data logger's front panel and stored on the computer.

Two models of the data logger are used (Fluke Model 2640A and 2645A NetDAQ Data Loggers). The Model 2640A has a maximum scan rate of 100 Hz and is used for recording slow response measurements like temperature, flow rate and gas emissions. The Model 2645A has a maximum scan rate of 1 kHz and is used for recording fast response measurements like pressure. The use of modern DAQ equipment greatly enhances the ease of experimental data collection and improves the quality of the data.

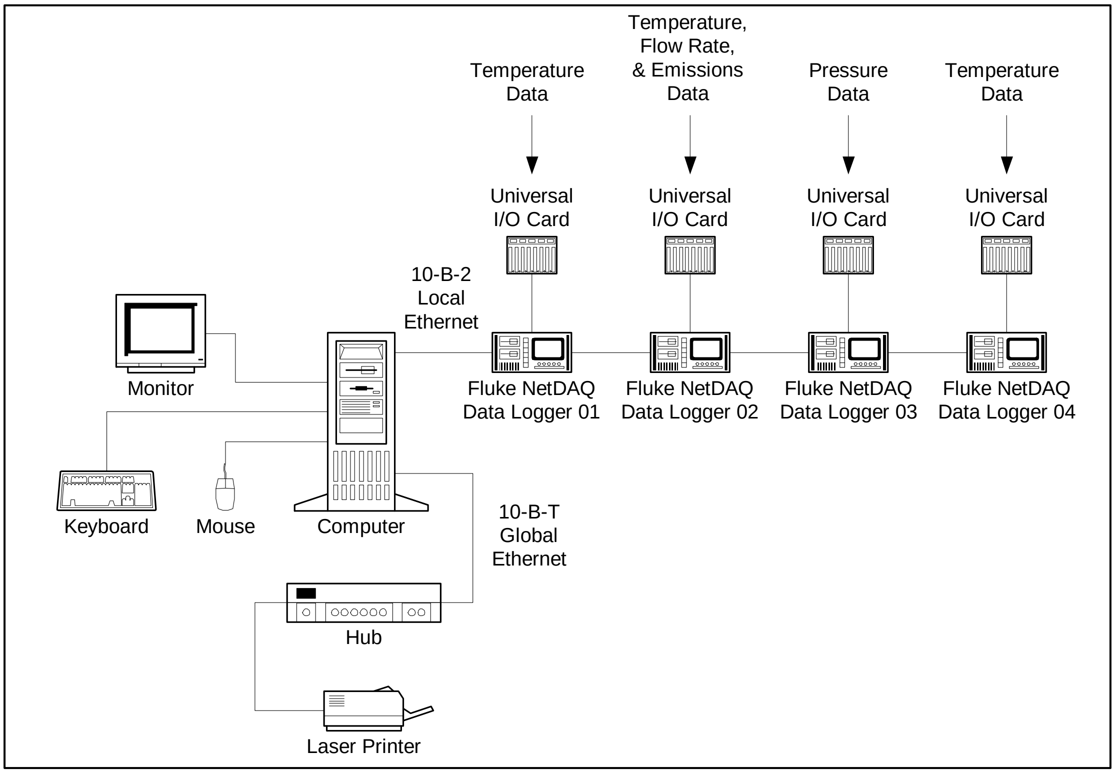

Figure 2.27. Schematic Diagram of the Data Acquisition System.

2.10 FUELS

Both laboratory and commercial grade gaseous and liquid fuels are studied. The fuel carbon to hydrogen (C:H) molar ratios for the fuels range from 0.25 (methane) to 1.0 (benzene). The gaseous and liquid normal alkane fuels studied are of high purity (99^{+}%) with the exception of bottled natural gas used to simulate methane (CH_4) and industrial propane used to simulate propane (C_3H_8). All reported fuel properties are either provided by the manufacturer or by independent laboratory analysis performed by Mr. George Suunna (310-513-2031) of Core Laboratories, Inc. of Carson, CA.

The gaseous fuels tested include natural gas (93^{+}% methane), research grade ethane (99^{+}% C_2H_6) and industrial propane (95^{+}% propane). The pure liquid fuels tested include n-pentane (C_5H_{12}), n-hexane (C_6H_{14}), n-heptane (C_7H_{16}), n-dodecane ($C_{12}H_{26}$), n-hexadecane ($C_{16}H_{34}$), toluene ($C_6H_5CH_3$), benzene (C_6H_6) and methanol (CH_3OH or MeOH). Butane and other heavier alkane fuels are not studied due to fuel handling and supply difficulties and health and safety concerns. The liquid fuels are all of either high pressure liquid chromatographic or spectrophotometric grade and are free of fuel bound nitrogen (FBN). Additionally, n-dodecane doped with n-ethylethylenediamine (n-$C_2H_5NHCH_2CH_2NH_2$ or n-$C_4H_{12}N_2$ or EEDA) to give 96 ppmw (parts per million by weight) of FBN has been tested.

Six commercial liquid fuels, Kern light naphtha (K-LN), U.S. Oil and Refinery light naphtha (USOR-LN), Cheveron No. 2 low sulfur diesel (C-LSD), U.S. Oil and Refinery No. 2 low sulfur diesel (USOR-LSD), Texaco No. 2 low sulfur diesel (T-LSD) and Texaco No. 2 high sulfur diesel (T-HSD), have also been studied. Detailed fuel properties for n-pentane, n-dodecane, K-LN, and C-LSD are presented in Table 2.6. As can be seen, the naphtha contains about equal parts of paraffins, isoparaffins and naphthens. The No. 2 diesel fuel contains about 34% paraffins, 7% isoparaffins, 8% aromatics and 4% naphthens. About 20 of the 47% unidentified components could possibly be aromatics as indicated by several material safety data sheets as provided by the manufacturer.

The FBN content, fuel sulfur content and molar C:H of all commercial fuels studied are listed in Table 2.7. It is important to note that the T-HSD was analyzed in 9/96 and showed an FBN content of 165 ppmw. Re-analysis of the T-HSD in 10/99 indicates a significant decrease in FBN to 84 ppmw. This reduction in FBN is possibly due to biological microbe activity in the fuel as reported by several marine diesel users (Lisseveld, 1997).

Table 2.6. Basic Fuel Properties and Chemical Composition.

Specifications	***n-Pentane***	***Kern Light Naphtha****	***n-Dodecane***	***Cheveron Low Sulfur Diesel***$^{+}$
Chemical Formula	C_5H_{12}	$C_{5.90}H_{12.45}$	$C_{12}H_{26}$	$C_{13.77}H_{26.28}$
Boiling Range (K)	303	305 - 386	489	444 - 600
Molecular Weight	70.10	83.20	170.34	191.55
Specific Gravity	0.646	0.693	0.750	0.832
Reid Vapor Pressure (kPa)	58.1	75.1 – 82.0	< 6.9	< 20.7
C/H Molar Ratio	0.417	0.473	0.462	0.524
Fuel Bound Nitrogen (ppm by wt.)	0	< 1	0	124
Fuel Bound Sulfur (ppm by wt.)	0	9	0	195
Paraffins (LV%)	100	30.59	100	33.65
Isoparaffins (LV%)	0	34.05	0	7.25
Olefins (LV%)	0	0.11	0	< 0.01
Naphthens (LV%)	0	34.70	0	4.13
Aromatics (LV%)	0	0.55	0	7.73
Unidentified (LV%)	0	< 0.01	0	47.24
Kinematic Viscosity ***(m^2/s) @ 40°C***	N/A	0.44	N/A	2.78
LHV (MJ/kg)	N/A	51.45	N/A	43.11
Autoignition Temp. (K)	558	< 553	478	< 450

* Lab Analysis: Core Laboratories, Inc.

\+ Lab Analysis: Combined from Core Laboratories, Inc. and Chemical Analysis Dept., Solar Turbines, Inc.

Table 2.7. Elemental Composition of the Commercial Liquid Fuels Tested with the SPP.

Specifications	***K-LN***	***USOR-LN***	***C-LSD***	***USOR-LSD***	***T-LSD***	***T-HSD***
Carbon Weight %	85.03	84.20	86.28	86.42	86.50	86.69
Hydrogen Weight %	14.97	15.80	13.72	12.73	12.56	12.45
C:H (mole ratio)	0.473	0.444	0.524	0.566	0.574	0.580
Fuel Nitrogen (ppmw)	< 1	3	46	49	91	84
Fuel Sulfur (ppmw)	9	46	500	400	195	3539

(Lab Analysis: Core Laboratories, Inc.)

2.11 OPERATING PROCEDURES

The operating procedures for the three generations of injector-JSR configurations are essentially identical. The operating procedure for the SPP-JSR is a bit more complex due to the staging technique, but is nevertheless representative of the other two injector-SPP setups and will be described in detail as follows:

1. Warm Up of All Electronic Devices: Electronic devices include the mass flow controllers, inlet temperature controllers, gas analyzers, pressure sensors and data loggers. A minimum warm up time of two hours is suggested for all components that utilize mechanical switching (i.e., the channel scanner in the data loggers, the flow control solenoid valve in the MFCs and the diaphragm in the pressure sensors), rotating choppers (i.e., the chopper wheel in the CO and CO_2 analyzers) and components that require heating (i.e., the ozonator in the NO-NO_X analyzer). Ignition and reactor warm up can be initiated during the thermal stabilization process for the electronic components.

2. Adjustment of Flow Supply Backpressure: Adjust the backpressure for all flow supplies, including supplies for both the gaseous and liquid media, to 4.4 atm (50 psig). Other backpressure levels may be used, but 50 psig is suggested for steady operation and control of the MFC solenoid valve.

3. Ignition: Locate the R-type TC 5 mm from the center of the JSR, while leaving the other three viewing ports unplugged. Adjust the airflow in 1st and 2nd stage MFCs to approximately 10 and 6 slpm, respectively. Adjust the atomizer airflow rate to 4 slpm. Situate the HV discharge tip of the ceramic ignition probe at the center of the JSR via one of the viewing ports. Switch on the igniter and gradually increase the hydrogen flow until ignition occurs as indicated by an audible “pop” and a flame temperature of approximately 800°C. Quickly switch off the igniter and extract it from the JSR. Prolonged exposure of the igniter tip to

flame conditions will cause melting of the stainless steel leads. The ignition process is at times challenging if the 4 mm nozzle block is used since the "fast" premixed hydrogen and air mixture has a tendency to flashback into the injector. If flashback does occur as indicated by the unusual high temperature (> 30°C) in the injector, immediately shut off the hydrogen (or gas) flow via the toggle valve (or kill valve) and reignite the JSR. Again, the critical step is the gradual introduction of the hydrogen flow.

4. Nominal Flow Adjustment: Gradually increase the injector air and hydrogen flows simultaneously while maintaining the reactor under 1100°C till both airflow rates are at 30 slpm. Hold the reactor at these conditions for 5 to 10 minutes. This procedure is suggested to prevent flashback and blowout of the flame.

5. Fuel Switching: Gradually increase the propane flow rate while reducing the hydrogen flow rate. This is possible since the gaseous hydrocarbon fuel flow and the hydrogen flow are controlled independently as shown in Figure 2.17. Do not allow the reactor temperature to exceed 1350°C during this process. Once fuel switching is accomplished, completely turn off the hydrogen supply at the bottle. As a cautionary reminder, hydrogen is prone to leakage, has a very wide flammability limit and a high flame velocity. In addition, a gradual increase in reactor temperature is required since rapid heating of the ceramic reactor introduces excessive amounts of thermal shock that will lead to cracking and catastrophic failure of the ceramic material.

6. Injector and Reactor Warm Up: Once the JSR is completely running on propane, insert 3.175 mm (1/8 in) ceramic rods into the three unplugged viewing ports to prevent excessive amounts of heat loss. Increase the injector temperature to the 150°C. Keep in mind that as the inlet temperature increases, the flame temperature will also increase if ϕ is held constant. Make sure the flame temperature does not exceed 1650°C, which is the R-type TC limit. The reactor

warm up time is approximately two hours. Reactor wall temperature as measured by the external surface mounted K-type TCs can also be used to indicate thermal stability of the JSR.

7. Gaseous Fuel Operation: Once the JSR reaches thermal equilibrium, the gaseous fuel is switched to the one of interest by reversing the fuel switching procedures as outlined in Step 5. Once the reactor is running on hydrogen, Step 5 is used again to switch the fuel to the one of interest. Time must be allowed for the re-stabilization of the JSR and SPP temperatures. Nominally, the required time is 10 to 20 minutes. Thermal re-stabilization time is also required when operating conditions (i.e., change in inlet temperature) are modified. Again, both the flame and external wall surface temperatures can be used as indicators for thermal stability.

8. Liquid Fuel Operation: Switching to liquid fuels requires the same care as stated in the fuel switching procedure of Step 5. The liquid fuel is gradually introduced while the gaseous fuel flow is reduced. Again, this possible since the two are on independent control channels (see Figures 2.17 and 2.18). Similar to gaseous fuel operation, thermal re-stabilization time is required for operation on liquid fuels. The atomizer air required for liquid fuel atomization is always maintained to prevent liquid fuel fouling of the atomizer.

9. Gas Sampling: Once the injector and JSR are at the desire temperature conditions, remove one of the ceramic rods and gradually insert the quartz gas sampling probe making sure that the sampling probe cooling water is flowing and suction is provided. The analyzers, particularly the O_2 sensor, require approximately 45 to 60 s to stabilize. Remove the sampling probe after each test case to prolong the life of the uncooled tip.

10. Shutdown: The shutdown procedure requires transition back to gaseous fuel operation for injector fouling prevention. Once the system is operating on gaseous fuel, reduce the inlet temperature to ambient values to prevent meltdown of the heater elements. Once the heaters are below 300°C, turn off the fuel flow and immediately reduce the airflow rates to a total of 10 slpm. This is to prevent rapid cooling down of and thermal shock to the JSR.

CHAPTER 3: FIRST GENERATION INJECTOR DESIGN AND RESULTS

The development of the prevaporizing-premixing injectors has been a central focus of this research. Similar to any LP and LPP research and development, the injector design is the key to optimizing the reduction in pollutant emissions. The development history of the three injectors used in this study is presented in the following sections. Additionally, the results obtained from the use of each injector are presented.

3.1 FIRST GENERATION INJECTOR

The first generation LPP injector was designed and constructed by Capehart (1995) as shown in Figure 3.1. The prevaporizing-premixing chamber consists of two sections with a total nominal injector residence time of about 200 ms. In the lower section, the fuel is injected, atomized, mixed with heated air in a cross flow pattern and vaporized. In the upper section, the vaporization and mixing processes are permitted to reach completion. Also, the upper section contains holes for injection of gaseous fuel, such as the startup fuel (hydrogen), methane and propane. Typically, the pressure of the prevaporizing-premixing chamber is 2 atm. Acceleration of the prevaporized-premixed gas occurs across the nozzle block (containing a single, 2 mm, centered hole for the jet).

Two liquid fuel atomizing nozzles are used. Because of the low fuel flow rates used (0.04 to 0.07 cc/s), most commercial nozzles are oversized by an order of magnitude for the present application. Nonetheless, for the pure liquid fuels tested it is possible to use a commercial nozzle operated below the minimum recommended operating regime. Specifically, a Delavan SN/Siphon solid cone air atomizing nozzle (part number 30609-2) is used in the gravity feed mode. According to the manufacturer, this nozzle produces a fine solid cone spray with a Sauter mean diameter of 61 μm and cone angle of 40° at 15 cm. Problems associated with the use of the Delavan nozzle include instability in the liquid fuel flow at low flow rates and extended vaporization time due to agglomeration of fuel droplets caused by the impact of the fuel spray on the prevaporizer wall. Thus, the results obtained from the Delavan atomizer are not presented.

For experiments with No. 2 diesel fuel and for comparative experiments with n-dodecane and with n-dodecane doped with EEDA, another atomizing nozzle was designed and incorporated into the system. This work was done under the present study. The new nozzle is essentially a Nukiyama-Tanasawa type airblast atomizer (Lefebvre, 1983) that contains a weak pressure atomizer housed in an air atomizer as shown in Figure 3.2. All results presented are based on the use of the Nukiyama-Tanasawa atomizer.

Liquid fuel is initially weakly atomized by the pressure atomizer. The air atomizer then provides second stage atomization and final cone angle adjustment. The double atomization process provides a wide range of operating conditions for complete atomization of liquid fuel. Although a detailed analysis (e.g., a Doppler particle analysis) has not been performed on the nozzle, initial inspection of the spray indicates a cone angle of approximately 17° at 15 cm for distilled water operated at a nominal flow rate of 0.05 cc/s with a back pressure of about 3 atm and airflow rate of 95 cc/s (at 3 atm). Furthermore, according to Lefebvre (1989), atomization performance of the Nukiyama-Tanasawa type nozzle is essentially independent of the liquid jet/spray condition, but is strongly dependent on the velocity or shear force generated by the air jet. For all conditions tested, the airflow velocity is near M=0.5 leading to extremely fine atomization of the liquid fuel. Pressure oscillation of the prevaporizer was not experienced after extensive use of the Nukiyama-Tanasawa type nozzle.

Completeness of vaporization is confirmed by examining light scattering from a 5 mw red He-Ne laser beam (Spectra Physics Model 155) passed through the outlet jet of the prevaporizing-premixing chamber operated under experimental preheat conditions with the jet-stirred reactor removed. No side scattering is observed by the naked eye when the prevaporizing system is properly set, indicating the lack of droplets (and aerosol) in the flow and, thus, complete vaporization of the liquid fuel.

The residence time of the prevaporizing-premixing chamber is 150 to 250 ms. Since the airflow rate of the present experiments is nominally constant, the variation in the residence time is due to variation in the inlet temperature. For the present experiments, the JSR inlet jet temperature is 420 to 725 K. The lower (vaporizing) section of the chamber accounts for about 1/3rd of the total residence time, and the upper (mixing) section accounts for the 2/3rd balance of the residence time in the prevaporizing-premixing chamber. As shown in Figure 3.1, mixing is enhanced by baffle plates located in the upper section. Gaseous fuel is injected through tiny jets in the tube located between the two baffle plates (see Figure 3.1). The baffle plates create turbulent eddies which have a turnover time of about 5 ms ($\tau \approx L_{gap}/U_{gap}$, where *gap* denotes the space between the baffle plate and chamber wall). Residence time in the space between the upper baffle plate and the JSR nozzle is 30 to 50 ms. Comparison of this residence time to the turn-over time of the eddies created by the baffle plate indicates that the degree of premixing in the chamber is high. Further, because of the intense mixing in the JSR, any fuel and air not completely mixed prior to entry into the JSR is rapidly mixed within the JSR (Rutar et al., 1997). Thus, the experiments are treated as fully premixed.

For the experiments with the pure hydrocarbon fuels, the inlet jet temperature is 420 K. For this case, conditions within the prevaporizing-premixing chamber are just adequate to fully vaporize the pure liquid hydrocarbons (Capehart, 1995). For the experiments with the No. 2 diesel fuel, the inlet jet temperature is increased to 700 to 725 K, in order to ensure vaporization of all fuel components. For comparison, n-dodecane and EEDA doped n-dodecane are also run at this temperature. Given the combination of relatively high temperature (at least 700 K) and relatively long residence time (about 150 ms), fuel pyrolysis reactions are possible in the prevaporizing-premixing injector at these conditions. Due to these concerns and difficulties, an injector of advanced design (i.e., the SPP injector) was designed and fabricated to minimize and avoid the preflame reactions that have been experienced through the use of the first generation injector.

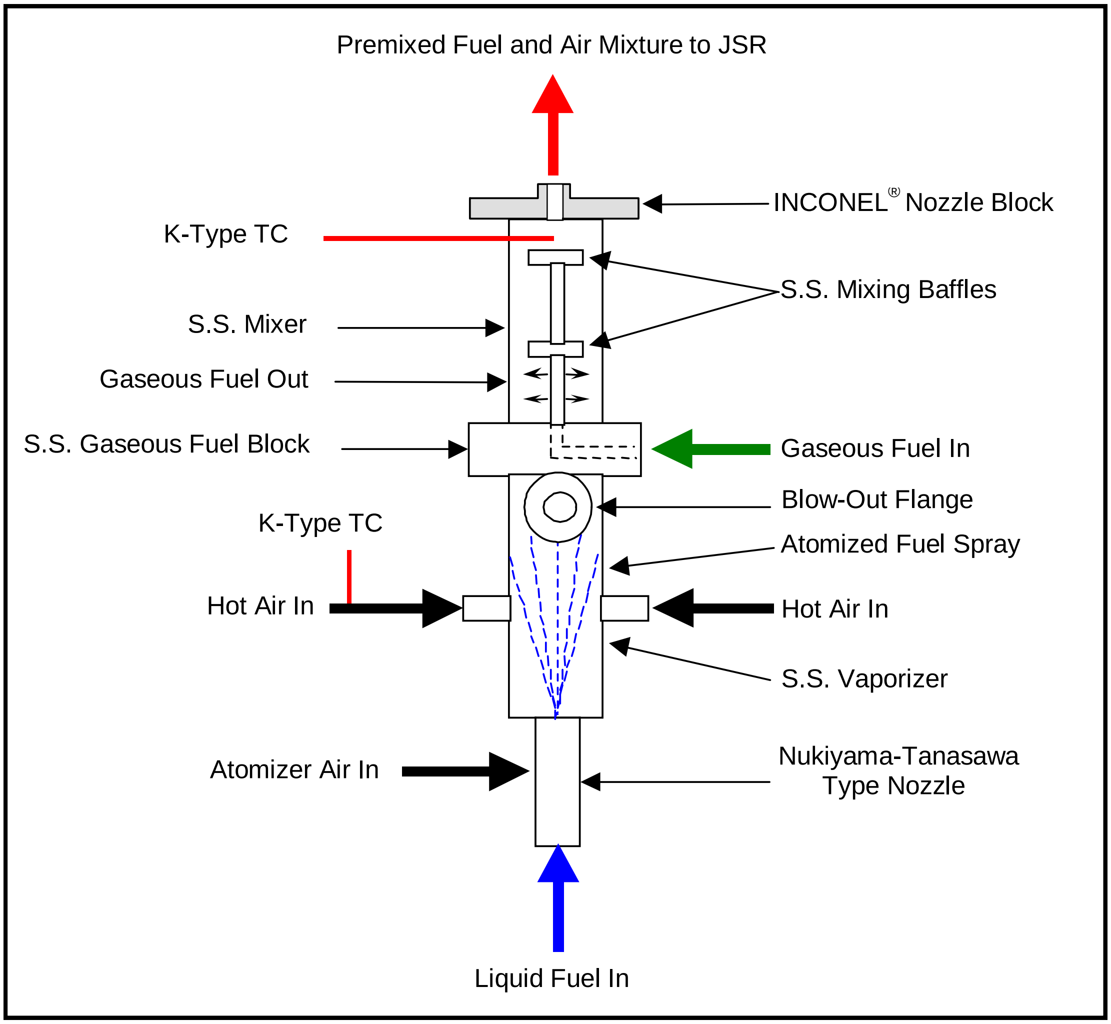

Figure 3.1. Schematic Drawing of the First Generation, Prevaporizing-Premixing Injector.

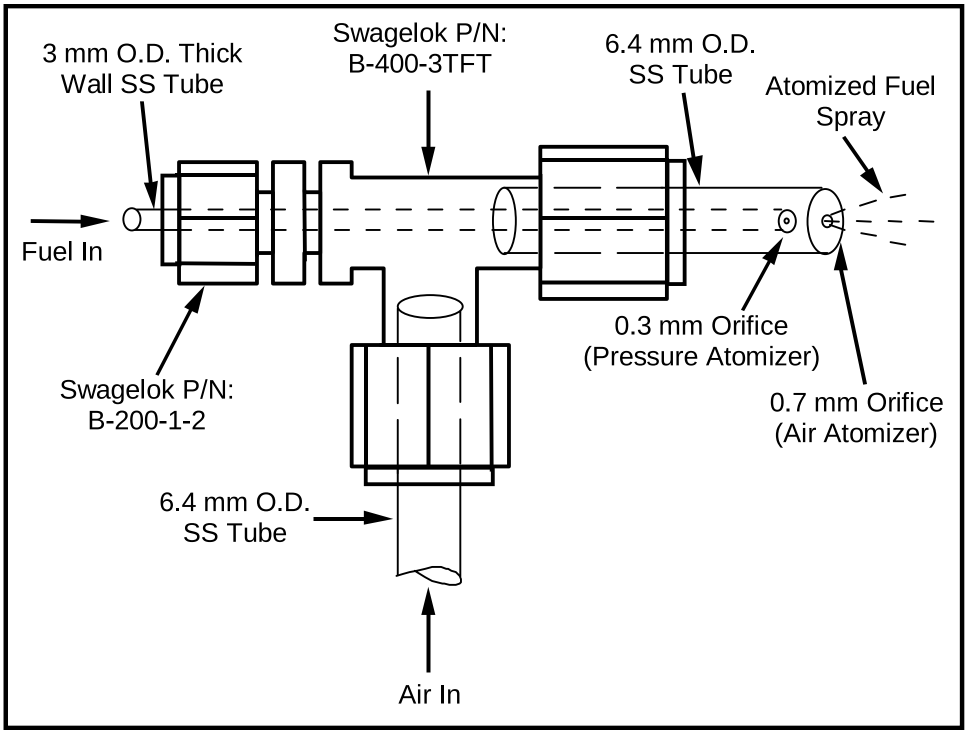

Figure 3.2. Schematic Drawing of the Two-Stage Liquid Fuel Atomizer (Nukiyama-Tanasawa Design).

3.2 RESULTS

Results for the NO_X yields of the fuels containing small amounts of organic nitrogen are plotted in Figures 3.3 through 3.5. The plots cover three fuels, including a Texaco No. 2 low sulfur diesel fuel (T-LSD*) with 124 ppmw nitrogen, n-dodecane doped with EEDA to give a nitrogen content of 96 ppmw and pure n-dodecane. The T-LSD is indicated by a (*) to differentiate it from the one use in the SPP study, which has a lower FBN content as indicated in Table 2.7. The nominal temperature of the JSR inlet jet is 700 K and the nominal residence time of the JSR is 4.0 ms. The relatively high inlet temperature of 700 K is used to ensure complete vaporization of the T-LSD*. However, because of the elevated temperature and long residence time in the prevaporizing-premixing chamber, pre-flame pyrolysis and/or oxidation reactions are likely to occur within the prevaporizing-premixing injector, though autoignition and significant pressure oscillations do not occur in the injector. Additionally, post-test detailed inspection of the prevaporizing-premixing injector indicates considerable amounts of coke and gum buildup within the injector further confirming the presence of preflame fuel breakdown. The clear evidence of preflame fuel oxidation further confirms the need for an injector of advance design that can provide “fast” vaporization and mixing and prevent the fuel and air from preflame reactions within the injector even under high inlet temperature conditions.

Figure 3.3 shows the NO_X data for the n-dodecane doped with EEDA and for the pure n-dodecane. The residence time varies from 4.0 to 4.4 ms with a mean value of 4.2 ms. Also shown are results obtained assuming 100% conversion of the EEDA nitrogen to NO_X and adding this NO_X to the measured NO_X for the pure n-dodecane. The results calculated by this method lie just under the measured data for the doped fuel and suggest that the doped fuel experiences 100% conversion of the fuel bound nitrogen to NO_X.

Figure 3.4 shows the NO_X data for the T-LSD* and for the dodecane. In these experiments there is a small difference between the residence times of the T-LSD* and n-dodecane runs. Thus, the n-dodecane NO_X data are adjusted to the residence time of the T-LSD* data for each temperature, assuming the linear dependency of NO_X (from N_2) on residence time. The residence time range of the measurements is 3.7 to 4.2 ms, and the mean residence time is 3.9 ms. The T-LSD* data are the result of separate experiments, one run for 700 K inlet temperature and the other run for 725 K.

The T-LSD* data relative to the n-dodecane data show an approximate doubling of the NO_X at 1800 K and a greater slope of NO_X versus temperature (i.e., a greater activation energy). Comparison of the calculated NO_X assuming 100% conversion of the organic nitrogen (added to the n-dodecane data) to the NO_X measured for T-LSD* suggests that the FBN undergoes 100% conversion, especially for temperatures above 1800 K.

The equation for the NO_X yield from 100% conversion of the fuel bound nitrogen in the T-LSD* is as follows:

$$NO_X\ (ppmv,\ wet,\ actual\ O_2) = 893\phi\ /\ (3.1134\phi + 49.336) \quad \text{............Eq. 3.1}$$

where ϕ is the fuel-air equivalence ratio.

In Figure 3.5, the NO_X data are replotted on the basis of ppmv, dry, 15% O_2. Comparison of the data shows that the two nitrogen containing fuels produce nearly identical levels of NO_X for temperatures below 1800 K. For the highest temperatures attained (> 1900 K), the NO_X from the T-LSD* approaches 25 ppmvd (15% O_2).

It is interesting to note that nearly identical NO_X emission data to Figure 3.5 for a No. 2 diesel fuel have been obtained by Wang et al. (1997) using ABB's laboratory EV burners. It is important to note that Wang et al. (1997) also used a No. 2 diesel fuel that had a FBN content of 124 ppmw. From Wang et al. (1997), a corrected (15% O_2) NO_X emission of 13 ppmv is obtained for LPP combustion with a reactor temperature of 1800 K. This compares well to the 12.5 ppmv NO_X level as shown in Figure 3.5. Furthermore, preflame fuel decomposition was also experienced by Wang et al., 1997. This further implicates the degree of difficulty involved in the prevaporization and premixing process for commercial blended fuels.

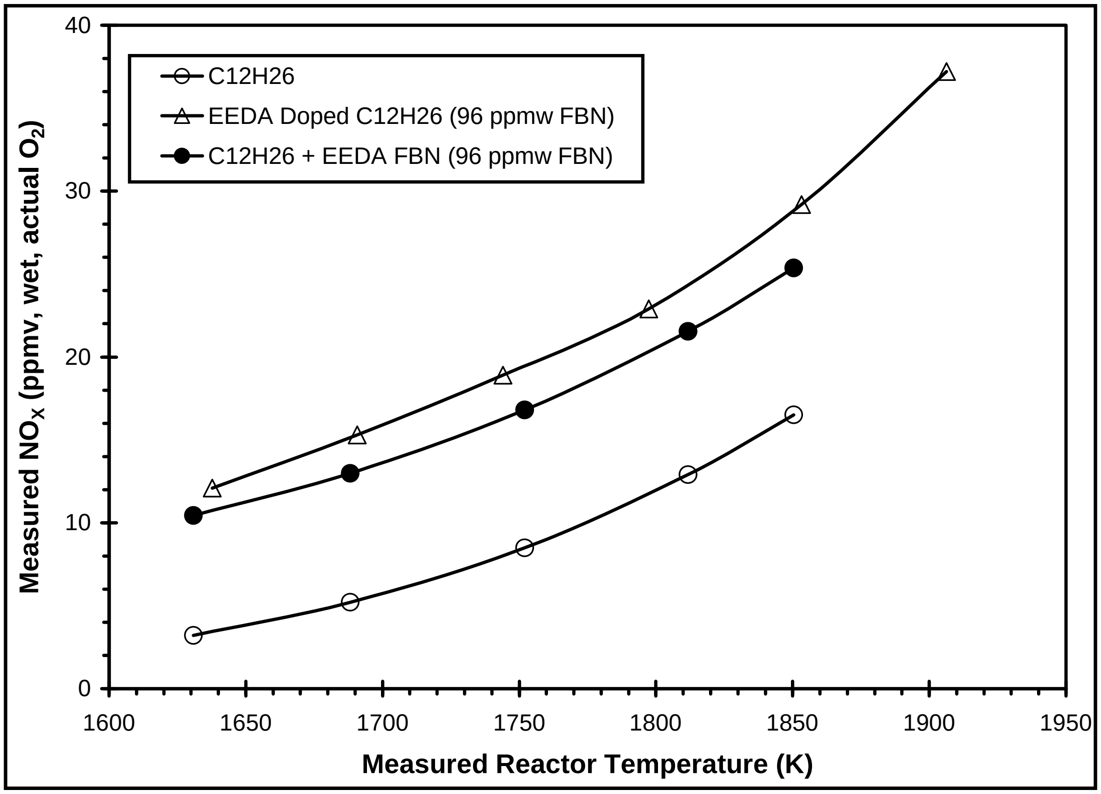

Figure 3.3. NO$_X$ versus Reactor Temperature (in the Recirculation Zone) for n-Dodecane and n-Dodecane Doped with n-Ethylethylenediamine Containing 96 ppm by weight FBN (Nominal Reactor Residence Time = 4.2 ms).

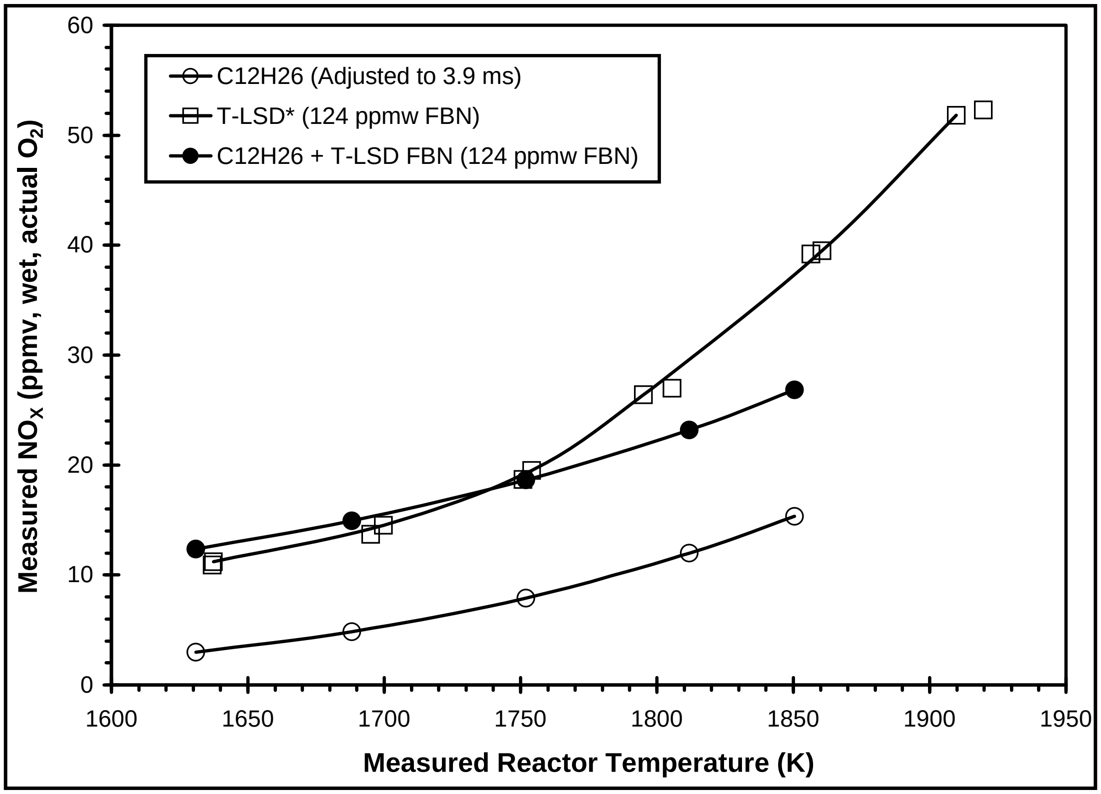

Figure 3.4. NO$_X$ versus Reactor Temperature (in the Recirculation Zone) for Texaco Low Sulfur Diesel Fuel (Nominal Reactor Residence Time = 3.9 ms).

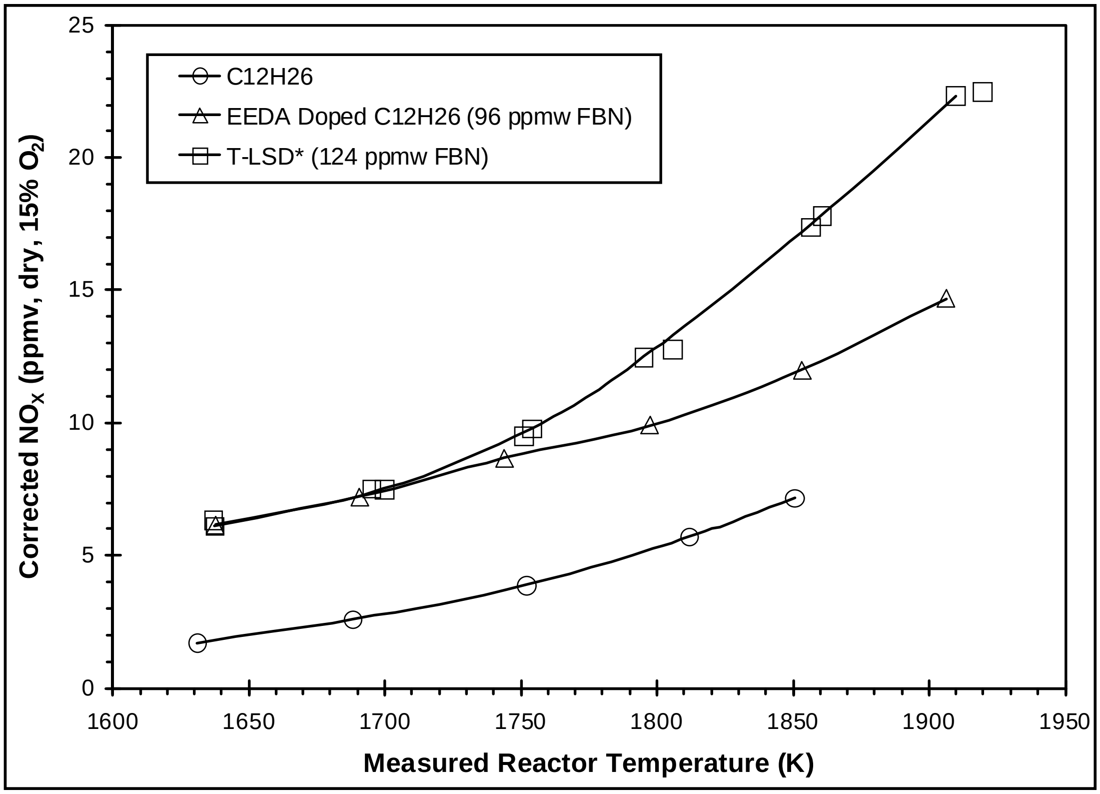

Figure 3.5. Adjusted NO$_X$ versus Reactor Temperature for n-Dodecane, n-Dodecane + n-Ethylethylenediamine, and Texaco No. 2 Low Sulfur Diesel Fuel from Figures 3.3 and 3.4. All Data Corrected to a Reactor Residence Time of 3.9 ms.

3.3 SUMMARY

This initial injector design provides several insights into the challenges involved in the prevaporizing and premixing process for commercial liquid fuels. In particular, the effects of fuel oxidation and pyrolysis (or preflame chemistry) are observed. The following aspects of the 1st generation injector promote preflame chemistry:

1. Long injector residence time provides the fuel sufficient time to react with the high temperature inlet air.

2. Oversized liquid fuel atomizer provides poor and unstable atomization of the liquid fuel.

3. Non-streamlined flow pattern promotes fuel accumulation within the injector.

Nevertheless, preliminary LPP testing was completed for the following fuels:

- N-dodecane.

- N-dodecane doped with n-ethylethylenediamine to give a fuel bound nitrogen content of 96 ppmw.

- Texaco low sulfur diesel containing 124 ppmw of FBN.

The results indicate that under LPP combustion in the JSR, the yield of NO_X from small amounts of fuel nitrogen appears to be 100%. However, the results on FBN conversion under LPP combustion conditions should be regarded as preliminary. Further investigation and verification of the degree of FBN conversion is presented below in Chapter 5.

CHAPTER 4: SECOND GENERATION INJECTOR DESIGN AND RESULTS

4.1 SECOND GENERATION INJECTOR

The second generation prevaporizing-premixing injector (as shown in Figure 4.1 and Appendix F) is designed specifically for studying the LPP combustion of pure fuels. Facility air is heated with a convective type, electrical resistance heater similar to the one used for the 1st generation injector. Stainless steel balls are stacked and used to direct the airflow and a blowout flange is utilized as an automatic overpressure relief valve. Both gaseous fuel and liquid fuel are injected in a 60° cross-flow scheme. Note "Gaseous Fuel In" and "Liquid Fuel and Atomizer Air In" in Figure 4.1. The gaseous fuel nozzle is a simple five-hole orifice-tip type nozzle and the liquid fuel nozzle is of the Nukiyama-Tanasawa design similar to the one used in the 1st generation injector. The degree of premixing in the prevaporizing-premixing injector is similar to that discussed in Section 3.1. Consequently, the experiments are again treated as fully prevaporized and premixed.

Both K-type thermocouples and gas sampling ports are positioned along the length of the prevaporizing-premixing chamber. Temperature readings from the uppermost and lowermost thermocouples are used as feedbacks to the cascade-type temperature controller used to control the inlet temperature. Lack of fuel breakdown and preflame chemical reaction are verified by sampling the gases at various locations and analyzing the sample with a GC-FID.

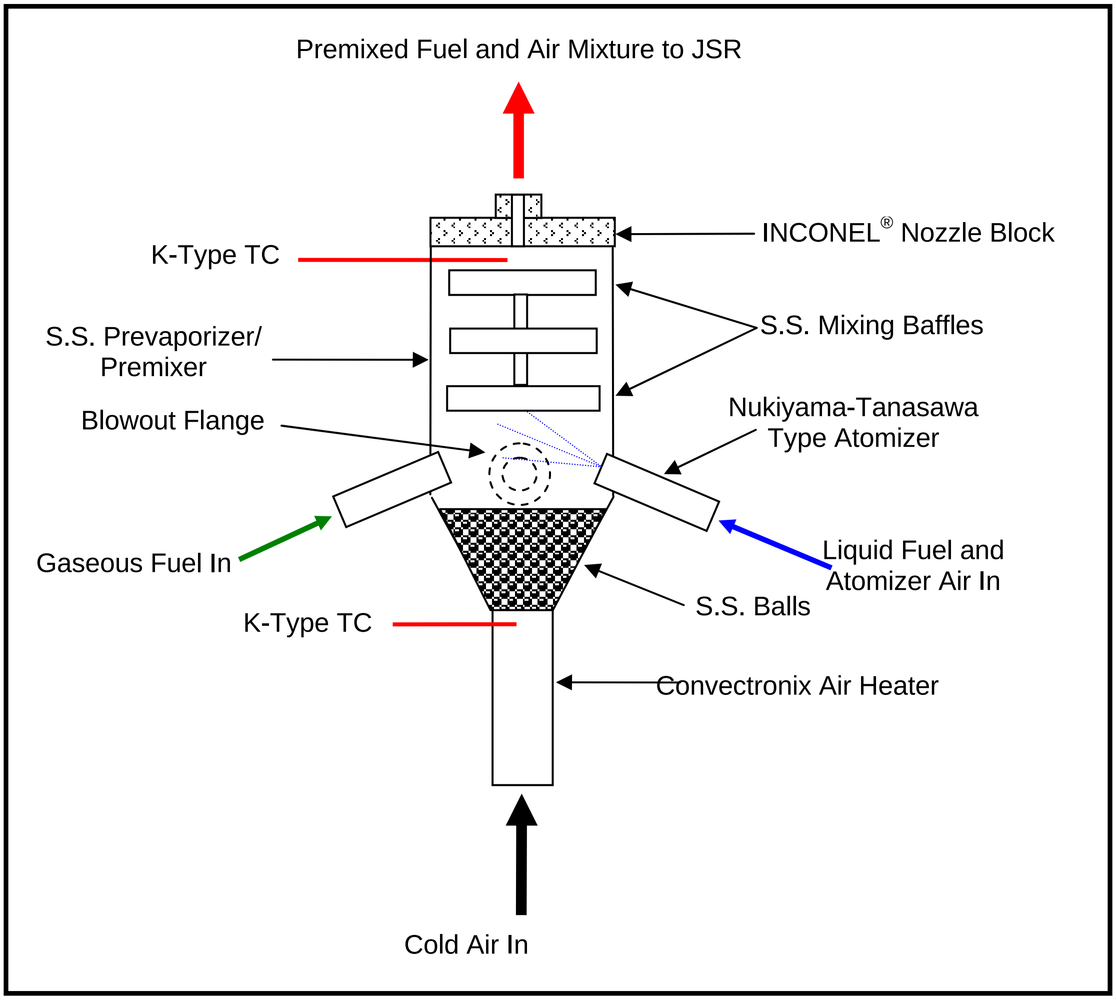

Figure 4.1. Schematic Drawing of the Second Generation, Prevaporizing-Premixing Injector.

4.2 RESULTS – INLET TEMPERATURE EFFECTS

The atmospheric pressure JSR in conjunction with the 2nd generation injector is used to determine the effect of inlet temperature on NO_X. Measurements are done with two inlet jet nozzle sizes (i.e., 2 and 4 mm diameter). The inlet temperature recorded is that measured for the fuel (natural gas) and air mixture just before the mixture leaves the premixer and accelerates through the nozzle to form the JSR inlet jet. With no preheating of the inlet air, the inlet temperature is 390 K. Because of back heating from the JSR to the premixer, the measured inlet temperature is greater than the ambient temperature. The maximum inlet temperature tested is 623 K.

Results are plotted in Figure 4.2. The measured NO_X, corrected to 15% O_2, is plotted versus the inlet temperature. The measured reactor temperature is corrected for radiation and conduction losses (see Rutar et al., 1998). The corrected temperature in the recirculation zone is 1788 K for all inlet temperatures, and the nominal residence time of the reactor is 3.2 ms. All NO_X data are adjusted to 3.2 ms assuming a linear dependency of NO_X on residence time for atmospheric pressure, lean-premixed JSRs, (Steele et al., 1997). This adjustment does not affect the trends shown in the data.

The effect of the inlet temperature on the NO_X is seen to be not insignificant. An increase in the inlet temperature from 390 K (i.e., without preheating) to 623 K decreases the NO_X from about 6 to about 4 ppmv, dry, 15% O_2. The results do not appear to be significantly affected by the change in the jet diameter from 2 to 4 mm, though more data are needed for the 4 mm diameter jet to confirm this. Since additional inlet temperature results are presented for the SPP, discussion of the effect of inlet temperature on NO_X yield is deferred to Chapter 5.

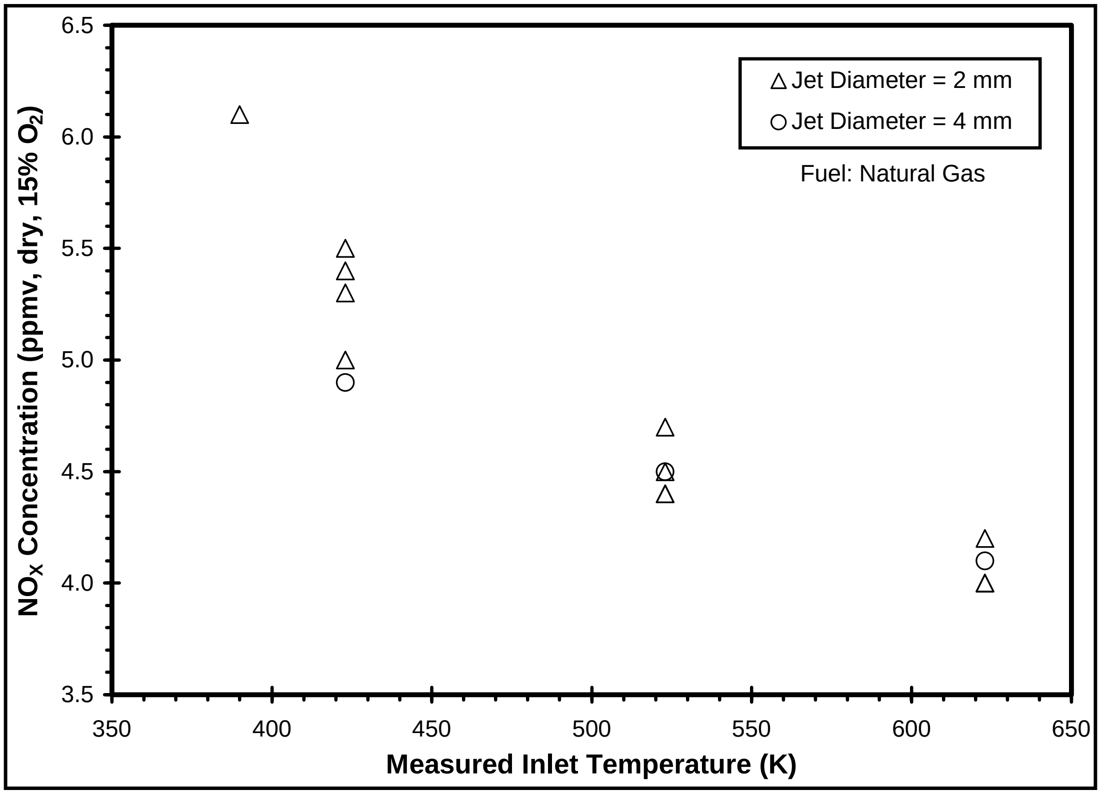

Figure 4.2. NO$_X$ versus Inlet Temperature for 1788 K Gas Temperature in the JSR. Inlet Nozzle Diameters are 2 and 4 mm.

4.3 RESULTS – FUEL TYPE EFFECTS

Results measured for the JSR burning nine different fuels for three different JSR conditions (i.e., for the JSR fitted with the three different nozzles) are listed in Table 4.1. The table lists the measurements of fuel-air equivalence ratio, NO_X concentration (as ppmv, dry, 15% O_2), and CO concentration (as volume %, dry, actual O_2). The values listed are averages of repeated runs of the individual cases. Overall, 51 runs comprise the 27 cases listed in Table 4.1. The NO_X and CO measurements are for the standard sampling location in the recirculation zone. As explained in Section 2.1.2, the nominal combustion temperatures are 1790 and 1850 K, respectively, for the single jet (2 and 4 mm) and diverging jets configurations. All NO_X data are adjusted to a mean residence time of 3.2 ms, assuming NO_X yield is proportional to residence time in the lean, atmospheric pressure JSR operated at constant combustion temperature. This follows from the work of Steele (1995) and Steele et al. (1998).

The main results of Table 4.1 are those for NO_X, which are discussed below in conjunction with Figures 4.3 and 4.4. The values for fuel-air equivalence ratio listed in the table behave as expected. That is, the fuel with the lowest adiabatic equilibrium flame temperature, methane, requires the largest fuel-air equivalence ratio to reach the set point combustion temperature (of 1790 K) and methanol, with its relatively high adiabatic equilibrium flame temperature, requires the lowest fuel-air equivalence ratio. The high-order alkanes also require a relatively low fuel-air equivalence ratio to reach the set point combustion temperature. However, unlike methanol, they exhibit elevated CO levels (especially for the 2 and 4 mm nozzles), and thus, their fuel-air equivalence ratios are somewhat enhanced.

The diverging-jets nozzle is operated at higher fuel-air equivalence than the single jet nozzles. For the JSR equipped with the single, 2 and 4 mm, centered jet nozzles, CO increases somewhat with increasing alkane size, a tendency also reported in the work of Zelina and Ballal (1996) and Zelina et al. (1996). Because of its higher temperature, the diverging-jets equipped JSR exhibits the lowest CO readings of the three configurations. A point of caution is offered with respect to the CO measurements. Because of the possibility of oxidation of CO in the short, hot tip of the sampling probe, the CO concentration reported may be lower than the CO concentration existing in the reactor. Thus, with respect to CO, the internals of the probe tip should be regarded as an extension of the reactor. Effectively, this adds a short section of plug flow reactor to the JSR. See Steele (1995) and Steele et al. (1995) for discussion and analysis of this effect. (However, the PFR component has little effect on the NO_X.) Furthermore, because the atmospheric pressure JSR does not permit burnout of the CO, the trade-off between CO and NO_X, as frequently discussed for gas turbine combustors, is not examined here.

Figure 4.3 presents the NO_x concentrations for the JSR equipped with the 2 mm, 4 mm and diverging-jets nozzles. The independent variable is the “Assigned Fuel Number,” which is the carbon number (i.e., the number of carbon atoms in a fuel molecule), except for methanol, which is assigned “0” in order to distinguish it from methane (“1”). For all three nozzles, the tendency is for the NO_X to increase significantly from methanol to methane. The increase continues as the carbon number increases from “1” (methane) to “5” (pentane). For carbon numbers above “5” the NO_X slightly decreases and then slightly increases as carbon number “16” is reached. Although the JSR equipped with the diverging-jets nozzle gives NO_X concentrations about double those of the JSR with the single 2 and 4 mm jet nozzles, the trends with the different fuels are remarkably similar for the three nozzles.

The behavior of NO_X with fuel-type is clearly observed in Figure 4.4. In this figure, NO_X normalized by the NO_X for ethane combustion is plotted. Ethane is chosen for normalization, since its NO_X yield is comparable to that of the other higher order alkanes and has high repeatability.

When the fuel range is divided into four regimes, the following percentage increases in NO_X are found with respect to fuel-type:

- Methanol to methane: 62±10%.
- Methane to ethane: 22±2%.
- Ethane to pentane: 11±2%.
- Ethane to hexadecane: 8±5%.

The results shown in Figure 4.4 are in general agreement with the NO_X measurements of Zelina and Ballal (1996), Zelina et al. (1996), and Blust et al. (1997). However, the present study shows a relatively low sensitivity of NO_X to carbon number for the highest order alkanes tested, compared to a steeper increase in this regime reported by Zelina and Ballal (1996) and Zelina et al. (1996). The difference may lie in the temperature. Whereas temperature is held constant in the present work, in the study of Zelina et al. (1996) the temperature varied with fuel type. Although Zelina et al. applied a temperature correction to adjust the NO_X data, this may introduce an element of uncertainty because of the strongly exponential dependency of NO_X on temperature.

Table 4.1. 2nd Generation Injector Results for Fuel-Air EquivalenceRatio, NO_X and CO Emissions for Nine Fuels and Three JSR-Conditions (i.e., Three Nozzles).

Nozzle	***MeOH***	***C_1***	***C_2***	***C_3***	***C_5***	***C_6***	***C_7***	***C_{12}***	***C_{16}***
Fuel-Air Equivalence Ratio									
2 mm	0.57	0.65	0.62	0.61	0.60	0.63	0.64	0.64	0.63
4 mm	0.57	0.65	0.62	0.61	0.60	0.61	0.64	0.62	0.62
Diverging	0.70	0.74	0.71	0.71	0.76	0.73	0.72	0.73	0.71
NO_X (ppmv, dry, 15% O_2)									
2 mm	2.7	4.4	5.4	5.3	5.9	5.9	5.7	5.4	6.0
4 mm	3.3	5.0	6.2	5.9	6.9	6.7	6.6	6.4	6.3
Diverging	5.5	9.4	11.2	11.8	12.6	12.1	11.6	12.0	12.7
CO (volume %, dry, actual O_2)									
2 mm	0.28	0.26	0.28	0.30	0.38	0.38	0.31	0.33	0.39
4 mm	0.34	0.42	0.37	0.30	0.47	0.49	0.49	0.50	0.55
Diverging	0.15	0.15	0.21	0.23	0.34	0.24	0.16	0.15	0.16

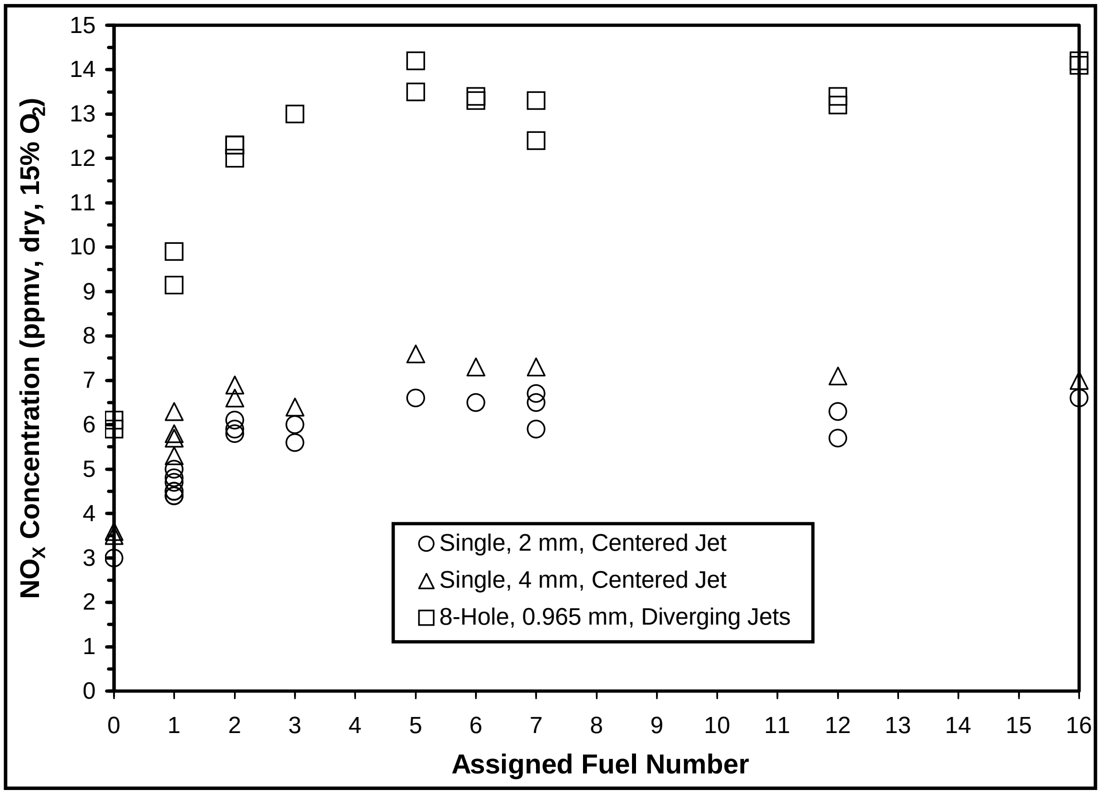

Figure 4.3. Measured NO_X Concentration versus Assigned Fuel Number (i.e., Number of Carbon Atoms in Fuel Molecule, Except for Assignment of Zero for Methanol) for JSR Equipped with the 2 mm Single-Jet Nozzle and the Diverging-Jets Nozzle.

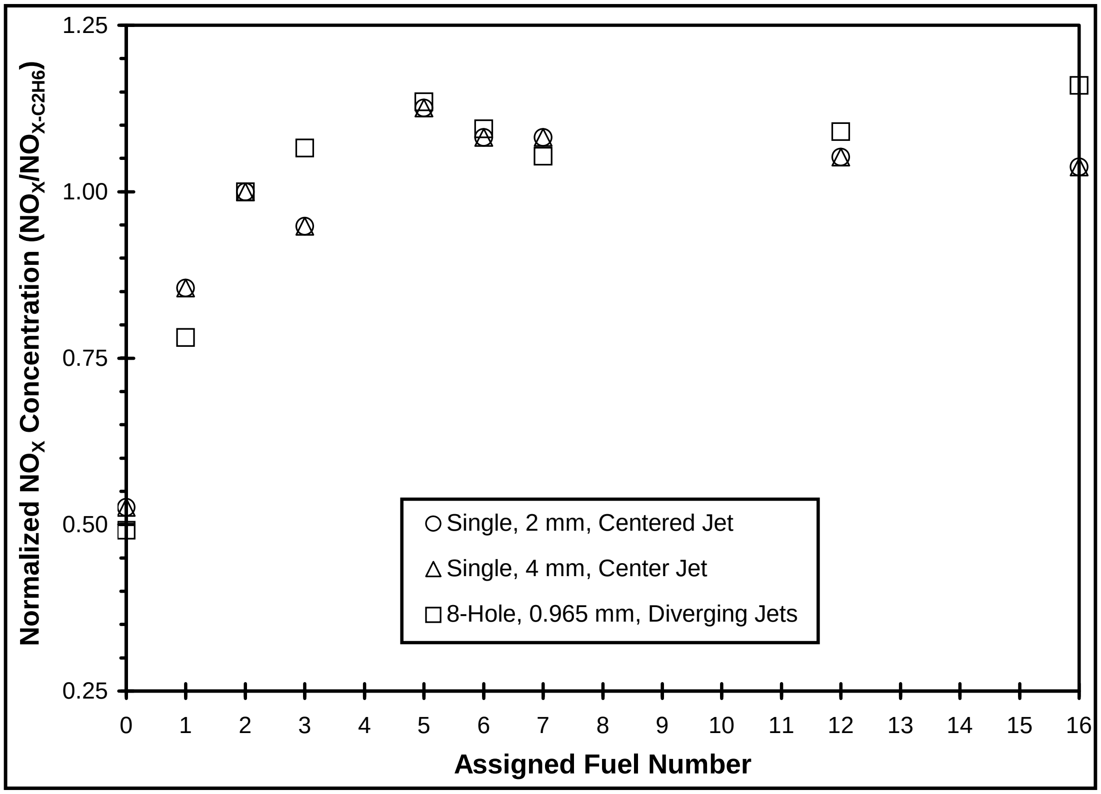

Figure 4.4. Measured NO_X Concentration Normalized by the NO_X Concentration for Ethane Combustion versus Assigned Fuel Number for the JSR Equipped with 2 mm and 4 mm Single-Jet Nozzles and the Diverging-Jets Nozzle.

4.4 SUMMARY

NO_X concentrations for an atmospheric pressure JSR coupled with the 2nd generation injector operated at a constant flame and inlet temperature and residence time have been obtained for normal alkane hydrocarbons ranging from C_1 to C_{16} and for methanol.

A decrease in NO_X of about 30% is observed as the mixture inlet temperature is increased from the no-preheat case to 623 K (with combustion temperature held constant at about 1788 K). These results are obtained using methane fuel and a single inlet jet, and may be restricted to these conditions.

With the effect of fuel type on NO_X, greatest sensitivity in the NO_X emission occurs for the light hydrocarbons and for methanol. The findings imply that natural gases rich in C_2 to C_5 hydrocarbons can form more NO_X than natural gases composed mainly of methane. The results also indicate low concentrations of NO_X occur when methanol is burned.

The inlet jet configuration plays a significant role in determining the NO_X level. However, the trend of NO_X versus fuel type is not affected by the nozzle choice.

CHAPTER 5: THIRD GENERATION (STAGED PREVAPORIZING-PREMIXING) INJECTOR DESIGN AND RESULTS

5.1 STAGED PREVAPORIZING-PREMIXING INJECTOR

Central concepts in the design of fuel injectors are the following:

- Vaporization and mixing processes must be "quick." Once the mixing is complete, immediate introduction of the mixture into the combustor is necessary to prevent autoignition.
- Flow must be streamlined. Flow separation and recirculation (i.e., dead zones) should be minimized.
- Surface fouling and wall deposition must be avoided if possible.
- Injector pressure drop should be as low as possible.
- In order to minimize production and engineering costs the design must be simple and easy to fabricate.

The patent-pending (see Lee and Malte, 1999b), dual fuel, staged prevaporizing-premixing injector is shown in Figure 5.1. The CAD drawing of the SPP is located in Appendix G. The SPP concept evolved from the extensive injector testing with various liquid fuels as described in Chapters 3 and 4 and from review of industrial prototype injectors. The SPP technology has significant implications for application to high compression ratio (30^+:1) gas turbine engines because of the severe autoignition conditions. It is also a viable technique for lower pressure applications provided that a secondary source of air or premixing medium is available.

Additionally, the SPP may have application to fuel cell reformer technology because of the need for complete vaporization and mixing.

The staged prevaporizer-premixer is a device for use in combustion systems that involve the burning of liquid fuels. Its purpose is to provide optimum prevaporizing and premixing of the liquid fuel and air prior to combustion. Under optimum prevaporizing and premixing conditions, maximum pollutant emission reduction can be achieved. The central idea employed in the SPP is the use of "staged" sections each having its own temperature and residence time. The individual sections (or stages) prevaporize and premix different hydrocarbon components of the original liquid fuel and ultimately provide an optimum fuel and air mixture for combustion with very low emissions.

Several high temperature resistant materials can be used to construct the SPP. For example, 316 stainless steel, any grade of INCONEL®, any grade of HASTELLOY® and advanced ceramics can be used. HASTELLOY® is an ideal material for the front-end nozzle due to its contact with the high temperature combustion environment. However, as mentioned above, other heat resistant materials can be used. The critical concept in the design is the staged injection of the high temperature air for prevaporizing and premixing of the liquid fuel and air. The following is a list of the key concepts used in the SPP:

- Staged prevaporizing and premixing processes for pure or commercial blended fuels:
    - Low temperature, for example 300-600 K, and relatively long residence time, for example 10-20 ms, first stage for vaporization of light-end hydrocarbon components and initiation of vaporization of heavy hydrocarbon components. This is shown in Figure 5.1 as First Stage. The current study uses first stage temperatures of 423 and 523 K.

  - ➢ High temperature, for example 500-900 K, and relatively short residence time, for example 1-10 ms, second stage for final vaporization of high-end hydrocarbon components (see Second Stage in Figure 5.1). The second stage temperatures used in the current study are 523, 623 and 723 K. A 623 K inlet temperature is required for the LPP combustion of the No. 2 diesel fuel used in this study.

- Liquid fuel nozzle with very small flow number for extremely fine atomization of inlet fuel stream (see Air Cooled Nozzle in Figure 5.1). The CAD drawing of the Air Cooled Nozzle is shown in Appendix G.

- Sharp-edged film atomizer for secondary atomization of large droplets (see Film Atomizer in Figure 5.1).

- Staggered high velocity jets for intense fuel and air mixing (see Staggered Mixing Jets in Figure 5.1).

- Dual fuel (both gaseous and liquid) firing capabilities (see Gaseous Fuel In in Figure 5.1).

- Diverging second stage for enhancement of mixing. The 2nd stage mixing jets are introduced along a diverging channel with a small divergence angle. The use of a diverging channel optimizes the mixing since overall flow velocity is held constant along the length of the diverging channel and this leads to higher momentum ratio (or exchange) between the core flow and the flow introduced by the 2nd stage high velocity jets.

- Converging nozzle for the prevention of flashback. The final section in the 2nd stage consists of a converging nozzle. The nozzle is used to accelerate the flow, preventing the flow from separating and, thus, prevent the occurrence of flashback.

It is important to note that the above mentioned temperature and residence time values are only sample values. The actual temperature and residence time settings will depend on the fuel type used, the pressure applied and the amount of prevaporizing and premixing desired. Additionally, the residence time can be altered with the addition of extension tube(s). The critical factor is that the limits of autoignition are not exceeded. As for the liquid fuel nozzle, any type of nozzle (e.g. pressure atomizer, air assist, airblast, etc.) will suffice as long as a small flow number is attainable leading to extremely fine atomization. Fine atomization is desired, since it leads to reduction in vaporization time of the liquid fuel droplets. The current fuel atomizer design is similar to the one used for the 1st and 2nd generation injectors. It is of the Nukiyama-Tanasawa design (Lefebvre, 1989). The liquid atomization nozzle is air cooled (see Appendix G) to prevent vapor lock and surface fouling of the liquid supply line. Additionally, the current design provides high turndown ratio.

As shown in Figure 5.1, the first stage heated air is introduced via a supply tube coaxial with the air cooled liquid fuel nozzle assembly (Note: The atomizing air used for the Nukiyama-Tanasawa liquid atomizer is not preheated). The first stage air is then split through injection holes between the nozzle assembly and film atomizer and between the film atomizer and the outer wall (as shown by the vertical red lines in Figure 5.1). The split provides the air required for the spray cone angle adjustment and also the air required for the film atomization technique. First stage extension tubes can be added to increase the first stage residence time. Depending on the flow rate and the length of the first stage, the first stage residence time can be varied independent of the second stage with the insertion of the first stage extension tubes. For the current study, the first stage residence time is fixed at approximately 12 ms.

After the first stage, the mixture enters a section of higher temperature that forms the second stage. High temperature air is injected into an outer shell through supply tubes, flows in the reverse direction and is introduced into the main flow via staggered high velocity jets as shown by the angled red lines in Figure 5.1. The staggered-jet configuration provides a very high degree of mixing. An extension tube can also be used to increase the second stage residence time. The main purpose of the second stage is to insure complete (or nearly complete) vaporization of all components in the original liquid fuel. Second stage residence times of approximately 5 and 12 ms are used in the current study. Figures 5.2 and 5.3 are photographic images of the long and short versions of the SPP, respectively.

Once the fuel and air are prevaporized and premixed, the mixture passes through a nozzle block, which accelerates the flow into the combustor where it is burned under prevaporized and premixed conditions leading to minimal formation of pollutants. A blowout flange is utilized as an automatic overpressure relief valve. The gaseous fuel is injected in a 90° cross-flow scheme. Note "Gaseous Fuel In" in Figure 5.1.

Both K-type thermocouples and gas sampling ports are positioned along the length of the SPP chamber. Temperature readings from the uppermost 2nd stage and uppermost 1st stage thermocouples are used as feedbacks to cascade-type temperature controllers used to control the temperature in each stage. The lack of fuel breakdown or preflame chemical reaction is verified by sampling the gases at various locations and analyzing the sample with a GC-FID.

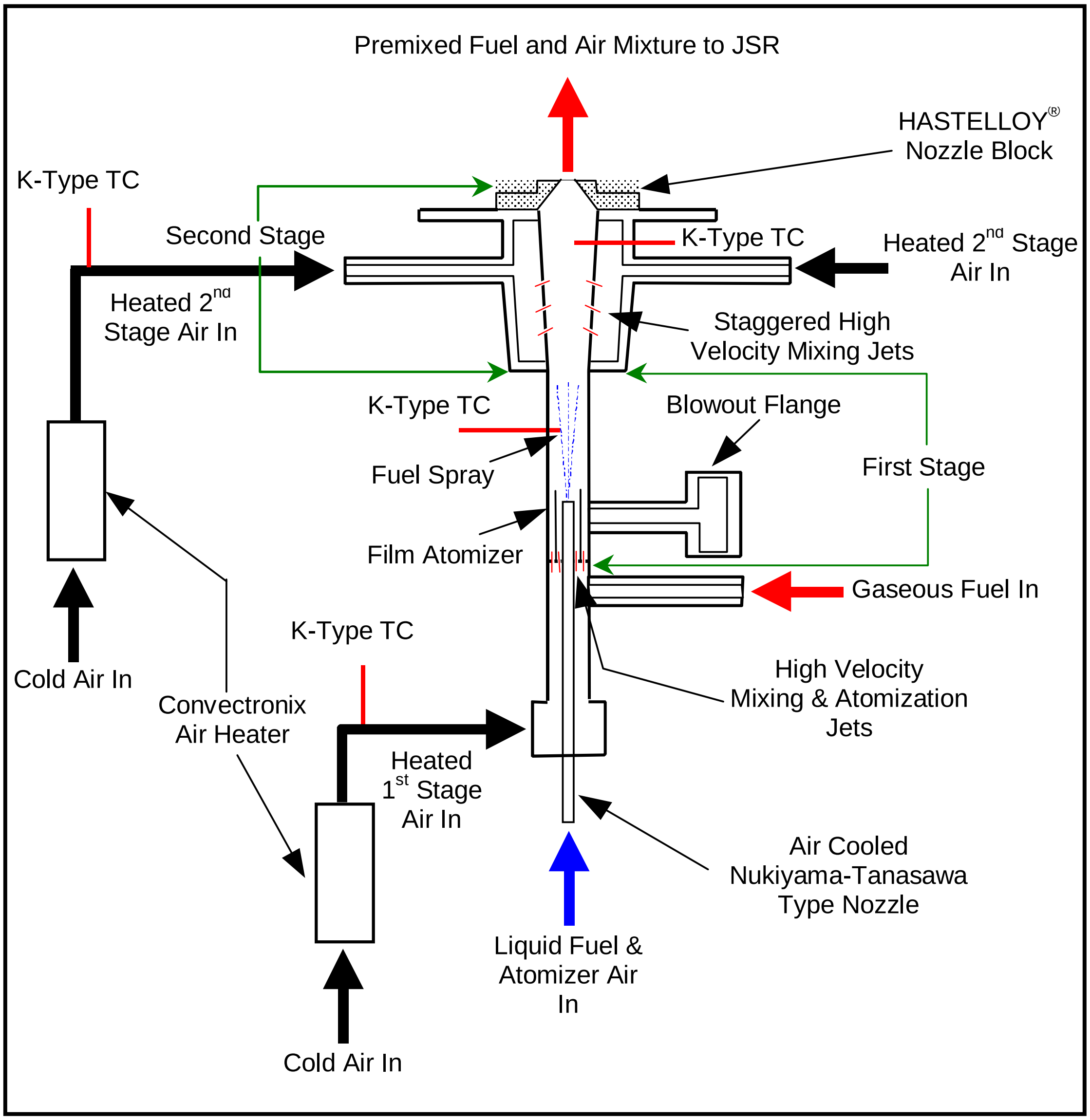

Figure 5.1. Schematic Drawing of the Third Generation, Staged Prevaporizing-Premixing Injector.

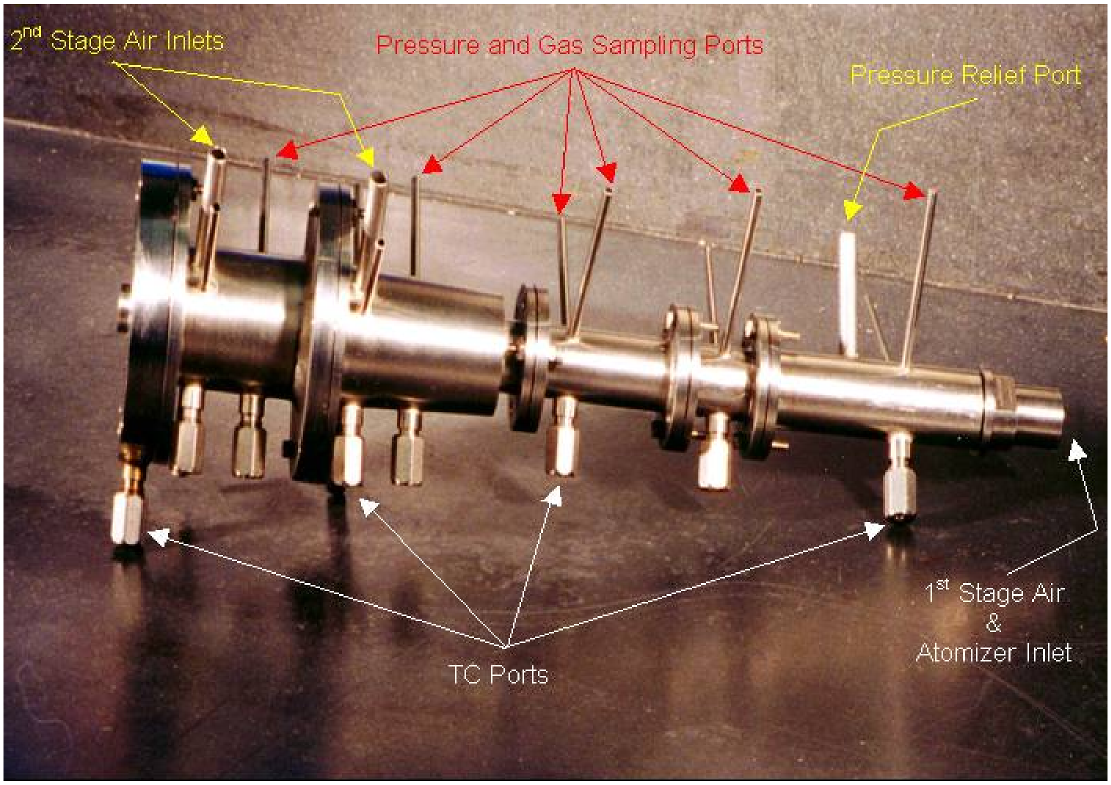

Figure 5.2. Image of the Long SPP Configuration.

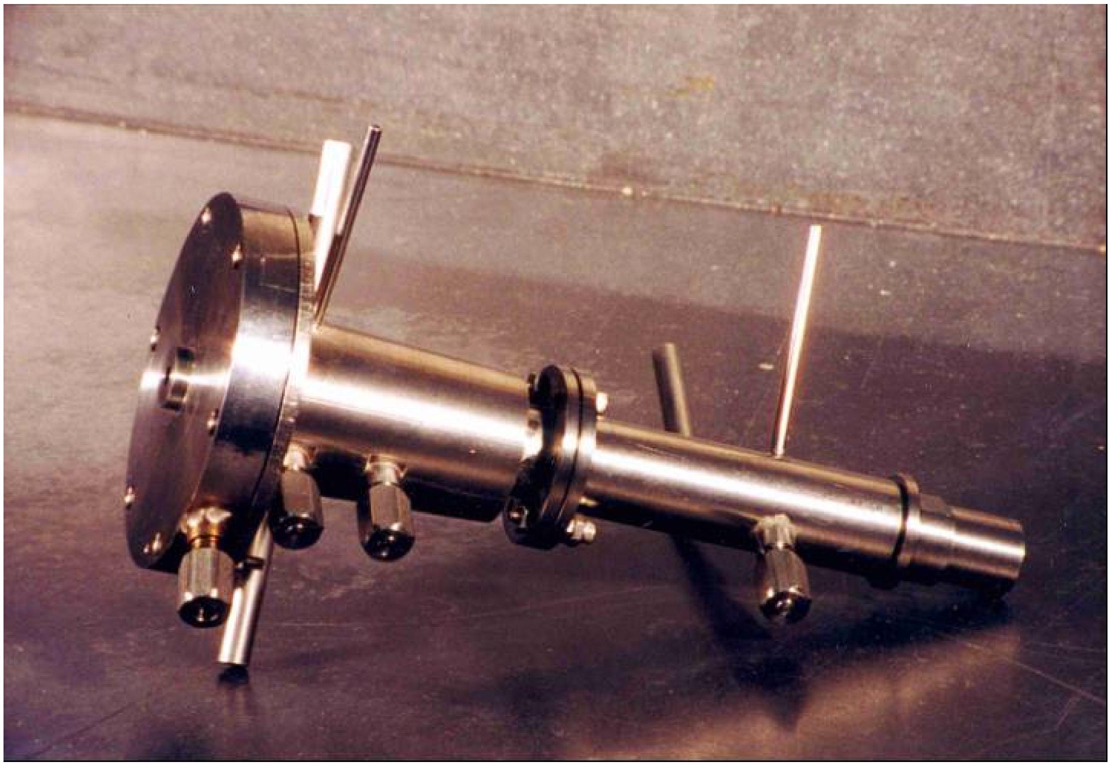

Figure 5.3. Image of the Short SPP Configuration.

5.2 DETERMINATION OF OPTIMAL OPERATING CONDITIONS

Due to the adjustability of the SPP design, a set of operating conditions for the optimization of NO_X formation is determined. Effects of airflow split, inlet temperature split, injector length and sampling location are presented in the following sections and also in Appendix H.

5.2.1 EFFECTS OF AIR SPLIT ON MIXING

The goal in the design of the SPP is to provide the fuel and air with good mixing prior to the onset of combustion. Quantitative measurements of the degree of fuel and air mixing at the outlet of the premixer prior to entry into the JSR is performed via the laser absorption technique (LAT) as described in Section 2.8. The long version of the SPP configuration is used for the LAT measurements. Mixing for the short version of the SPP is inferred from the JSR NO_X measurements and will be discussed in Section 5.2.3.

Figure 5.4 represents the unmixedness as a function of both the inlet temperature split (or the temperature used in each stage) and the air split (or the airflow used in each stage) in the stream of premixed natural gas and air at the outlet of the SPP. The nomenclature indicated in the figure legend is the airflow (in slpm) in the 1st and 2nd stages, respectively, followed by the nominal 1st stage temperature. For example, “20/40, 293 K” means 20 slpm airflow to the first stage, 40 slpm airflow to the second stage and a first stage temperature of 293 K. The equivalence ratio for all cases is constant at 0.68. As can be seen, under most conditions the degree of unmixedness decreases with increasing first stage airflow (from the 20/40 cases to the 40/20 cases). This behavior is expected since the higher airflow in the first stage leads to higher mixing intensity in this stage giving the mixture maximum time for mixing. As the airflow is reduced in the 1st stage, the mixing intensity decreases leading to higher degree of unmixedness. As a note, the noise base for the LAT system is at $\sigma/\langle X \rangle = 2.3\%$ for all conditions tested and is discussed in detail in Section 2.8.

Shown in Figure 5.5 is the NO_X yield for the combustion of natural gas and air running under similar flow and inlet temperature conditions as used in Figure 5.4. As can be seen, the 40/20 cases do not exhibit the lowest NO_X as suggested by the unmixedness measurements. Lowest NO_X level is consistently obtained with the 30/30 split condition. This behavior is most likely due to flow stratification in the second stage. In other words, with the 2nd stage airflow reduced to 20 slpm, the degree of penetration by the 2nd stage mixing jets is reduced. Thus, the mixing intensity of the 2nd stage mixing jets with the core flow from the 1st stage is reduced. This leads to the formation of layered or stratified flow in the second stage with the air introduced in the 2nd stage forming a layer around the fuel and air mixture from the 1st stage. The airflow stratification is not measured by the LAT since it is only sensitive to variations in hydrocarbon concentration. On the other hand, the NO_X formation in the JSR is sensitive to any variations in hydrocarbon concentration and flow stratification. With respect to NO_X formation in the JSR, flow stratification is equivalent to a source of unmixedness. The possibility of stratification needs to be verified via CFD calculations. Additionally, a more appropriate measure of the effects of airflow split on NO_X emission is the characterization of the JSR unmixedness rather than the SPP unmixedness. This is a difficult measurement since visual access to the JSR is limited and hydrocarbon concentration is greatly reduced under reacting conditions.

Similar trends for the effect of air split on unmixedness and NO_X yield are seen for the industrial propane and air mixtures as shown in Figures 5.6 and 5.7. It is important to note that for the industrial propane cases, the unmixedness level is, in general, under 3% (or 0.7% relative to the noise base of 2.3%). The low level of unmixedness indicates a limitation of the LAT method. As indicated in Appendix H, with an equivalence ratio of 0.68, the propane mole fraction is approximately 0.028.

According to Equation 2.3, this leads to a transmission level between 73 to 93% depending on the inlet temperature as indicated by Figure 2.26. For conditions with high transmission levels (> 90%), the signal to noise ratio is greatly reduced leading to difficulties in interpreting the LAT data for unmixedness. A similar limitation is encountered for the LAT data for naphtha and No. 2 low sulfur diesel fuel as shown in Figures 5.8 and 5.9. Except for runs with natural gas, the absorption is too small with the present setup to provide a clear measure of the unmixedness effect.

Nevertheless, it is determined that for the current SPP prototype design, the optimum air split setting is at the 30/30 level. This equal split in airflow setting is limited to the current design and operating conditions and may be quite different for other SPP injector designs and operating conditions.

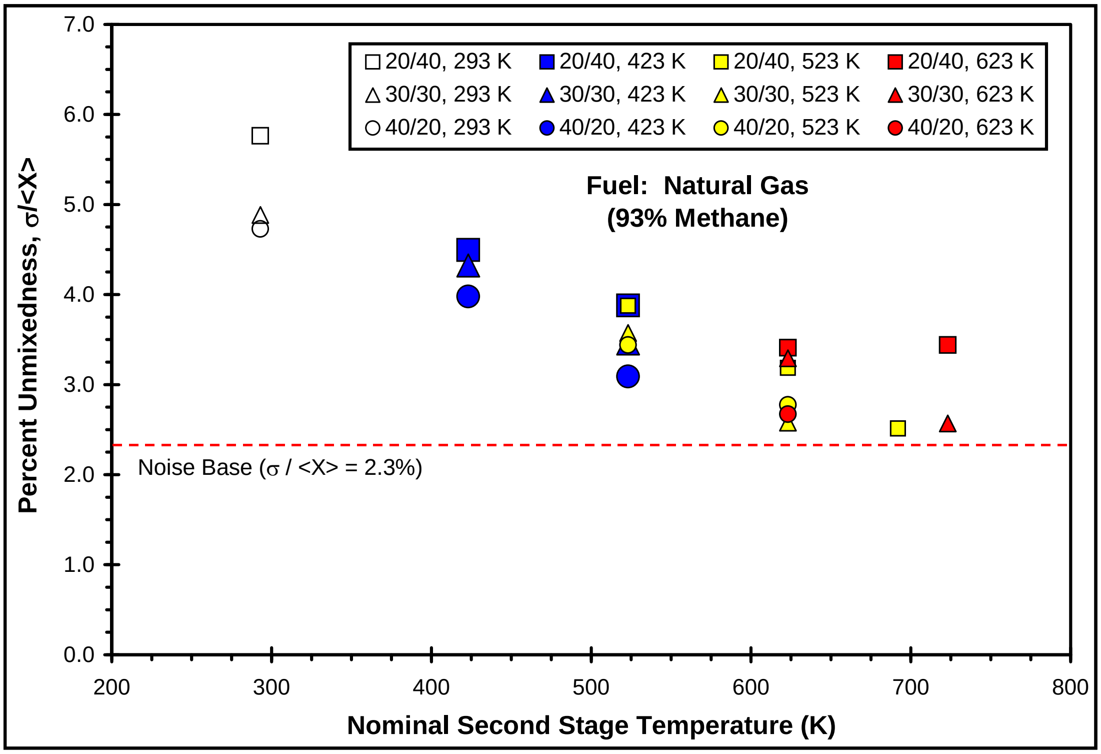

Figure 5.4. Effects of Air Split and Inlet Temperature Split on the Degree of Mixing for the SPP with Natural Gas and Air Mixture at $\phi = 0.68$. Legend: 1st Stage Airflow Rate in SLPM / 2nd Stage Airflow Rate in SLPM, Nominal 1st Stage Temperature in Kelvin.

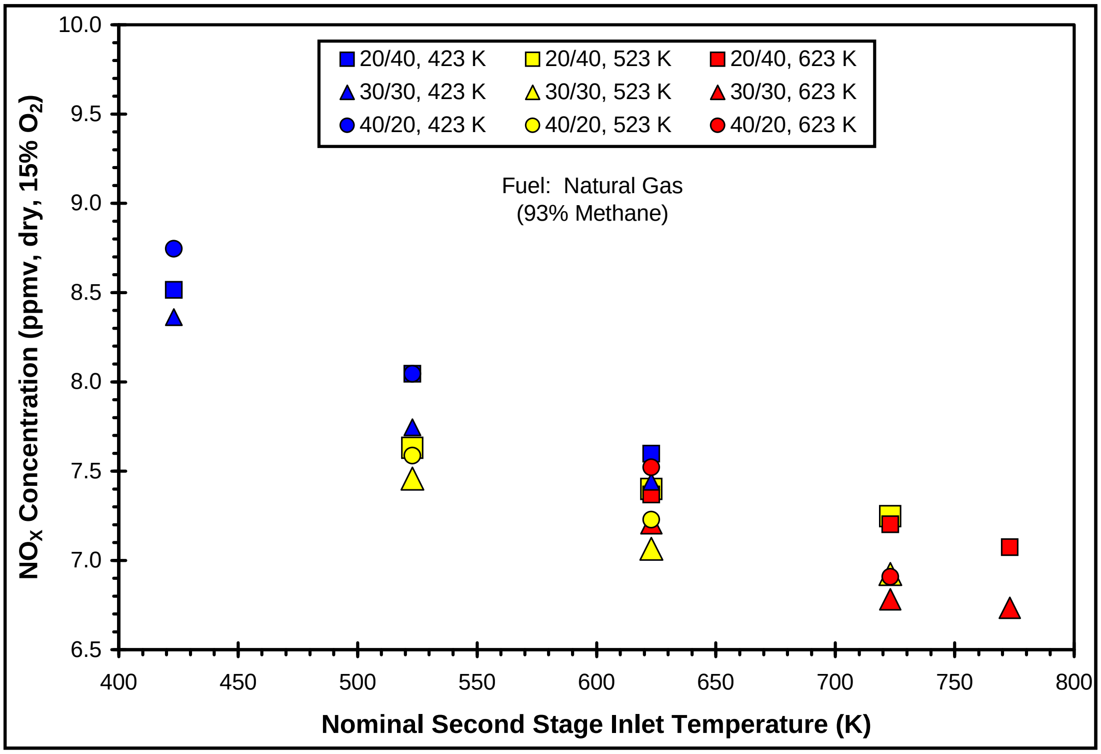

Figure 5.5. Effects of Air Split and Inlet Temperature Split on NO_X Yield for the SPP with Natural Gas and Air Mixture at $\phi = 0.68$. Legend: 1st Stage Airflow Rate in SLPM / 2nd Stage Airflow Rate in SLPM, Nominal 1st Stage Temperature in Kelvin.

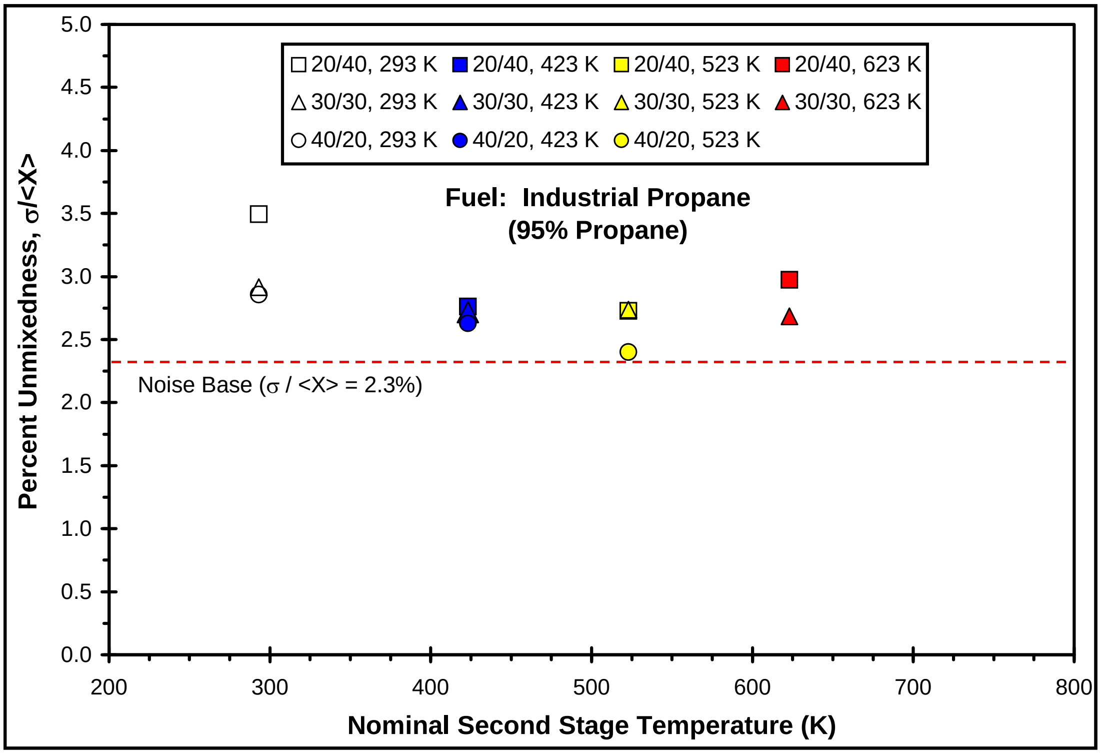

Figure 5.6. Effects of Air Split and Inlet Temperature Split on the Degree of Mixing for the SPP with Industrial Propane and Air Mixture at ϕ = 0.68. Legend: 1st Stage Airflow Rate in SLPM / 2nd Stage Airflow Rate in SLPM, Nominal 1st Stage Temperature in Kelvin.

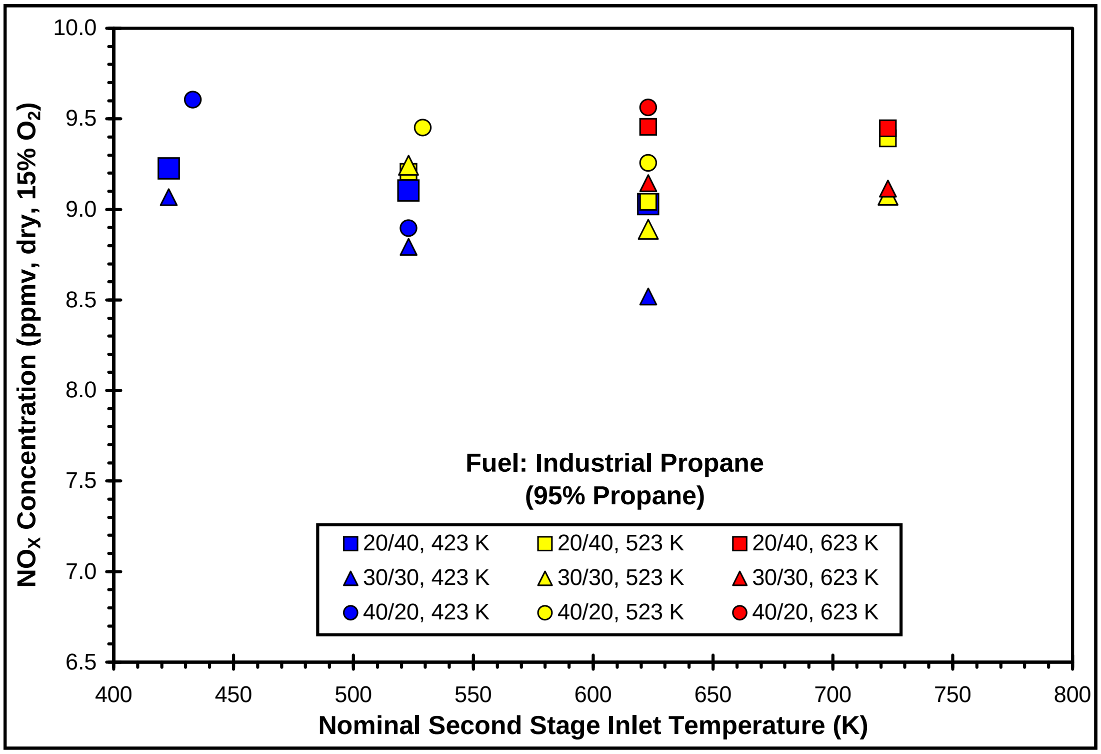

Figure 5.7. Effects of Air Split and Inlet Temperature Split on NO$_X$ Yield for the SPP with Industrial Propane and Air Mixture at $\phi = 0.68$. Legend: 1st Stage Airflow Rate in SLPM / 2nd Stage Airflow Rate in SLPM, Nominal 1st Stage Temperature in Kelvin.

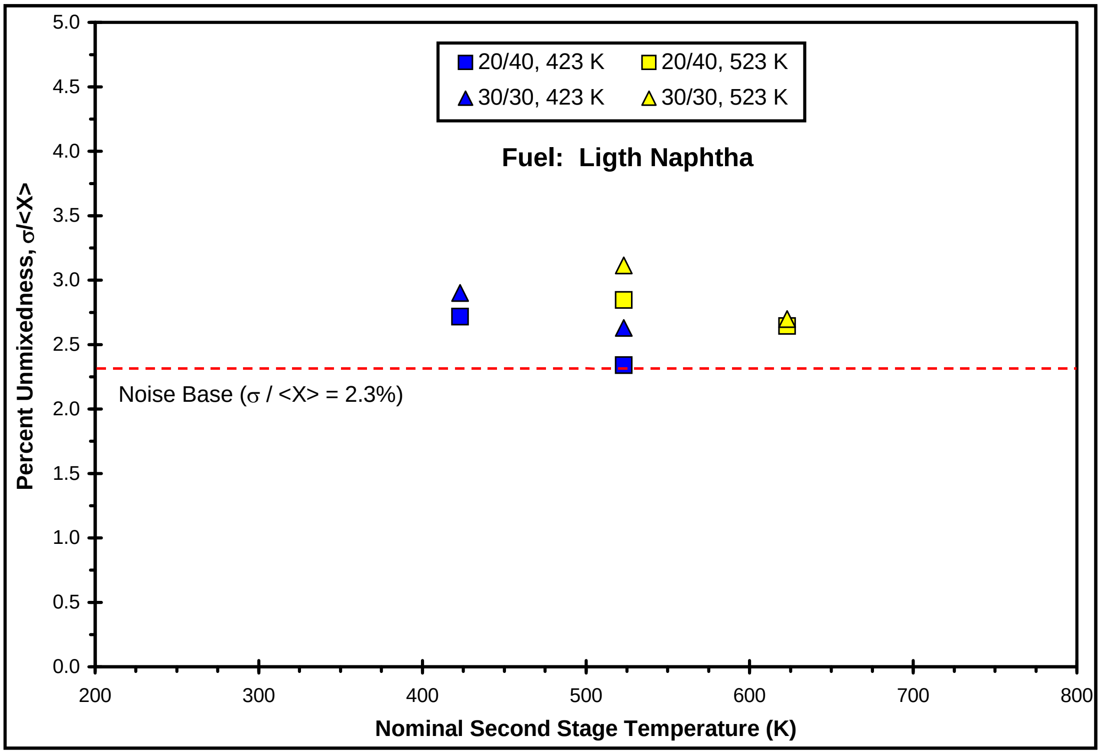

Figure 5.8. Effects of Air Split and Inlet Temperature Split on the Degree of Mixing for the SPP with Light Naphtha and Air Mixture at $\phi = 0.68$. Legend: 1st Stage Airflow Rate in SLPM / 2nd Stage Airflow Rate in SLPM, Nominal 1st Stage Temperature in Kelvin.

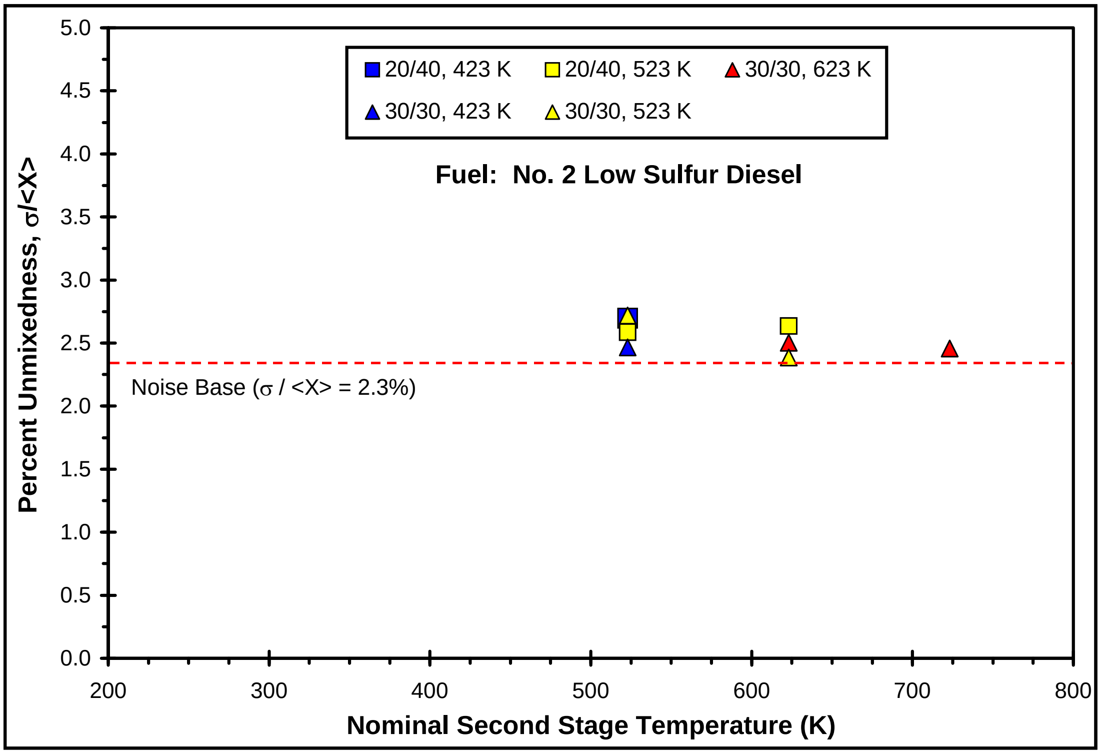

Figure 5.9. Effects of Air Split and Inlet Temperature Split on the Degree of Mixing for the SPP with No. 2 Low Sulfur Diesel and Air Mixture at $\phi = 0.68$. Legend: 1st Stage Airflow Rate in SLPM / 2nd Stage Airflow Rate in SLPM, Nominal 1st Stage Temperature in Kelvin.

5.2.2 EFFECTS OF INLET TEMPERATURE SPLIT ON MIXING

The effects of inlet temperature split on mixing are shown in Figures 5.4, 5.8 and 5.9. In general, the 1st stage temperature has a weak influence on the degree of mixing. The degree of mixing is reduced as the 1st stage temperature is increased while operating at a fixed 2nd stage temperature. This is most likely due to the reduction in flow penetration and mixing (see the Ricou-Spalding formula, Equation 2.9, Beér and Chigier, 1983) as the 1st stage temperature is increased. Additional data are required to confirm this trend.

On the other hand, the 2nd stage temperature does have a significant influence on the measured $\sigma/\langle X \rangle$ for methane/air mixtures as shown in Figure 5.4. As can be seen, the degree of unmixedness is reduced as the 2nd stage temperature is increased. Careful examination of the LAT data indicates that this effect is an artifact of the LAT system and not an indication of the actual degree of mixing of the flow exiting the SPP. Shown in Figure 5.10 is effect of the 2nd stage temperature on the measured σ and $\langle X \rangle$. As can be seen, the standard deviation in transmission is essentially independent of the 2nd stage temperature. In contrast, the mean transmission increases with increasing 2nd stage temperature (also shown in Figure 2.26). Thus, the reduction in measured unmixedness as the 2nd stage temperature is increased is primarily due to the higher laser transmission levels and not an indication of the actual degree of mixing.

As for the propane/air, naphtha/air and No. 2 diesel fuel/air unmixedness data as shown in Figures 5.6, 5.8 and 5.9, respectively, the 2nd stage temperature has minimal effect on the degree of mixing. Again, this is due to the inherent limitations of the LAT system as discussed in Section 5.2.1. The above findings indicate that the LAT system used in the present study require careful attention to and detail for interpreting the results and may have limited application for studying the effects of inlet temperature variation on unmixedness.

In regards to NO_X emission, NO_X produced for methane (natural gas)/air LP combustion (see Figures 4.2 and 5.5) decreases with increasing (second stage) inlet temperature. The reduction is about 20% for the 30/30 cases shown in Figure 5.5. Similar but less prominent effects of the second stage temperature on NO_X are also seen for ethane and propane (see Figure 5.11 and Figure 5.7, respectively). For methane/air combustion, the rate of fuel oxidation is strongly dependent on the level of preheat since the fuel is difficult to oxidize. In contrast, larger hydrocarbon fuels (i.e., ethane and propane) are much more unstable (in the sense of molecular vibration and breakup) and are readily oxidized with a small amount of preheat. Figure 5.12 represents the CO profile from centerline to the wall of the JSR. As can be seen, CO formation, which is related to the fuel breakup and oxidation, for methane is slow in the jet zone, reaches a peak off of centerline and then levels out in the recirculation zone. In contrast, the CO formation for both ethane and propane is rapid and peaks close to centerline and then steadily levels out in the recirculation zone. In addition, the rate of CO formation increases with increasing inlet temperature as indicated by the shift in peak location for methane and the change in shape for ethane (from the 523 K cases to the 623 K cases). Thus, the degree of preheat plays a significant role in fuel breakup and oxidation, particularly for methane.

The mixing level in the JSR can be inferred qualitatively through the use of an extensive inlet temperature study. The inference of the degree of premixing with the use of scales such as inlet temperature and pressure has been addressed previously by Leonard and Steigmaier (1993). As shown in Figure 5.5, the NO_X yield in the atmospheric pressure JSR-SPP setup varies only by about 1.5 ppmv (corrected to 15% O_2) as the inlet temperature is varied from approximately 423 to 773 K while holding the reactor temperature constant at 1790 K. Thus, it is reasonable to assume that the fuel and air mixture exiting the SPP is highly premixed due to its insensitivity to large variations in inlet temperature.

Another indication of the degree of premixing is realized through the elevated NO_X yield when the mixing intensity is reduced for the first stage as represented by the 20/40 air split cases in Figure 5.5. For the 20/40 air split cases, mixing in the first stage is not as intense due to the reduction in airflow as mentioned in Section 5.2.1. This higher degree of unmixedness leads to higher yields in NO_X formation. For the 30/30 air split cases, there exists sufficient mixing intensity in both the first and second stages leading to lower levels of unmixedness and consequently lower levels of NO_X output.

Second order inlet temperature effects can also be seen in Figure 5.5. As the inlet temperature is increased from 423 to 773 K there is a slight decrease in NO_X yield most likely due to the reduction in equivalence ratio and, thus, prompt NO_X (see Rutar et al., 1998). That is, prompt NO_X formed in the jet region may be a significant contributor to the overall NO_X of the reactor. By leaning the mixture, less prompt NO_X is likely to form, thereby reducing the overall NO_X emission of the JSR. Similar trends for NO_X versus inlet temperature have been observed in studies involving the 2nd generation injector as presented in Section 4.2.

Thus, there exist optimum SPP operating conditions (in regards to air split and inlet temperature split) for the minimization of NO_X formation. An optimum nominal 2nd stage temperature of 623 K is chosen for the remainder of this work. The selection of the 623 K inlet temperature is also partially due to failure issues with the convective type air heaters.

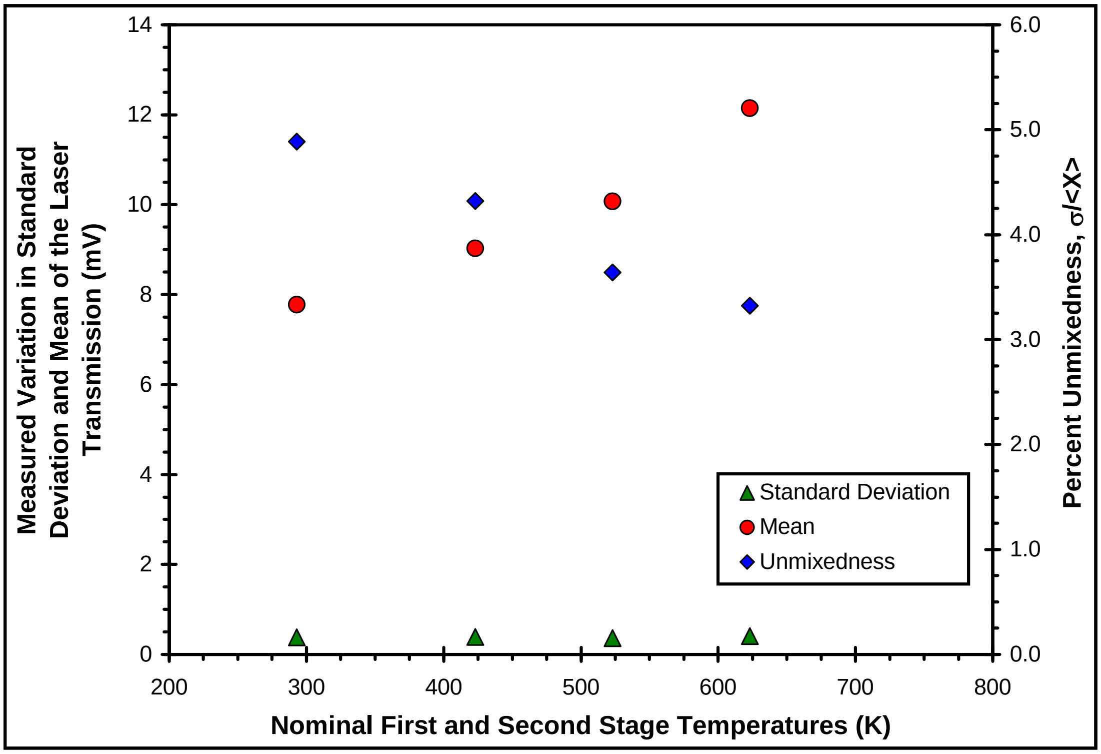

Figure 5.10. Effects of Second Stage Temperature on Measured Standard Deviation (σ) and Mean (<X>) of the Laser Transmission for Methane/Air Mixtures at 1 atm, $\phi = 0.68$ and 30/30 Air Split Conditions. The Injector Temperature is Identical for Both First and Second Stages.

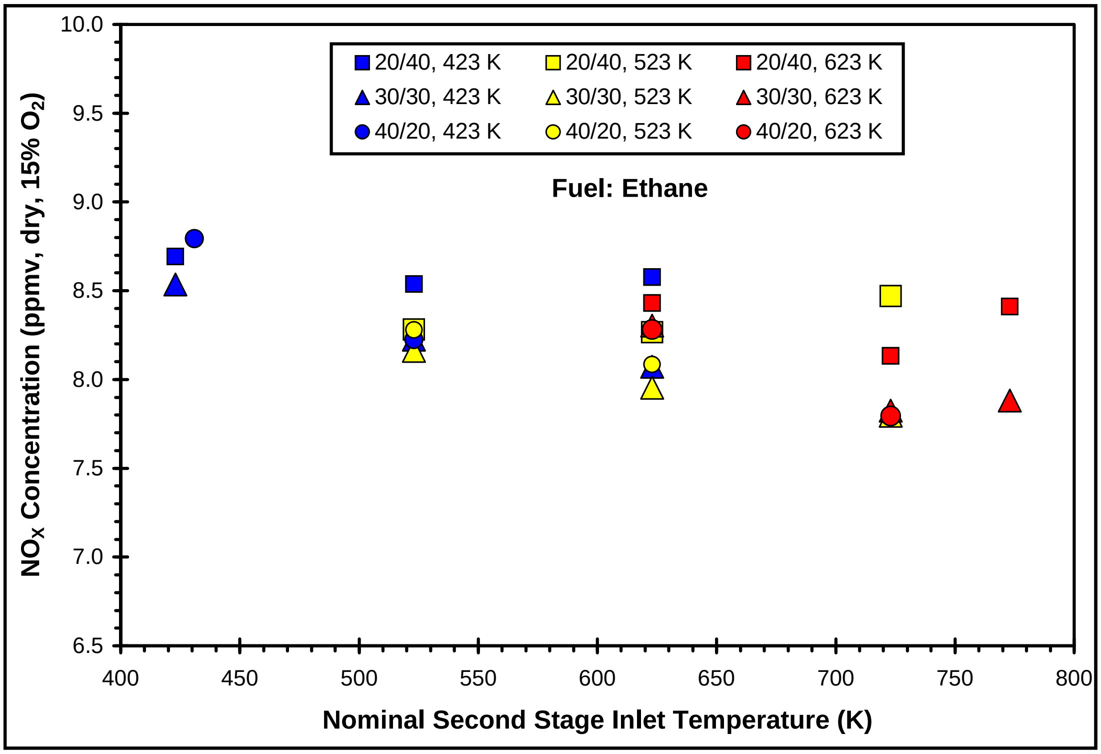

Figure 5.11. Effects of Air Split and Inlet Temperature Split on the Degree of Mixing for the SPP with Ethane and Air Mixture at $\phi = 0.68$. Legend: 1st Stage Airflow Rate in SLPM / 2nd Stage Airflow Rate in SLPM, Nominal 1st Stage Temperature in Kelvin.

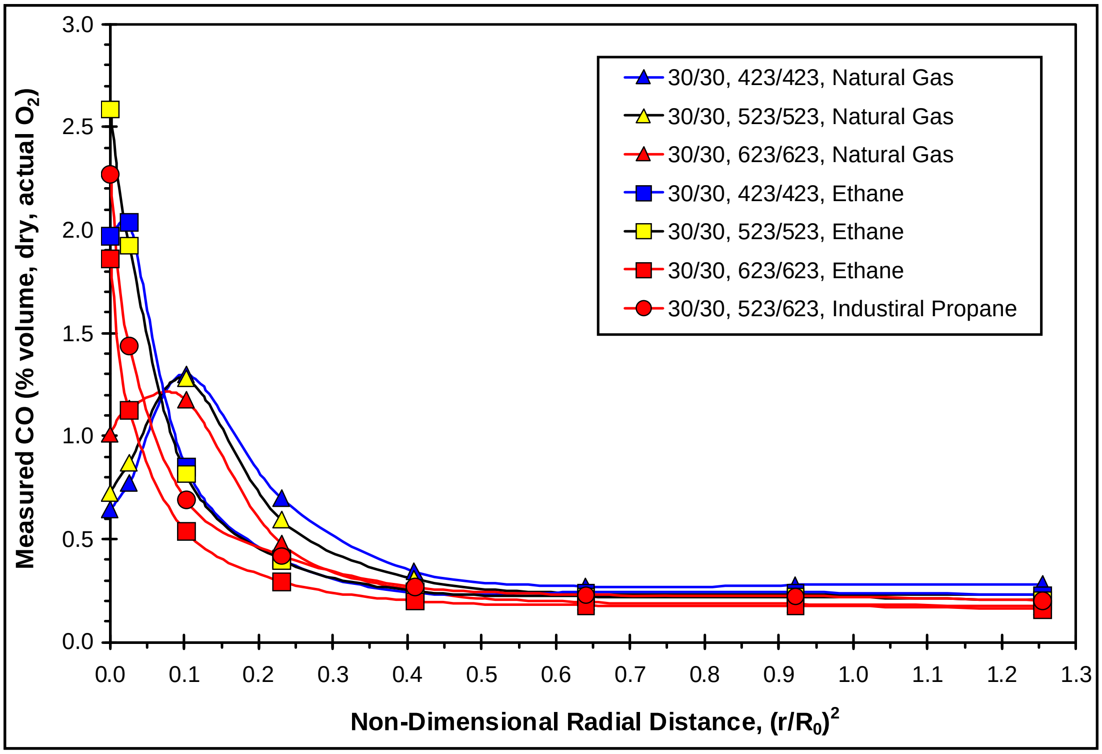

Figure 5.12. JSR-SPP CO Profiles for Natural Gas (93% Methane), Ethane and Industrial Propane (95% Propane). JSR Reactor Temperature = 1790 K, Nominal Residence Time = 2.3 ms. Legend: Air Split in SLPM, Inlet Temperature Split in Kelvin, Fuel Type.

5.2.3 EFFECTS OF INJECTOR LENGTH

Mixing in the injector is dependent on the mixing intensity and on the amount of time allowed for fuel and air premixing. Two configurations of the SPP were tested to study the effects of injector length. Both configurations have a 1st stage residence time of 12 ms. The residence time in the 2nd stage is 12 and 5 ms for the long and short versions, respectively, as shown in Figure 5.13. As can be seen, the level of NO_X emission is essentially independent of injector length (except for the gaseous fuels, which have a slightly higher value for the short SPP) indicating that mixing in the short SPP is sufficient. It must be noted that the high degree of mixing provided by the mixing jets is at the cost of large pressure drops (20 to 40%) across the injecting orifice. Additionally, the pressure drop across the 4 mm nozzle block is about 20%. This is not seen in practical systems, which nominally have a 4 to 5% pressure drop across the entire injector-combustor sections. For the remainder of this study the long version of the SPP is used to investigate the effects of fuel type.

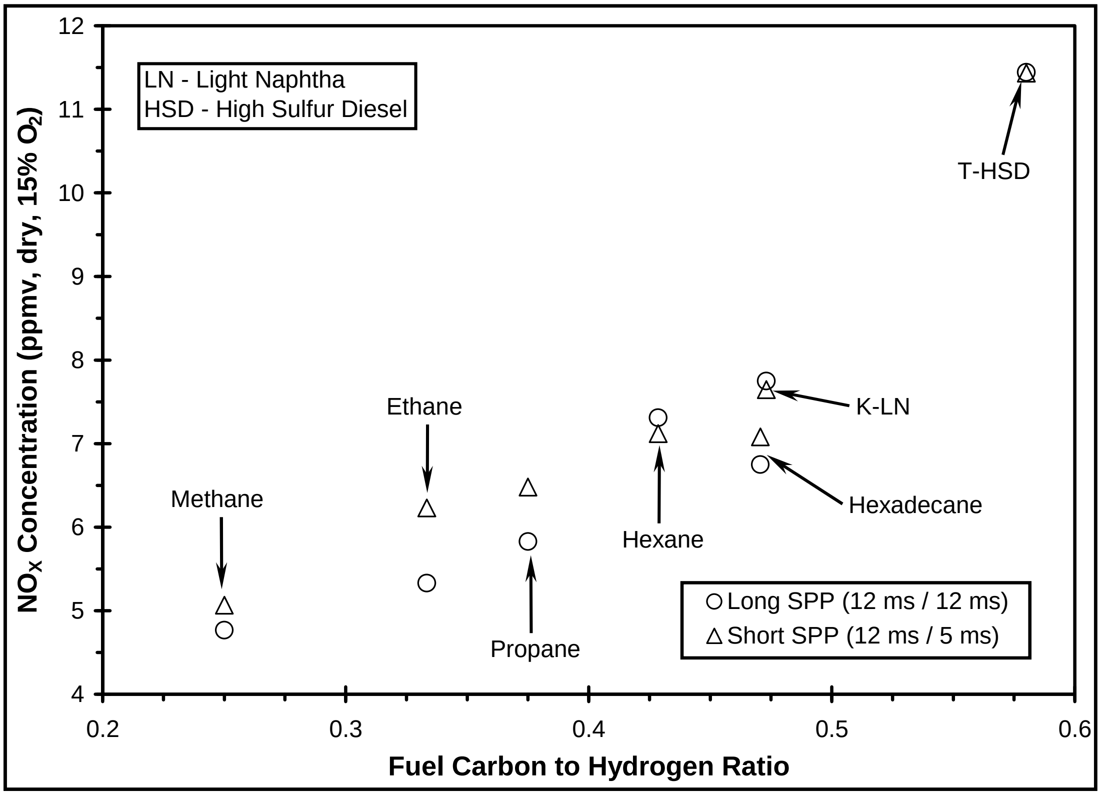

Figure 5.13. Effects of SPP Injector Length on NO$_X$ Emission for Various Fuels. JSR Combustion Temperature = 1790 K, Air Split = 30 SLPM/30 SLPM, 2nd Stage Inlet Temperature = 623 K, Nominal Residence Time = 2.3 ms.

5.2.4 EFFECTS OF SAMPLING LOCATION

The levels of NO_X and CO emissions are investigated at one of the exhaust ports with an exhaust gas manifold fabricated from a standard tube weld fitting (Parker Model 3-4 TRBZ-SS). This is done to compare the emissions at the exhaust of reactor to those measured at the standard sampling location in the recirculation zone of the JSR. The JSR was operated with the following conditions:

- Nominal JSR Combustion Temperature: 1790 K.
- Nominal JSR Residence Time: 2.3 ms.
- Airflow Split: 30 slpm/30 slpm.
- Inlet Temperature Split: 423 K/623 K
- Fuel: Natural Gas.

The results are listed in Table 5.1 and indicate that NO_X emission is identical for both locations implicating that with a high enough throughput (i.e., a 2.3 ms reactor residence time), even the single, 4 mm, centered jet nozzle can generate a highly uniform recirculation zone without the presence of a hotspot as reported in Section 2.2 As for the CO emissions, the exhaust gas level is significantly less than that measured in the recirculation zone indicating burnout due to the increased residence time in the exhaust port. Thus, the standard sampling location within the recirculation zone of the JSR is used for the remainder of the investigation.

Table 5.1. NO_X and CO Emissions for the Recirculation Zone and Exhaust Port.

Sampling Location	***NO_X (ppmv, dry, 15% O_2)***	***CO (% volume, dry, actual O_2)***
Recirculation Zone (r / R_0 = 0.71)	4.90	0.190
Exhaust Port	4.88	0.082

5.3 RESULTS – FUEL TYPE EFFECTS

Investigation on the effects of fuel type on NO_X emission is performed with the following optimum operating conditions as determined in the previous sections:

- JSR Operating Pressure: 1 atm.
- Nominal JSR Combustion Temperature: 1790 K.
- Nominal JSR Residence Time: 2.3 ms.
- Airflow Split: 30 slpm/30 slpm.
- 1st Stage Injector Temperatures: 423 K for all fuels except for hexadecane and No. 2 diesel fuel, which requires at least 453 K for full vaporization, and 523 K for all fuels.
- 2nd Stage Inlet Temperature: 623 K.
- Injector Length: Both long and short versions. The 1st stage residence time is between 12 and 10 ms depending on the stage temperature (423 or 523 K). The second stage residence times are 5 and 12 ms for the short and long versions, respectively.
- Sampling Location: Standard recirculation zone position ($r/R_0 = 0.71$).

The results are discussed in the following figures and the corresponding experimental data is presented in Appendix H. Shown in Figure 5.14 is the NO_X yield for the various fuels studied under either LP or LPP conditions. The trends from methanol to hexadecane are similar to that report in Section 4.3 and Lee et al. (1999) for the 2nd generation injector. NO_X yield is lowest for methanol (3.5 ppmv, dry, 15% O_2). There is approximately a 37% increase by switching the fuel from methanol to methane (or natural gas). This increase is very likely caused by prompt NO_X effects, which is a very weak contributor in methanol combustion, but can be significant in methane combustion. Methane combustion yields the least amount of NO_X for all alkane fuels tested. The increase continues to hexane (about 52% higher NO_X yield than methane) through ethane, propane and pentane. Then there is a slight (7%) decrease as the fuel size is further increased to hexadecane through heptane and dodecane. The results for the pure fuels are essentially identical to those measured with the 2nd generation injector (see Figure 4.3). As for the commercial fuels, the two light naphtha fuels exhibit similar NO_X yields as the pure alkanes since they contain no fuel bound nitrogen. As for the No. 2 diesel fuels, NO_X emission is elevated due to the conversion of FBN to fuel NO_X. The two aromatic fuels, benzene and toluene, yield the highest NO_X emissions (approximately 10.1 ppmv, dry, 15% O_2) among all pure laboratory fuels tested. The NO_X level is approximately 42% higher than hexane.

In order to validate the effects of FBN conversion to fuel NO_X as discussed in Section 3.2 and Capehart et al. (1997), the amount of NO_X formed by 100% conversion of the FBN for each commercial fuel is deducted from the overall NO_X emission and the results are shown in Figure 5.15. As can be seen, there is essentially a linear increase in NO_X yield for fuels with C:H ratios ranging from 0.25 to 0.63 (with the exception of methanol). For fuels with high C:H ratios (i.e., the aromatic fuels), there is a "leveling-off" in NO_X yield. The increase in NO_X formation is most likely due to the increased O-atom concentration as the C:H ratio is increased as discussed in Lee et al. (1999) and will be investigated in detail in Chapter 6 with various chemical reactor models.

Shown in Figure 5.16 is the CO emission for the various fuels. As can be seen, CO yield is essentially linearly dependent on the fuel carbon to hydrogen ratio for ethane through the diesel fuels. The lowest CO yield is measured for ethane. Methane (or natural gas) has a higher CO yield than ethane most likely due to its slower reacting (more difficult to burn) tendencies as shown in Figure 5.12. This behavior will be discuss further in Chapter 6. Again, there exists a leveling-off in CO production, similar to that in NO_X formation, for the aromatic hydrocarbons.

The NO_X versus CO plots for the various fuels tested are presented in Figures 5.17 and 5.18. As can be seen NO_X production is linearly correlated with the CO production in the recirculation zone where CO is not allowed to burnout. The exceptions are methanol (low prompt NO_X formation), methane (slow CO production and destruction) and the aromatic fuels.

Thus, NO_X output from LP and LPP combustion of high mixing intensity can be predicted with fairly high certainty based on the following two fuel properties:

- The fuel C:H ratio.
- The amount of fuel bound nitrogen.

In addition, NO_X and CO yields are essentially linear functions of the fuel carbon to hydrogen ratio with the exception of methanol and methane. NO_X formation is also linearly dependent on the CO yield for C_2 to C_{16} alkanes (including naphtha and the diesel fuels).

Similar results and trends in both measured NO_X and CO emissions have been reported by Zelina and Ballal (1996), Zelina et al. (1996), Blust et al. (1997) and Maurice et al. (1999) all of whom are associated with the University of Dayton Research Institute (UDRI). The UDRI results as obtained with the use of an atmospheric pressure toroidal jet-stirred reactor also indicate an increase in NO_X emission as the fuel C:H ratio is increased. As for the CO emission, ethane exhibits the lowest value followed by a slight increase to methane and increases further as the fuel C:H ratio is increased. The UDRI CO trend is identical to that obtained in the present study. Due to concerns with differences in reactor configuration and operating conditions, the UDRI results are not plotted against the ones obtained in the present study.

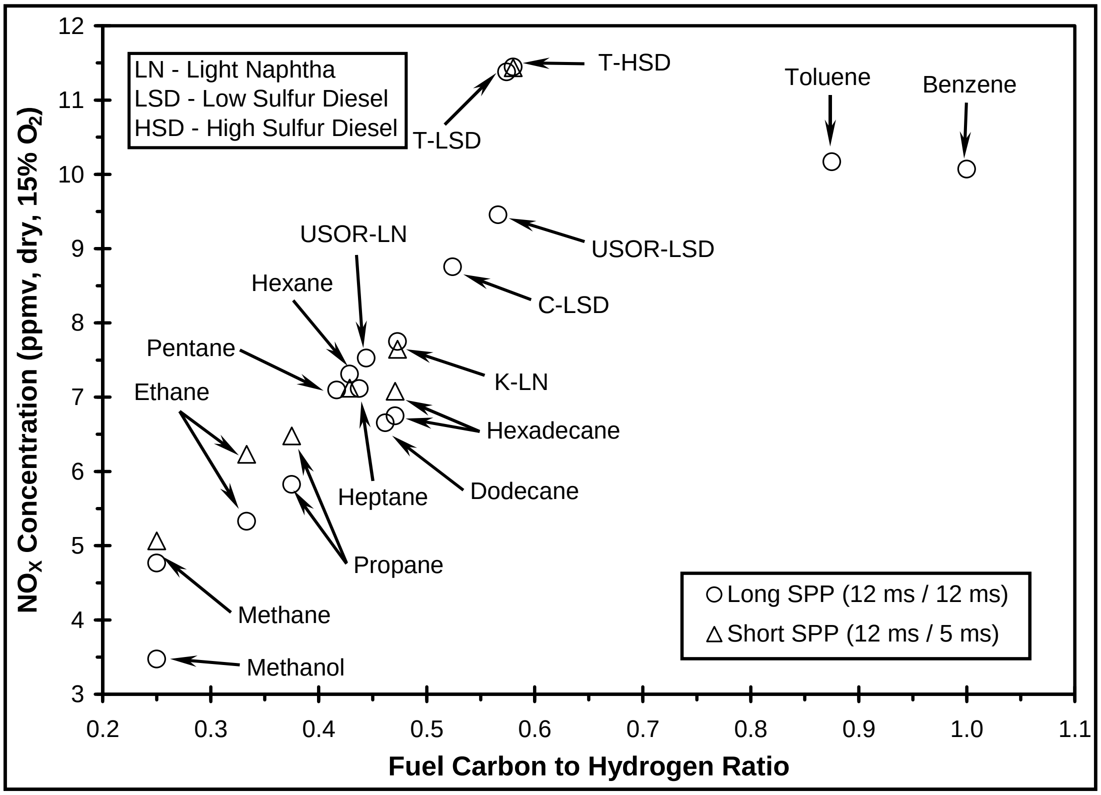

Figure 5.14. Effects of Fuel Type or Composition on NO_X Formation for a JSR Combustion Temperature of 1790 K, a 2nd Stage Inlet Temperature of 623 K, a Airflow Split of 30 SLPM/30 SLPM and a Nominal Residence Time of 2.3 ms.

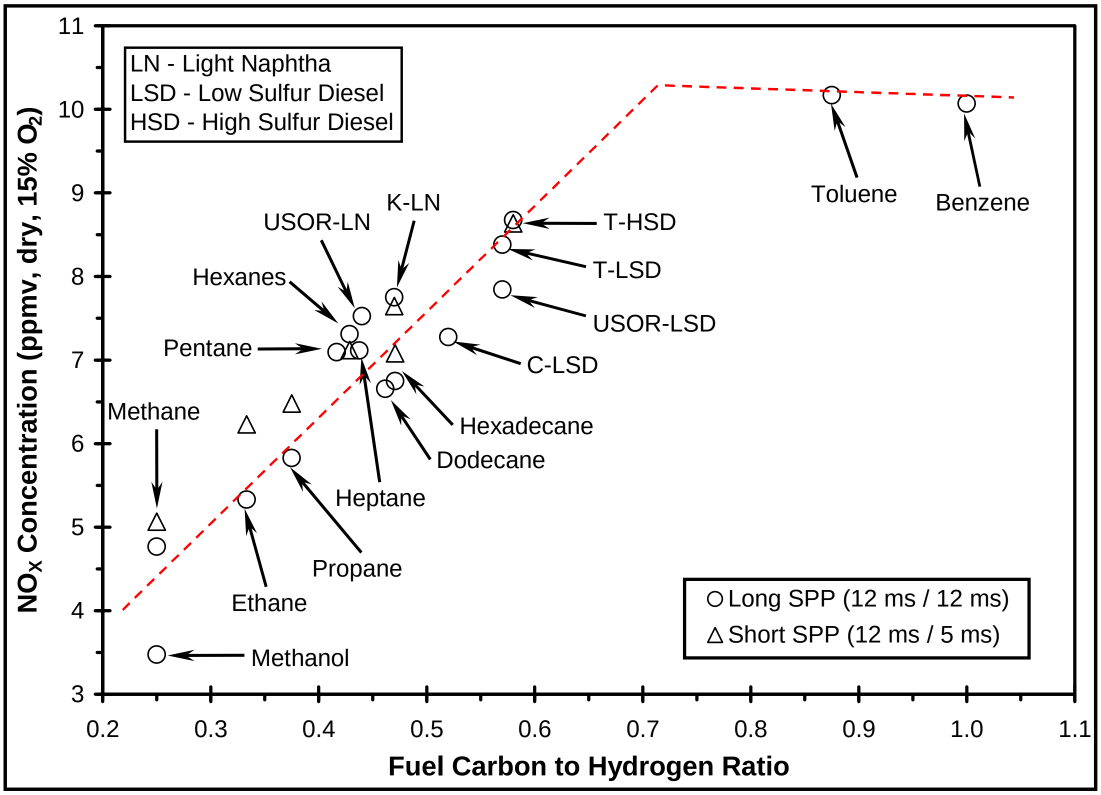

Figure 5.15. Effects of Fuel Type or Composition on NO_X Formation for a JSR Combustion Temperature of 1790 K, a 2nd Stage Inlet Temperature of 623 K, a Airflow Split of 30 SLPM/30 SLPM and a Nominal Residence Time of 2.3 ms. Fuel NO_X formed through 100% Conversion of FBN is Deducted for the Commercial Fuels.

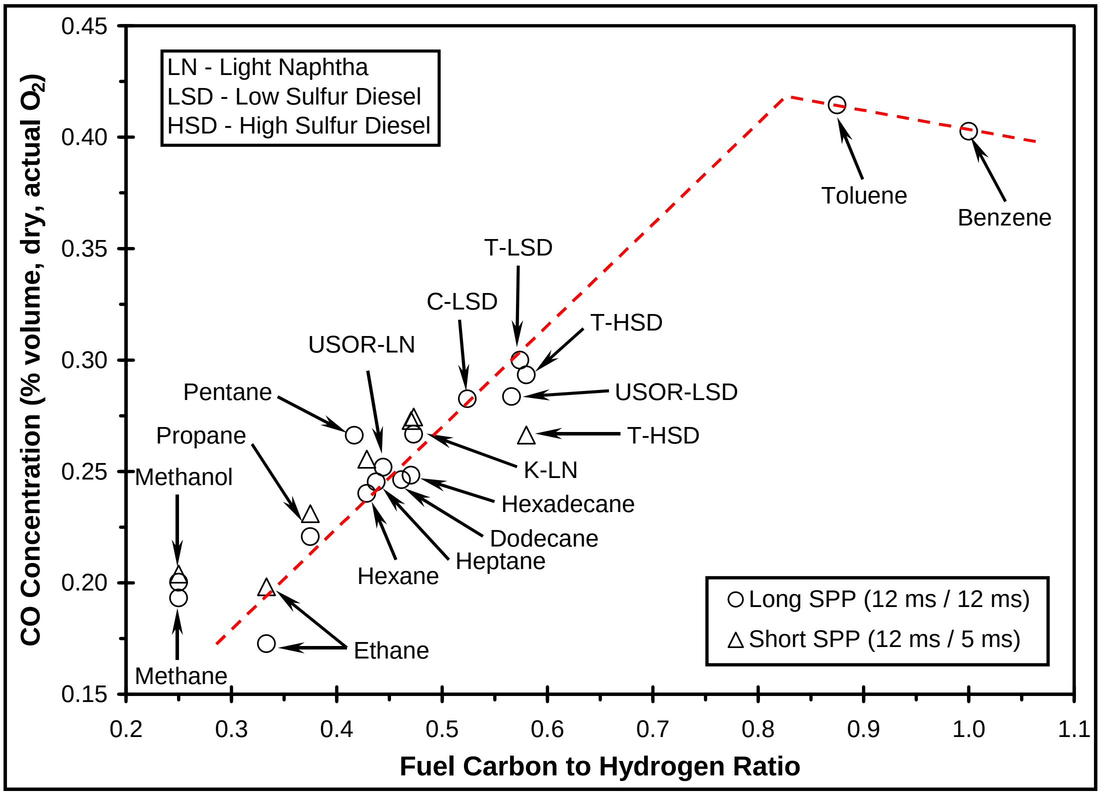

Figure 5.16. Effects of Fuel Type or Composition on CO Formation for a JSR Combustion Temperature of 1790 K, a 2nd Stage Inlet Temperature of 623 K, a Airflow Split of 30 SLPM/30 SLPM and a Nominal Residence Time of 2.3 ms.

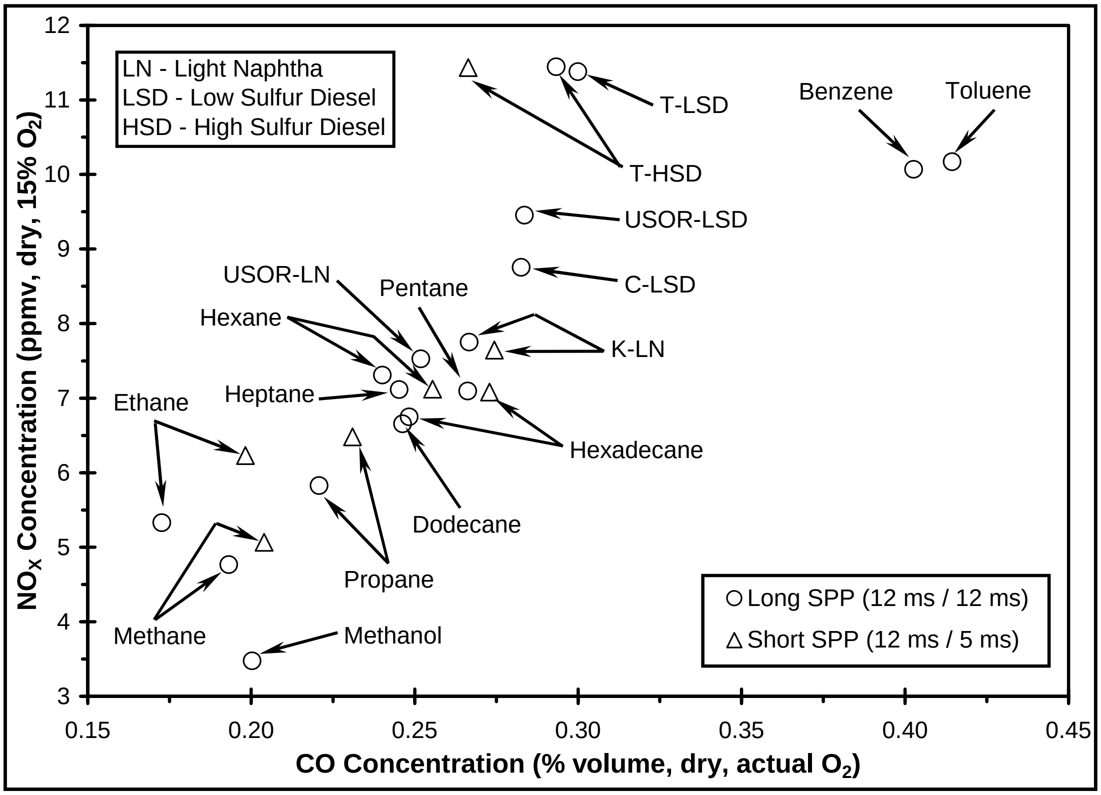

Figure 5.17. Effects of Fuel Type or Composition on NO_X and CO Formation for a Reactor Temperature of 1790 K, a 2^{nd} Stage Inlet Temperature of 623 K, a Airflow Split of 30 SLPM/30 SLPM and a Nominal Residence Time of 2.3 ms.

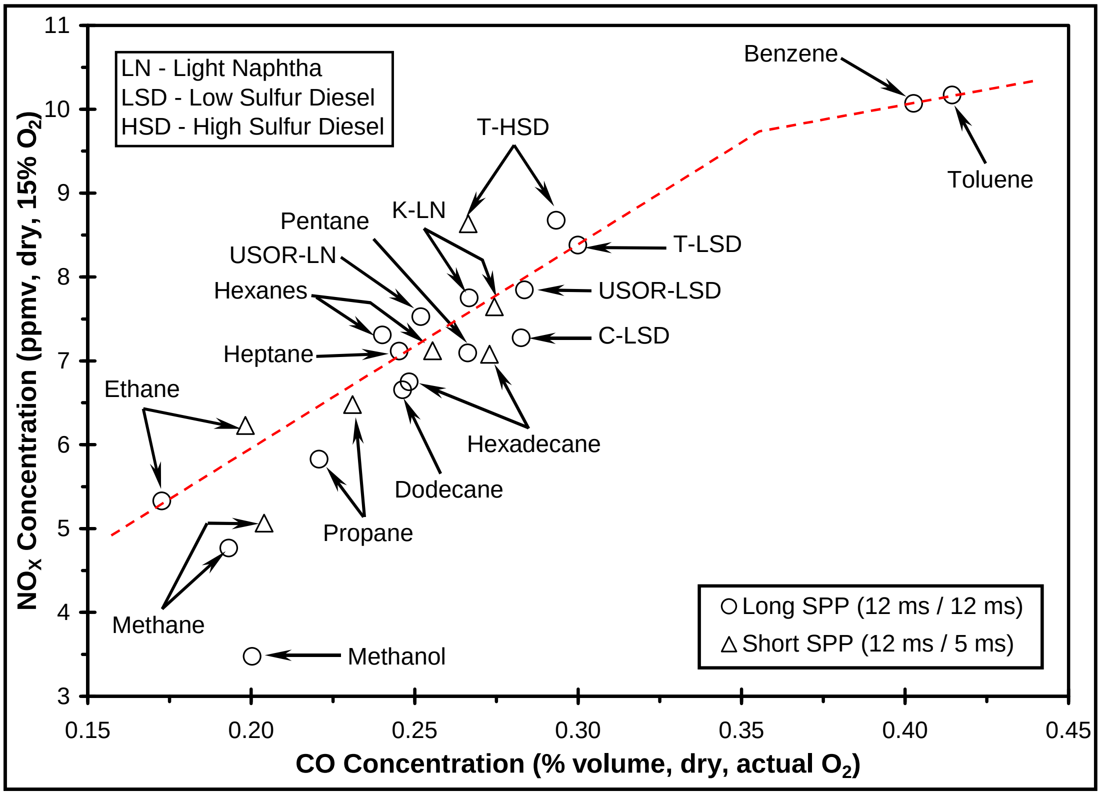

Figure 5.18. Effects of Fuel Type or Composition on NO_X and CO Formation for a Reactor Temperature of 1790 K, a 2nd Stage Inlet Temperature of 623 K, a Airflow Split of 30 SLPM/30 SLPM and a Nominal Residence Time of 2.3 ms. Fuel NO_X formed through 100% Conversion of FBN is Deducted for the Commercial Fuels.

5.4 SUMMARY

Atmospheric pressure testing of the dual fuel, staged prevaporizing-premixing injector has been completed. The SPP technique shows great promise for the optimized reduction of NO_X emission under LP and LPP combustion conditions. The following are key findings of the SPP investigation:

- Mixing is optimized with an airflow split of 30 slpm and 30 slpm in the 1st and 2nd stage, respectively. Stratification most likely occurs if insufficient airflow (or penetration) is introduced in the 2nd stage.

- The effects of inlet temperature are minimal if a high degree of mixing is achievable. This is particularly true for hydrocarbon fuels other than methane.

- NO_X emission for fuels with no fuel bound nitrogen, like naphtha, is essentially equivalent to NO_X emissions for pure fuels with similar C:H ratios.

- Small amounts of fuel bound nitrogen, in fuels like diesel, are completely converted to fuel NO_X under LPP combustion conditions.

- NO_X and CO emission is essentially linearly proportional to fuel C:H ratio, except for methanol and methane.

- NO_X production is linearly dependent on the rate of CO production for most hydrocarbon fuels, except for methanol and methane.

- Both the short and long versions of the staged prevaporizer-premixer provide a high degree of prevaporizing and premixing for a wide range of gaseous and liquid fuels leading to extremely low NO_X emissions without breaching the criterion of autoignition.

CHAPTER 6: CHEMICAL REACTOR MODELING

NO_X can be formed through several pathways or mechanisms under lean premixed combustion conditions. The following sections will briefly describe the various pathways and their importance in the LP combustion process. The Miller and Bowman, 1989 (MB, 1989), the Gas Research Institute (1996 and 1999) 2.11 and 3.0 (GRI 2.11 and GRI 3.0) and the Maurice et al., 1999 [heptane oxidation mechanism in conjunction with GRI 3.0 NO_X sub-mechanism (LQM-GRI 1999)] mechanisms are utilized in this study to interpret the experimental results.

6.1 NO_X FORMATION PATHWAYS

The following sections provide a concise description of the major NO_X formation pathways that are believed to occur during the lean premixed combustion process. The listed reaction mechanisms are believed to be the major pathways leading to the formation of NO_X under LP combustion conditions.

6.1.1 ZELDOVICH PATHWAY

The extended Zeldovich mechanism consists of the following three principal reactions:

$N_2 + O \leftrightarrow \mathbf{NO} + N$ .... Rx. 6.1

$N + O_2 \leftrightarrow \mathbf{NO} + O$ .... Rx. 6.2

$N + OH \leftrightarrow \mathbf{NO} + H$ .... Rx. 6.3

The NO_X formed near the flame front where the intermediates (O, H and OH) are at super-equilibrium concentrations are considered as Zeldovich NO_X. The NO_X formed in the post flame zone where the intermediates are at equilibrium conditions is termed thermal NO_X.

The Zeldovich mechanism is only significant for temperatures above about 1800 K due to the high activation energy involved in the initiation step (see Reaction 6.1). Thus, for LP and LPP combustion systems where the nominal combustion temperature is below 1800 K, NO_X emission from the Zeldovich mechanism is not dominating as is the case in stoichiometric combustion.

An approximation of the overall reaction rate for the formation of Zeldovich NO can be written as:

$$\frac{d[NO]}{dt} = 2 \cdot k_{f_1} \cdot [N_2] \cdot [O] \quad \text{Eq. 6.1}$$

where k_{f_1} is the forward rate constant of Reaction 6.1. The rate assumes negligible reverse rates of Reactions 6.1 through 6.3.

6.1.2 PROMPT PATHWAY

The mechanism that leads to the rapid formation of NO through reaction of N_2 with the short-lived hydrocarbon radicals, such as CH and CH_2, in the flame zone is termed prompt. It is important to emphasize that the hydrocarbon radicals only exist in the flame zone for a short period of time of about 0.1 ms. The key intermediates formed in the prompt pathway are HCN and N. The HCN and N atom formed are readily oxidized to NO under LP combustion conditions. However, prompt NO is not thought to be a dominant mechanism under lean combustion conditions due to the reduced hydrocarbon radical concentration. The pathways leading to the formation of prompt NO under lean combustion are shown by the following reactions:

$\mathrm{CH} + \mathrm{N_2} \rightarrow \mathbf{HCN} + \mathrm{N}$ .... Rx. 6.4

$\mathrm{CH_2} + \mathrm{N_2} \rightarrow \mathbf{HCN} + \mathrm{NH}$ .... Rx. 6.5

$\mathrm{HCN} + \mathrm{H} \rightarrow \mathbf{CN} + \mathrm{H_2}$ .... Rx. 6.6

$\mathrm{CN} + \mathrm{OH} \rightarrow \mathbf{NCO} + \mathrm{H}$ .... Rx. 6.7

$\mathrm{NCO} + \mathrm{O} \rightarrow \mathbf{NO} + \mathrm{CO}$ .... Rx. 6.8

$\mathrm{CN} + \mathrm{O} \rightarrow \mathrm{CO} + \mathbf{N}$ .... Rx. 6.9

$\mathrm{NH} + \mathrm{O} \rightarrow \mathbf{NO} + \mathrm{H}$ .... Rx. 6.10

Conversion of the N atom formed in Reactions 6.4 and 6.9 to NO is effected by Reaction 6.2.

The hydrocarbon radicals involved in the prompt mechanism can be formed quite readily under LP and LPP operating conditions. Fuel oxidation and pyrolysis to small hydrocarbon radicals occurs in the flame zone. Furthermore, for large hydrocarbons, fuel breakdown to smaller fragments can occur within the premixing chamber under moderate inlet temperatures. This has been seen in the present research and is discussed in Section 2.4.

Prompt $\mathrm{NO_X}$ formation can be approximated with the following overall rate equation:

$$\frac{d[NO]}{dt} = 2 \cdot k_{f_4} \cdot [N_2] \cdot [CH] \quad \text{Eq. 6.2}$$

where k_{f_4} is the forward rate constant of Reaction 6.4. This equation assumes all of the HCN and N formed by Reaction 6.4 ultimately oxidize to NO under LP combustion conditions.

6.1.3 NITROUS OXIDE PATHWAY

For combustion temperatures near 1800 K, NO_X formation through the nitrous oxide (N_2O) pathway must be considered (see Malte and Pratt, 1974 and Steele et. al., 1997). In fact, under LP and LPP conditions, the N_2O pathway can play a dominant role in NO_X formation. The N_2O pathway to NO_X is given below.

$N_2 + O + M \leftrightarrow \mathbf{N_2O} + M$ .... Rx. 6.11

$N_2O + O \rightarrow \mathbf{N_2} + O_2$ .... Rx. 6.12

$N_2O + H \rightarrow \mathbf{N_2} + OH$ .... Rx. 6.13

$N_2O + O \rightarrow \mathbf{NO} + \mathbf{NO}$ .... Rx. 6.14

$N_2O + H \rightarrow \mathbf{NO} + \mathbf{NH}$ .... Rx. 6.15

$N_2O + CO \rightarrow \mathbf{NO} + \mathbf{NCO}$ .... Rx. 6.16

Reaction 6.11 is the initiation step. The N_2O is oxidized directly to NO (Reactions 6.14 through 6.16). The NH formed in Reaction 6.15 can be oxidized readily to NO (Reaction 6.10) or convert to N and HNO under LP conditions. The N and HNO ultimately oxidize to NO. The NCO formed in Reaction 6.16 reacts completely to NO via Reaction 6.8. The N_2O is reduced to N_2 via Reactions 6.12 and 6.13.

The rate equation for the formation of NO_X via the nitrous mechanisms can be approximated by the following two expressions:

$$\frac{d[NO]}{dt} = 2 \cdot k_{f_{14}} \cdot [N_2O] \cdot [O] \quad \text{Eq. 6.3}$$

$$\frac{d[NO]}{dt} = 2 \cdot k_{f_{15}} \cdot [N_2O] \cdot [H] \quad \text{Eq. 6.4}$$

where $k_{f_{14}}$ and $k_{f_{15}}$ are the forward rate constants of Reactions 6.14 and 6.15, respectively. Equation 6.4 assumes complete conversion of the NH formed by Reaction 6.15 to NO.

6.1.4 NNH PATHWAY

The controversial NNH pathway consist of the following reaction steps (Bozzelli et al., 1994 and Harrington et al., 1996):

$$H + N_2 \rightarrow \mathbf{NNH} \quad \text{Rx. 6.17}$$

$$NNH + O \rightarrow \mathbf{NO} + NH \quad \text{Rx. 6.18}$$

The approximate rate equation for the formation of NO_X via the NNH pathway can be written as:

$$\frac{d[NO]}{dt} = 2 \cdot k_{f_{15}} \cdot [NNH] \cdot [O] \quad \text{Eq. 6.5}$$

where $k_{f_{18}}$ is the forward rate constant of Reaction 6.18. This expression assumes complete conversion of the NH formed by Reaction 6.18 to NO. The NNH pathway to NO is included in the GRI 2.11 and 3.0 mechanisms, but is not in the Miller-Bowman 1989 mechanism.

6.1.5 FUEL BOUND NITROGEN PATHWAY

Most fossil fuels contain small amounts of fuel bound nitrogen. The FBN amount in certain coals can be as high as 1.5% of the total weight. Most light and medium distillate fuels contain 100 to 300 ppm by weight of FBN. For most commercial liquid fuels, the fuel bound sulfur concentration is reduced and controlled in the refining process. Consequently, the FBN content in the commercial liquid fuels is also reduced through the refining and desulfurization process. The types of the organic nitrogen species that are present in the parent fuel are not well known. In general, it has been accepted that the majority of the FBN is of the amino or cyano type.

In the combustion of most fossil fuels, FBN is an important source of NO_X emission. The extent of conversion of the FBN to NO_X is almost independent of the properties of the parent fuel, but is strongly dependent on the combustion conditions and the initial FBN concentration in the reactant (Bowman, 1991). Under LP and LPP conditions, small amounts of FBN are completely converted to NO_X (see Chapter 3 of this work, Capehart et. al., 1997, Wang et. al., 1997 and Sarofim et al., 1975). For example, a fuel oil containing 200 ppmw of FBN can yield as high as 11 ppmv (dry, 15% O_2) of fuel NO under LPP combustion conditions. This is particularly significant when NO_X emission goals are set at 25 ppmv.

Currently, details of the kinetic mechanisms involved in the FBN conversion have not been fully resolved. The FBN mechanism used by most investigators is shown in Figure 6.1. As can be seen, the initiation step is the formation of HCN through the pyrolysis and oxidation of the FBN that can occur under relatively low temperatures. Once the HCN is formed, the remaining reactions are similar to those in the prompt mechanism.

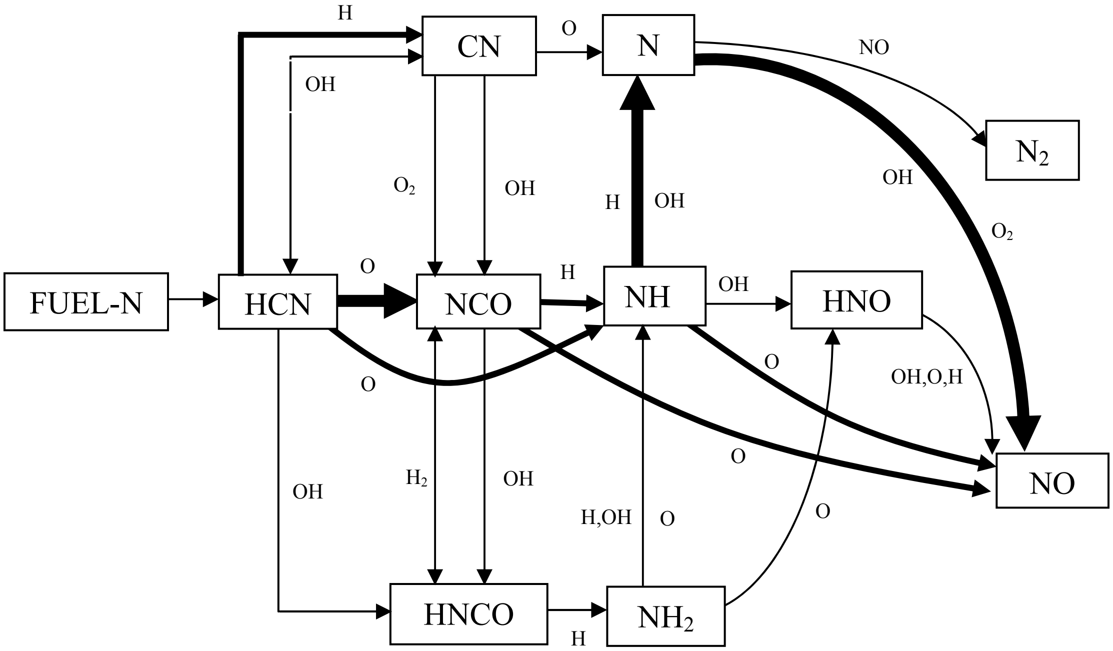

Figure 6.1. Principal Reaction Paths in the Fuel Bound Nitrogen Conversion Process in Flames (From Bowman, 1991).

6.2 CHEMICAL KINETIC MECHANISMS

The chemical kinetic mechanisms used in this study are all “full” mechanisms. They are all developed through predominantly government-funded projects and are in the public domain or are obtained from the authors (i.e., Maurice) with explicit permission for use and publication. As a note, a difficulty associated with chemical kinetic modeling is the availability and accuracy of reaction mechanisms. In addition, interpolation and extrapolation of the pressure fit coefficients of the existing database, which is determined for pressures other than 1 atm used in this study, is required and this may lead to inaccuracies in the results (Nicol, 1995).

The mechanisms used this research basically consist of three parts: 1) thermodynamic data for all species used in the mechanism, 2) fuel oxidation chemistry and 3) pollutant formation chemistry. Since the original Maurice et al., 1999 mechanism was developed for rich combustion its nitrogen related thermodynamic data and reactions have been replaced with the nitrogen chemistry of GRI 3.0. The hybrid mechanism is termed the LQM-GRI 1999 mechanism.

The number of species and reaction steps used in each mechanism is listed in Table 6.1. As can be seen, the LQM-GRI 1999 mechanism has over 170 species and close to 900 reaction steps. This is typical of mechanisms for large hydrocarbon species oxidation. Also listed in Table 6.1 are the fuels modeled with each mechanism in this study. Detailed description and listings of each mechanism are presented in Appendix I.

Table 6.1. Mechanisms used for Chemical Reactor Modeling.

Mechanism	***No. of Species***	***No. of Reaction Steps***	***Fuels Tested***	***Notes***
MB 1989	25	84	Methane Ethane CO/H_2	Modeling of CO/H_2 fuel is void of any hydrocarbon chemistry.
GRI 2.11	48	279	Methanol Methane Ethane	Contains NNH NO_X chemistry
GRI 3.0	52	325	Methanol Methane Ethane Propane Ethylene Acetylene	Contains NNH NO_X chemistry.
LQM-GRI 1999	176	934	Methanol Methane Ethane Propane Heptane Benzene	Contains GRI 3.0 NO_X chemistry.

6.3 CHEMICAL REACTOR MODELING AND RESULTS

Chemical reactor models have been used extensively at the University of Washington to understand the detailed combustion kinetics of various fuels. CRMs have been developed extensively by Pratt and Wormeck (1976), Pratt (1977) and Radhakrishnan and Pratt (1988). The current Mark III CRM computer code, developed by Pratt and as modified by Nicol (1995), is used throughout this research. The Mark III code simulates the combustion zone by subdividing the zone into various flow elements. Each flow element can be assigned a variety of different perfectly stirred reactors and plug flow reactors. The flow elements can be linked in series or in parallel. Furthermore, recycling is permitted. Within each flow element, chemical reactions are assumed to proceed at a finite rate. In general, some combination of PSRs and PFRs are used to simulate the combustion zone.

The PSR, which assumes that both backmixing (or recirculation) and micromixing are infinitely fast compared to the reaction rates, assumes neither spatial nor temporal variations in species concentrations and temperature. This is an idealized condition when applied to the JSR, since the JSR with its WSR approximation for the recirculation zone does exhibit finite rates of micromixing. Nevertheless, the PSR model is used to approximate the flame zone and the post flame zone, where the O-atom concentration is not allowed to relax and is at super-equilibrium values. The PFR, which neglects mixing and transport allows the species to relax towards equilibrium concentrations, represents the sampling probe.

Steele et al. (1997) investigated N_2O kinetics for LP methane and LP CO/H_2 flames. Nicol et al., 1997 used CRMs to formulate global mechanisms (5 steps, 7 species) for methane combustion with NO formation. Maurice et at. (1999) used a PFR followed by a PSR in conjunction with large hydrocarbon kinetic mechanisms to study NO_X and CO emission for methane, ethane, heptane, dodecane, toluene, ethylbenzene, Jet A and a simulated endothermic fuel and compared the results to experimental data.

For interpretation of the trends of the JSR experiments, a single PSR operating at the experimental residence time and measured combustion temperature is used. In order to explore the effect of Fenimore prompt NO_X, a two PSRs in series model is used. In addition, a three PSRs in series model is used to improve the predicted values of the two PSRs model.

Results from chemical reactor modeling with the various mechanisms are compared to each other and to the experimental results with the fuel NO_X deducted from the No. 2 diesel fuels. The results are presented in the following sections and are also listed in Appendix H.

6.3.1 SINGLE PSR MODEL

For NO_X formation in the atmospheric pressure JSR, modeling using a single PSR has been found to be quite useful (see Steele, 1995 and Steele et al., 1995). Both absolute values of NO_X and trends in NO_X are typically well predicted by the model when the PSR is assigned the measured values of combustion temperature and mean residence time. The good agreement appears to occur in large part because of the behavior of the O atom. For lean, atmospheric pressure combustion in the JSR, super-equilibrium levels of O atom, of about 1000 ppmv, tend to persist in the reactor. Thus, NO_X formation by super-equilibrium O atom attack on N_2 through the Zeldovich and nitrous oxide mechanisms occurs throughout the JSR.

Thus, the single PSR model assumes that the overall mixing in the JSR is infinitely fast and approaches the ideal PSR condition with respect to NO_X formed by O atom attack on N_2. It neglects the existence of the jet zone, which starts cold, ignites and contains much of the fuel oxidation to CO, H_2 and H_2O and free radical formation (O, H, OH). The single PSR model is executed with inputs matching those of the actual experimental conditions. Namely, the PSR is run under assigned temperature and residence time. The assigned temperature is equal to that of the JSR combustion temperature of 1790 K and the assigned residence time is equal to the nominal reactor residence time of 2.3 ms. The inlet temperature is set at 623 K. The simple single PSR model provides information on the trends of the various fuels.

As shown in Figure 6.2, single PSR modeling with the various mechanisms provides the following results:

- Methanol exhibits the lowest NO_X levels for the mechanisms tested. The increase in NO_X formation from methanol to methane is indicated by the two GRI mechanisms where the difference in the amount of NO_X formation is mainly due to the different oxidation chemistry of methanol. The increase is 6% and 59% for the GRI 2.11 and 3.0 mechanisms, respectively. The experimental increase is 37%. In terms of absolute value, both GRI mechanisms over predict the experimental methanol and methane NO_X values by a factor two to three.

- The MB 1989 mechanism predicts NO_X concentrations of 4.9 and 6.6 ppmv for methane and ethane, respectively. The methane prediction is very close to the experimental value of 4.8 ppmv. The predicted increase from methane to ethane is 35%. This is higher than the experimental increase of 10 to 20%. The increase from methane to ethane is 24% and 10% for the GRI 2.11 and 3.0 mechanisms, respectively. The percent of increase as predicted by the GRI 3.0 mechanism is the same as the experimental value.

- The predicted NO_X increase from ethane to propane is 4% for the GRI 3.0 mechanisms. This is slightly lower than the experimental value of 9%.

- The LQM-GRI 1999 mechanism is also used to predict the NO_X emission for methanol, methane, ethane, propane, heptane and benzene. As can be seen methanol emission is under predicted by about 34% compared to the experiment. Methane has a predicted value of 6.7 ppmv. This is approximately 40% higher than the experimental value. The LQM-GRI 1999 mechanism also exhibits a disturbing trend where NO_X decreases from methane to ethane. This is completely contrary to the experimental findings and to the predicted trends as obtained with other mechanisms. Maurice et al. (1999) show a similar predicted trend for methane where NO_X emission is higher than any other fuel tested.

- The LQM-GRI 1999 mechanism predicts NO_X emission for propane and heptane with good agreement to the experimental results. The predicted values are close to the experimental values. The predicted increase from propane to heptane is 7%. This compares well to the experimental increase of 9%.

- With the LQM-GRI 1999 mechanism, there is about a 13% increase in the predicted NO_X as the fuel is switched from heptane to benzene. This is low compared to the experimental increase of 42%. The predicted benzene NO_X emission from LQM-GRI 1999 for benzene is significantly lower than the experimental value (by 23%).

- The MB 1989 mechanism is also run by assuming instantaneous oxidative pyrolysis of the parent fuel (i.e., $C_nH_m + 0.5nO_2 \rightarrow nCO + 0.5mH_2$). Thus, CO/H_2 combustion is modeled. The predicted NO_X concentration compares well to the experimental values with the exception of the light hydrocarbons. This indicates that NO_X production is mainly through the Zeldovich and nitrous oxide mechanisms since the CO/H_2 modeling is void of any prompt NO_X reactions and the MB 1989 mechanism does not treat NO formation from NNH.

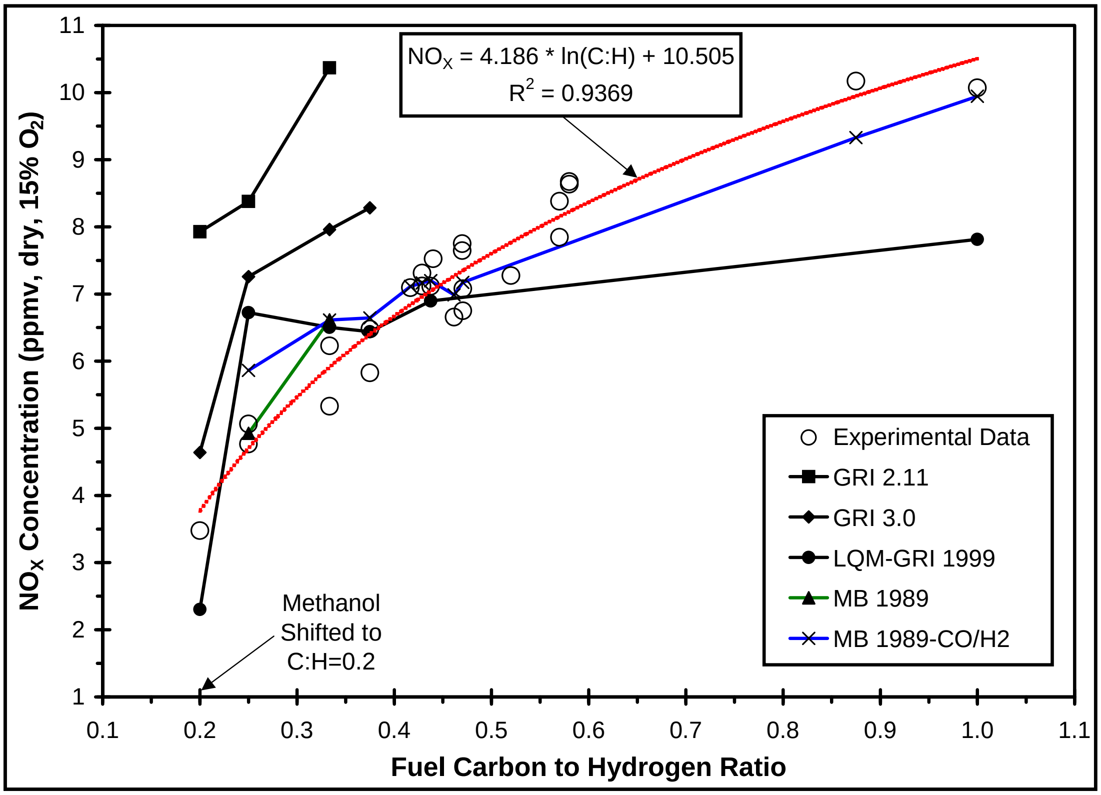

Figure 6.2. Single PSR (T = 1790 K, τ = 2.3 ms, T_{inlet} = 623 K) NO$_X$ Modeling with Various Mechanisms. The Methanol C:H Ratio is Shifted to 0.2 for Differentiation from Methane (C:H=0.25).

6.3.2 DUAL PSR MODEL

The goal of the dual PSR in series model is to address the existence of the two zones in the JSR and to understand the importance of prompt NO_X formation. Steele (1995) and Bengtsson et al. (1998) used such a model to examine NO_X formation in high pressure JSRs. From Figure 2.11, it is clear that stirring with a single, centered jet generates two distinctive zones in the JSR, namely the jet zone and the recirculation zone. The primary flame front is established at the interface of the jet and recirculation zones.

The dual PSR model permits the examination of two zones of free radical activity. The first PSR is used to establish the combustion process and to simulate the flame front where free radical, including the short lived CH radical, concentrations are high. The first PSR is assigned a residence time equal to 5% of the total residence time of the reactor and is assumed to be adiabatic. This 0.115 ms residence time is slightly greater than the PSR blowout residence time for most of the fuels tested. Because of its short lifetime, the CH radical is effectively restricted to the first PSR, and prompt NO_X mainly forms in this zone as shown in Table 6.2. Also shown in Table 6.2 are the NO_X formation rates via each of the major pathways as listed in Section 6.1 for fuels with C:H ratios ranging from 0.25 to 1.0. As can be seen, very little prompt NO is formed for methanol in the first PSR as expected. The rates of prompt NO formation in the first PSR is approximately 30 ppmv/ms for all of the other fuels tested. On the other hand, the rates of NO formation via the nitrous oxide and NNH pathways increase with increasing fuel C:H ratio. In the first PSR, the dominant mechanisms are prompt NO and the NNH mechanism.

The second PSR continues the combustion process and is used to simulate the post flame (or recirculation) zone and accounts for the remaining 95% of the reactor residence time. The second PSR is assigned the JSR combustion temperature of 1790 K. The second PSR simulates the reduced levels of free radical activity with emphasis on the O, H and OH radicals. As shown in Table 6.2, due to the depletion of the short-lived CH free radical, prompt NO formation is essentially null. And as expected, the Zeldovich and nitrous oxide NO, which depend on the attack of N_2 by O, H and OH radicals, are important in the second PSR and their rates increase with increasing fuel C:H ratio. It is important to note that NO formation rates via the NNH mechanism are comparable in trend and absolute value to those of the Zeldovich and nitrous oxide rates. In general, the amount of NO formed in the two zones are nearly identical, with prompt and NNH being the main contributors in the first PSR and Zeldovich, nitrous and NNH being the contributors in the second zone.

In order to simulate the effects of chemical reaction inside the sampling probe, a PFR is add to the dual PSR model. The addition of the PFR allows the hot inlet tip of the probe to be treated. In the tip, free radical concentrations decay and CO continues to burn out. The PFR is assigned a temperature of 1790 K and a residence time of 0.075 ms (corresponding to a probe length of)as obtained from simple one-dimensional gas dynamic calculations of the probe.

As shown in Figure 6.3, dual PSR NO_X modeling with various mechanisms indicates the following:

- Predicted NO_X levels via the GRI 3.0 mechanism closely match those of the experimental values for ethane and propane. On the other hand, values for methanol is under predicted by 29% and values for methane is over predicted by 29%. In fact, the predicted NO_X yield decreases by 13% by switching the fuel from methane to ethane. This is counter to the experimental finding. Referring to Table 6.2, it can be seen that the rates of prompt and NNH NO formation for methane are both over 30% higher that those of ethane. This is counter to the fact that methane is a much more difficult fuel to oxidize and burn and leads to concerns with the methane oxidation chemistry in the GRI

3.0 mechanism. As for the addition of the PFR, it has negligible effect on NO_X yield as expected.

- The GRI 2.11 mechanism shows similar trends as the GRI 3.0 mechanism and over predicts the experimental values for methanol and methane.
- The MB 1989 mechanism with methane, ethane and CO/H_2 fuels under predicts the experimental values, but provides correct trends. The increase in the predicted NO_X yield from methane to ethane is 24%.
- The LQM-GRI 1999 mechanism not only under predicts the experimental values, but also shows trends that are of concern. Peak NO_X is predicted for methane, followed by nearly flat behavior for the other fuels. The mechanism does not replicate the consistent increase in NO_X with increasing C:H ratio seen the in the experimental results.
- Lower predictions of NO_X are obtained with the dual PSR modeling compared to the single PSR modeling. This tendency is noted for all mechanisms and is caused by a reduction in free radical concentration in the second PSR compared to the free radical concentration of the single PSR model.

CO results for dual PSR modeling with various mechanisms are shown in Figure 6.4 and are described as follows:

- In general, the predicted CO yield is higher than the experimental values as expected since the dual PSR model does not account for CO relaxation in the sampling probe. By adding a small PFR element, CO matching is obtained for methanol and methane data via the GRI 3.0 mechanism.

- The predicted CO increases with increasing fuel C:H ratio for fuels with C:H ratio of 0.33 (i.e., ethane) and above. This is in agreement with the experimental trends.

- All mechanisms predict an increase in CO yield by switching the fuel from methane to ethane. This is not observed in the experimental results where there is a slight decrease of about 11%. The drop in the measured CO yield for ethane (or more appropriately the higher CO yield for methane) is expected since methane is a more difficult fuel to oxidize and burn. As shown in Figure 6.5, the rate of fuel oxidation and reaction is seen to correlate with the rate of increase in measured flame temperature. Methane, being the slowest burning fuel, has the slowest rise in flame temperature in the jet zone. Propane, being the largest fuel molecule of the three fuels, is less stable and is more easily oxidized in the jet zone. The propane temperature profile shows the quickest rise in flame temperature. Ethane being the intermediate fuel does show flame temperature behavior that is between that of methane and propane. The corresponding measured NO_X and CO profiles are shown in Figure 6.6. As can be seen, both ethane and propane show highest CO yield on centerline due to their rapid breakup and oxidation under jet zone conditions. On the other hand, CO for methane does not peak until the jet mixes further with the recirculation zone gases, confirming the fact that methane is a slower burning fuel. The delayed formation of CO for methane and the rapid production of CO for ethane and propane lead to the experimental finding that CO emission as measured at the standard sampling location ($r/R_0 = 0.71$) is higher for the slower burning methane fuel since the CO does not have as much opportunity to oxidize.

Table 6.2. Rates of NO_X Formation through Various Pathways for the Dual PSR Model using GRI 3.0 Mechanism. Total Residence Time = 2.3 ms, Temperature Assignment: 1st Zone = Adiabatic and 2nd Zone = 1790 K, Inlet Temperature = 623 K.

First PSR (5% of Total Residence Time)

Fuel	***Temp. (K)***	***Prompt (ppm/ms)***	***Zeldovich (ppm/ms)***	***Nitrous (ppm/ms)***	***NNH (ppm/ms)***	***Total Rate (ppm/ms)***	***Total (ppm)***
Methanol	1659	1.9	0.3	1.0	4.2	7.3	0.8
Methane	1698	36.6	1.0	1.6	24.5	63.6	7.3
Ethane	1678	26.6	0.7	1.6	16.1	45.0	5.2
Ethylene	1650	25.4	0.8	2.3	40.0	68.6	7.9
Acetylene	1604	28.9	0.6	3.6	67.4	100.5	11.6

Second PSR (95% of Total Residence Time)

Fuel	***Temp. (K)***	***Prompt (ppm/ms)***	***Zeldovich (ppm/ms)***	***Nitrous (ppm/ms)***	***NNH (ppm/ms)***	***Total Rate (ppm/ms)***	***Total (ppm)***
Methanol	1790	0.0	0.5	0.7	0.3	1.6	3.4
Methane	1790	0.0	0.6	0.9	0.4	2.0	4.3
Ethane	1790	0.0	0.8	1.0	0.5	2.2	4.9
Ethylene	1790	0.0	1.0	1.3	0.8	3.2	6.9
Acetylene	1790	0.0	1.8	2.3	1.7	5.8	12.6

Total Predicted

Fuel	***Total (ppm)***	***Total (ppmv, 15% O_2)***
Methanol	4.3	2.2
Methane	11.8	5.7
Ethane	10.2	5.0
Ethylene	15.0	8.0
Acetylene	24.3	14.7

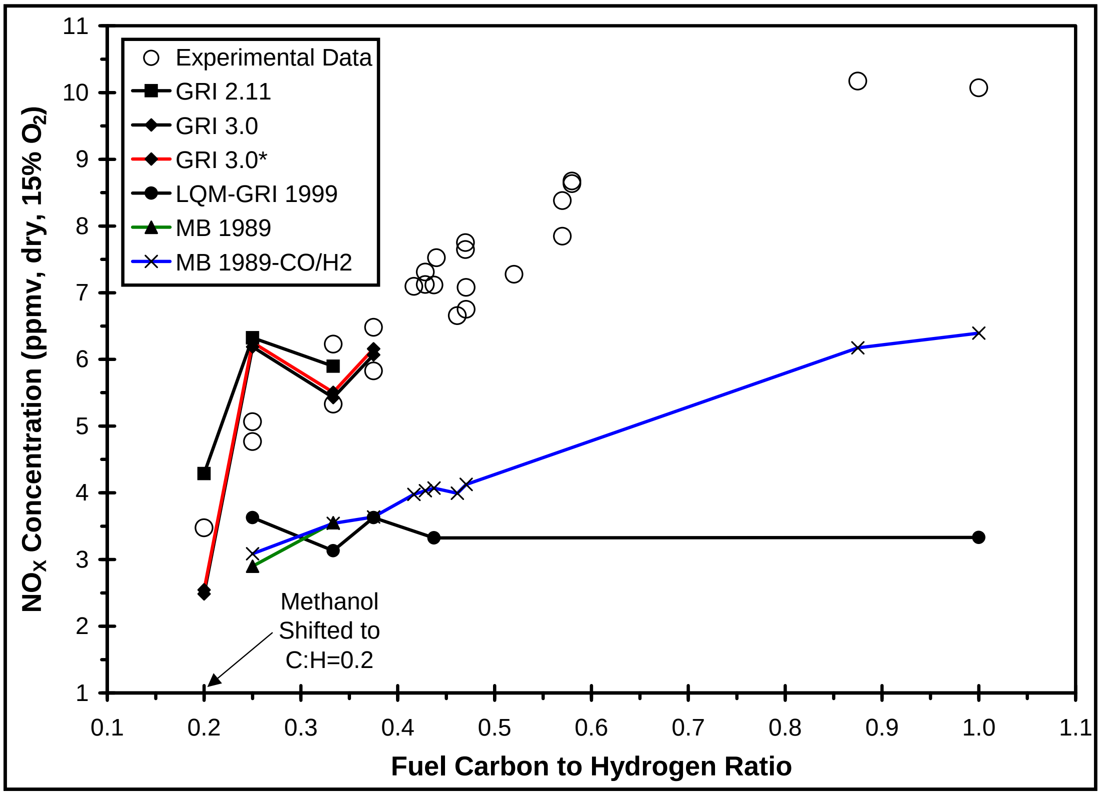

Figure 6.3. Two PSRs in Series NO_X Modeling with Various Mechanisms. The Methanol C:H Ratio is Shifted to 0.2 for Differentiation from Methane (C:H=0.25). The Dual PSR with the Addition of a Short PFR is indicated by GRI 3.0*.

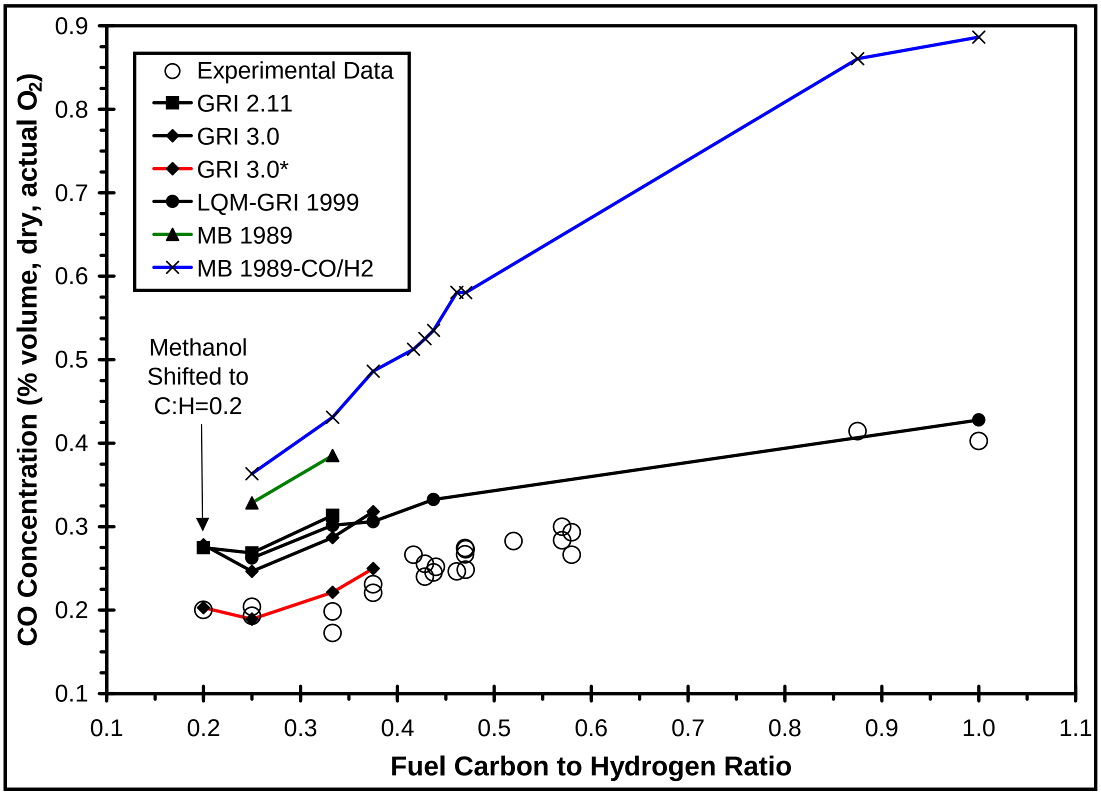

Figure 6.4. Two PSRs in Series CO Modeling with Various Mechanisms. The Methanol C:H Ratio is Shifted to 0.2 for Differentiation from Methane (C:H=0.25). The Dual PSR with the Addition of a Short PFR is indicated by GRI 3.0*.

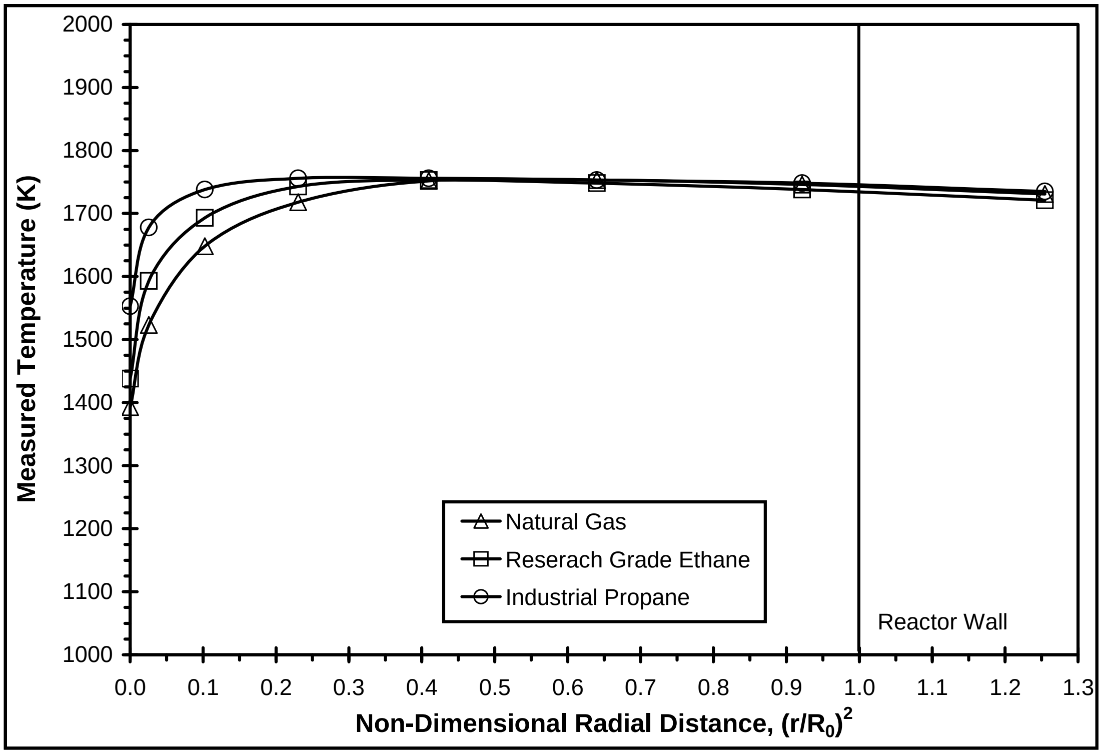

Figure 6.5. Temperature Profiles for Combustion of Natural Gas, Research Grade Ethane and Industrial Propane with Air. JSR Combustion Temperature = 1790 K, 2nd Stage Inlet Temperature = 623 K, Nominal Reactor Residence Time = 2.3 ms.

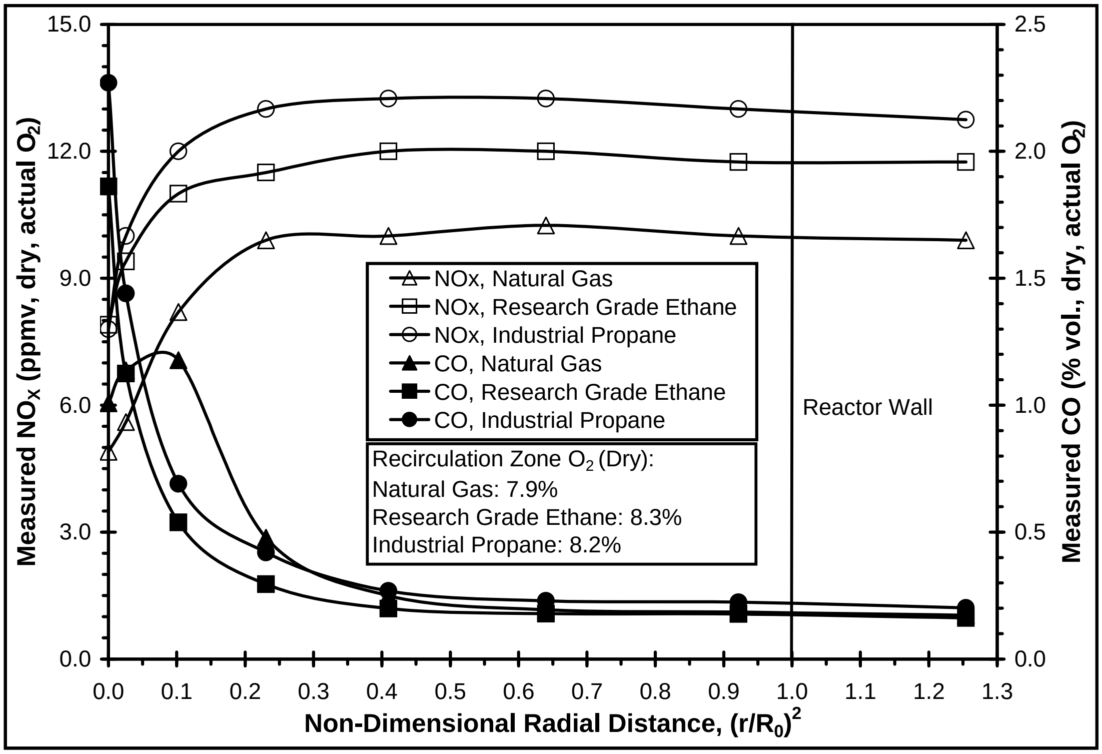

Figure 6.6. NO_X and CO Profiles for Combustion of Natural Gas, Research Grade Ethane and Industrial Propane with Air. JSR Combustion Temperature = 1790 K, 2nd Stage Inlet Temperature = 623 K, Nominal Reactor Residence Time = 2.3 ms.

6.3.3 THREE PSR MODEL

The three PSRs in series model assumes that combustion in the JSR can be divided into the following three zones:

- Flame front – assigned the adiabatic blowout condition, a region high in hydrocarbon radicals. Prompt NO and NO from the NNH mechanism occur primarily in this zone.

- Immediate post flame zone – assigned 10% of the total residence time, which is approximately the jet eddy turnover time. This zone is assigned the temperature of 1790 K. The production of NO_X mainly occurs via the Zeldovich and nitrous oxide mechanisms.

- Post flame recirculation zone – balance of the total residence time of 2.3 ms with an assigned temperature of 1790 K. This last PSR produces NO_X mainly through the Zeldovich and nitrous oxide mechanisms, but the amount is curtailed since the free radical concentrations are reduced by the introduction of the intermediate or second PSR and the relatively long τ of the third PSR.

The three PSR NO_X and CO modeling results are presented in Figures 6.7 and 6.8, respectively. With the three PSR model, the predicted NO_X yield from the GRI 3.0 mechanism closely matches the experimental values with a slightly under prediction for methanol and a slight over prediction for methane as can be seen in Figure 6.7. The trend in NO_X increase from methane to ethane is also confirmed with the three PSR modeling using the GRI 2.11 mechanism in contrast to the dual PSR modeling where predicted NO_X yield decreases from methane to ethane. Three PSR modeling yields slightly higher NO_X values using the MB 1989 mechanism than with the dual PSR model. The MB 1989 trends for methane, ethane and CO/H_2 (of increasing NO_X with increasing C:H ratio) are consistent with experimental data. The LQM-GRI

1999 mechanism provides a “flat” result for NO_X. The mechanism does not simulate the increase of NO_X with increasing C:H ratio.

The predicted CO yield is significantly reduced with the three PSR model as shown in Figure 6.8. CO matching is obtained for ethane and propane with the use of the GRI 3.0 mechanism without the use of any PFR element. The predicted CO trend from methane to ethane still does not provide satisfactory comparison to experimental values. Nevertheless, the three PSR model provides overall CO trend that emphasizes the effect of fuel C:H ratio. Namely, CO increases with increasing fuel C:H ratio as measured experimentally with the exception of methanol and methane.

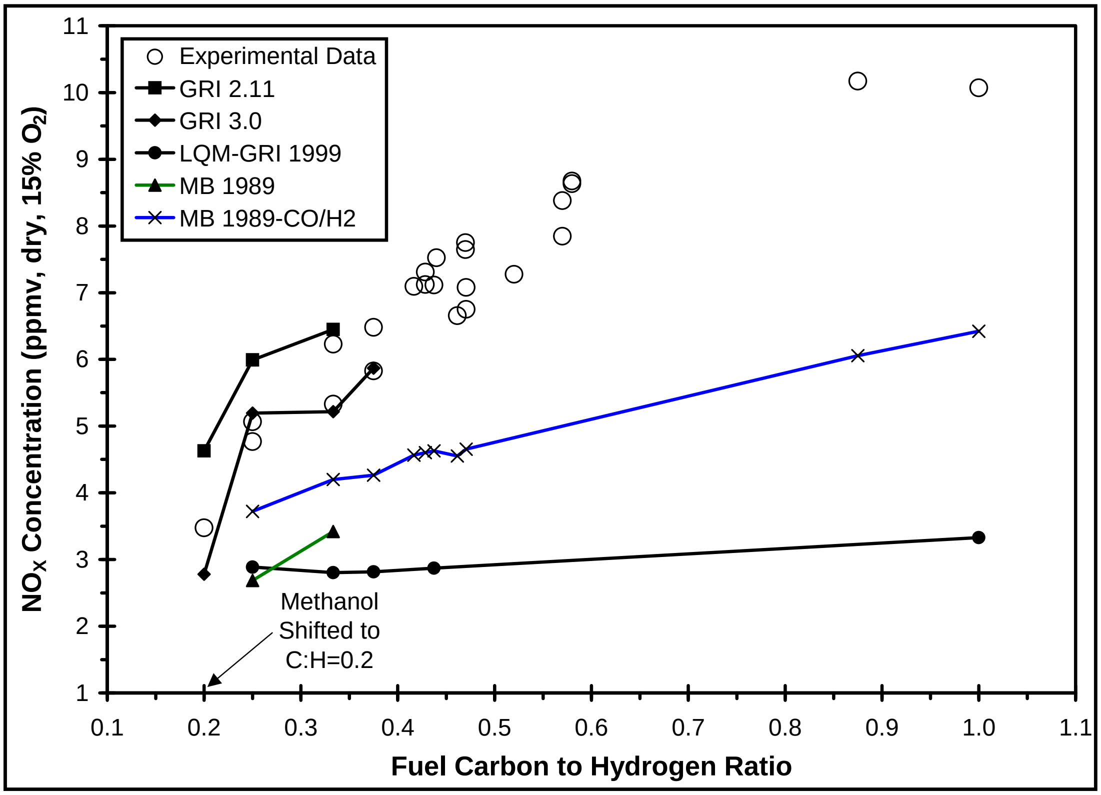

Figure 6.7. Three PSRs in Series NO$_X$ Modeling with Various Full Mechanisms. The Methanol C:H Ratio is Shifted to 0.2 for Differentiation from Methane (C:H=0.25).

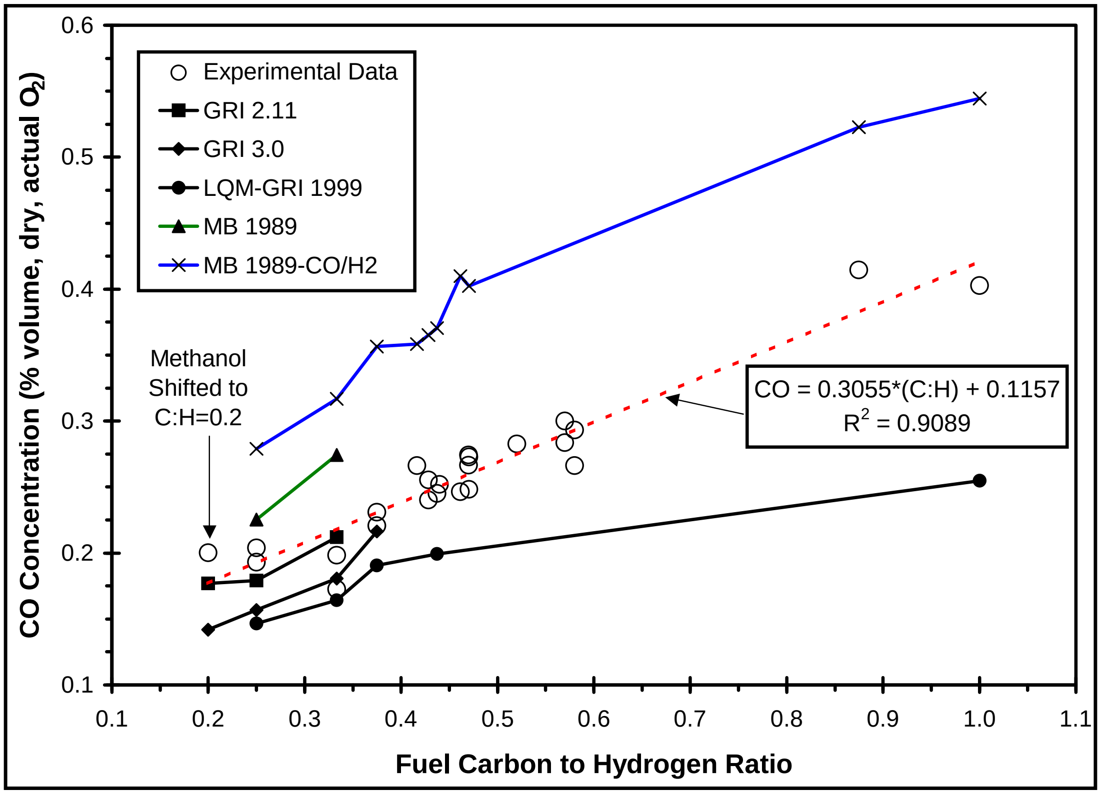

Figure 6.8. Three PSRs in Series CO Modeling with Various Full Mechanisms. The Methanol C:H Ratio is Shifted to 0.2 for Differentiation from Methane (C:H=0.25).

6.4 SUMMARY

Modeling of the JSR with CRMs provides simple and quick information on the overall behavior of fuel oxidation and pollutant formation. At the same time, chemical reactor modeling provides many challenges. In particular, accuracies in the kinetic rate constants for both fuel oxidation and pollutant formation must be improved. The choice and selection of reactor network arrangement must also be significantly enhanced with the aid of more complex computational fluid dynamic models if the combustor to be modeled is not a "true" PSR. Nevertheless, chemical reactor modeling provides great insight to the various NO_X formation pathways. Valuable information on the behavioral trends of the various fuels tested can also be obtained. The following summarizes the CRM results:

- Even under LP and LPP combustion conditions, NO_X production via the prompt, Zeldovich, nitrous oxide and NNH pathways are all important. The key is in identifying the region(s) where each NO_X formation pathways is critical.

- NO_X and CO yields increase with increasing fuel C:H ratio with the exception of methanol and methane.

- The three PSR model in conjunction with the GRI 3.0 mechanism provides the closest prediction to the experimental results for light hydrocarbons for which the mechanism was developed.

- The single PSR model in conjunction with the MB 1989-CO/H_2 mechanism provides good prediction for hydrocarbons in the C:H range of 0.375 (propane) to 1.0 (benzene).

- The single PSR model in conjunction with the LQM-GRI 1999 mechanism provides close prediction for propane and heptane and its use may be limited to these two fuels since the LQM oxidation chemistry was developed for heptane.

- The quality of the CRM predictions can be “fine-tuned” to match experimental results. Physical reasoning and conditions most be used to make sense of CRM results.

CHAPTER 7: CONCLUSIONS AND RECOMMENDATIONS

7.1 CONCLUSIONS

Three generations of prevaporizing-premixing injectors have been tested. The experiences gained through the extensive testing of the 1st and 2nd generation injectors have led to the development of the current 3rd generation, staged prevaporizing-premixing injector. Initial testing of the SPP indicates that it has a high potential for suggesting techniques that will enable the optimized reduction of NO_X emission for practical LP and LPP combustion processes.

The use of different reactor injection patterns (e.g., a single centered jet versus an 8-hole diverging jet) leads to significant differences in the reactor temperature fields due to the enhanced entrainment characteristics of the small jets used in the diverging jets nozzle. Additionally, differences in flow field lead to altered reactor wall heat transfer conditions. However, it is important to note that modifications in the reactor injection pattern have no apparent effect on the overall trend in NO_X emission as a function of fuel type.

Effects of airflow split and, thus, jet mixing in the SPP on premixing the fuel and air mixture and on NO_X emission have been quantified. Use of a simple laser absorption technique indicates that optimum mixing is achieved with a 30 slpm/30 slpm airflow split leading to minimum NO_X formation in the SPP-JSR configuration.

The NO_X emission is essentially independent of SPP injector length if the degree of premixing is high. As for the effect of inlet temperature, it appears that the NO_X emission for methane-air combustion has a slightly negative dependency on inlet temperature from 423 to 723 K depending on the degree of premixing.

The NO_X yield is most sensitive to fuel type for light hydrocarbons, aromatic hydrocarbons and methanol. Methanol exhibits the lowest NO_X emission level among all fuels tested since it does not produce prompt NO_X. Among the pure fuels tested, benzene and toluene exhibit the highest levels of NO_X emission.

For fuels containing small amounts of FBN (< 130 ppm by weight), the FBN is completely converted to fuel NO_X under LPP combustion conditions.

The NO_X emissions increase linearly with increasing fuel C:H ratio for hydrocarbon fuels with C:H ratio from 0.25 to 0.63. There exists a "leveling-off" for fuels with higher C:H ratio (i.e., toluene and benzene).

The CO formation increases linearly with increasing fuel C:H ratio for most hydrocarbon fuels with the exception of methanol and light gaseous hydrocarbon fuels, such as methane and ethane.

A near linear relationship exists between NO_X and CO for most hydrocarbon fuels tested with the exception of methanol and aromatic hydrocarbons.

In general, chemical reactor modeling confirms the experimental NO_X and CO trends. The choice of reactor network arrangement has significant effect on the overall yield in pollutant formation. The prompt, Zeldovich, nitrous oxide and NNH pathways are all important contributors to NO_X formation chemistry. The three PSR model in conjunction with GRI 3.0 mechanism provides the best agreement of the modeled NO_X to the measured NO_X.

7.2 RECOMMENDATIONS

In order to validate the viability of the SPP technology under practical LPP combustion conditions, additional research is required. This is listed as follows:

- Since the SPP concept requires the use of a secondary air source, a detailed cycle feasibility analysis must be undertaken. Incorporating the SPP design into a combined cycle should be considered. One possibility is to use the steam turbine discharge to partially cool the compressor discharge air that will be used in the first stage. This can be done most likely in a high efficiency regenerator. The loss of compressor efficiency may be overcome by recycling the regenerator steam discharge back into the steam turbine and, thus, increasing the steam turbine output. Regardless, a complete and detailed cycle analysis is required.

- The concept and design of the SPP address and alleviate the issues regarding the short autoignition delay time (< 1 ms) for gas turbines combustors operating at pressures of 30 atm and above. Testing of the SPP prototype or a close variant under high pressure (e.g., 30 to 40 atm) conditions will be required to validate the staging design philosophy.

- CFD analysis of the SPP-JSR arrangement is required. Detailed flow analysis of the SPP is required to validate the possibility of flow stratification as indicated by the 40 slpm/20 slpm cases. With respect to the JSR, detailed flow analysis of the jet entrainment and mixing effects with the use of CFD models are necessary in order to improve the accuracies in CRM flow element selection and arrangement.

- Upon completion of the above three recommended tasks, a redesign of the SPP is necessary to reduce the pressure drop across the injector to levels used in practical GT systems. The jet mixing technique with its associated requirement of high pressure drop will most likely be replaced by the use of swirl vanes and other lower pressure loss mixing devices.

BIBLIOGRAPHY

ABB Power Generation Ltd. (1998), *ABB Review: GTX100 – A New High-Performance Gas Turbine*, ABB Power Generation Ltd., Baden, Switzerland.

Advanced Gas Turbine Systems Research (1998), "Request for Proposals," RFP No. AGTSR 98-01, South Carolina Energy Research and Development Center, Clemson, SC.

Advanced Gas Turbine Systems Research (1999), "Request for Proposals," RFP No. AGTSR 99-01, South Carolina Energy Research and Development Center, Clemson, SC.

Aigner, M. and Muller, G. (1992), "Second-Generation Low Emission Combustors for ABB Gas Turbines: Field Measurements with GT11N-EV," ASME Paper No. 92-GT-322 presented at the International Gas Turbine and Aeroengine Congress & Exhibition, Cologne, Germany.

Ainslie, N.G., Morelock, C.R. and Turnbull, D. (1962), "Devitrification Kinetics of Fused Silica," *Symposium on Nucleation and Crystallization in Glasses and Melts*, pp. 97 – 107.

Andhrapradesh Industries, Ltd. (1998), http://www.andhrapradesh.com/busnhouse/private.html.

Beér, J.M. and Chigier, N.A. (1983), *Combustion Aerodynamics*, Krieger, Malabar, FL.

Bengtsson, K.U.M., Benz, P., Schären, R. and Frouzakis, C.E. (1998), "N_YO_X Formation in Lean Premixed Combustion of Methane in a High-Pressure Jet-Stirred

Reactor," Paper presented at the *Twenty-Seventh Symposium (International) on Combustion*, Boulder, CO.

Blust, J.W., Ballal, D.R. and Sturgess, G.J. (1997), "Emissions Characteristics of Liquid Hydrocarbons in a Well Stirred Reactor," AIAA Paper No. 97-2710 presented at the 33rd AIAA/ASME/ SAE/ASEE Joint Propulsion Conference & Exhibit, Seattle, WA.

Bozzelli, J.W., Chang, A.Y. and Dean, A.M. (1994), "Analysis of the Reactions H + N_2O and NH + NO: Pathways and Rate Constants over a Wide Range of Temperature and Pressure," *Twenty-Fifth Symposium (International) on Combustion*, pp. 965 – 979, The Combustion Institute, Pittsburgh, PA.

Bowman, C.T. (1991), "Chemistry of Gaseous Pollutant Formation and Destruction," *Fossil Fuel Combustion: A Source Book*, pp. 215 – 260, Wiley, New York, NY.

Brushwood, J. and McElwee, T. (1997), "Design Considerations for Naphtha Fuel Systems in Combustion Turbines," ASME Paper No. 97-GT-37 presented at the International Gas Turbine and Aeroengine Congress & Exhibition, Orlando, FL.

Burton, K.A., Ladouceur, H.D. and Fleming, J.W. (1992), "An Improved Noncatalytic Coating for Thermocouples," *Combustion Science and Technology*, Vol. 81, pp. 141 – 145.

Capehart, S.A. (1995), "NO_X Formation in Lean-Premixed Combustion of Liquid Hydrocarbons, " M.S. Thesis, University of Washington, Seattle, WA.

Capehart, S.A., Lee, J.C.Y., Williams, J.T. and Malte, P.C. (1997), "Effect of Fuel Composition on NO_X Formation in Lean Premixed Prevaporized Combustion," ASME Paper No. 97-GT-336 presented at the International Gas Turbine and Aeroengine Congress & Exhibition, Orlando, FL.

Cowell, L.H., Rajput, A. and Rawlins, D.C. (1996), "Development of a Dual-Fuel Injection System for Lean Premixed Industrial Gas Turbines," ASME Paper No. 96-GT-195 presented at the International Gas Turbine and Aeroengine Congress & Exhibition, Birmingham, UK.

Davis, L.B. (1996), "Dry Low NO_X Combustion Systems for GE Heavy-Duty Gas Turbines," ASME Paper No. 96-GT-27 presented at the International Gas Turbine and Aeroengine Congress & Exhibition, Birmingham, U.K.

Dibble, R.W. (1999), Personal Communication, University of California, Berkeley, CA.

Dutta, P., Cowell, L.H., Yee, D.K. and Dalla Betta, R.A. (1997), "Design and Evaluation of a Single –Can Full Scale Catalytic Combustion System for Ultra-Low Emissions Industrial Gas Turbines," ASME Paper No. 97-GT-292 presented at the International Gas Turbine and Aeroengine Congress & Exhibition, Orlando, FL.

Foglesong, R.E., Frazier, T.R., Flamand, L.M., Peters, J.E. and Lucht, R.P. (1999), "Flame Structure and Emissions Characteristics of a Lean Premixed Gas Turbine Combustor," AIAA Paper No. 99-2399 presented at the 35th AIAA/ASME/SAE/ASEE Joint Propulsion Conference and Exhibit, Los Angles, CA.

Gas Research Institute (1995), *GRI Mechanism 2.11*, http://www.gri.org.

Gas Research Institute (1999), *GRI Mechanism 3.0*, http://www.gri.org.

Halthore, R.N. and Gouldin, F.C. (1986), "Laser Scattering Measurements for Gas Densities in a Swirling Flow Combustor," *AIAA Journal*, Vol. 24, pp. 1129 – 1136.

Harrington, J.E., Smith, G.P., Berg, P.A., Noble, A.R., Jeffries, J.B. and Crosley, D.R. (1996), "Evidence for a New NO Production Mechanism in Flames." *Twenty-*

Sixth Symposium (International) on Combustion, pp. 2133 – 2138, The Combustion Institute, Pittsburgh, PA.

Janus, M.C., Richards, G.A., Yip, M.J. and Robey, E.H. (1997), "Effects of Ambient Conditions and Fuel Composition on Combustion Stability," ASME Paper No. 97-GT-266 presented at the International Gas Turbine and Aeroengine Congress & Exhibition, Orlando, FL.

Joshi, N.D., Epstein, M.J., Durlak, S., Marakovits, S. and Sabla, P.E. (1994), "Development of a Fuel Air Premixer for Aeroderivative Dry Low Emissions Combustors," ASME Paper No. 94-GT-253 presented at the International Gas Turbine and Aeroengine Congress & Exhibition, The Hague, Netherlands.

Kanury, A.M. (1975), *Introduction to Combustion Phenomena*, Gordon & Breach, New York, NY.

Keller, J.J. (1995), "Thermoacoustic Oscillations in Combustion Chambers of Gas Turbines," *AIAA Journal*, Vol. 33, No. 12, pp. 2280 – 2287.

Krämer, H., Dinkelacker, F., Leipertz, A., Poeschl, G., Huth, M. and Lenze, M. (1999), "Optimization of the Mixing Quality of a Real Size Gas Turbine Burner with Time-Resolved Planar Laser Techniques," ASME Paper No. 99-GT-135 presented at the International Gas Turbine and Aeroengine Congress & Exhibition, Indianapolis, IN.

Kramlich, J.C. and Malte, P.C. (1978), "Modeling and Measurement of Sample Probe Effects on Pollutant Gases Drawn From Flame Zones," *Combustion Science and Technology*, Vol. 18, pp. 91 – 102.

Lee, J.C.Y. and Malte, P.C. (1999a), "Combustion Characteristics of Naphtha under Lean Prevaporized and Premixed Conditions," Final Report submitted to Solar Turbines Incorporated, San Diego, CA.

Lee, J.C.Y. and Malte, P.C. (1999b), "Staged Prevaporizer-Premixer," U.S. Patent Application No. 09/276,251, March 25, 1999.

Lee, J.C.Y., Malte, P.C. and Nicol, D.G. (1999), "NO_X as a Function of Fuel Type: C_1 – to – C_{16} Hydrocarbons and Methanol," ASME Paper No. 99-GT-270 presented at the International Gas Turbine and Aeroengine Congress & Exhibition, Indianapolis, IN.

Lefebvre, A.H. (1983), *Gas Turbine Combustion*, Taylor & Francis, Bristol, PA.

Lefebvre, A.H. (1989), *Atomization and Sprays*, Taylor & Francis, Bristol, PA.

Leonard, G. and Stegmaier, J. (1993), "Development of an Aeroderivative Gas Turbine Dry Low Emissions Combustion System," ASME Paper No. 93-GT-288 presented at the International Gas Turbine and Aeroengine Congress & Exhibition, Cincinnati, OH.

Lipinski, J.J., Brine, P.R., Buch, R.D. and Lester, G.R. (1998), "Development and Test of a Catalytic Combustor for an Automotive Gas Turbine," ASME Paper No. 98-GT-390 presented at the International Gas Turbine and Aeroengine Congress & Exhibition, Stockholm, Sweden.

Lisseveld, W. (1997), Personal Communication, Enviro Response Products, Inc., Fort Myers Beach, FL.

Longwell, J.P. and Weiss, M.A. (1955), "High Temperature Reaction Rates in Hydrocarbon Combustion," *Industrial and Engineering Chemistry*, Vol. 47, No. 8, pp. 1634 – 1643.

Malte, P.C. and Pratt, D.P. (1974), "The Role of Energy-Releasing Kinetics in NOX Formation: Fuel-Lean, Jet-Stirred CO-Air Combustion," *Combustion Science and Technology*, Vol. 9, pp. 221 – 231.

Malte, P.C. and Kramlich, J.C. (1980), “Further Observations of the Effect of Sample Probe on Pollutant Gases Drawn From Flame Zones,” *Combustion Science and Technology*, Vol. 22, pp. 263 – 269.

Maurice, L.Q., Blust, J.W., Leung, K.M. and Lindstedt, R.P. (1999), “Emissions from Combustion of Hydrocarbons in a Well-Stirred Reactor,” AIAA Paper No. 99-1038, presented at the 35th AIAA/ASME/ SAE/ASEE Joint Propulsion Conference & Exhibit, Reno, NV.

McMahon, J., Troup G.J. and Hubbert, G. (1972), “The Effect of Pressure and Temperature on the Half-Width of the Methane Absorption at 3.39 μm,” *Journal of Quantitative Spectroscopy and Radiative Transfer*, Vol. 12, pp. 797 – 805.

Miller, J.A. and Bowman, C.T. (1989), “Mechanism and Modeling of Nitrogen Chemistry in Combustion,” *Progress in Energy and Combustion Science*, Vol. 15, pp. 287 – 338.

Molière, M., Geiger, F., Deramond, E. and Becker, T. (1998), “Volatile, Low Lubricity Fuels in Gas Turbine Plants: A Review of Main Fuel Options and Their Respective Merits,” ASME Paper No. 98-GT-231 presented at the International Gas Turbine and Aeroengine Congress & Exhibition, Stockholm, Sweden.

Mongia, R.K. (1998), “Optical Probe for Measuring the Extent of Air and Fuel Mixing in Lean Premixed Combustors and the Effect of Air and Fuel Mixing on Combustor Performance,” Ph.D. Dissertation, University of California-Berkeley, Berkeley, CA.

Myerson, A.L. (1975), “The Reduction of Nitric Oxide in Simulated Combustion Effluents by Hydrocarbon-Oxygen Mixtures,“ *Fifteenth Symposium (International) on Combustion,* pp. 1085 – 1092, The Combustion Institute, Pittsburgh, PA.

Narula, R.G. (1998), “Alternative Fuels for Gas Turbine Plants – An Engineering Procurement, and Construction Contractor’s Perspective,” ASME Paper No. 98-GT-122 presented at the International Gas Turbine and Aeroengine Congress & Exhibition, Stockholm, Sweden.

Nicol, D.G. (1995), “A Chemical Kinetic and Numerical Study of NO_X and Pollutant Formation in Low-Emission Combustion,” Ph.D. Dissertation, University of Washington, Seattle, WA.

Nicol, D. G., Rutar, T., Martin, S. M., Malte, P. C. and Pratt, D. T. (1997) "Chemical Reactor Modeling Applied to the Prediction of Pollutant Emissions from an LP Combustor," presented at the 33rd AIAA/ASME/SAE/ASEE Joint Propulsion Conference and Exhibit, Seattle, WA.

Odgers, J. and Kretschmer, D. (1986), *Gas Turbine Fuels and Their Influence on Combustion*, Abacus Press, Cambridge, MA.

Ozawa, Y., Tochihara, Y., Mori, N., Yuri, I., Kanazawa, T. and Sagimori, K. (1998), “High Pressure Test Results of a Catalytically Assisted Ceramic Combustor for a Gas Turbine,” ASME Paper No. 98-GT-381 presented at the International Gas Turbine and Aeroengine Congress & Exhibition, Stockholm, Sweden.

Perrin, M.Y. and Hartmann, J.M. (1989), “High Temperature Absorption of the 3.39 μm He-Ne Laser Line by Methane,” *Journal of Quantitative Spectroscopy and Radiative Transfer*, Vol. 42, No. 6, pp. 459 – 464.

Pratt, D.T. (1977), “Calculation of Chemically Reactive Flows with Complex Chemistry,” *Studies in Convection, Vol. 2*, B.E. Launder, Editor, Academic Press, London.

Pratt, D.T. and Wormeck, J.D. (1976), “CREK, A Computer Program for Calculation of Combustion Reaction Equilibrium and Kinetics in Laminar and Turbulent Reacting

Flows," Report No. TEL-76-1, Department of Mechanical Engineering, Washington Stage University, Pullman, WA.

Radhakrishnan, K and Pratt, D.T. (1988), "Fast algorithm for Calculating Chemical Kinetics in Turbulent Reacting Flows," *Combustion Science and Technology*, Vol. 58, pp. 155 – 176.

Rawlins, D.C. (1995), "SoLoNO$_X$ Combustion System Update," Turbomachinery Technology Seminar, Solar Turbines Incorporated, San Diego, CA.

Rutar, T. (2000), "NO$_X$ and CO Formation in Lean Premixed Methane-Air Combustion in a Jet-Stirred Reactors Operated at Elevated Pressure," Ph.D. Dissertation, University of Washington, Seattle, WA.

Rutar, T., Martin, S.M., Nicol, D.G., Malte, P.C. and Pratt, D.T. (1997), "Effects of Incomplete Premixing on NO$_X$ Formation at Temperature and Pressure Conditions of LP Combustion Turbines," ASME Paper No. 97-GT-335 presented at the International Gas Turbine and Aeroengine Congress & Exhibition, Orlando, FL.

Rutar, T., Horning, D.C., Lee, J.C.Y. and Malte, P.C. (1998), "NO$_X$ Dependency on Residence Time and Inlet Temperature for Lean-Premixed Combustion in Jet-Stirred Reactors," ASME Paper No. 98-GT-433 presented at the International Gas Turbine and Aeroengine Congress & Exhibition, Stockholm, Sweden.

Sample, K. (1999), Personal Communication, Trius Engineering, Durant, OK.

Sarofim, A.F., Williams, G.C., Modell, M. and Slater, S.M. (1975), "Conversion of Fuel Nitrogen to Nitric Oxide in Premixed and Diffusion Flames," *AIChE Symposium Series*, Vol. 71, No. 148, pp. 51 – 61.

Sattlemayer, T., Felchlin, M.P., Haumann, J., Hellat, J. and Styner, D. (1992), "Second-Generation Low-Emission Combustors for ABB Gas Turbines: Burner

Development and Tests at Atmospheric Pressure," *ASME Journal of Engineering for Gas Turbines and Power*, Vol. 114, pp. 11 – 126.

Schlatter, J.C., Dalla Betta, R.A., Nickolas, S.G., Cutrone, M.B., Beebe, K.W. and Tsuchiya, T. (1997), "Single-Digit Emissions in a Full Scale Catalytic Combustor," ASME Paper No. 97-GT-57 presented at the International Gas Turbine and Aeroengine Congress & Exhibition, Orlando, FL.

Shih, H.H. (1997), Personal Communication, Taiwan Power Company, Tunghsiao Power Station, Miaoli, Taiwan.

Singh, S, Grosshandler, W., Malte, P.C. and Crain, R.W. Jr. (1978) "Oxides of Nitrogen Formed in High-Intensity Methanol Combustion," *Seventeenth Symposium (International) on Combustion*, pp. 689 – 699, The Combustion Institute, Pittsburgh, PA.

Snyder, T.S., Rosfjord, T.J., McVey, J.B., Hu, A.S. and Schlein, B.C. (1996), "Emission and Performance of a Lean-Premixed Gas Fuel Injection System for Aeroderivative Gas Turbine Engines," *ASME Journal of Engineering for Gas Turbines and Power*, Vol. 118, pp. 38 – 45.

Spadaccini, L.J. and TeVelde, J.A. (1982), "Auto-Ignition of Aircraft-Type Fuels," *Combustion and Flame*, Vol. 46, pp. 283 – 300.

Steele, R.C. (1995), "NO_X and N_2O Formation in Lean-Premixed Jet-Stirred Reactors Operated from 1 to 7 atm," Ph.D. Dissertation, University of Washington, Seattle, WA.

Steele, R.C., Malte, P.C., Nicol, D.G. and Kramlich, J.C. (1995), "NO_X and N_2O in Lean-Premixed Jet-Stirred Flames," *Combustion and Flame*, Vol. 100, No. 3, pp.440 – 449.

Steele, R.C., Jarrett, A.C., Malte, P.C., Tonouchi, J.H. and Nicol, D.G. (1997), “Variables Affecting NO_X Formation in Lean-Premixed Combustion,” *ASME Journal of Engineering for Gas Turbines and Power*, Vol. 119, pp. 102 – 107.

Steele, R.C., Tonouchi, J.H., Nicol, D.G., Horning, D.C., Malte, P.C. and Pratt, D.T. (1998), “Characterization of NO_X, N_2O, and CO for Lean-Premixed Combustion in a High-Pressure Jet-Stirred Reactor,” *ASME Journal of Engineering for Gas Turbines and Power*, Vol. 120, pp. 303 – 310.

Steinbach, C., Ruck, T., Lloyd, J., Jansohn, P., Döbbeling, K., Sattelmayer, T. and Strand, T. (1998), “ABB’s Advanced EV Burner – A Duel Fuel Dry Low NO_X Burner for Stationary Gas Turbines,” ASME Paper No. 98-GT-519 presented at the International Gas Turbine and Aeroengine Congress & Exhibition, Stockholm, Sweden.

Stufflebeam, J.H., Kendrick, D.W., Sowa, W.A. and Snyder, T.S. (1999), “Quantifying Fuel/Air Unmixedness in Premixing Nozzles using an Acetone Fluorescence Technique,” ASME Paper No. 99-GT-399 present at the International Gas Turbine and Aeroengine Congress & Exhibition, Indianapolis, IN.

Thornton, M.M., Malte, P.C. and Crittenden, A.L. (1987), “A Well-Stirred Reactor for the Study of Pyrolysis and Oxidation Kinetics: Carbon Monoxide and n-Pentane Oxidation,” *Combustion Science and Technology*, Vol. 54, pp. 275 – 297.

Thornton, M.M. (1989), “Oxidative Pyrolysis of Furan and Furfural in a Jet-Stirred Reactors,” Ph.D. Dissertation, University of Washington, Seattle, WA.

Tsuboi, T., Inomata, K., Tsunoda, Y., Isobe, A. and Nagaya, K. (1985), “Light Absorption by Hydrocarbon Molecules at 3.392 μm of He-Ne Laser,” *Japanese Journal of Applied Physics*, Vol. 24, No. 1, pp. 8 – 13.

Wang, Y., Reh, L., Pennel, D., Winkler, D. and Döbbeling, K. (1997), "Conversion of Liquid to Gaseous Fuel for Prevaporized Premixed Combustion in Gas Turbines," ASME Paper No. 97-GT-225 presented at the International Gas Turbine and Aeroengine Congress & Exhibition, Orlando, FL.

Watlow Controls (1997), *Series 988 User's Manual*, Watlow Controls, Winona, MN.

Yee, D, Malte, P.C. and Kamber, P.D. (1983), "Mixing in Jet Flames by Laser Rayleigh Scattering," AIAA Paper No. 83-0403 presented at the AIAA 21st Aerospace Sciences Meeting, Reno, NV.

Yoshiyama, S., Hamamoto, Y., Tomita, E. and Minami, K. (1996), "Measurement of Hydrocarbon Fuel Concentration by Means of Infrared Absorption Technique with 3.39 μm He-Ne Laser," *JSAE Review*, Vol. 17, pp. 339 – 345.

Zelina, J. and Ballal, D.R. (1996), "Emissions Studies in a Well-Stirred Reactor and Applications to Combustion Modeling," *Proceeding of FACT, Vol. 21*, ASME International Joint Power Generation Conference, Houston, TX, pp. 255-263.

Zelina, J., Blust, J.W. and Ballal, D.R. (1996), "Combustion of Liquid Fuels in the Well Stirred Reactor," ASME Paper No. 96-GT-47 presented at the International Gas Turbine and Aeroengine Congress, Birmingham, UK.

APPENDIX A: JET-STIRRED REACTOR CONSTRUCTION PROCEDURES AND DRAWINGS

The current JSRs are made from castable ceramic that contains 94^{+}% alumina (Al_2O_3) and is reinforced with monolithic glass fibers (AP Green Model Greencast 94 Plus). This ceramic has a maximum continuous working temperature of 1870°C. Strict adherence to drying and curing protocols as provided by the manufacturer (including critical stages of mixing, hydro-setting, air drying, initial heat-up to 100°C and final firing temperature) is suggested for the curing process. Table A.1 is the curing chart used for the fabrication of the current JSRs. Preparation and curing of the ceramic reactors are performed in the Materials Fabrication Laboratories of the Material Science Engineering Department at the University of Washington. The technical contact is Mr. David Rice (206) 685-7290. Shown in Figures A.1 to A.7 are the standard JSR mold parts CAD drawings. The multi-sampling port JSR parts CAD drawings are shown in Figures A.8 to A.16. The original electronic copies of the Pro Engineer CAD drawings are located in the \CAD Drawings\ folder.

Table A.1. Curing Schedule for Atmospheric Pressure JSR

(Greencast 94 Plus Castable Ceramic)

Temperature Limit (°C)	***Ramp Rate (°C/Hour)***	***Dwell Temperature (°C)***	***Dwell Time (Hours)***	***Notes***
Room Temp.	-	Room Temp.	24	Time required for hydrosetting.
Room Temp.	-	Room Temp.	24	Time required for air dry.
Room Temp. – 60	10	60	10	Max. ramp rate should not exceed 17°C/hour. Min. dwell time should not be less than 1 hr/in of castable thickness. Max firing temp. is limited to 1200°C due to oven limitations.
60 – 120	10	120	10	
120 – 260	10	260	10	
260 – 540	10	540	10	
540 – 815	10	815	10	
815 – 1200	15	1200	10	
1200 – 20	250	-	-	Time required for cool down.

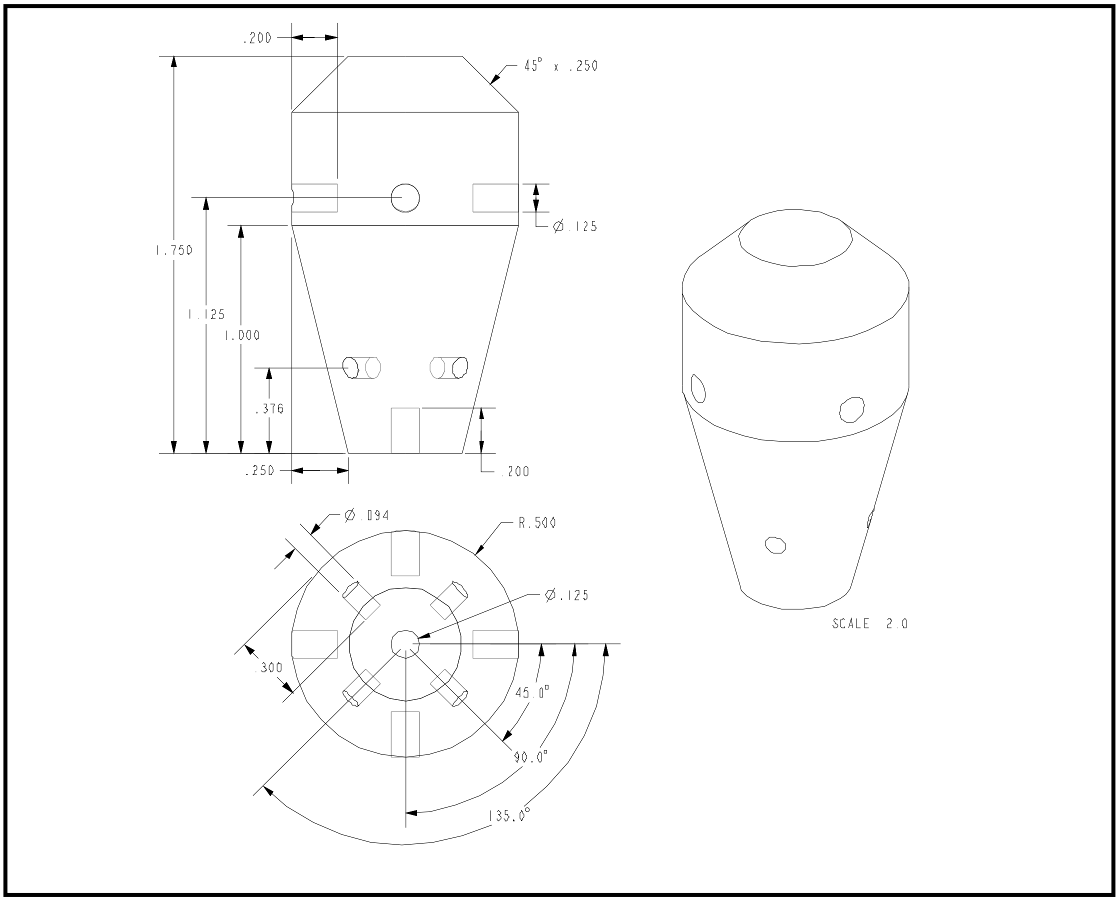

Figure A.1. CAD Drawing of the Standard JSR Mold – Cavity Mold (Material: Low Temperature Machinable Wax, Filename: standardmold.drw).

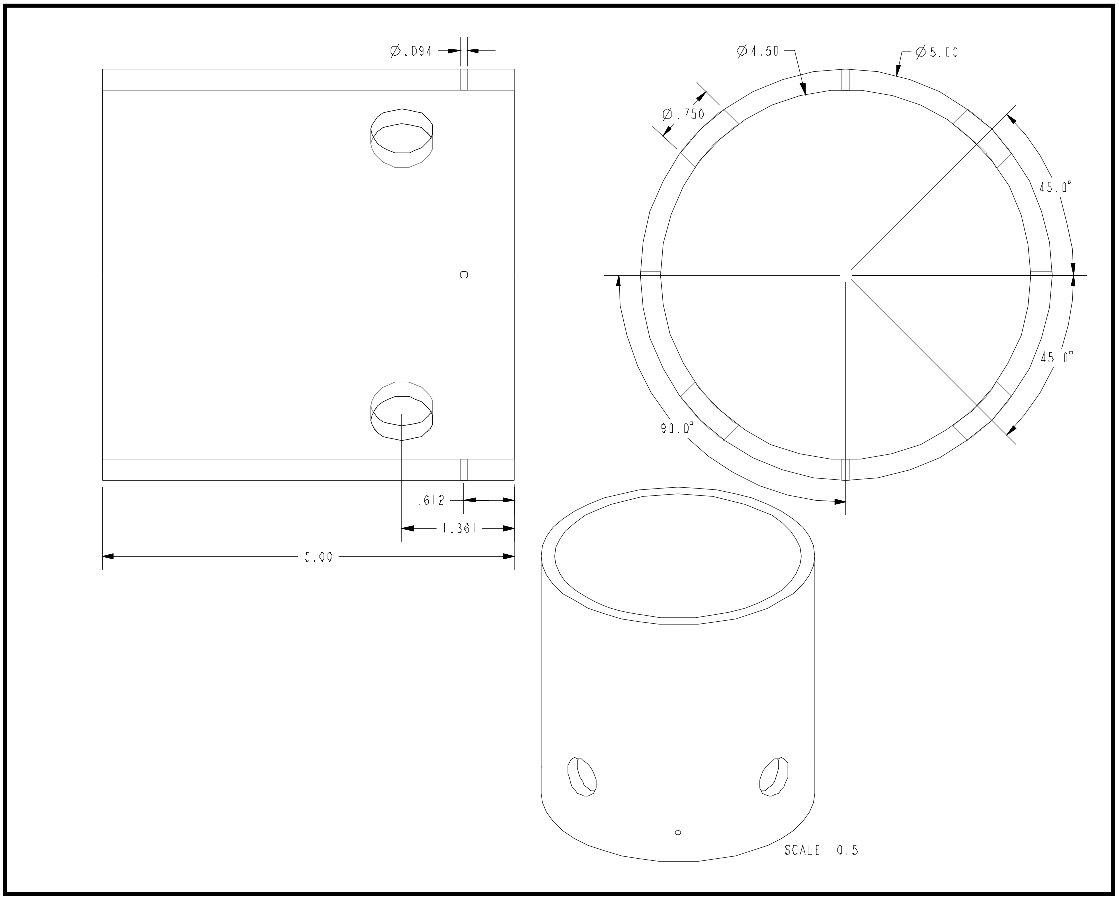

Figure A.2. CAD Drawing of the Standard JSR Mold – Outer Shell (Material: Aluminum, Filename: standardshell.drw).

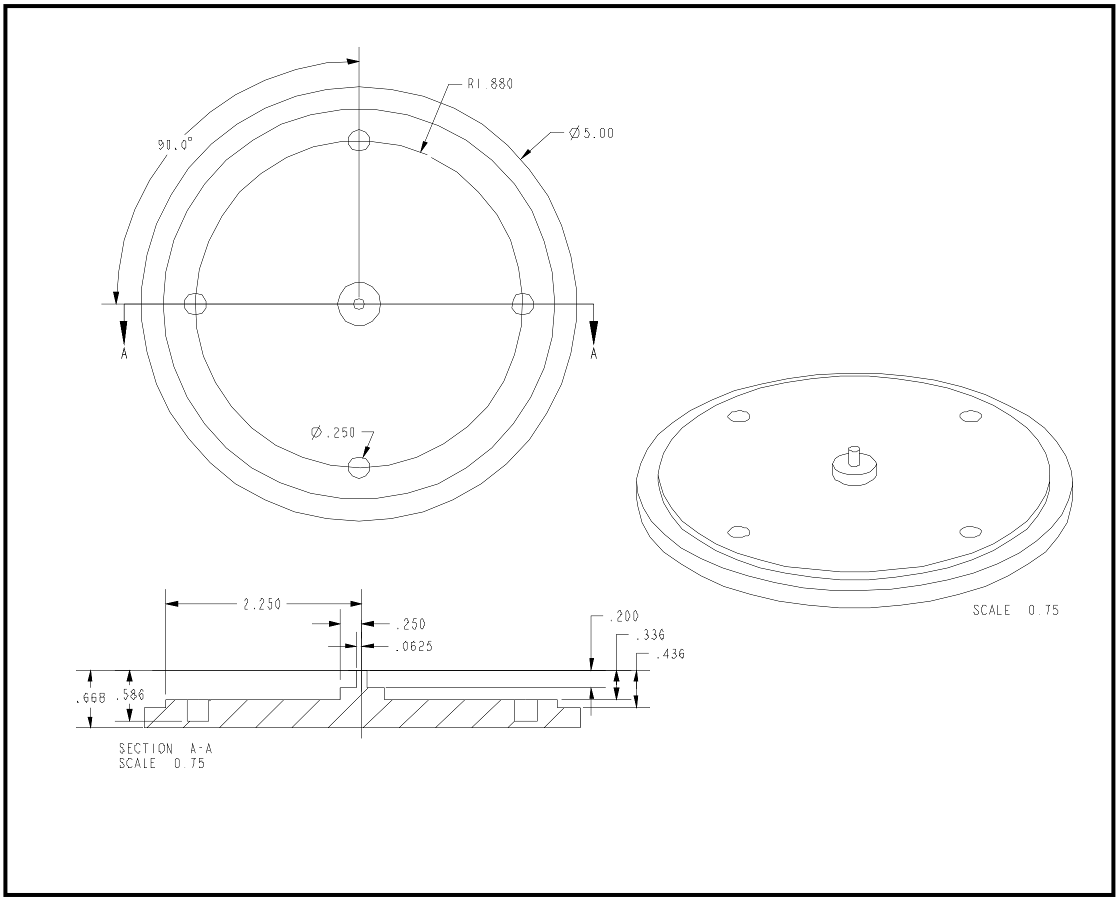

Figure A.3. CAD Drawing of the Standard JSR Mold – Bottom Plate (Material: Aluminum, Filename: standardbottom.drw).

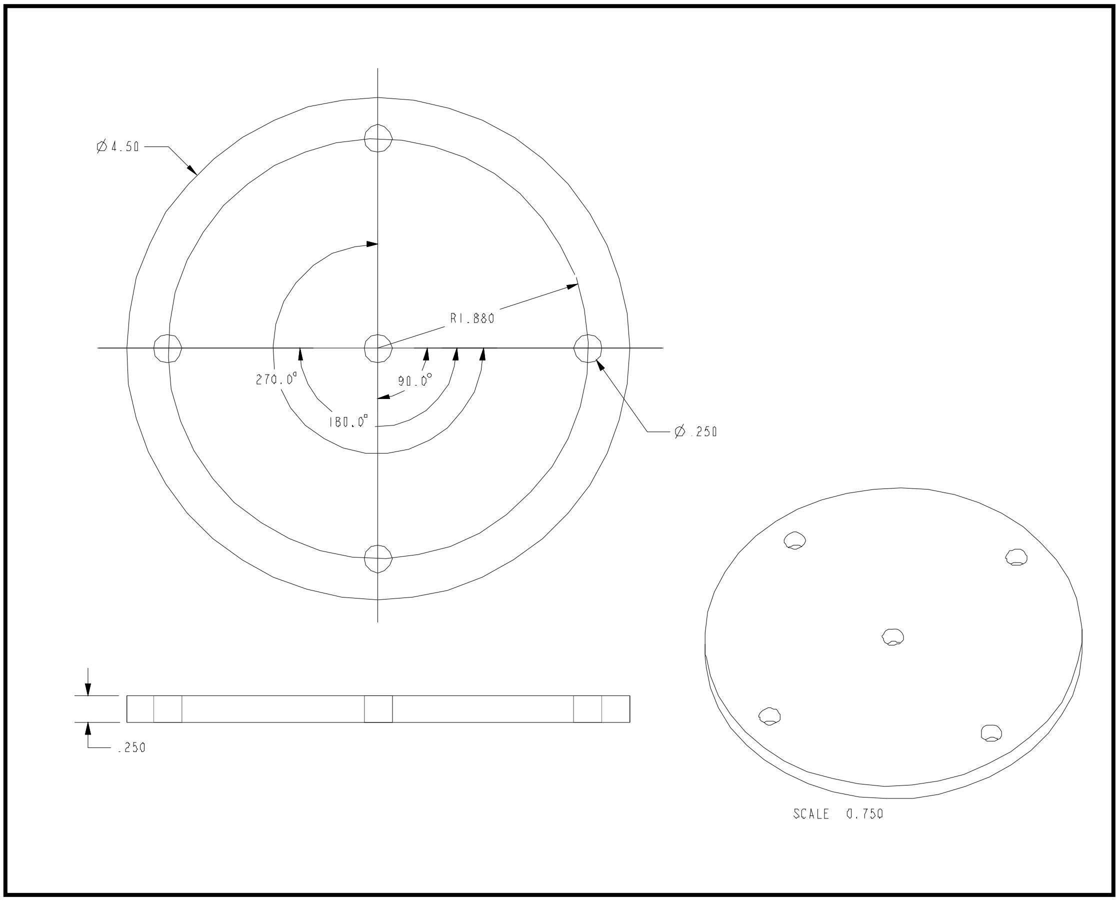

Figure A.4. CAD Drawing of the Standard JSR Mold – Top Plate (Material: Stainless Steel, Filename: standardtop.drw).

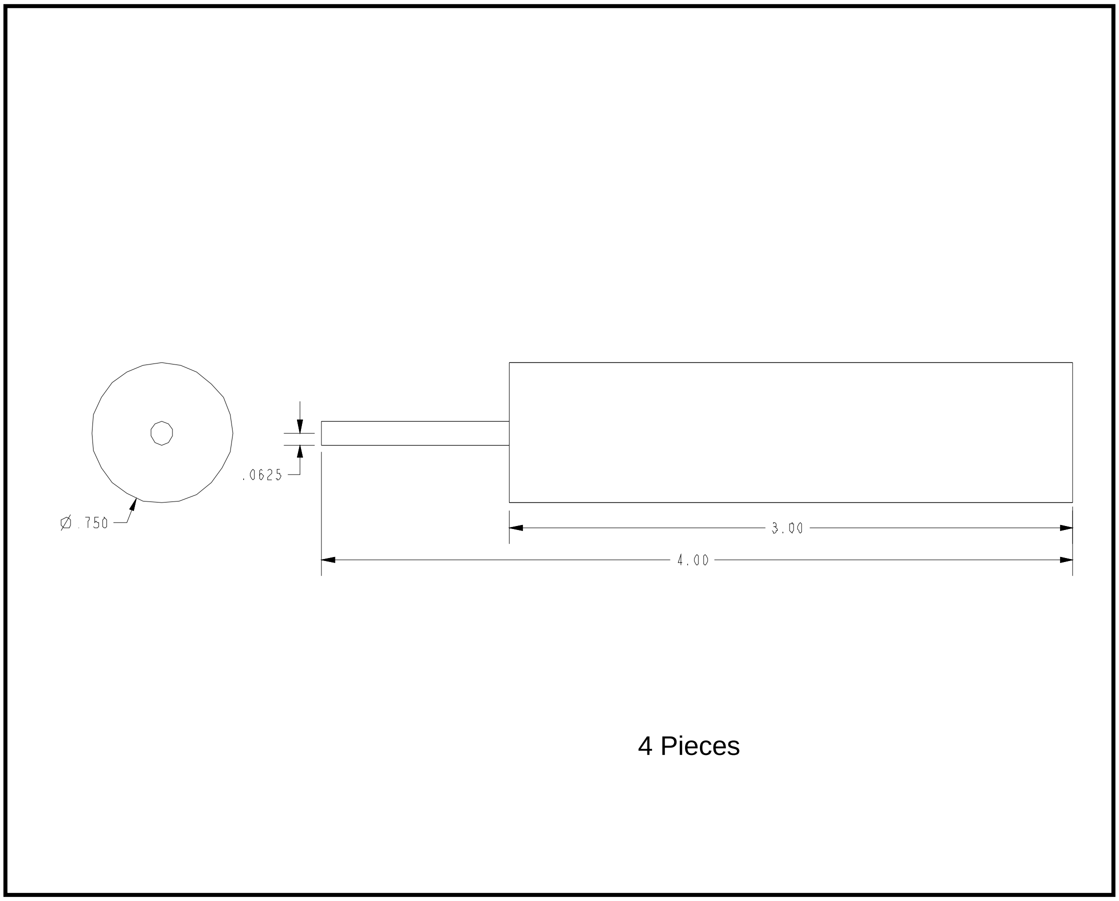

4 Pieces

Figure A.5. CAD Drawing of the Standard JSR Mold – Sampling Hole Rods (Material: Aluminum, Filename: standardsamplingrod.drw).

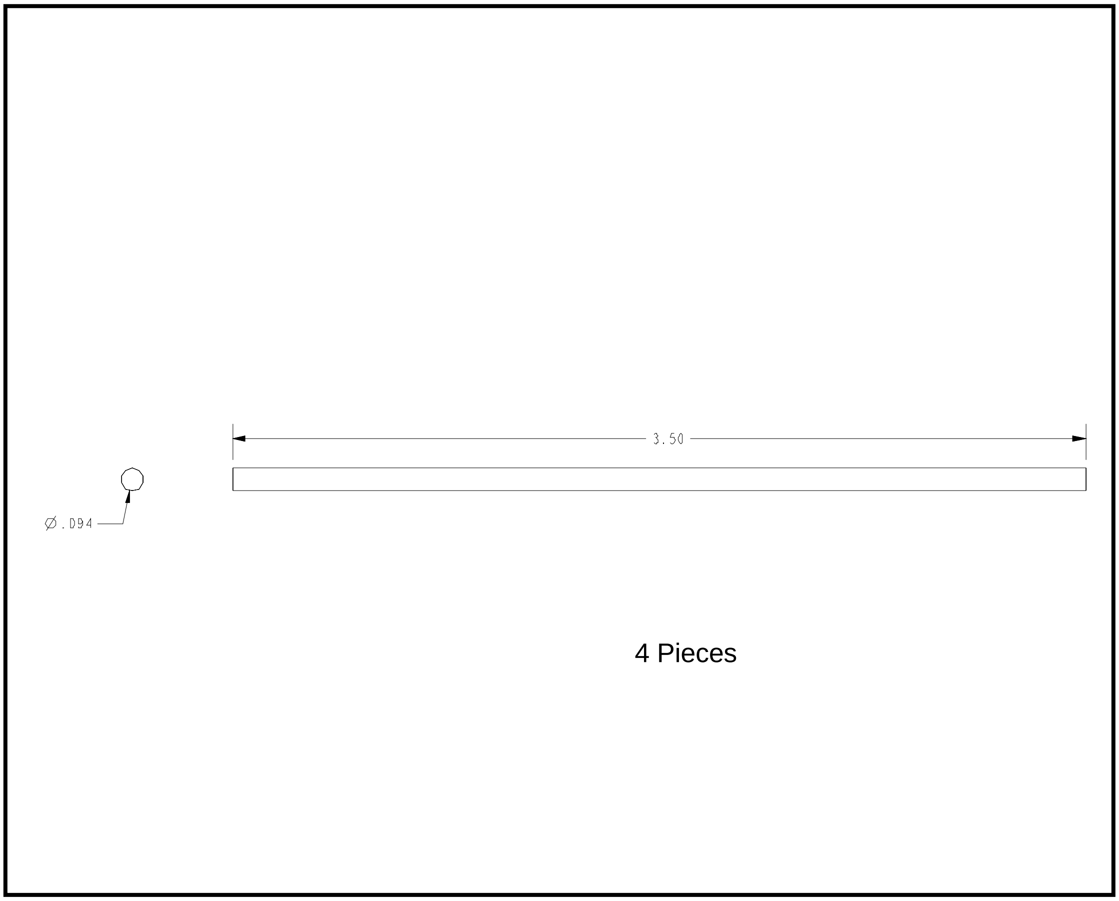

Figure A.6. CAD Drawing of the Standard JSR Mold – Exhaust Hole Rods (Material: Aluminum, Filename: standardexhaustgrod.drw).

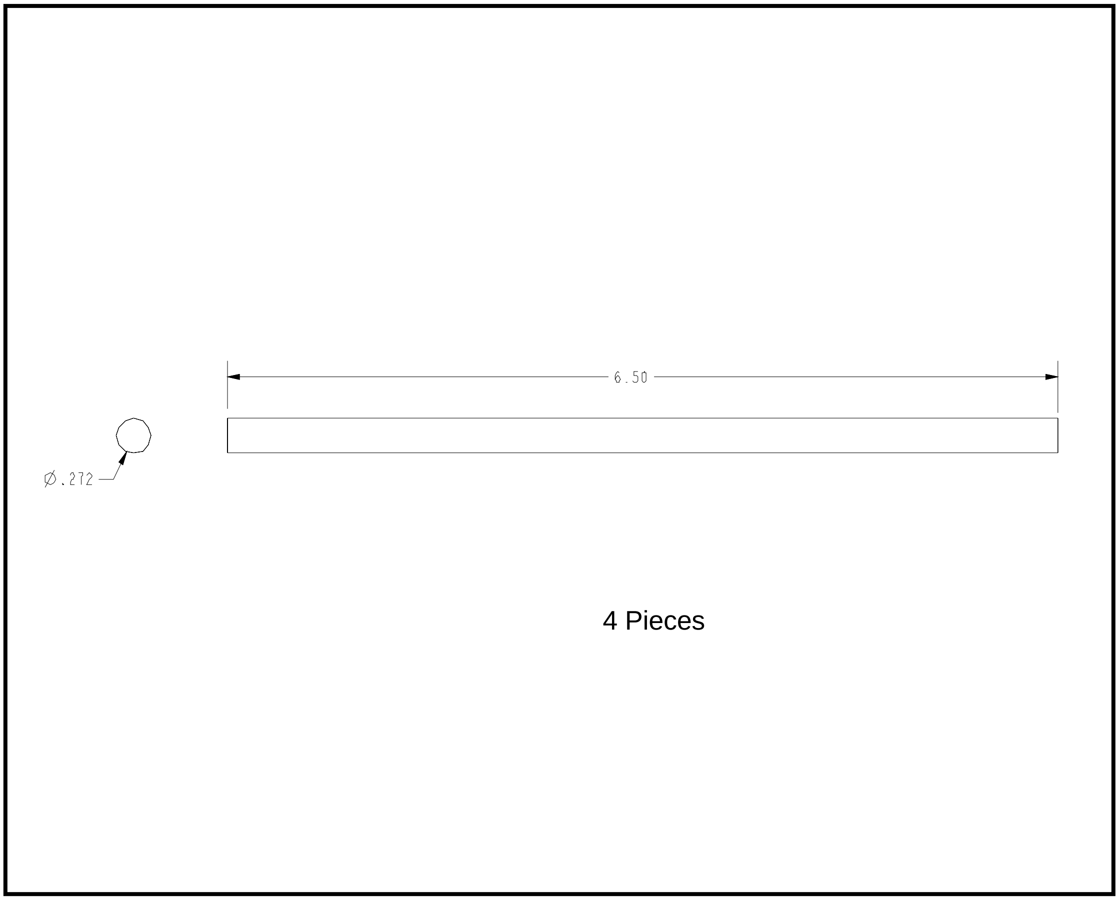

Figure A.7. CAD Drawing of the Standard JSR Mold – Reactor Placement Rods (Material: Stainless Steel, Filename: standardholdrod.drw).

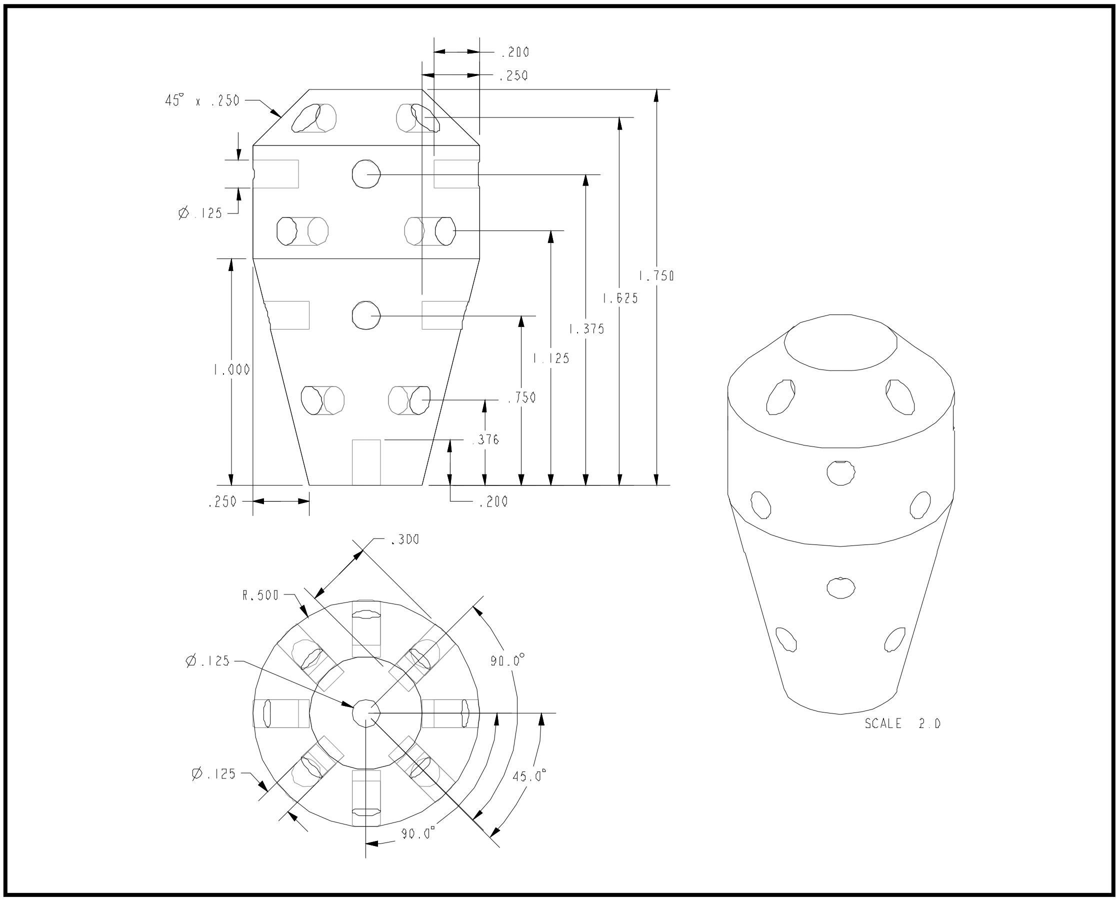

Figure A.8. CAD Drawing of the Multi-Sampling Port JSR Mold – Cavity Mold (Material: Low Temperature Machinable Wax, Filename: multiheightmold.drw).

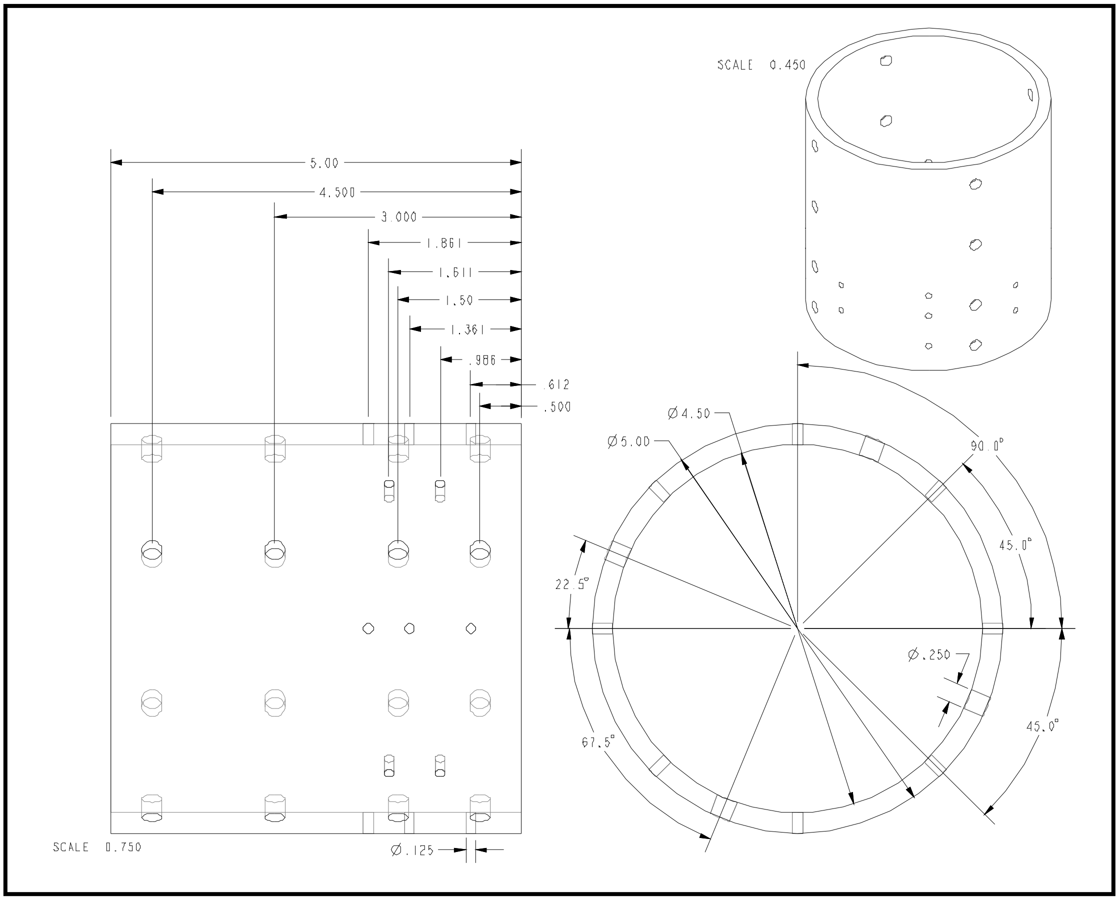

Figure A.9. CAD Drawing of the Multi-Sampling Port JSR Mold – Outer Shell (Material: Aluminum, Filename: multiheightshell.drw).

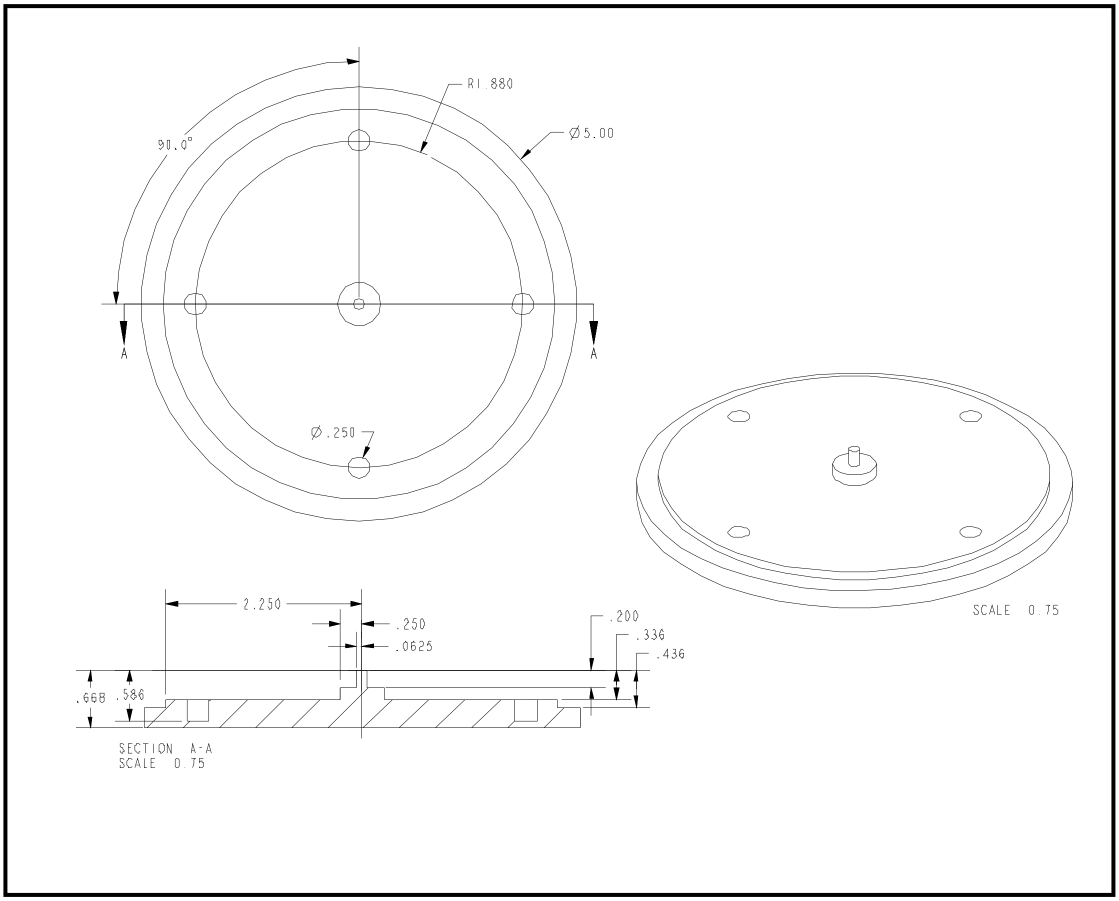

Figure A.10. CAD Drawing of the Multi-Sampling Port JSR Mold – Bottom Plate (Material: Aluminum, Filename: standardbottom.drw).

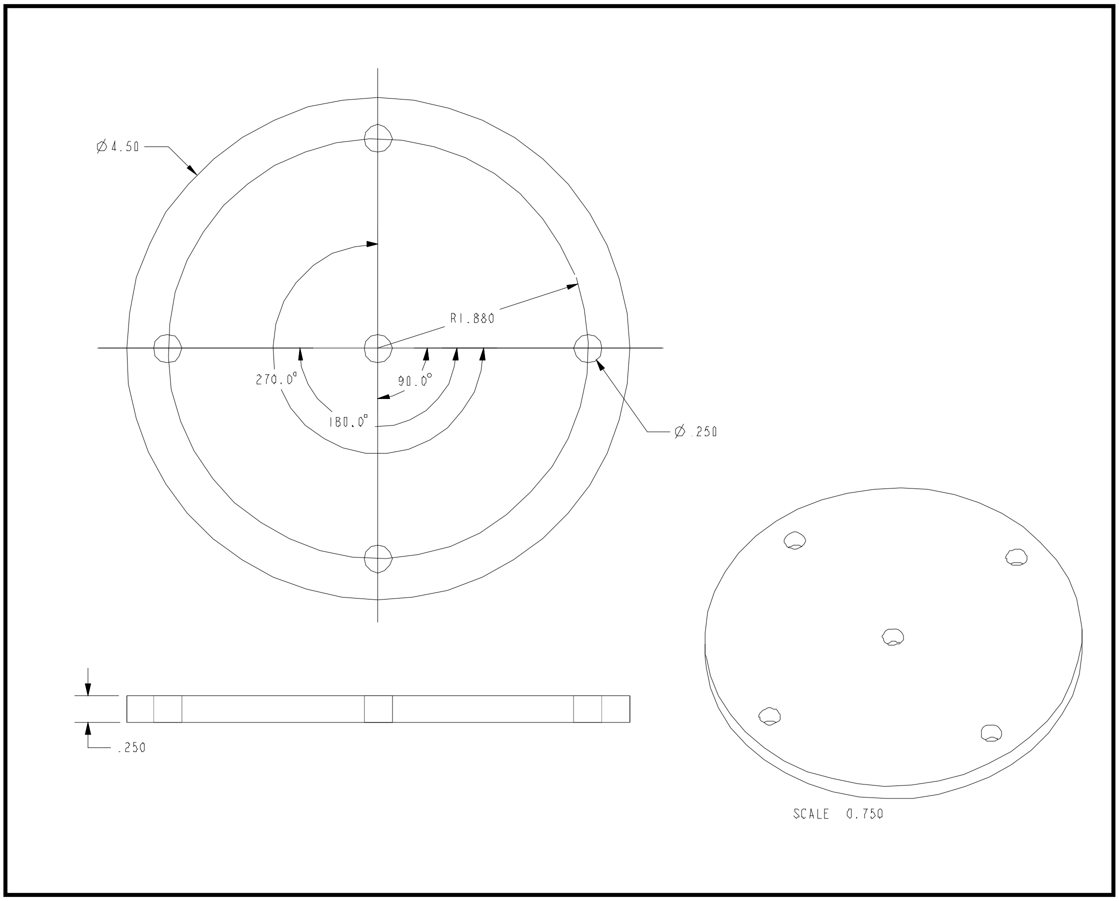

Figure A.11. CAD Drawing of the Multi-Sampling Port JSR Mold – Top Plate (Material: Stainless Steel, Filename: standardtop.drw).

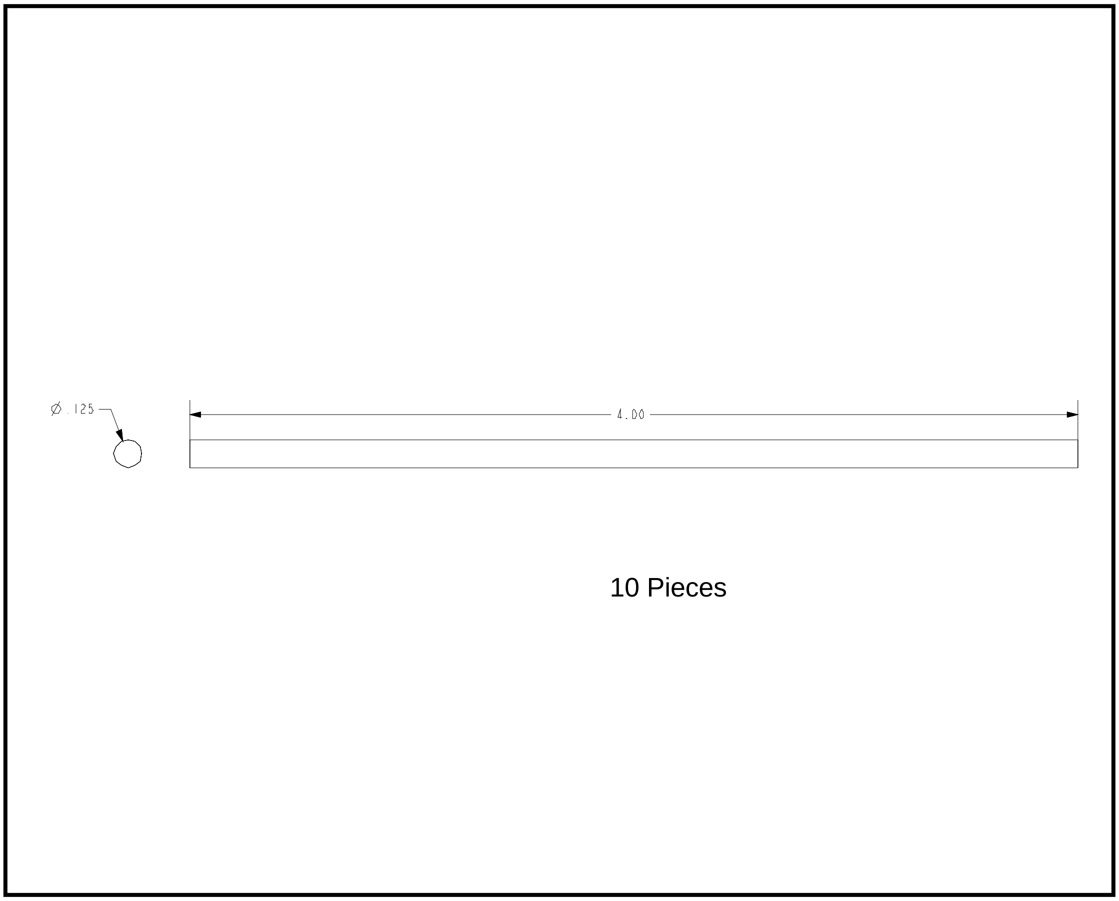

Figure A.12. CAD Drawing of the Multi-Sampling Port JSR Mold – Sampling and Exhaust Holes Rod (Material: Stainless Steel, Filename:multiheightsamplingrod.drw).

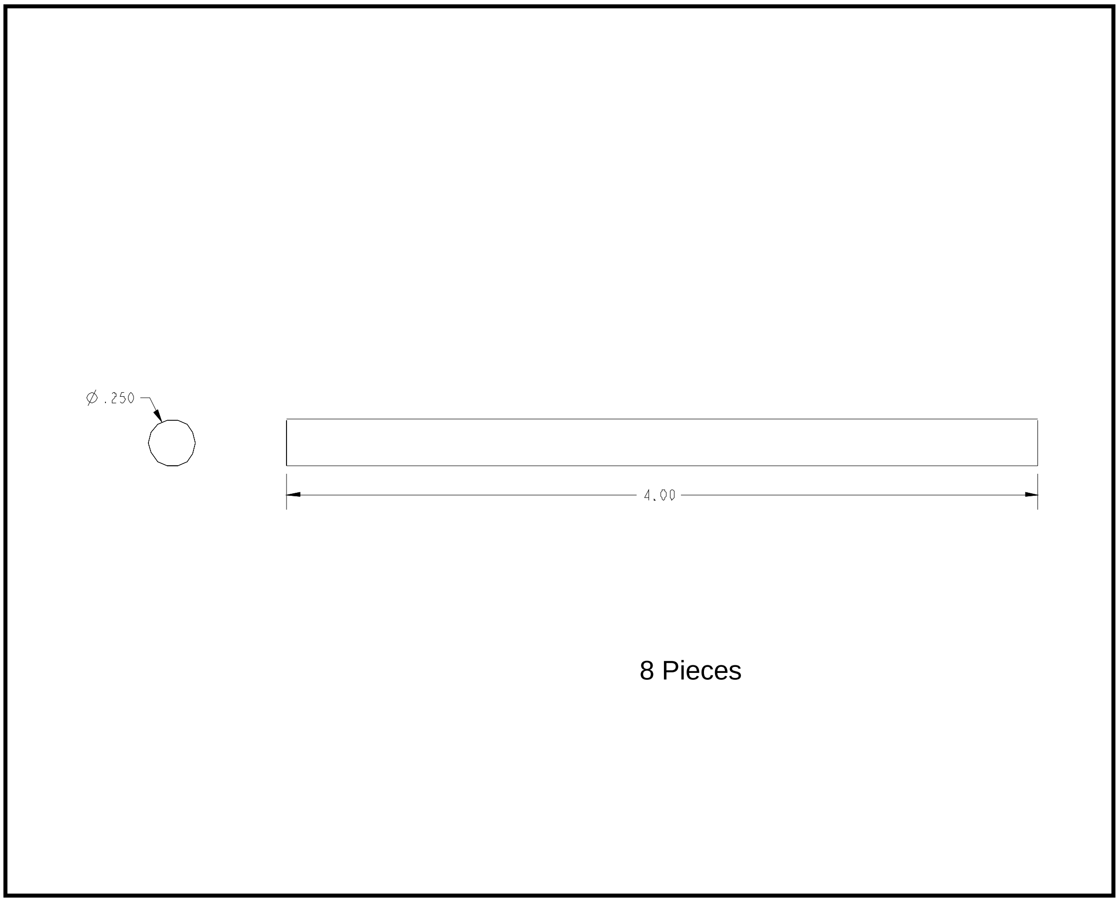

Figure A.13. CAD Drawing of the Multi-Sampling Port JSR Mold – Lower Side Wall Temperature Rod (Material: Stain. Steel, Filename: multiheightwalltemplorod.drw).

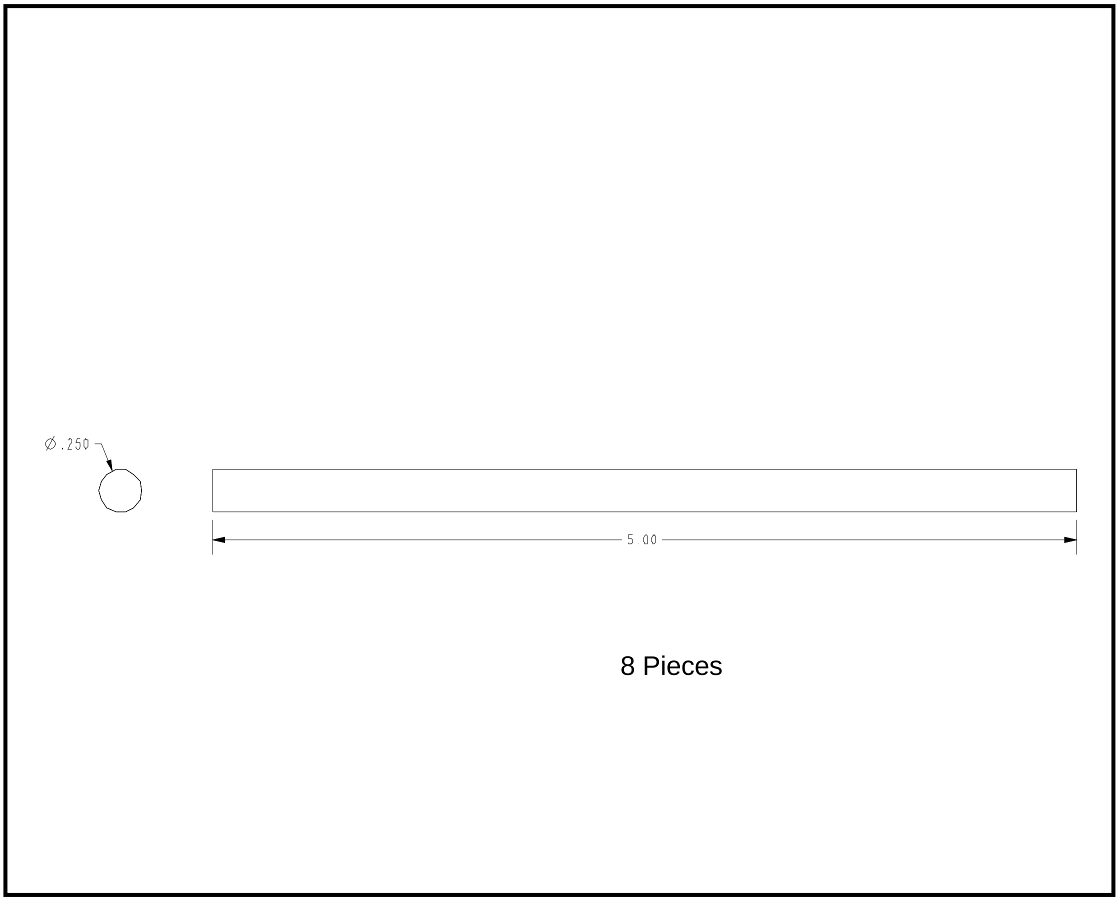

Figure A.14. CAD Drawing of the Multi-Sampling Port JSR Mold – Upper Side Wall Temperature Rod (Material: Stain. Steel, Filename: multiheightwalltemphirod.drw).

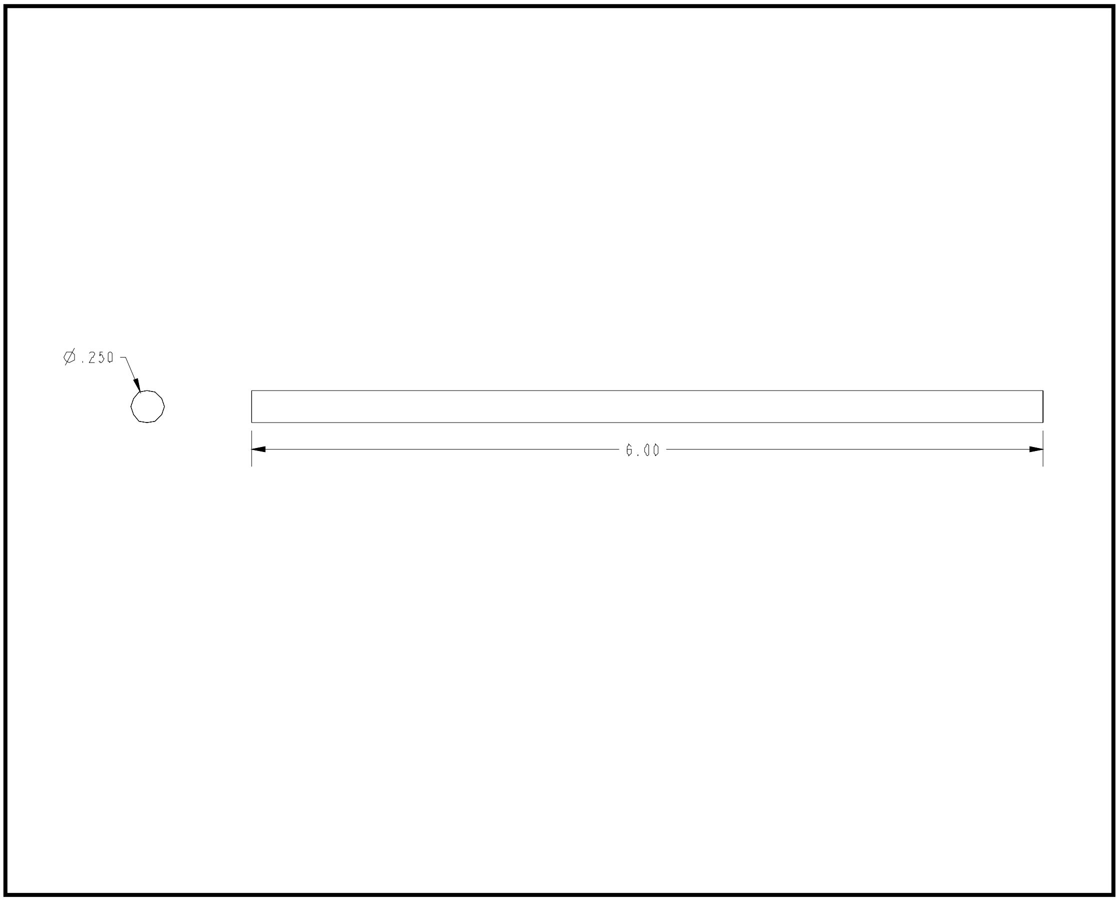

Figure A.15. CAD Drawing of the Multi-Sampling Port JSR Mold – Top Center Wall Temperature Rod (Material: Stain. Steel, Filename: multiheightwalltemptoprod.drw).

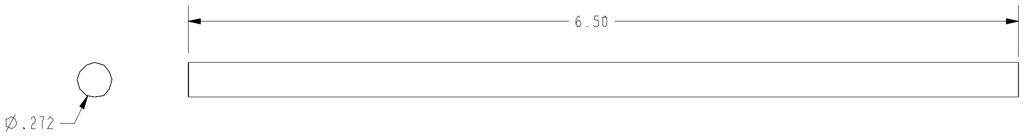

4 Pieces

Figure A.16. CAD Drawing of the Multi-Sampling Port JSR Mold – Reactor Placement Rods (Material: Stainless Steel, Filename: standardholdrod.drw).

APPENDIX B: NOZZLE BLOCK DESIGN AND CONSTRUCTION

Figure B.1 is the CAD drawing of the single, 2 mm, straight channel, centered jet nozzle block used for the 1st generation injector. The nozzle block is constructed from INCONEL® 800. Figures B.2 to B.4 are CAD drawings of the nozzle blocks used for the 2nd generation injector. The nozzle blocks include the single, 2 mm, centered jet, single, 4 mm, centered jet and 8-hole, 0.965 mm, diverging jets designs. The three nozzle blocks are all of the straight channel design and are constructed from INCONEL® 800. The HASTELOY® X nozzle blocks fabricated for the SPP are shown in Figures B.5 and B.6 and include a single, 4 mm, converging channel, centered jet and an 8-hole, 1.414 mm, straight channel, diverging jets with a single, 0.762 mm, centered pilot. The SPP nozzle blocks have equivalent total flow cross sectional area. The diverging jets in both diverging jet nozzle blocks are angled at 14° from the vertical allowing the jets to flow parallel to the reactor wall. The original electronic copy of the Pro Engineer and AutoCAD CAD drawings are located in the \CAD Drawings\ folder.

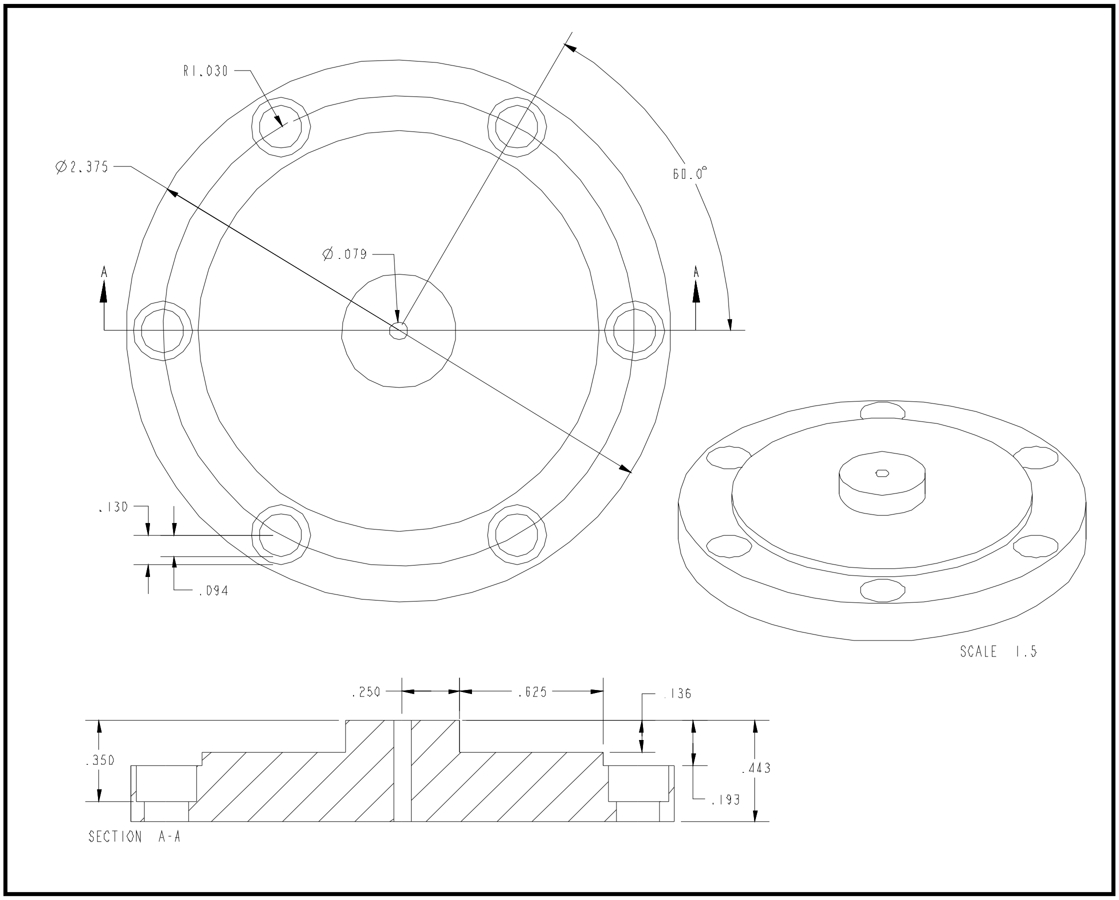

Figure B.1. CAD Drawing of the Single, 2 mm, Straight Channel, Centered Jet Nozzle Block used for the 1st Generation Injector (Filename: firstgen2mm.drw).

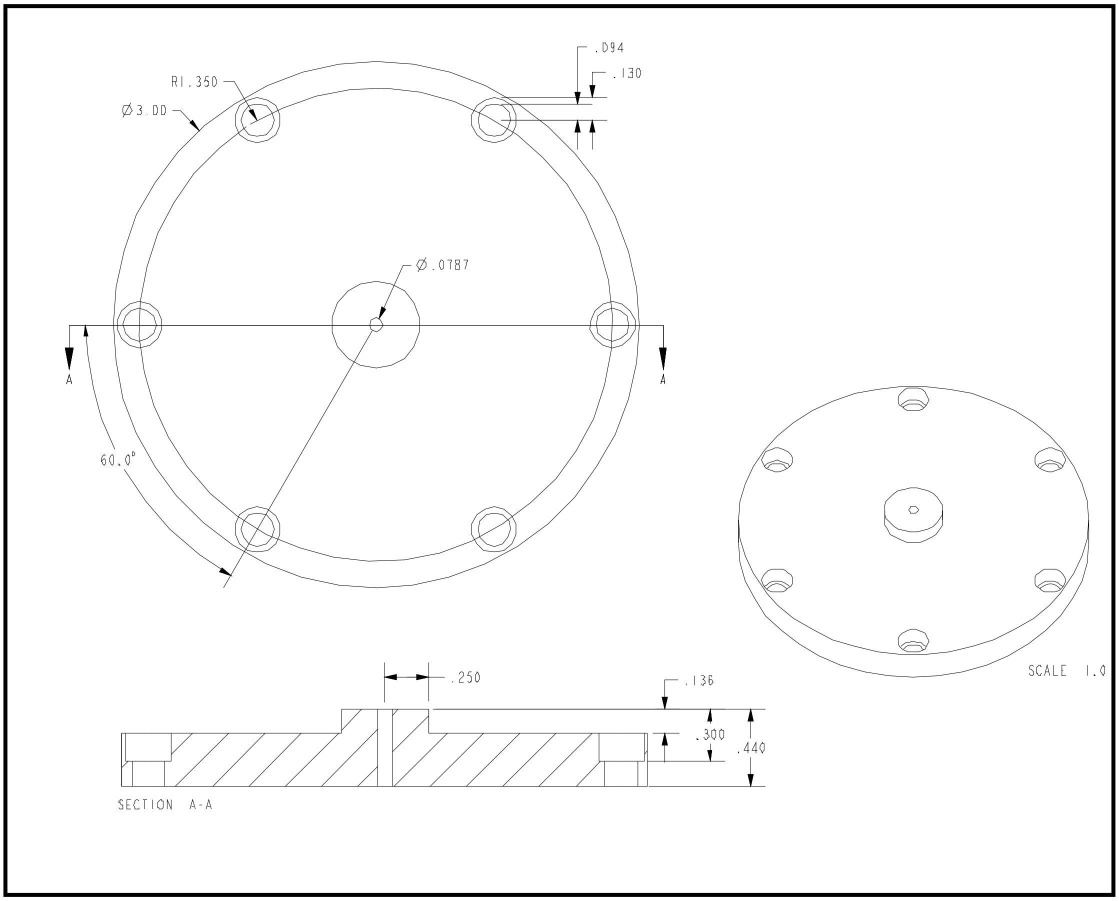

Figure B.2. CAD Drawing of the Single, 2 mm, Straight Channel, Centered Jet Nozzle Block used for the 2nd Generation Injector (Filename: secondgen2mm.drw).

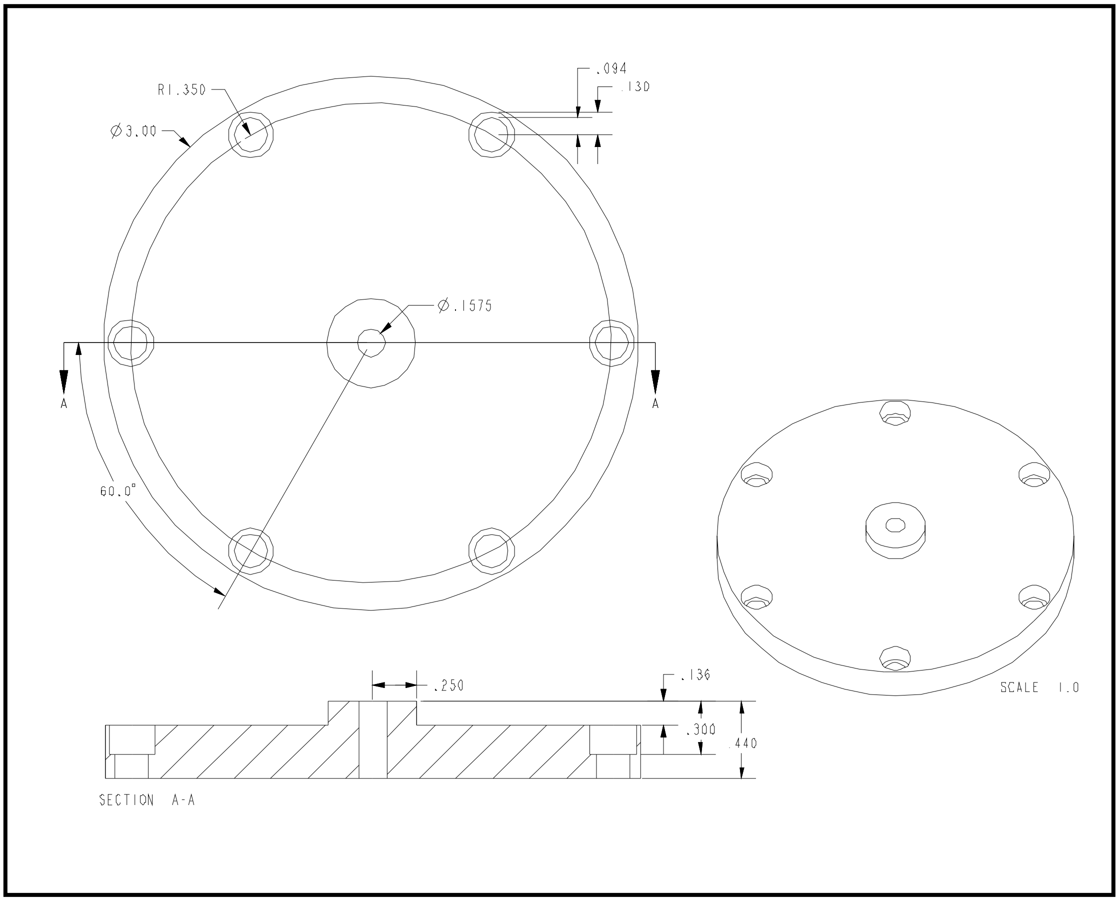

Figure B.3. CAD Drawing of the Single, 4 mm, Straight Channel, Centered Jet Nozzle Block used for the 2nd Generation Injector (Filename: secondgen4mm.drw).

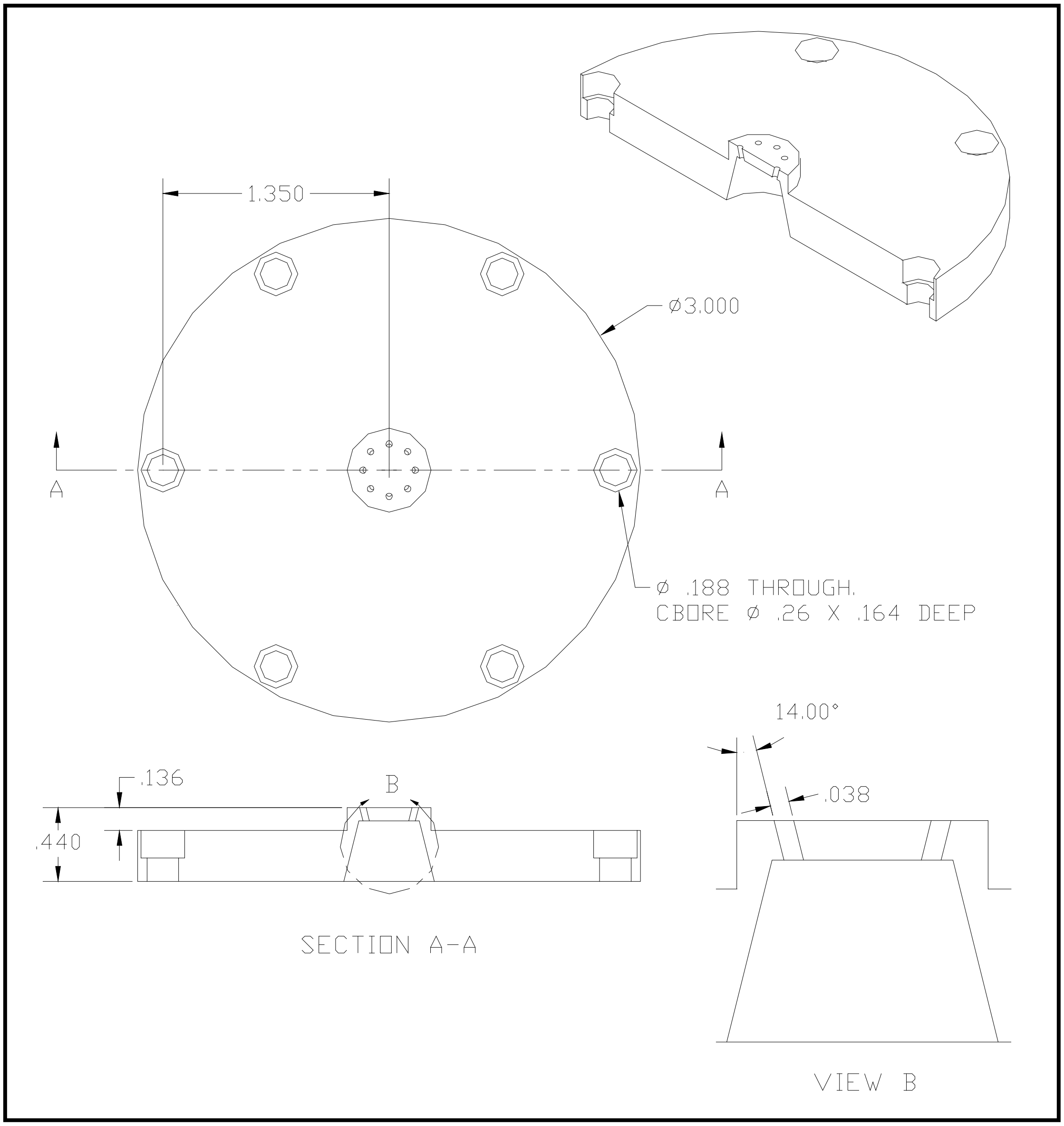

Figure B.4. CAD Drawing of the 8-Hole, 0.965 mm, Straight Channel, Diverging Jets Nozzle Block used for the 2nd Generation Injector (Filename: secondgendiv.dwg).

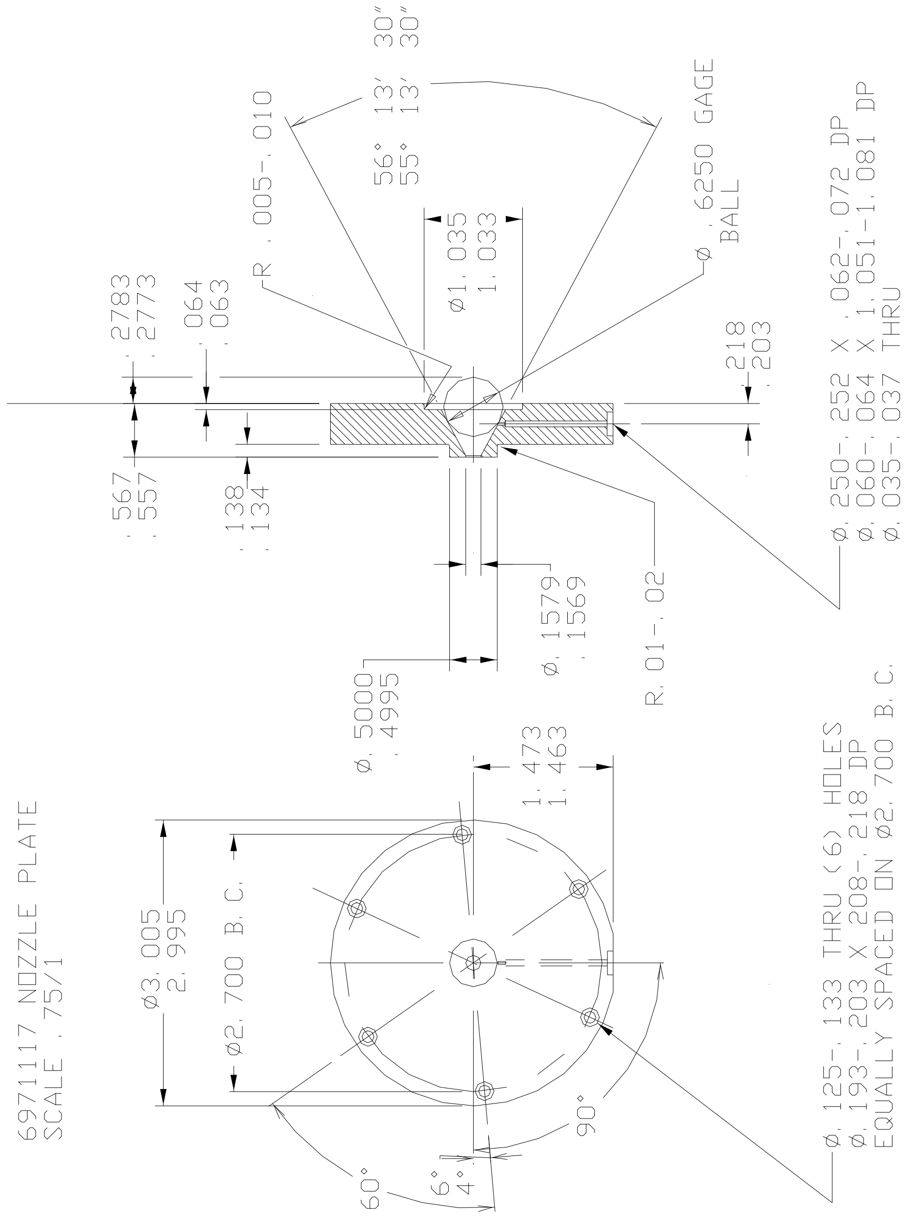

Figure B.5. CAD Drawing of the Single, 4 mm, Converging Channel, Centered Jet Nozzle Block used for the SPP Injector (Filename: spp4mm.dwg).

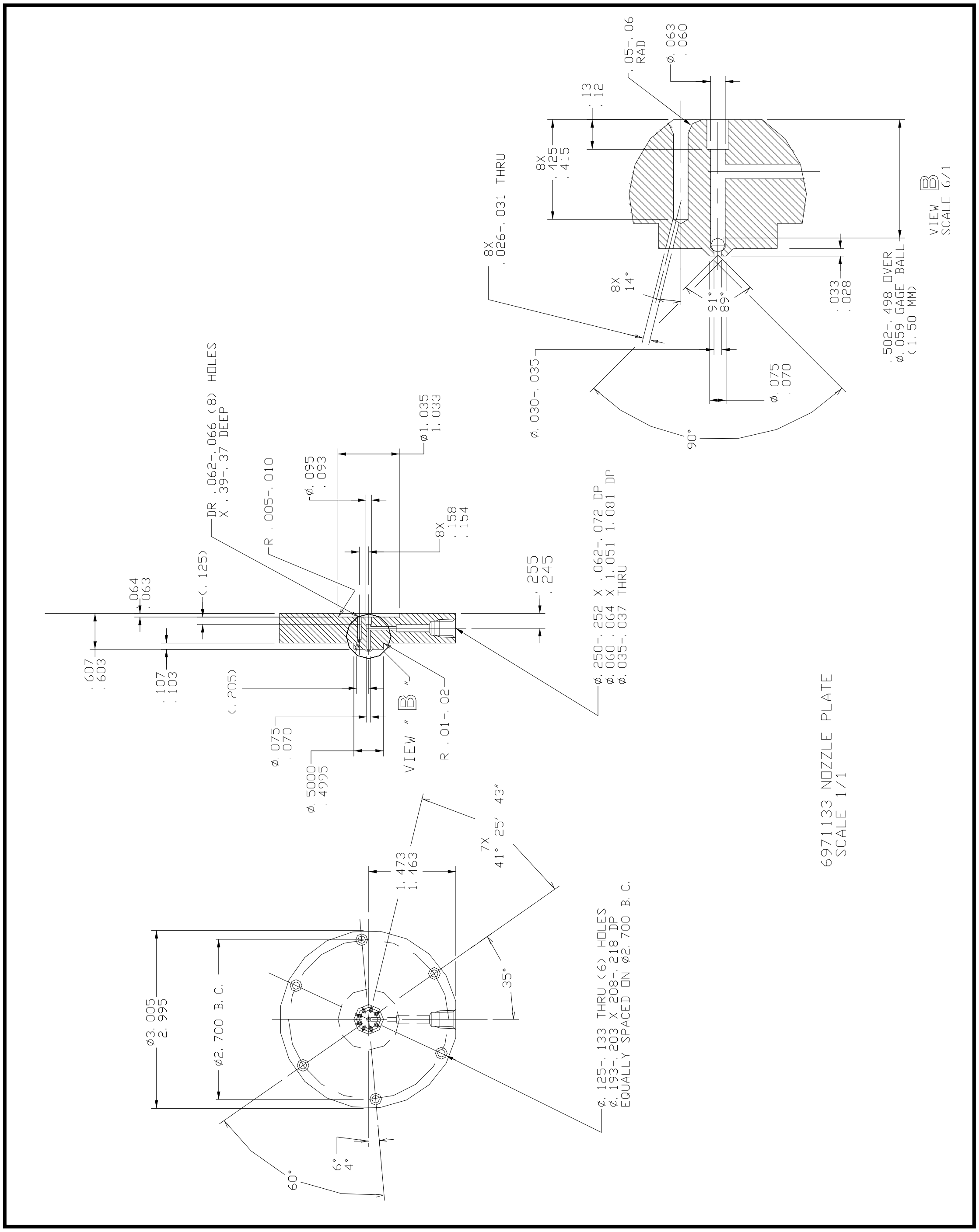

Figure B.6. CAD Drawing of the 8-Hole, 1.414 mm, Straight Channel, Diverging Jets Nozzle Block used for the SPP Injector with Piloting Capabilities (Filename: sppdiv.dwg).

APPENDIX C: LIQUID FUEL ROTAMETER CALIBRATION CURVES

Calibration data for the liquid fuel rotameter are presented in Tables C.1 through C.14. Rotameter calibration is determined via the bucket-and-stopwatch technique. A digital balance (Sartorius Model L610D+**V20C) with an accuracy of 0.01 g is used in conjunction with a digital stopwatch (Sportline Model 219) with an accuracy of 0.01 s. As expected, the liquid fuel flow rates are linearly proportional to the rotameter scale height and independent of the applied backpressure. An electronic form of the SPP liquid fuel rotameter calibration data can be found in the \Liquid Fuels\spp rotameter calibration.xls\ file.

Table C.1. Calibration Data for Methanol.

Fuel	Methanol		
Temperature (°C)	20		
Pressure (psig)	20		
Float Type	Stainless Steel		
Tube	FP-1/16-19.5-G-6 3/4/61		
Calibration Curve	y = 9.378573E-04x + 3.990810E-03		
Linearity	R^2 = 9.992016E-01		
Scale	***Mass (g)***	***Time (s)***	***Flow Rate (g/s)***
80	9.99	125.81	0.0794
80	9.99	125.94	0.0793
100	13.26	135.66	0.0977
100	12.31	126.16	0.0976
120	13.48	116.72	0.1155
120	14.33	124.19	0.1154
140	17.20	126.07	0.1364
140	16.79	123.03	0.1365
160	19.09	124.31	0.1536
160	18.79	122.06	0.1539

Table C.2. Calibration Data for Pentane.

Fuel	n-Pentane		
Temperature (°C)	20		
Pressure (psig)	20		
Float Type	Saphire		
Tube	FP-1/16-19.5-G-6 3/4/61		
Calibration Curve	y = 6.856587E-04x + 5.932565E-03		
Linearity	R^2 = 9.995233E-01		
Scale	***Mass (g)***	***Time (s)***	***Flow Rate (g/s)***
20	2.61	133.07	0.0196
20	3.49	182.25	0.0191
40	4.19	123.13	0.0340
40	4.57	136.06	0.0336
60	6.00	127.38	0.0471
60	5.97	127.50	0.0468
80	7.83	129.44	0.0605
80	8.47	139.03	0.0609
60	7.96	169.09	0.0471
(Last 60 Scale @50 psig)			

Table C.3. Calibration Data for Hexane.

Fuel	n-Hexane		
Temperature (°C)	20		
Pressure (psig)	20		
Float Type	Saphire		
Tube	FP-1/16-19.5-G-6 3/4/61		
Calibration Curve	y = 6.267883E-04x + 2.445394E-03		
Linearity	R^2 = 9.994015E-01		
Scale	***Mass (g)***	***Time (s)***	***Flow Rate (g/s)***
40	8.50	309.35	0.0275
40	5.32	195.15	0.0273
59	7.45	187.22	0.0398
60	9.47	238.47	0.0397
80	8.20	155.06	0.0529
80	6.83	128.54	0.0531
100	8.79	135.19	0.0650
99	8.39	131.03	0.0640

Table C.4. Calibration Data for Heptane.

Fuel	n-Heptane		
Temperature (°C)	20		
Pressure (psig)	20		
Float Type	Saphire		
Tube	FP-1/16-19.5-G-6 3/4/61		
Calibration Curve	y = 5.879664E-04x + 1.178991E-04		
Linearity	R^2 = 9.996107E-01		
Scale	***Mass (g)***	***Time (s)***	***Flow Rate (g/s)***
40	5.69	241.22	0.0236
40	6.84	290.47	0.0235
60	11.91	335.28	0.0355
60	7.83	221.69	0.0353
80	8.57	181.00	0.0473
80	11.58	243.22	0.0476
100	19.49	333.37	0.0585
41	4.13	169.81	0.0243
40	5.69	242.87	0.0234
(Last 41 Scale @10 psig, Last 40 Scale @50 psig)			

Table C.5. Calibration Data for Dodecane.

Fuel	n-Dodecane		
Temperature (°C)	20		
Pressure (psig)	20		
Float Type	Stainless Steel		
Tube	FP-1/16-19.5-G-6 3/4/61		
Calibration Curve	y = 7.858991E-04x - 2.786740E-02		
Linearity	R^2 = 9.990740E-01		
Scale	***Mass (g)***	***Time (s)***	***Flow Rate (g/s)***
100	7.25	141.50	0.0512
100	8.70	169.25	0.0514
120	8.01	121.96	0.0657
120	11.52	175.53	0.0656
141	10.02	121.12	0.0827
141	10.04	121.34	0.0827
161	12.54	126.50	0.0991
161	12.17	122.94	0.0990

Table C.6. Calibration Data for Hexadecane.

Fuel	n-Hexadecane		
Temperature (°C)	20		
Pressure (psig)	50		
Float Type	Tantalum		
Tube	FP-1/16-19.5-G-6 3/4/61		
Calibration Curve	y = 1.154020E-03x - 5.723532E-02		
Linearity	R^2 = 9.995281E-01		
Scale	***Mass (g)***	***Time (s)***	***Flow Rate (g/s)***
91	3.87	80.19	0.0483
91	3.92	82.13	0.0477
99	3.72	65.41	0.0569
99	3.73	65.72	0.0568
111	4.56	64.68	0.0705
111	4.38	61.94	0.0707
119	5.20	64.72	0.0803
119	5.19	64.62	0.0803

Table C.7. Calibration Data for Benzene.

Fuel	Benzene		
Temperature (°C)	20		
Pressure (psig)	50		
Float Type	Saphire		
Tube	FP-1/16-19.5-G-6 3/4/61		
Calibration Curve	y = 6.222117E-04x - 1.054499E-02		
Linearity	R^2 = 9.991103E-01		
Scale	***Mass (g)***	***Time (s)***	***Flow Rate (g/s)***
110	3.84	65.96	0.0582
110	3.56	61.93	0.0575
120	3.93	61.38	0.0640
120	3.95	61.44	0.0643
130	4.59	65.12	0.0705
130	4.58	65.12	0.0703
140	4.95	64.75	0.0764
140	5.14	67.13	0.0766

Table C.8. Calibration Data for Toluene.

Fuel	Toluene		
Temperature (°C)	20		
Pressure (psig)	50		
Float Type	Saphire		
Tube	FP-1/16-19.5-G-6 3/4/61		
Calibration Curve	y = 6.202334E-04x - 7.035176E-03		
Linearity	R^2 = 9.988155E-01		
Scale	***Mass (g)***	***Time (s)***	***Flow Rate (g/s)***
100	3.36	61.31	0.0548
101	3.81	68.34	0.0558
110	3.97	64.54	0.0615
110	3.96	64.65	0.0613
120	4.10	61.07	0.0671
120	4.39	65.50	0.0670
130	4.43	60.19	0.0736
130	4.40	59.56	0.0739

Table C.9. Calibration Data for U.S. Oil and Refinery Light Naphtha.

Fuel	USOR Light Naphtha		
Temperature (°C)	20		
Pressure (psig)	50		
Float Type	Saphire		
Tube	FP-1/16-19.5-G-6 3/4/61		
Calibration Curve	y = 5.785217E-04x + 9.666931E-03		
Linearity	R^2 = 9.980494E-01		
Scale	***Mass (g)***	***Time (s)***	***Flow Rate (g/s)***
70	4.81	96.94	0.0496
70	4.50	89.25	0.0504
80	4.02	72.03	0.0558
80	4.00	70.91	0.0564
90	4.47	72.25	0.0619
90	3.75	60.66	0.0618
100	4.18	62.00	0.0674
100	4.12	61.16	0.0674

Table C.10. Calibration Data for Kern Light Naphtha.

Fuel	Kern Light Naphtha		
Temperature (°C)	20		
Pressure (psig)	20		
Float Type	Saphire		
Tube	FP-1/16-19.5-G-6 3/4/61		
Calibration Curve	y = 6.157472E-04x + 1.174527E-03		
Linearity	R^2 = 9.994205E-01		
Scale	**Mass (g)**	**Time (s)**	**Flow Rate (g/s)**
20	2.43	185.03	0.0131
20	3.34	252.47	0.0132
40	5.00	192.53	0.0260
40	4.42	171.25	0.0258
60	5.49	142.09	0.0386
60	6.30	162.96	0.0387
80	6.00	118.72	0.0505
80	6.78	134.16	0.0505
101	7.96	126.22	0.0631
100	7.83	126.19	0.0620
120	7.66	103.22	0.0742
124	10.22	130.09	0.0786

Table C.11. Calibration Data for USOR Low Sulfur Diesel.

Fuel	USOR Low Sulfur Diesel		
Temperature (°C)	20		
Pressure (psig)	50		
Float Type	Tantalum		
Tube	FP-1/16-19.5-G-6 3/4/61		
Calibration Curve	y = 6.997689E-04x - 4.095514E-02		
Linearity	R^2 = 9.993150E-01		
Scale	***Mass (g)***	***Time (s)***	***Flow Rate (g/s)***
129	4.56	92.31	0.0494
130	3.77	74.97	0.0503
140	3.69	65.19	0.0566
140	3.81	66.97	0.0569
150	4.17	65.00	0.0642
150	4.40	68.91	0.0639
160	6.49	91.15	0.0712
160	4.54	63.94	0.0710

Table C.12. Calibration Data for Cheveron Low Sulfur Diesel.

Fuel	Cheveron Low Sulfur Diesel		
Temperature (°C)	20		
Pressure (psig)	50		
Float Type	Tantalum		
Tube	FP-1/16-19.5-G-6 3/4/61		
Calibration Curve	y = 8.120213E-04x - 3.979409E-02		
Linearity	R^2 = 9.984299E-01		
Scale	***Mass (g)***	***Time (s)***	***Flow Rate (g/s)***
110	4.19	84.72	0.0495
110	3.31	66.16	0.0500
120	3.68	63.71	0.0578
120	3.60	62.84	0.0573
130	4.41	67.50	0.0653
130	4.46	68.19	0.0654
140	4.79	64.34	0.0744
140	4.85	65.59	0.0739

Table C.13. Calibration Data for Texaco Low Sulfur Diesel.

Fuel	Texaco Low Sulfur Diesel		
Temperature (°C)	20		
Pressure (psig)	50		
Float Type	Tantalum		
Tube	FP-1/16-19.5-G-6 3/4/61		
Calibration Curve	y = 8.227040E-04x - 3.697089E-02		
Linearity	R^2 = 9.979346E-01		
Scale	***Mass (g)***	***Time (s)***	***Flow Rate (g/s)***
110	4.18	77.72	0.0538
110	3.98	73.81	0.0539
120	3.77	61.38	0.0614
120	3.76	61.06	0.0616
131	5.43	77.34	0.0702
131	4.22	59.97	0.0704
140	4.89	61.94	0.0789
141	5.03	63.53	0.0792

Table C.14. Calibration Data for Texaco High Sulfur Diesel.

Fuel	Texaco High Sulfer Diesel		
Temperature (°C)	20		
Pressure (psig)	50		
Float Type	Tantalum		
Tube	FP-1/16-19.5-G-6 3/4/61		
Calibration Curve	y = 7.469363E-04x - 3.978258E-02		
Linearity	R^2 = 9.988169E-01		
Scale	***Mass (g)***	***Time (s)***	***Flow Rate (g/s)***
120	3.75	74.97	0.0500
121	3.08	60.40	0.0510
131	3.59	62.12	0.0578
131	3.64	63.19	0.0576
140	4.00	61.81	0.0647
141	4.13	63.22	0.0653
150	4.70	64.78	0.0726
150	4.46	61.59	0.0724

APPENDIX D: THERMOCOUPLE CONSTRUCTION PROCEDURES AND TEMPERATURE CORRECTION ANALYSIS

D.1 R-TYPE TC FABRICATION PROCEDURES

Care must be taken during the production of the R-type thermocouple. Contamination of the noble metal wires can lead to inaccuracies in the measured temperature over time (see Burton et al., 1992). An oversized hot junction bead can lead to excessive amount of heat loss. Cracking and delaminating of the ceramic coating can lead to higher temperature measurements due to catalytic effects. Thus, the following procedures are recommended for the fabrication of the R-type thermocouple:

- Wipe clean the R-type TC wires (Omega Engineering Model SPPL-005 and SP13RH-005) with either methanol or acetone. Make sure to leave no residue on the wire surface. This is particularly critical for the hot junction leads.
- Place the hot junction leads in the grounding clamp of the TC welder (Tigtech Model 116 SRL) making sure that the two leads are in contact with each other and do not protrude from the base of the grounding clamp for more than 2 mm.
- Turn on the TC welder and set the current flow to medium and the time to minimum.
- Place the grounding clamp-TC wire arrangement in the TC welder and purge the welder with argon for 5 s and then immediately activate the welding process by pressing the “weld” button. This completes the welding process.

- Check for continuity with a digital multimeter (e.g., Fluke Model 87 True RMS Digital Multimeter) making sure that the bead is properly formed and that the bead size (or diameter) is at most twice that of the wire diameter.

- Insert the welded R-type wires into the protective 1/8 in (0.3175 mm), double bore ceramic sheath (Omega Engineering Model TRX04018) and cut to length.

- Secure the ceramic sheath and TC wires in an R-type mini plug (Omega Engineering Model SMP-R-M) making sure that the polarity is correct by connecting to a digital TC reader (Fluke Model 714 Thermocouple Calibrator).

- The protective ceramic tip coating is fabricated by dipping the hot junction tip into a small solution of the ceramic paste (Aremco Model Ceramabond 569). Initially, a thin layer is formed on the TC wire. Air dry this initial layer for about half an hour and repeat the dipping-drying process for another two coatings. The three layers of ceramic coating are necessary to prevent cracking and delaminating. (Note the Ceramabond has a shelf life of six months after which the paste hardens and looses its adhesive properties.)

- Cure the coated TC in a low temperature oven (Blue M Model Single Wall Gravity Convection Laboratory Oven) by slowly ramp up the oven temperature. Dwell times of two hours are required at 60°C, 100°C and 150°C. The slow drying process allows moisture to gradually evaporate from the paste and prevents cracking. In addition, the initial oven heating process allows the paste to cure and bind to the TC and ceramic sheath under moderate temperature and thermal expansion conditions.

- Once the low temperature curing process is complete, the TC is inspected for cracks, particularly, at the paste-sheath interface. If cracks are detected, then the ceramic coating is dissolved in water and a new tip coating is fabricated per the above instructions.

In general, the R-type TCs fabricated have a maximum use life of approximately 200 hours after which cracking and delaminating occur.

D.2 JSR COMBUSTION GAS TEMPERATURE CORRECTION ANALYSIS

The R-type TC temperature correction analysis is mainly based on a three-body radiative heat transfer exchange between the hot TC tip, the reactor wall and the reactor cold spots. The measured TC temperature is lower than the actual gas temperature due to radiative losses to the reactor wall and reactor cold spots and due to conductive losses along the TC wires and along the TC ceramic sheath that is exposed to the hot combustion gases inside the JSR. The TC wires and exposed sheath segment are lumped as one body and is termed the TC tip. The lumping assumption is valid since the JSR temperature is essentially uniform between the standard temperature measuring location and the reactor wall as shown in Figure 2.6. Thus, the portion of the TC assembly that is within the JSR is assumed to be at the combustion gas temperature as shown in Figure D.1, minus the radiative and conductive losses.

Under steady state conditions, the heat exchange between the TC tip and its surrounding can be written as:

$$\dot{Q}_{convection} + \dot{Q}_{catalytic} = \dot{Q}_{raditaion} + \dot{Q}_{conduction} \text{ .... Eq. I.1}$$

where $\dot{\mathrm{Q}}_{\mathrm{convection}}$, $\dot{\mathrm{Q}}_{\mathrm{catalytic}}$, $\dot{\mathrm{Q}}_{\mathrm{radiation}}$ and $\dot{\mathrm{Q}}_{\mathrm{conduction}}$ are the net heat transfer rates (or fluxes) due to convective, catalytic, radiative and conductive effects. Catalytic effects are negligible (see Figure 2.21) since a ceramic coating is placed over the surface of the hot junction bead. Although conduction losses are generally low (< 5%), nevertheless they are incorporated into the correction analysis. Thus, the net heat balance is between the heat gain via convection and the heat loss via radiation and conduction. The individual fluxes can be further expanded. For the convective portion it is:

$$\dot{Q}_{convection} = h_{tip} \cdot A_{tip} \cdot (T_{gas} - T_{tip}) \text{ ....Eq. I.2}$$

where h_{tip} is the convective heat transfer coefficient of the hot combustion gases as they flow over the TC tip, A_{tip} is the surface area of the ceramic sheath that is exposed to the hot combustion gases (4.688e-5 m^2), T_{gas} is actual combustion gas temperature and T_{tip} is the measured TC temperature with a nominal value of 1760 K. The key element in Equation I.2 is the estimation of the heat transfer coefficient that will be discussed later.

The conduction term is based on heat loss along the TC wires and along the TC ceramic sheath material that is assumed to be a pin fin (see Mills, 1992) and can be expressed as:

$$\dot{Q}_{conduction} = \dot{Q}_{conduction,wire} + \dot{Q}_{conduction,sheath} \text{ ....Eq. I.3}$$

$$\dot{Q}_{conduction,wire} = 2 \cdot k_{TC} \cdot A_{TC,c} \cdot \frac{T_{TC} - T_{ambient}}{L_{TC,cold}} \text{ ....Eq. I.3a}$$

$$\dot{Q}_{conduction,sheath} = k_{sheath} \cdot A_{sheath,c} \cdot (T_{tip} - T_{ambient}) \cdot$$
$$tanh(\beta_{sheath} \cdot L_{TC,cold}) \text{ ....Eq. I.3b}$$

where k_{TC} is the thermal conductivity of the TC wires (75 W/m-K), $A_{TC,c}$ is the cross sectional area of the TC wires (1.267e-8 m^2), T_{TC} is measured TC temperature and is the equal to T_{tip}, $T_{ambient}$ is the ambient room temperature with a nominal value of 300 K, the length of the cold TC wires is $L_{TC,\ cold}$ (0.15 m), k_{sheath} is the thermal conductivity of the ceramic sheath material (8.5 W/m-K), $A_{sheath,c}$ is the cross sectional area of the ceramic sheath (7.107e-6 m^2) and β_{sheath} (= $\sqrt{\frac{h_{cold} \cdot P_{sheath}}{k_{sheath} \cdot A_{sheath,c}}}$) is the pin fin parameter of the ceramic sheath (182 m^{-1}). The term h_{cold} is the heat transfer coefficient of the cold air and P_{sheath} is the fin (or ceramic sheath) perimeter estimated to be 9.975e-3 m. Again, the key aspect is the estimation of the heat transfer coefficient.

The three-body interaction radiation term assumes that both the reactor wall and the reactor cold spots have radiosities equal to the respective black body emissive powers (i.e., $J = e_b$). Thus, the radiation loss for the TC tip can be expanded as:

$$\begin{aligned}\dot{Q}_{raditaion} &= \sigma \cdot \varepsilon_{tip} \cdot A_{tip} \cdot [T_{tip}^4 - \\ &\quad (F_{tip-wall,hot} \cdot \varepsilon_{wall,hot} \cdot T_{wall,hot}^4 + \\ &\quad F_{tip-wall,cold} \cdot \varepsilon_{wall,cold} \cdot T_{wall,cold}^4)] \quad \text{.....................................Eq. I.4}\end{aligned}$$

where σ is the Stefan-Boltzmann constant (5.67e-8 W/m^2-K), ε_{tip} is the TC tip emissivity as measured with the optical pyrometer (0.258), $F_{tip\text{-}wall,\ hot}$ is the estimated shape factor between the TC tip and the reactor wall (0.95), $\varepsilon_{wall,\ hot}$ is the estimated emissivity of the reactor wall (1.0), $T_{wall,\ hot}$ is the wall temperature as measured with the optical pyrometer (1602 K typically), $F_{tip\text{-}wall,\ cold}$ is the estimated shape factor between the TC tip and the reactor cold spots (0.05), $\varepsilon_{wall,\ cold}$ is the estimated emissivity of the cold spots (1.0) and $T_{wall,\ cold}$ is the average temperature of the cold spots (1000 K). The cold spots consist of the plugged viewing ports, the exhaust ports and the jet inlet. Since the viewing ports are plugged with ceramic rods, the estimated temperature of 1000 K is most likely an underestimate. The TC tip has an angled view of the exhaust ports and, thus, an estimate of 1000 K is reasonable. Lastly, an estimate of 1000 K for the jet inlet is a bit high, considering that the nominal injector temperature is between 523 and 623 K. Nevertheless, 1000 K is used for the "averaged" cold spot temperature. ε_{tip} is determined by adjusting the pyrometer emissivity setting until a match is achieved between the temperature as determined by the pyrometer and the corresponding measured TC value. The wall emissivities are assumed to be unity, consistent with the above assumption for radiosity.

The heat transfer coefficients (h_{tip} and h_{cold}) are determined by:

$$h = Nu_D \cdot \frac{k_{air}}{D} \text{ .... Eq. I.5}$$

where Nu_D is the Nusselt number for flow across a cylinder of diameter, D = 3.175e-3 m with Pr (Prandtl number) greater than 0.5 and k_{air} is the thermal conductivity of the air. From Mills (1992), the Nusselt number can be written as:

$$Nu_D = 1.15 \cdot Re_D^{1/2} \cdot Pr^{1/3} \text{ .... Eq. I.6}$$

where Re_D is the Reynolds number ($= \frac{D \cdot V}{\nu}$) based on the sheath or tip diameter, Pr is equal to 0.70 and 0.69 for the hot combustion gases and the cold ambient air, respectively and ν is the kinematic viscosity of air.

For the hot combustion gases, the velocity, V, term is replaced with V_{tip}, which represents the JSR recirculation zone gas velocity. V_{tip} is based on the reactor height ($H_{reactor}$ = 4.445e-2 m), the number of cycles, N_{cycle}, that the gases make in the JSR (assumed to be 4) and the mean or nominal JSR residence time, τ_{mean} (see Steele, 1995). The velocity can be expressed as:

$$V_{tip} = \frac{2.0 \cdot H_{reactor} \cdot N_{cycles}}{\tau_{mean}} \text{ .... Eq. I.7}$$

The V term for the airflow outside of the JSR is induced by the forced convective draft that is generated by the exhaust hood located directly above the JSR ceramic body and is measured to be about V_{cold} = 2.5 m/s with an airflow meter (Alnor Model Velometer Series 6000).

The thermal conductivity, k, and the kinematic viscosity, ν, of both the hot gases and cold air can be determined by the following second order polynomials:

$$k_{air} = 7.9 \cdot 10^{-3} + 6.476 \cdot 10^{-5} \cdot T_{air} - 5.607 \cdot 10^{-9} \cdot T_{air}^{2} \text{ ....Eq. I.8}$$

$$\nu = -1.066 \cdot 10^{-5} + 6.585 \cdot 10^{-8} \cdot T_{air} + 6.191 \cdot 10^{-11} \cdot T_{air}^{2} \text{ ....Eq. I.9}$$

where T_{air} is substituted with T_{gas} for the hot combustion gases and $T_{ambient}$ for the outside air.

The actual correction routine is located in the \Temperature Correction\ folder. The program is based on estimating (by using the Goal Seek command in Excel) the combustion gas temperature (T_{gas}) to match the rate of convective heat transfer as determined by $\dot{Q}_{convection}$ to that of the sum of $\dot{Q}_{radiation}$ and $\dot{Q}_{conduction}$. In general, T_{gas} is approximately 30 to 50 K higher than the measured TC temperature.

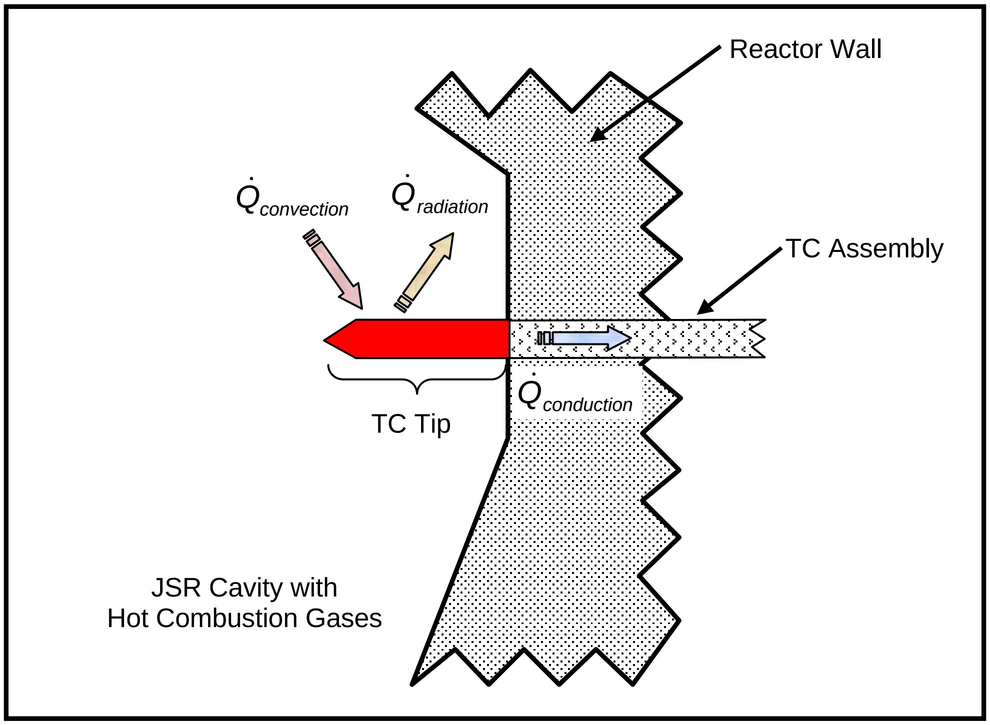

Figure D.1. Schematic Diagram of the TC Tip which Includes All Parts of the TC Assembly that is Exposed to the Hot Combustion Gases.

APPENDIX E: FLUKE NETDAQ DATA ACQUISITION SYSTEM SETUP FILES

Following are setup files for the Fluke NetDAQ data loggers. Tables E.1 through E.3 are setup files for the operation of the SPP-JSR. Notice that the fast responding pressure sensors are connected to the 1 kHz Model 2645A data logger. Calibration constants for the emissions analyzers are determined by measuring the VDC output as the analyzers are zeroed and spanned. The DC voltage is measured with a Fluke Model 87 True RMS Digital Multimeter. Table E.4 is the setup file for the multi sampling height JSR. The setup files are located in the \NetDAQ\ folder. The spp.stp is the actual Fluke setup file that can only be executed in conjunction with the Fluke NetDAQ Logger software. Files netdaq1.txt, netdaq2.txt, netdaq3.txt, netdaq4.txt and netdaq.xls are the data logger configuration text file.

Table E.1. Setup File for Fluke Model NetDAQ 2640A Data Logger: Temperature Measurements for SPP-JSR Configuration.

INSTRUMENT CONFIGURATION - 01	
Description:	Temperature Measurements
Model:	2640A
Trigger Type:	Interval
Interval	1.000 sec
Interval	NA
Reading Rate:	Medium
Drift Correction:	Yes
Duration:	NA
Temp Units:	Celsius
Monitor Channel:	0102
Total Debounce:	Yes
Data File:	NetDAQ1
File Mode:	Append
File Format:	CSV

Channel	**Function**	**Range**	**Alarm 1**	**Alarm 2**	**Trigger**	**Mx+B**	**Units**	**Label**
0101	OFF	OFF	OFF	OFF	OFF	OFF	OFF	OFF
0102	TC	R	OFF	OFF	NA	OFF	°C	Reactor Viewing
0103	TC	K	OFF	OFF	NA	OFF	°C	Inlet Nozzle
0104	TC	K	OFF	OFF	NA	OFF	°C	Stage 2E IN
0105	TC	K	OFF	OFF	NA	OFF	°C	Stage 2E OUT
0106	TC	K	OFF	OFF	NA	OFF	°C	Stage 2 IN
0107	TC	K	OFF	OFF	NA	OFF	°C	Stage 2 OUT
0108	TC	K	OFF	OFF	NA	OFF	°C	Stage 1E
0109	TC	K	OFF	OFF	NA	OFF	°C	Stage 1E
0110	TC	K	OFF	OFF	NA	OFF	°C	Atomizer
0111	OFF	OFF	OFF	OFF	OFF	OFF	OFF	OFF
0112	TC	K	OFF	OFF	NA	OFF	°C	Stage 2 Heater
0113	TC	K	OFF	OFF	NA	OFF	°C	Stage 1 Heater
0114	TC	K	OFF	OFF	NA	OFF	°C	Ceramic 0.00T
0115	TC	K	OFF	OFF	NA	OFF	°C	Ceramic 1.25T
0116	TC	K	OFF	OFF	NA	OFF	°C	Ceramic 2.25T
0117	TC	K	OFF	OFF	NA	OFF	°C	Ceramic 1.50S
0118	TC	K	OFF	OFF	NA	OFF	°C	Ceramic 3.00S
0119	TC	K	OFF	OFF	NA	OFF	°C	Ceramic 4.50S
0120	TC	K	OFF	OFF	NA	OFF	°C	Ambient

Table E.2. Setup File for Fluke Model NetDAQ 2640A Data Logger: Flow Rate and Emission Measurements for SPP-JSR Configuration.

INSTRUMENT CONFIGURATION - 02

Description:	Concentration and Flow Rate Measurements
Model:	2640A
Trigger Type:	Interval
Interval	1.000 sec
Interval	NA
Reading Rate:	Medium
Drift Correction:	Yes
Duration:	NA
Temp Units:	Celsius
Monitor Channel:	0215
Total Debounce:	Yes
Data File:	NetDAQ2
File Mode:	Append
File Format:	CSV

Channel	Function	Range	Alarm 1	Alarm 2	Trigger	Mx+B	Units	Label
0201	OFF	OFF	OFF	OFF	OFF	OFF	OFF	OFF
0202	VDC	30 V	OFF	OFF	NA	ON	ppmv	2.5 ppmv NOx
0203	VDC	30 V	OFF	OFF	NA	ON	ppmv	10 ppmv NOx
0204	VDC	30 V	OFF	OFF	NA	ON	ppmv	25 ppmv NOx
0205	VDC	30 V	OFF	OFF	NA	ON	ppmv	100 ppmv NOx
0206	VDC	30 V	OFF	OFF	NA	ON	ppmv	2500 ppmv CO
0207	VDC	30 V	OFF	OFF	NA	ON	% Vol.	1% Vol. CO
0208	VDC	30 V	OFF	OFF	NA	ON	% Vol.	2% Vol. CO
0209	VDC	30 V	OFF	OFF	NA	ON	% Vol.	% Vol. CO2
0210	VDC	30 V	OFF	OFF	NA	ON	% Vol.	% Vol. O2
0211	OFF	OFF	OFF	OFF	OFF	OFF	OFF	OFF
0212	VDC	30 V	OFF	OFF	NA	ON	SLPM	Primary Air
0213	VDC	30 V	OFF	OFF	NA	ON	SLPM	Secondary Air
0214	VDC	30 V	OFF	OFF	NA	ON	SLPM	Atomizer Air
0215	VDC	30 V	OFF	OFF	NA	ON	SLPM	Gaseous Fuel
0216	OFF	OFF	OFF	OFF	OFF	OFF	OFF	OFF
0217	OFF	OFF	OFF	OFF	OFF	OFF	OFF	OFF
0218	OFF	OFF	OFF	OFF	OFF	OFF	OFF	OFF
0219	OFF	OFF	OFF	OFF	OFF	OFF	OFF	OFF
0220	OFF	OFF	OFF	OFF	OFF	OFF	OFF	OFF

Table E.3. Setup File for Fluke Model NetDAQ 2645A Data Logger: Pressure and Temperature Measurements for SPP-JSR Configuration.

INSTRUMENT CONFIGURATION - 03

Description:	Temperature and Pressure Measurements
Model:	2645A
Trigger Type:	Interval
Interval	1.000 sec
Interval	NA
Reading Rate:	Slow (High Res.)
Drift Correction:	Yes
Duration:	NA
Temp Units:	Celsius
Monitor Channel:	0305
Total Debounce:	Yes
Data File:	NetDAQ3
File Mode:	Append
File Format:	CSV

Channel	**Function**	**Range**	**Alarm 1**	**Alarm 2**	**Trigger**	**Mx+B**	**Units**	**Label**
0301	OFF	OFF	OFF	OFF	OFF	OFF	OFF	OFF
0302	TC	R	OFF	OFF	NA	OFF	°C	Reactor
0303	VDC	30 V	OFF	OFF	NA	ON	psig	Stage 2E IN
0304	VDC	30 V	OFF	OFF	NA	ON	psig	Stage 2E OUT
0305	VDC	30 V	OFF	OFF	NA	ON	psig	Stage 2 IN
0306	VDC	30 V	OFF	OFF	NA	ON	psig	Stage 2 OUT
0307	VDC	30 V	OFF	OFF	NA	ON	psig	Stage 1E
0308	VDC	30 V	OFF	OFF	NA	ON	psig	Stage 1E
0309	VDC	30 V	OFF	OFF	NA	ON	psig	Atomizer
0310	VDC	30 V	OFF	OFF	NA	ON	psig	Atomizer Line
0311	OFF	OFF	OFF	OFF	OFF	OFF	OFF	OFF
0312	VDC	30 V	OFF	OFF	NA	ON	psig	Label
0313	VDC	30 V	OFF	OFF	NA	ON	psig	Label
0314	VDC	30 V	OFF	OFF	NA	ON	psig	Label
0315	OFF	OFF	OFF	OFF	OFF	OFF	OFF	OFF
0316	OFF	OFF	OFF	OFF	OFF	OFF	OFF	OFF
0317	OFF	OFF	OFF	OFF	OFF	OFF	OFF	OFF
0318	OFF	OFF	OFF	OFF	OFF	OFF	OFF	OFF
0319	OFF	OFF	OFF	OFF	OFF	OFF	OFF	OFF
0320	OFF	OFF	OFF	OFF	OFF	OFF	OFF	OFF

Table E.4. Setup File for Fluke Model NetDAQ 2645A Data Logger: Temperature Measurements for Multi Sampling Height JSR Configuration.

INSTRUMENT CONFIGURATION - 04	
Description:	Temperature Measurements
Model:	2645A
Trigger Type:	Interval
Interval	1.000 sec
Interval	NA
Reading Rate:	Slow (High Res.)
Drift Correction:	Yes
Duration:	NA
Temp Units:	Celsius
Monitor Channel:	0401
Total Debounce:	Yes
Data File:	NetDAQ4
File Mode:	Append
File Format:	CSV

Channel	**Function**	**Range**	**Alarm 1**	**Alarm 2**	**Trigger**	**Mx+B**	**Units**	**Label**
0401	TC	R	OFF	OFF	NA	OFF	°C	Reactor Viewing
0402	TC	K	OFF	OFF	NA	OFF	°C	Top Center 1.00
0403	TC	K	OFF	OFF	NA	OFF	°C	Top Center 0.50
0404	TC	K	OFF	OFF	NA	OFF	°C	Top Center 0.00
0405	TC	K	OFF	OFF	NA	OFF	°C	W. Side 1: 1.250
0406	TC	K	OFF	OFF	NA	OFF	°C	W. Side 1: 0.875
0407	TC	K	OFF	OFF	NA	OFF	°C	W. Side 1: 0.500
0408	TC	K	OFF	OFF	NA	OFF	°C	W. Side 2: 1.250
0409	TC	K	OFF	OFF	NA	OFF	°C	W. Side 2: 0.875
0410	TC	K	OFF	OFF	NA	OFF	°C	W. Side 2: 0.500
0411	OFF	OFF	OFF	OFF	OFF	OFF	OFF	OFF
0412	TC	K	OFF	OFF	NA	OFF	°C	W. Side 3: 1.250
0413	TC	K	OFF	OFF	NA	OFF	°C	W. Side 3: 0.875
0414	TC	K	OFF	OFF	NA	OFF	°C	W. Side 3: 0.500
0415	TC	K	OFF	OFF	NA	OFF	°C	W. Side 4: 1.250
0416	TC	K	OFF	OFF	NA	OFF	°C	W. Side 4: 0.875
0417	TC	K	OFF	OFF	NA	OFF	°C	W. Side 4: 0.500
0418	TC	K	OFF	OFF	NA	OFF	°C	Label
0419	TC	K	OFF	OFF	NA	OFF	°C	Label
0420	TC	K	OFF	OFF	NA	OFF	°C	Label

APPENDIX F: SECOND GENERATION INJECTOR DRAWINGS

The following are the CAD drawings used for the fabrication of the 2nd generation injector. The representative assembly drawing is shown in Figure 4.1. All components are constructed from stainless steel and are assembled via T.I.G. welding and silver soldering. Mr. Tom Collins (206-543-5289) of the Mechanical Engineering Department machine shop is the technical contact for parts fabrication and assembly. The CAD drawings for the following parts are located in the \CAD Drawings\ folder.

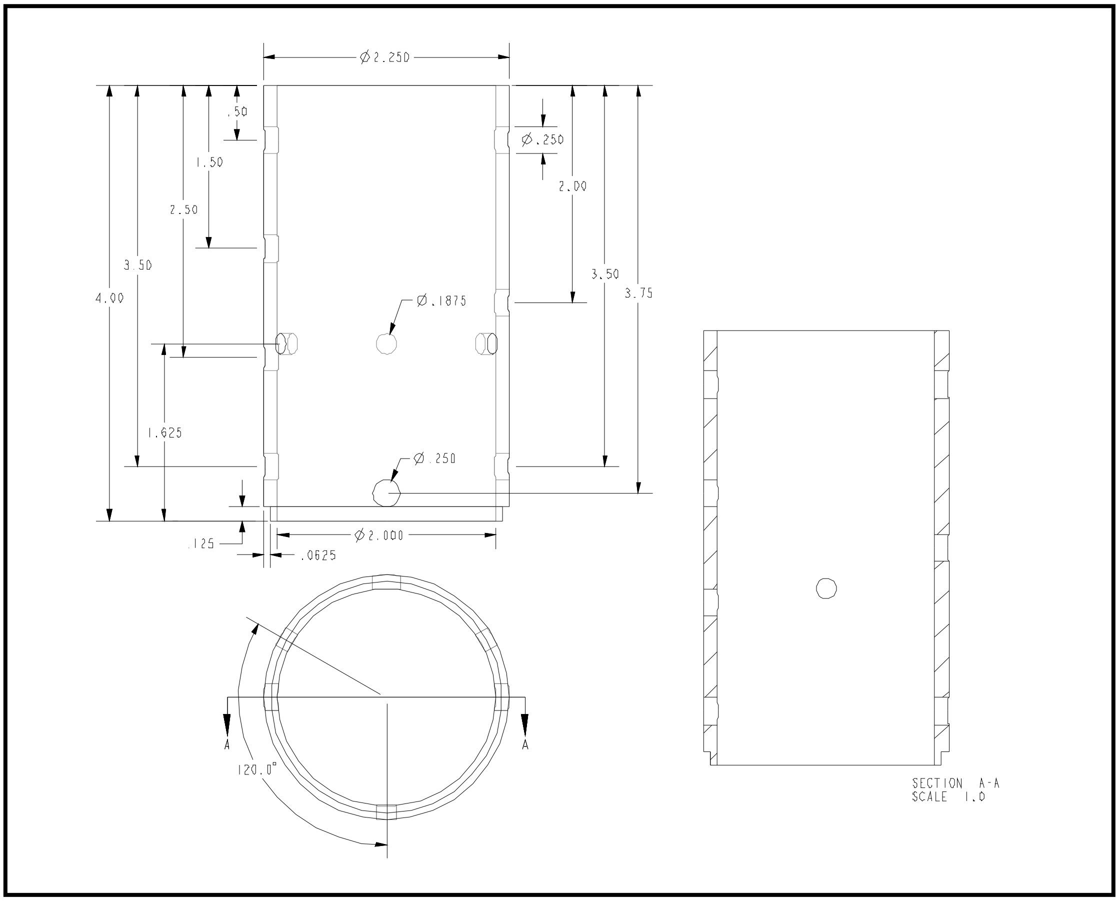

Figure F.1. CAD Drawing of the 2nd Generation Injector – Main Mixing Section (Filename: secondtube.drw).

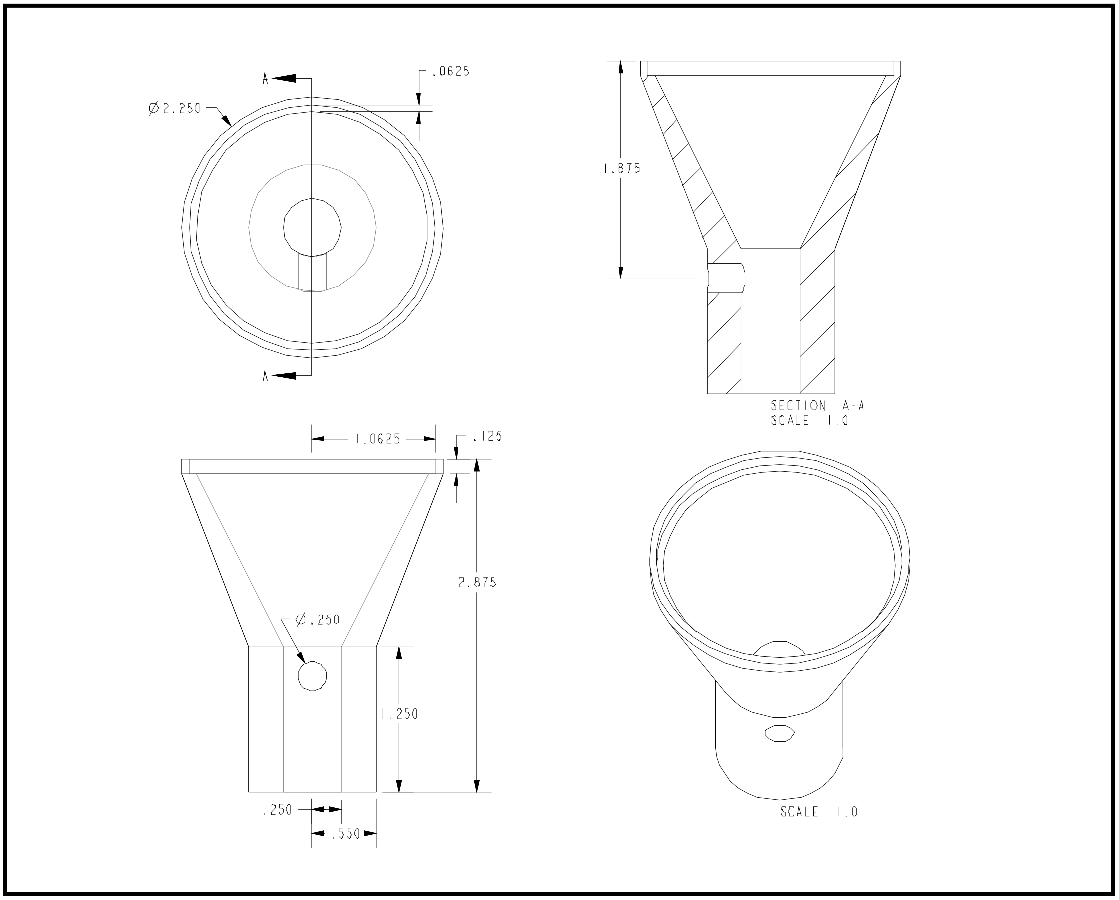

Figure F.2. CAD Drawing of the 2nd Generation Injector – Heater Interface and Air Distribution Section (Filename: secondcone.drw).

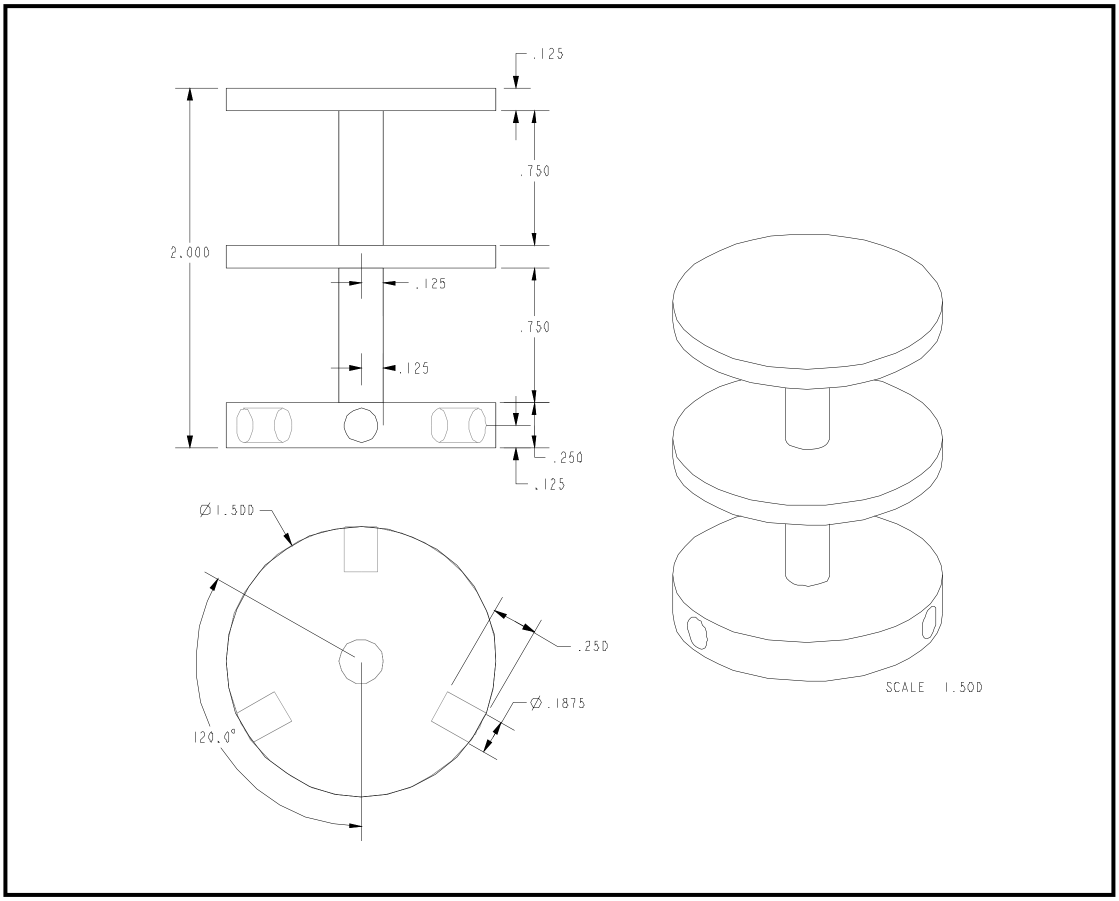

Figure F.3. CAD Drawing of the 2nd Generation Injector – Mixing Baffles (Filename: secondcone.drw).

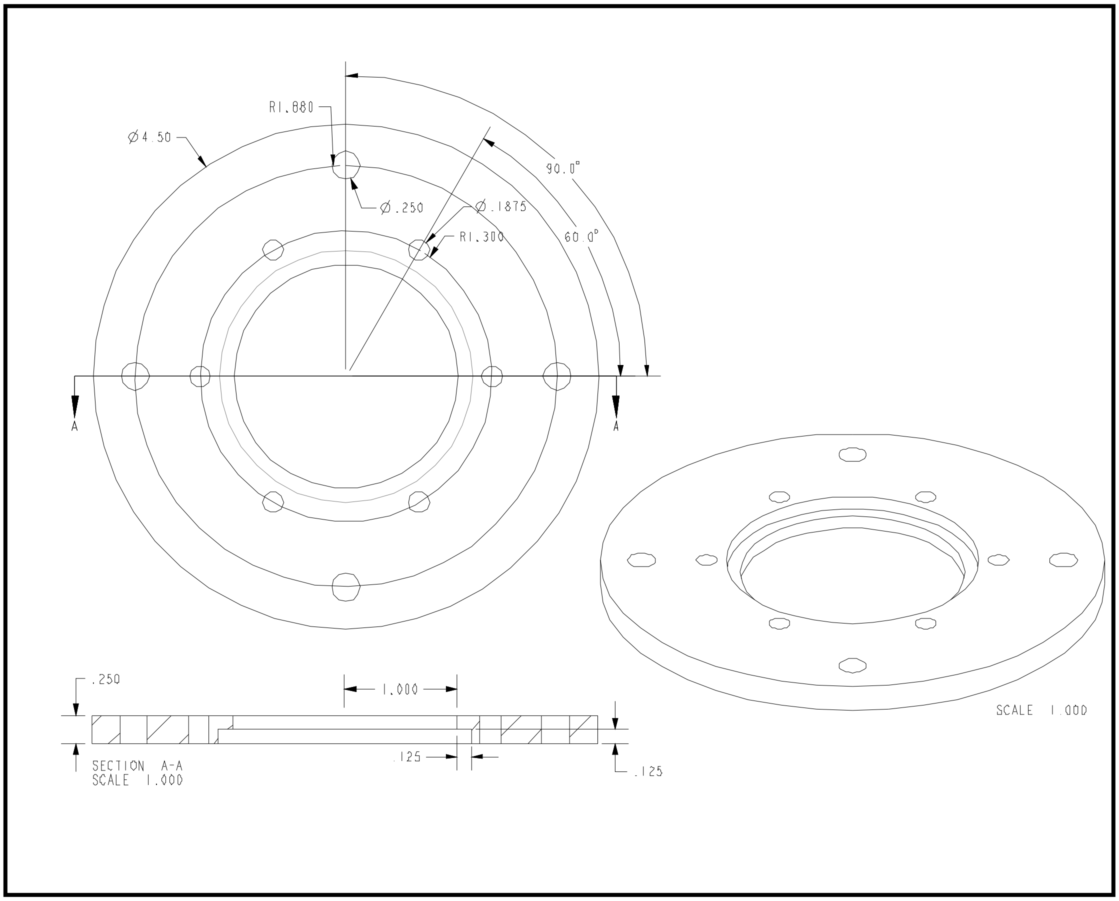

Figure F.4. CAD Drawing of the 2nd Generation Injector – JSR Interface and Top Flange (Filename: secondflange.drw).

APPENDIX G: STAGED PREVAPORIZING-PREMIXING INJECTOR DRAWINGS

Dr. Michael Benjamin (440-954-8105) and Mr. Jim Duncan (440-954-8117) both of whom are with the Gas Turbine Fuel System Division of the Parker Hannifin Corporation (PHC) provided assistance in the design and fabrication of the prototype SPP injector. Due to legal and proprietary concerns, detailed CAD drawings of the SPP are not presented. Shown in Figure G.1 is the overall assembly drawing of the SPP prototype that is constructed from 316 stainless steel. . Detailed part and assembly CAD drawings of the air cooled liquid fuel nozzle that is used in conjunction with the SPP are shown in Figures G.2 through G.4. Assembly of all SPP parts is via high temperature brazing with nickel based compounds – a manufacturing process proprietary to PHC. The technical contact for the fabrication of the SPP is Dr. Michael Benjamin. The following CAD drawings are located in the \CAD Drawings\ folder.

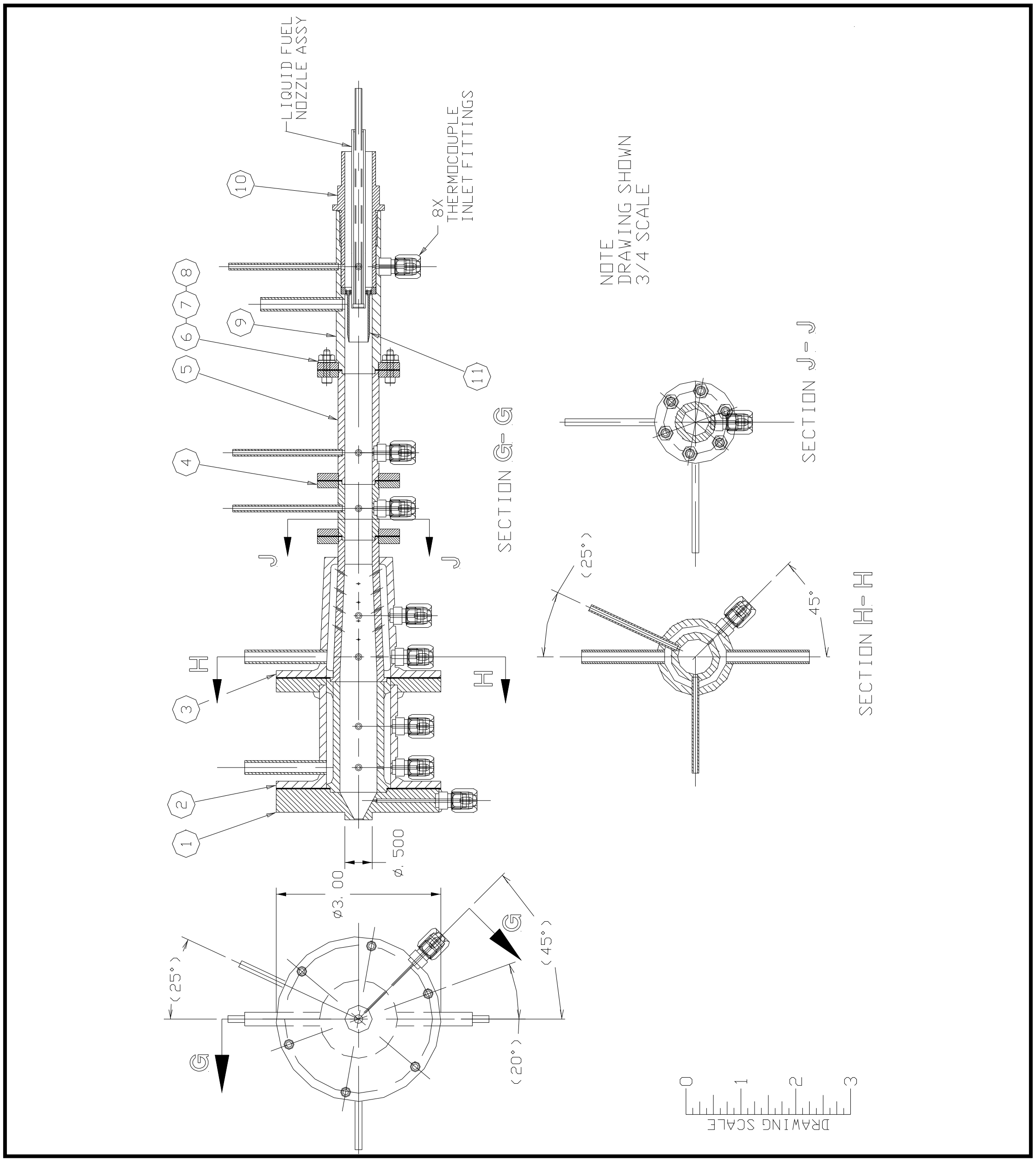

Figure G.1. CAD Drawing of the SPP Prototype – Overall Assembly of the SPP (Filename: spp.dwg).

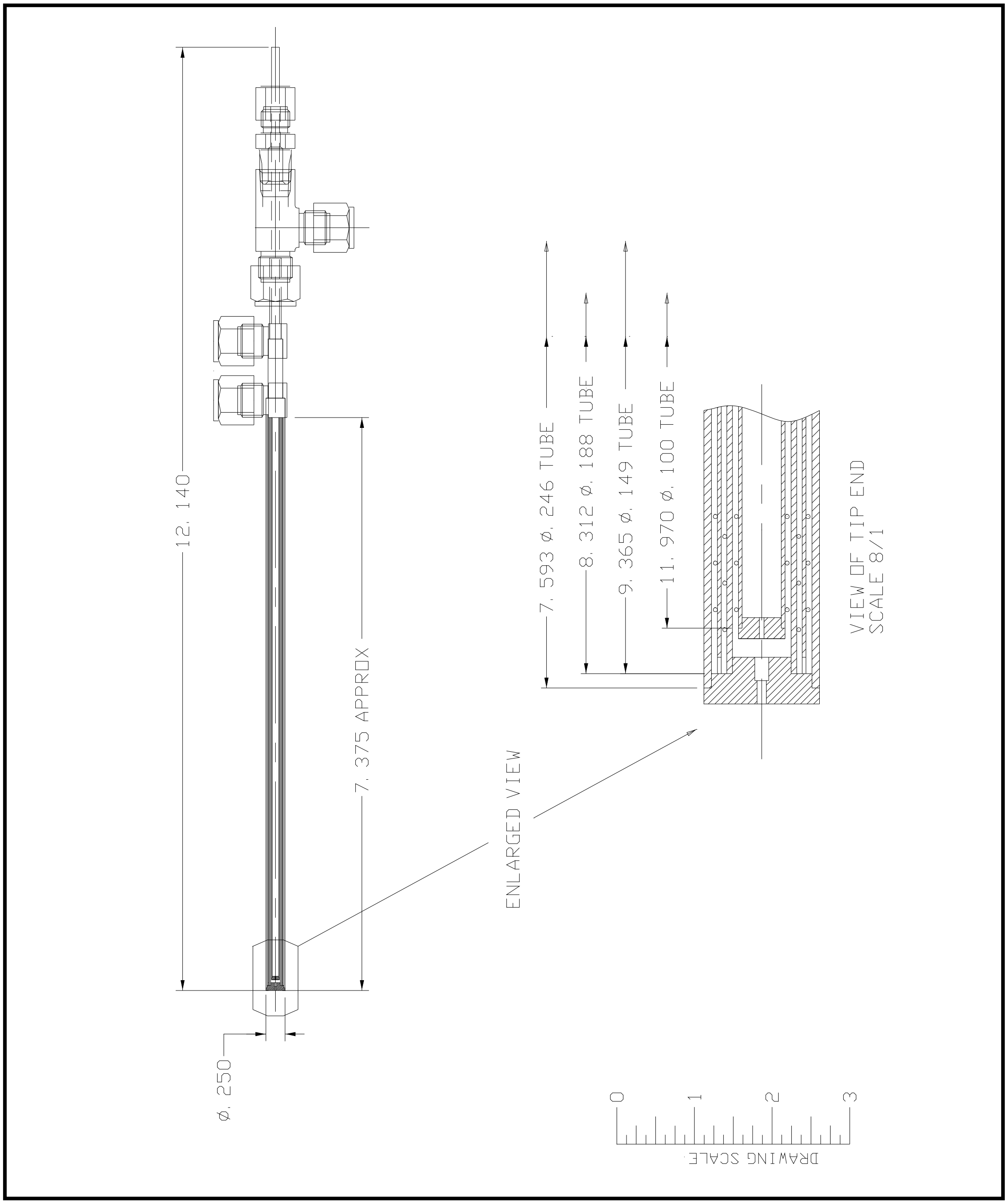

Figure G.2. CAD Drawing of the SPP Prototype – Overall Assembly of the Air Cooled Nukiyama-Tanasawa Type Liquid Fuel Atomizer (Filename: sppatomizer.dwg).

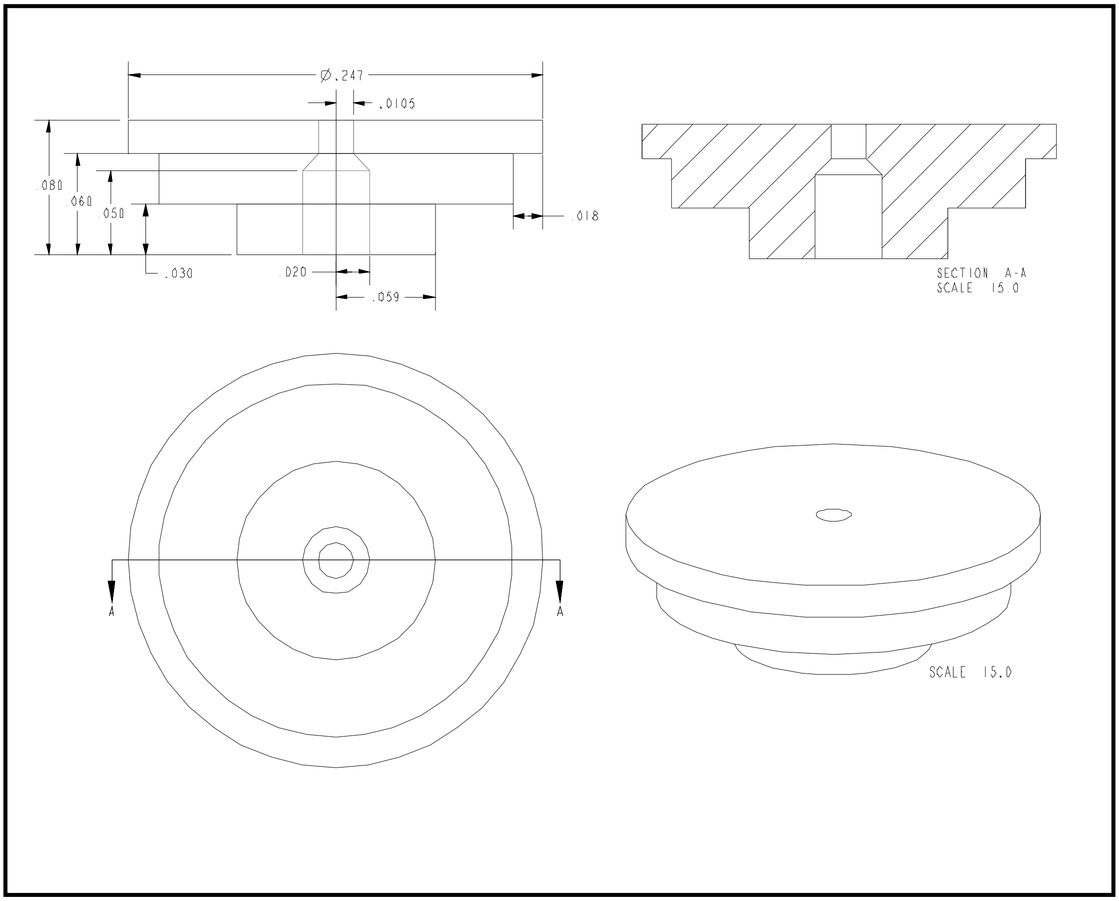

Figure G.3. CAD Drawing of the SPP Prototype – Air Cooled Nozzle Outer Tip (Filename: sppatomizertipout.drw).

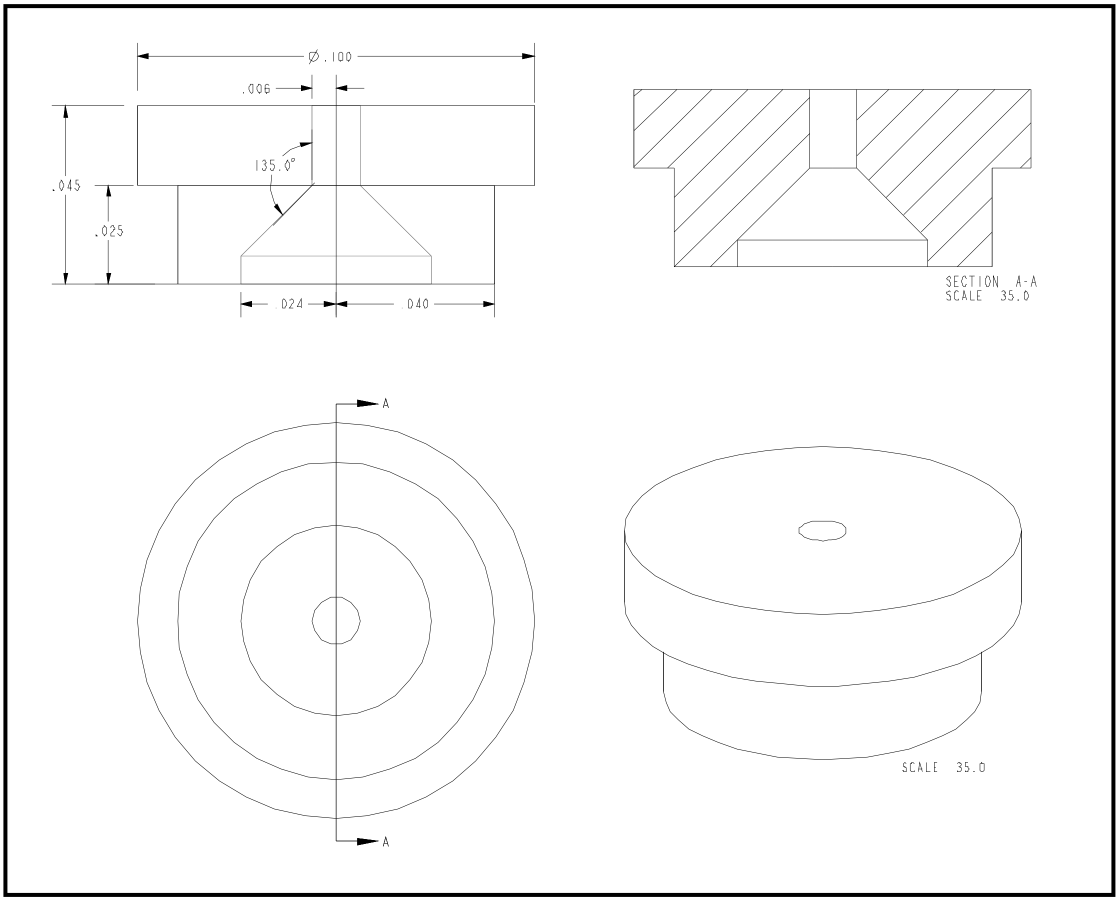

Figure G.4. CAD Drawing of the SPP Prototype – Air Cooled Nozzle Inner Tip (Filename: sppatomizertipin.drw).

APPENDIX H: EXPERIMENTAL DATA AND CRM RESULTS FOR THE SPP-JSR CONFIGURATION

All experimental data and CRM results are located in the \SPP Results\ folder. For ease of reference the corrected NO_X (ppmv, dry, 15% O_2) and measured CO (% volume, dry, actual O_2) results for studies on the effects of fuel type for the following cases are provided on the following pages:

- Long SPP Configuration Experimental Results
- Short SPP Configuration Experimental Results
- Single PSR Modeling Results
- Two PSR in Series Modeling Results
- Two PSR in Series + PFR Modeling Results
- Three PSR in Series Modeling Results

Table H.1. Effects of Fuel Type – Long SPP Configuration Experimental Results.

Fuel	***Split Conditions (flow, temp.)***	N_C	N_H	N_O	***C:H***	***FBN (ppm wt%)***	***Fuel NO (ppmvd, 15% O_2)***	ϕ	ϕ_{AVE}	***NO_X (ppmvd, 15% O_2)***	$NO_{X,AVE}$	***CO (% vol., dry, actual O_2)***	CO_{AVE}
Methanol	30/30, 150/350 30/30, 250/350	1	4	1	0.25	0	0.0	0.6023 0.6076	0.60	3.46 3.49	3.5	0.1962 0.2044	0.20
Methane	30/30, 150/350 30/30, 250/350 30/30, 350/350	1	4	0	0.25	0	0.0	0.6440 0.6453 0.6469	0.65	4.90 4.65 4.75	4.8	0.1901 0.2054 0.1840	0.19
Ethane	30/30, 150/350 30/30, 250/350 30/30, 350/350	2	6	0	0.33	0	0.0	0.6265 0.6218 0.6208	0.62	5.30 5.23 5.46	5.3	0.1686 0.1666 0.1829	0.17
Propane	30/30, 150/350 30/30, 250/350 30/30, 350/350	3	8	0	0.38	0	0.0	0.6339 0.6319 0.6379	0.63	5.61 5.85 6.02	5.8	0.2167 0.2340 0.2116	0.22
Pentane	30/30, 150/350 30/30, 250/350	5	12	0	0.42	0	0.0	0.6096 0.6141	0.61	7.12 7.07	7.1	0.2351 0.2974	0.27
Hexanes	30/30, 150/350 30/30, 250/350	6	14	0	0.43	0	0.0	0.6121 0.6122	0.61	7.31 7.31	7.3	0.2391 0.2412	0.24
Heptane	30/30, 150/350 30/30, 250/350	7	16	0	0.44	0	0.0	0.6119 0.6127	0.61	7.06 7.17	7.1	0.2442 0.2463	0.25
Dodecane	30/30, 150/350 30/30, 250/350	12	26	0	0.46	0	0.0	0.6294 0.6272	0.63	6.64 6.67	6.7	0.2473 0.2453	0.25
Hexadecane	30/30, 180/350 30/30, 250/350	16	34	0	0.47	0	0.0	0.6191 0.6154	0.62	6.73 6.77	6.8	0.2504 0.2463	0.25
Benzene	30/30, 150/350 30/30, 250/350	6	6	0	1.00	0	0.0	0.5727 0.5740	0.57	10.08 10.06	10.1	0.4016 0.4037	0.40
Toluene	30/30, 150/350 30/30, 250/350	7	8	0	0.88	0	0.0	0.5815 0.5817	0.58	10.17 10.17	10.2	0.4180 0.4108	0.41
K-LN	30/30, 150/350 30/30, 250/350	5.9	12.45	small	0.47	< 1	0.0	0.6074 0.6046	0.61	7.79 7.71	7.8	0.2667 0.2667	0.27
USOR-LN	30/30, 150/350 30/30, 250/350	-	-	small	0.44	< 3	0.0	0.5927 0.5900	0.59	7.51 7.54	7.5	0.2514 0.2524	0.25
C-LSD	30/30, 180/350 30/30, 250/350	13.77	26.28	small	0.52	46	1.5	0.6230 0.6230	0.62	8.70 8.81	8.8	0.2872 0.2780	0.28
USOR-LSD	30/30, 180/350 30/30, 250/350	-	-	small	0.57	49	1.6	0.6241 0.6259	0.63	9.36 9.55	9.5	0.2851 0.2821	0.28
T-LSD	30/30, 180/350 30/30, 250/350	-	-	small	0.57	91	3.0	0.6344 0.6330	0.63	11.37 11.39	11.4	0.3005 0.2994	0.30
T-HSD	30/30, 180/350 30/30, 250/350	-	-	small	0.58	84	2.8	0.6286 0.6281	0.63	11.44 11.45	11.4	0.2923 0.2943	0.29

Table H.2. Effects of Fuel Type – Short SPP Configuration Experimental Results.

Fuel	***Split Conditions (flow, temp.)***	***N_C***	***N_H***	***N_O***	***C:H***	***FBN (ppm wt%)***	***Fuel NO (ppmvd, 15% O_2)***	***ϕ***	***ϕ_{AVE}***	***NO_X (ppmvd, 15% O_2)***	***$NO_{X,AVE}$***	***CO (% vol., dry, actual O_2)***	***CO_{AVE}***
Methane	30/30, 150/350 30/30, 250/350	1	4	0	0.25	0	0.0	0.6524 0.6423	0.65	5.14 4.99	5.1	0.2085 0.1993	0.20
Ethane	30/30, 150/350 30/30, 250/350	2	6	0	0.33	0	0.0	0.6310 0.6235	0.63	6.25 6.21	6.2	0.1972 0.1993	0.20
Propane	30/30, 150/350 30/30, 250/350	3	8	0	0.38	0	0.0	0.6324 0.6245	0.63	6.50 6.46	6.5	0.2351 0.2269	0.23
Hexanes	30/30, 150/350 30/30, 250/350	6	14	0	0.43	0	0.0	0.6280 0.6244	0.63	7.10 7.14	7.1	0.2565 0.2545	0.26
Hexadecane	30/30, 150/350 30/30, 250/350	16	34	0	0.47	0	0.0	0.6235 0.6212	0.62	7.07 7.09	7.1	0.2749 0.2708	0.27
K-LN	30/30, 150/350 30/30, 250/350	5.9	12.45	small	0.47	< 1	0.0	0.6194 0.6168	0.62	7.63 7.66	7.6	0.2739 0.2749	0.27
T-HSD	30/30, 150/350 30/30, 250/350	-	-	small	0.58	84	2.8	0.6140 0.6140	0.61	11.40 11.47	11.4	0.2189 0.3138	0.27

Table H.3. Effects of Fuel Type – Single PSR Modeling Results.

Mechanism	***Fuel***	τ ***(s)***	***T (K)***	***CO (% vol.)***	***NO_C (ppmv)***
MB 1989	Methane	2.3E-03	1790	0.5376	4.928
	Ethane	2.3E-03	1790	0.6535	6.616
MB 1989-CO/H_2	CO:H_2=1:2	2.3E-03	1790	0.6275	5.862
	CO:H_2=2:3	2.3E-03	1790	0.6979	6.614
	CO:H_2=3:4	2.3E-03	1790	0.7701	6.644
	CO:H_2=5:6	2.3E-03	1790	0.7775	7.112
	CO:H_2=6:7	2.3E-03	1790	0.7901	7.164
	CO:H_2=7:8	2.3E-03	1790	0.7998	7.198
	CO:H_2=12:13	2.3E-03	1790	0.8692	6.988
	CO:H_2=16:17	2.3E-03	1790	0.8560	7.173
	CO:H_2=7:4	2.3E-03	1790	1.0610	9.329
	CO:H_2=2:1	2.3E-03	1790	1.0990	9.946
GRI 2.11	Methanol	2.3E-03	1790	0.5098	7.926
	Methane	2.3E-03	1790	0.4682	8.379
	Ethane	2.3E-03	1790	0.5464	10.370
GRI 3.0	Methanol	2.3E-03	1790	0.4768	4.640
	Methane	2.3E-03	1790	0.4392	7.260
	Ethane	2.3E-03	1790	0.5081	7.961
	Propane	2.3E-03	1790	0.5605	8.284
LQM-GRI 1999	Methanol	2.3E-03	1790	0.4856	2.301
	Methane	2.3E-03	1790	0.4442	6.724
	Ethane	2.3E-03	1790	0.4776	6.503
	Propane	2.3E-03	1790	0.5287	6.440
	Heptane	2.3E-03	1790	0.5515	6.896
	Benzene	2.3E-03	1790	0.7490	7.814

Table H.4. Effects of Fuel Type – Two PSRs in Series Modeling Results.

Mechanism	***Fuel***	***C:H***	τ_{psr1} ***(s)***	T_{psr1} ***(K)***	τ_{psr2} ***(s)***	T_{psr2} ***(K)***	***CO (% vol.)***	NO_C ***(ppmv)***
MB 1989	Methane	0.25	1.15E-04	1661	2.185E-03	1790	0.3286	2.899
	Ethane	0.33	1.15E-04	1599	2.185E-03	1790	0.3852	3.552
MB 1989-CO/H_2	CO:H_2=1:2	0.25	1.15E-04	1486	2.185E-03	1790	0.3634	3.088
	CO:H_2=2:3	0.33	1.15E-04	1397	2.185E-03	1790	0.4310	3.545
	CO:H_2=3:4	0.38	1.15E-04	1379	2.185E-03	1790	0.4863	3.638
	CO:H_2=5:6	0.42	1.15E-04	1327	2.185E-03	1790	0.5126	3.976
	CO:H_2=6:7	0.43	1.15E-04	1318	2.185E-03	1790	0.5252	4.033
	CO:H_2=7:8	0.44	1.15E-04	1312	2.185E-03	1790	0.5350	4.073
	CO:H_2=12:13	0.46	1.15E-04	1320	2.185E-03	1790	0.5808	3.994
	CO:H_2=16:17	0.47	1.15E-04	1302	2.185E-03	1790	0.5805	4.128
	CO:H_2=7:4	0.88	1.932E-04	1080	2.107E-03	1790	0.8605	6.174
	CO:H_2=2:1	1.00	2.481E-04	1083	2.052E-03	1790	0.8866	6.394
GR1 2.11	Methanol	0.20	1.15E-04	1666	2.185E-03	1790	0.2749	4.289
	Methane	0.25	1.15E-04	1702	2.185E-03	1790	0.2686	6.325
	Ethane	0.33	1.15E-04	1682	2.185E-03	1790	0.3137	5.897
GRI 3.0	Methanol	0.20	1.233E-04	1659	2.177E-03	1790	0.2784	2.485
	Methane	0.25	1.15E-04	1698	2.185E-03	1790	0.2464	6.189
	Ethane	0.33	1.15E-04	1678	2.185E-03	1790	0.2868	5.427
	Propane	0.38	1.15E-04	1687	2.185E-03	1790	0.3181	6.070
LQM-GRI 1999	Methanol	0.20	1.70E-04	1659	2.130E-03	1790	-	-
	Methane	0.25	1.15E-04	1697	2.185E-03	1790	0.2624	3.629
	Ethane	0.33	1.15E-04	1660	2.185E-03	1790	0.3015	3.133
	Propane	0.38	1.15E-04	1680	2.185E-03	1790	0.3059	3.629
	Heptane	0.44	1.15E-04	1642	2.185E-03	1790	0.3324	3.325
	Benzene	1.00	1.15E-04	1659	2.185E-03	1790	0.4280	3.332

Mechanism	***Fuel***	***C:H***	T_{psr1} ***(K)***	T_{psr2} ***(K)***	T_{PFR} ***(K)***	τ ***(ms)***	τ_1 / τ ***(%)***	τ_{PFR} ***(ms)***	***CO (% volume)***	***NO (ppmv, 15% O_2)***
GRI 3.0	Methanol	0.20	1659	1790	1790	2.3	5.4	0.075	0.20	2.5
	Methane	0.25	1698	1790	1790	2.3	5.0	0.075	0.19	6.3
	Ethane	0.33	1678	1790	1790	2.3	5.0	0.075	0.22	5.5
	Propane	0.375	1687	1790	1790	2.3	5.0	0.075	0.25	6.2

Table H.5. Effects of Fuel Type – Two PSRs in Series + PFR Modeling Results.

Table H.6. Effects of Fuel Type – Three PSRs in Series Modeling Results.

Mechanism	***Fuel***	***C:H***	τ_{psb} ***(s)***	T_{psb} ***(K)***	τ_{psr1} ***(s)***	T_{psr1} ***(K)***	τ_{psr2} ***(s)***	T_{psr2} ***(K)***	***CO (% vol.)***	NO_C ***(ppmv)***
MB 1989	Methane	0.25	7.122E-05	1544	2.3E-04	1790	1.999E-03	1790	0.2253	2.689
	Ethane	0.33	5.842E-05	1455	2.3E-04	1790	2.012E-03	1790	0.2744	3.421
MB 1989-CO/H_2	CO:H_2=1:2	0.25	3.240E-05	1115	2.3E-04	1790	2.038E-03	1790	0.2791	3.721
	CO:H_2=2:3	0.33	4.618E-05	1099	2.3E-04	1790	2.024E-03	1790	0.3167	4.201
	CO:H_2=3:4	0.38	5.073E-05	1097	2.3E-04	1790	2.019E-03	1790	0.3566	4.266
	CO:H_2=5:6	0.42	6.124E-05	1090	2.3E-04	1790	2.041E-03	1790	0.3583	4.564
	CO:H_2=6:7	0.43	6.333E-05	1089	2.3E-04	1790	2.040E-03	1790	0.3653	4.603
	CO:H_2=7:8	0.44	6.494E-05	1088	2.3E-04	1790	2.040E-03	1790	0.3706	4.630
	CO:H_2=12:13	0.46	6.446E-05	1089	2.3E-04	1790	2.040E-03	1790	0.4100	4.552
	CO:H_2=16:17	0.47	6.843E-05	1087	2.3E-04	1790	2.039E-03	1790	0.4025	4.655
	CO:H_2=7:4	0.88	1.932E-04	1071	2.3E-04	1790	2.011E-03	1790	0.5227	6.056
	CO:H_2=2:1	1.00	2.481E-04	1071	2.3E-04	1790	2.001E-03	1790	0.5445	6.421
GR1 2.11	Methanol	0.20	8.387E-05	1592	2.3E-04	1790	1.986E-03	1790	0.1768	4.629
	Methane	0.25	7.778E-05	1619	2.3E-04	1790	1.992E-03	1790	0.1792	5.992
	Ethane	0.33	8.674E-05	1606	2.3E-04	1790	1.983E-03	1790	0.2120	6.450
GRI 3.0	Methanol	0.20	1.233E-04	1658	2.3E-04	1790	1.947E-03	1790	0.1419	2.781
	Methane	0.25	7.339E-05	1602	2.3E-04	1790	1.997E-03	1790	0.1567	5.195
	Ethane	0.33	8.571E-05	1607	2.3E-04	1790	1.984E-03	1790	0.1805	5.217
	Propane	0.38	7.087E-05	1561	2.3E-04	1790	1.999E-03	1790	0.2162	5.871
LQM-GRI 1999	Methanol	0.20	1.703E-04	1659	2.3E-04	1790	1.900E-03	1790	-	-
	Methane	0.25	9.620E-05	1621	2.3E-04	1790	1.974E-03	1790	0.1464	2.888
	Ethane	0.33	1.040E-04	1610	2.3E-04	1790	1.966E-03	1790	0.1643	2.805
	Propane	0.38	7.472E-05	1547	2.3E-04	1790	1.995E-03	1790	0.1906	2.818
	Heptane	0.44	8.505E-05	1538	2.3E-04	1790	1.985E-03	1790	0.1993	2.871
	Benzene	1.00	3.033E-04	1657	2.3E-04	1790	1.767E-03	1790	0.2548	3.330

APPENDIX I: CHEMICAL KINETIC MECHANISMS

The various chemical kinetic mechanisms, the fuels tested, the CRM configuration tested and the corresponding output filename strings are listed in Table I.1. The CRM configuration listed in Table I.1 are: PSB = blowout PSR, PSR = single PSR, Dual PSR = two PSRs in series, Tri PSR = three PSRs in series and Dual PSR + PFR = two PSRs in series plus a single PFR. Only the single PSR solution was obtainable for the (*) fuels. All input file, output file and MARK III executable are located in the \CRM Results\ folder.

Table I.1. CRM Test Matrix and Output Filename.

Mechanism	***Fuel Tested***	***CRM Configuration.***	***Output Filename***
MB 1989	Methane Ethane CO/H_2	PSB PSR Dual PSR Tri PSR	mbpsb.dat mbpsr.dat mbdualpsr.dat mbtripsr.dat
GRI 2.11	Methanol Methane Ethane	PSB PSR Dual PSR Tri PSR	oldgripsb.dat oldgripsr.dat oldgridualpsr.dat oldgritripsr.dat
GRI 3.0	Methanol Methane Ethane Propane Ethylene Acetylene	PSB PSR Dual PSR Tri PSR Dual PSR + PFR	gripsb.dat gripsr.dat gridualpsr.dat gritripsr.dat gridualpsrpfr.dat
LQM-GRI 1999	Methanol* Methane Ethane Propane Heptane Benzene	PSB PSR Dual PSR Tri PSR	lqmgripsb.dat lqmgripsr.dat lqmgridualpsr.dat lqmgritripsr.dat

POCKET MATERIAL: ELECTRONIC COPY OF DISSERTATION

The CD-ROM located on the inside back cover contains the electronic version of all text, figures, tables, spreadsheets, CAD drawings and setup files presented and used in this dissertation. In order to utilizes these files the following programs are required for the execution of the corresponding file types:

- Microsoft Word: *.doc
- Microsoft Excel: *.xls
- Microsoft PowerPoint: *.ppt
- Parametric Pro Engineer: *.drw and *.prt
- Autodesk AutoCAD: *.dwg
- Visio Corp. Visio Technical: *.vsd
- Fluke NetDAQ Logger with Trending: *.stp

VITA

John C.Y. Lee

EDUCATION:

Ph.D., Mechanical Engineering, 2000

University of Washington, Seattle, Washington

M.S., Mechanical and Aerospace Engineering, 1991

State University of New York at Buffalo, Buffalo, New York

B.S.A.A.E., Aeronautical and Astronautical Engineering, 1989

Purdue University, West Lafayette, Indiana.

PROFESSIONAL EXPERIENCE:

Senior Combustion Engineer, 2000 – Present

SOLO Energy Corporation, Alameda, California